Pure

Bangor University

DOCTOR OF PHILOSOPHY

Observations of cold pool jets in the continental shelf of the Celtic Sea

Bibriezca, Laura Elena Carrillo

Award date:
2002

Awarding institution:
University of Wales, Bangor

Link to publication

General rights
Copyright and moral rights for the publications made accessible in the public portal are retained by the authors and/or other copyright owners and it is a condition of accessing publications that users recognise and abide by the legal requirements associated with these rights.

- Users may download and print one copy of any publication from the public portal for the purpose of private study or research.
- You may not further distribute the material or use it for any profit-making activity or commercial gain
- You may freely distribute the URL identifying the publication in the public portal ?

Take down policy
If you believe that this document breaches copyright please contact us providing details, and we will remove access to the work immediately and investigate your claim.

Download date: 16. Jun. 2024

University of Wales **BANGOR**

Observations of cold pool jets in the continental shelf of the Celtic Sea

A thesis submitted in accordance with the requirements of the University of Wales for the degree of Doctor of Philosophy.

By Laura Elena Carrillo Bibriezca

University of Wales Bangor
School of Ocean Sciences
Menai Bridge
Anglesey
United kingdom

March 2002

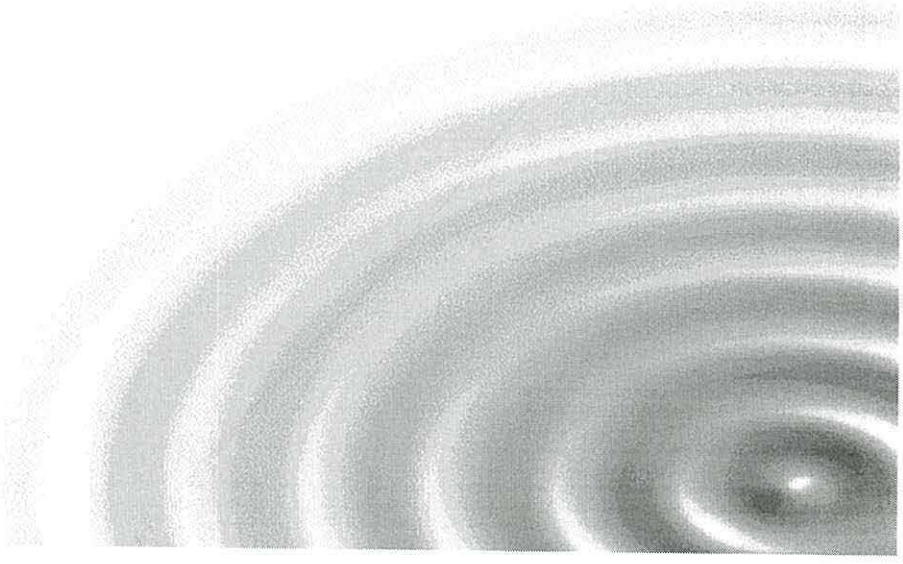

ABSTRACT

An observational study of the summer circulation in the Celtic Sea is presented which focuses on the density-driven (baroclinic) near-surface currents associated with bottom fronts. A combination of instrumentation, such as ship-mounted ADCP, satellite-tracked drifters, bottom-mounted ADCP and towed undulating CTD vehicle (Scanfish), was used. The analysed data set constitutes the first direct current measurements and extensive hydrographic data collected during the summertime in the Celtic Sea to date. The extensive analysis of the resulting data set is presented. In particular, a comparison of two detiding techniques for ship-mounted ADCP data has been performed and an alternative approach to removing the tidal signal is proposed.

The collected high-resolution hydrographic information allows us to define a dense, cold-pool bottom structure bounded by sharp bottom fronts. Although the dense cold-pool is mainly a thermal structure, salinity contributes to reinforce the frontal areas. Moreover, the findings have revealed that strong near-surface currents (up to 0.30 - 0.40 m s^{-1}) can be observed at the margin of the sharp bottom fronts. The area with the strongest horizontal density gradients was the St. George's Channel, where a cyclonic circulation was observed. The exchange between the Celtic Sea and the Irish Sea, seems to be restricted, however, but intermittent intrusion of surface water may occur with considerable velocities (up to 0.30 m s^{-1}). These results have shown the importance of baroclinic conditions for maintenance of near-surface flows and have shown flow variability away from frontal regions. In addition, other structures such as an eddy-like feature can co-exist with bottom fronts, which can influence the predicted density-driven flows.

The results of this thesis add to the hypothesis that baroclinic conditions during the summer, in particular bottom fronts, can drive, in a broad context, the residual circulation in shelf seas.

ACKNOWLEDGEMENTS

I would like to express my acknowledgement to my supervisor Dr. Ed Hill, who found time for a high-quality of supervision, gave invaluable guidance and support during the development of this study, and helped me see ways of making it a better Ph.D. thesis.

I have also benefited from detailed comments, attention and encouragement from Dr. Juan Brown and the invaluable expert technical support from Dr. Liam Fernand.

I appreciate the continuous flow of advice and support that came from Dr. Alex Souza, who was always accessible for stimulating comments and key suggestions for analyzing the data.

I am grateful to the University of Wales Bangor (UWB) and the Proudman Oceanographic Laboratory (POL) for allowing me to use their facilities and for having the opportunity to share a working place with such quality of human resources in physical oceanography. Thanks to the application group for supplying a version of POLPRED and the tidal constituents and to the BODC for providing historic current meter data. In particular, my thanks go to Dr. Erik Jones and Dr. Jason Holt from POL and Dr. Kevin Horsburgh and Dr. Des Barton from UWB.

I also want to thank to J. Candela for providing computer programs and very useful advice for detiding ship-mounted ADCP data.

I wish to thank to the officers and crew of CEFAS *R.V. Corystes* and all the scientists that participated in the observational programmes reported here.

The satellite images used in this study were processed by the NERC Remote Sensing Data Analysis Service, Plymouth, U.K. The wind data was obtained from the U.K. Met. Office.

The data set was collected with financial support from the UK Ministry of Agriculture Fisheries and Food and the Natural and Environmental Research Council.

Financial support for the studentship was awarded from CONACyT in Mexico (student reference number 84560).

Lastly and most importantly: thanks to my family for their unconditional advice, love, and support.

"Science is the search for neat, predictable curves, compact ways of summarizing the data. But there is always the danger that the curves we see are illusory, like pictures of animals in the clouds"

Extract from Fire in the Mind by George Johnson

TABLE OF CONTENTS

Chapter 1

Introduction

Continental shelf sea areas are transition zones between land and ocean. The extent of these areas depends on their tectonic setting, but in general, they are submerged continental margins sloping gently seawards from littoral zones to the shelf break at usually 100 to 250 m depth. Shelf seas are characterized by particularly energetic wind-driven and tidal currents. However, most of the long-term coherent circulation in these regions depends on currents with frequencies low compared to the dominant tidal and inertial oscillations. Such currents can be driven by the spatial density distribution. These organized density driven flows, in the continental shelf of the Celtic Sea, are the topic of this thesis.

1.1 Bottom fronts and cold pools in shelf seas

The spatial density distribution in shelf seas and coastal areas depends on the inputs or losses of buoyancy and on the internal redistribution of this buoyancy by horizontal advection and vertical mixing. The competition between surface buoyancy input, due to solar heating or river discharge, and tide/wind-generated vertical mixing, determines whether the water column stratifies or remains permanently mixed. This competition can be called the heating-stirring problem and coastal and shelf seas with these dynamics are called heating stirring systems (Simpson and Bowers, 1984; Hill, 1998a).

During spring and summer seasons, there is buoyancy input at the surface of the heating-stirring systems and a seasonal thermocline develops in areas characterized by large depths and a low tidal energy regime. However, in shallower areas, tidal vertical mixing dominates and the heat gained by the surface is redistributed throughout the water column. As a consequence, density structures are formed dividing regions of well-mixed water columns from stratified regions. These structures are called tidal mixing fronts (Fig 1.1).

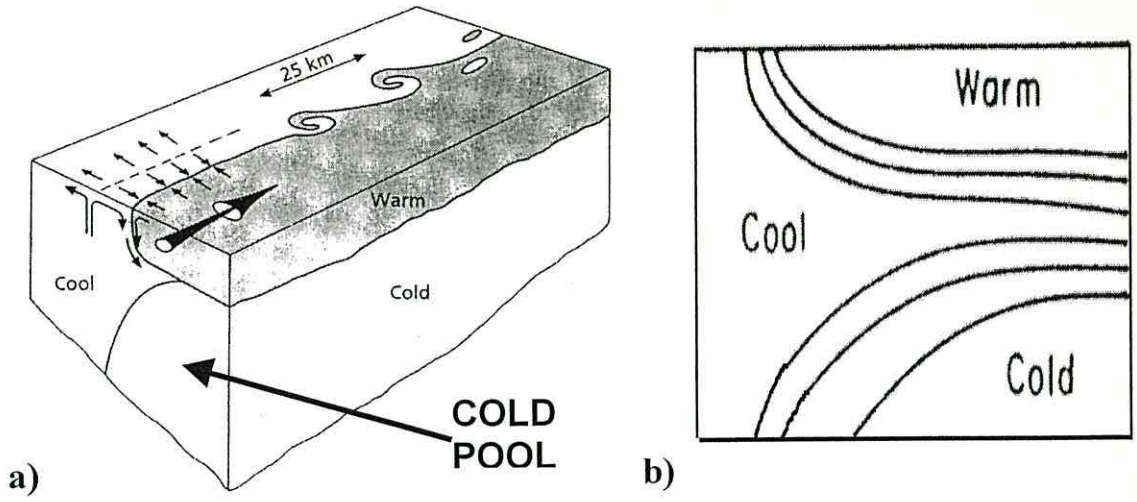

Figure 1.1 a) Schematic representation of a tidal mixing front structure and circulation associated (From Simpson, 1981), b) diagram showing a forked shape front.

Once established, tidal mixing fronts show a remarkable consistency in position with only small horizontal excursions (10-20 km) from their mean position (Bowers and Simpson, 1987), which can be predicted, to a first approximation, with the stratification parameter of h/u^3 proposed by Simpson and Hunter (1974) (see Appendix 1). This variability in the position is attributed to simple tidal advection, adjustment to the spring-neaps cycle in vertical mixing, and as a response to stirring due to wind stresses (Simpson *et al.*, 1978; Simpson, 1981; Simpson and Bowers, 1981). Some apparently random fluctuations in the frontal position (~7 km) that remains after removal of the tidal advection and the spring-neaps cycle, can be attributed to eddy instabilities in the frontal zone.

In general, tidal mixing fronts have a fork-shape (Fig 1.1b), with isopycnals diverging from the pycnocline outcropping at the seabed and sea surface. The surface fronts allow them to be detected by infrared-imagery. However, in some areas, only the bottom front is present (van Aken *et al.*, 1987; Durazo-Arvizu, 1993; Hill *et al.*, 1993; Brown *et al.*, 1999a). In some shelf seas, bottom fronts together with a strong thermocline isolate dense and cold relatively static water in the deepest areas of the basin, this dense structure is termed a *cold (or dense) pool* (Fig 1.2).

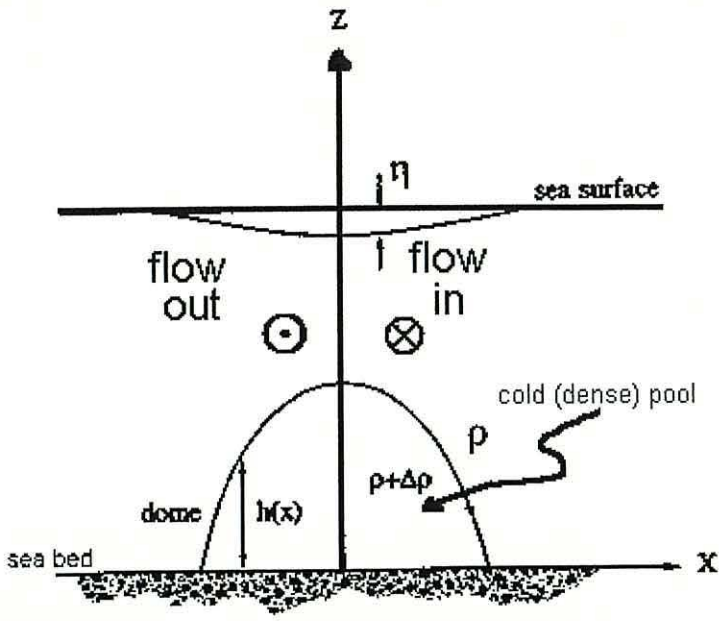

Figure 1.2 Dome-like structure and cyclonic circulation associated. (From Durazo-Arvizu, 1993)

Frontal zones are usually distinguished from the rest of the ocean by the relatively large current velocities associated with the sharp cross-front density-gradient. However, while shelf sea surface fronts may be baroclinically unstable, since they are sometimes observed to distort in meanders and eddies on the scale of the internal Rossby radius (Fig 1.3) (Simpson and Pingree, 1978; Pingree, 1978; Pingree, 1979; Griffiths and Linden, 1981; van Heijst, 1986; James, 1988), in contrast, shelf sea bottom fronts seem to be far more stable structures. Linden and van Heisjt (1984) observed that initial unstable bottom front structures stabilize by the bottom Ekman layer dissipating the kinetic energy of longer baroclinic waves. Sloping topography is also capable of stabilizing baroclinic flows (Pedlosky, 1979; James, 1990; Hill *et al.*, 1993). This relative stability and the strong baroclinicity of the bottom fronts and cold pools make them structures dynamically significant for the maintenance of along-front flows or organized density driven flows, which are the particular interest of this thesis. A closer exploration of the theory concerning bottom frontal dynamics is presented next.

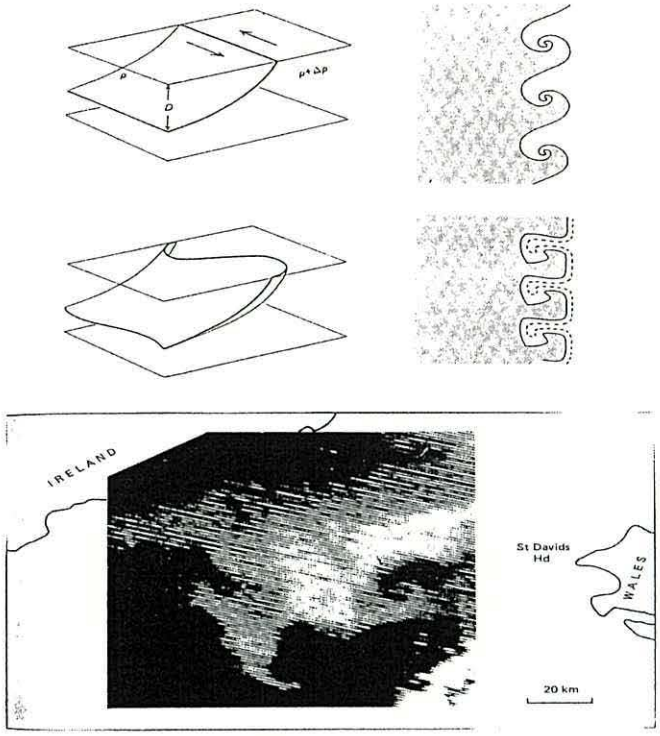

Figure 1.3 Eddy-like disturbances on the frontal boundary due to baroclinic instabilities occasionally observed in satellite imagery (From Pingree, 1978).

1.2 Basic Theory of Frontal Dynamics

The flow field associated with the frontal area can be obtained considering the equations of motion and continuity. In the absence of viscous effects we have:

$$\frac{Du}{Dt} = fv - \frac{1}{\rho}\frac{\partial P}{\partial x} + F_x \tag{1.1}$$

$$\frac{Dv}{Dt} = -fu - \frac{1}{\rho}\frac{\partial P}{\partial y} + F_y \tag{1.2}$$

$$\frac{\partial u}{\partial x} + \frac{\partial v}{\partial y} + \frac{\partial w}{\partial z} = 0 \tag{1.3}$$

$$\frac{1}{\rho}\frac{\partial P}{\partial z} + g = 0 \tag{1.4}$$

where f is the Coriolis parameter

F_x and F_y are external forces, for example friction terms in the x and y directions, respectively

u, v and w are orthogonal components of the velocity

x, y and z is a right handed Cartesian coordinate system

ρ is the water density

g is gravitational acceleration

P is pressure within the water column.

Let us consider the simple case of an ideal frontal structure with a coordinate system as shown in Figure 1.4. Here h(x) is depth of the interface that separates two fluids of densities ρ_1 and ρ_2. The x- and y-axis are orientated in the across-front and along-front directions respectively, and the z-axis vertically upwards with its origin at the mean sea surface.

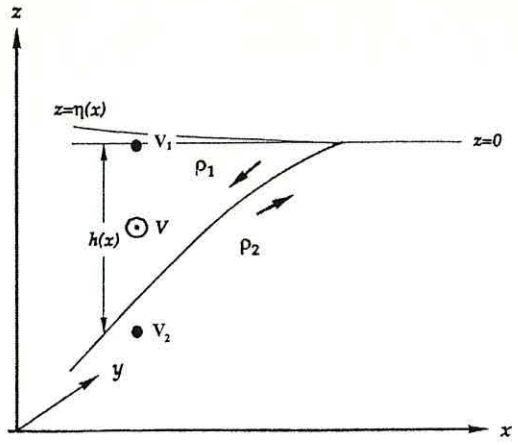

Figure 1.4 Schematic diagram showing the coordinate system used in the two-layer frontal model. (From Durazo-Arvizu, 1993).

In a steady flow, which is independent of the y direction, without external forces (*e.g.* no friction and no mixing), from equations given before, the difference in velocities across the interface is given by

$$V = v_1 - v_2 = -\frac{g'}{f}\frac{\partial h}{\partial x} \tag{1.5}$$

where $g' = (\rho_2 - \rho_1)g/\rho$ is the reduced gravity (i.e. the vertical velocity difference across the interface is proportional to the steepness of the interface).

In the case when the lower layer is at rest, equation (1.5) gives the absolute geostrophic velocity of the upper layer driven by the pressure gradients across the front. In the region of maximum density gradient, the current takes the character of an along-front jet flow.

An exact agreement between observations and the predicted along-front jet cannot be expected because of the effect of friction (Lwiza *et al.*, 1991). Let us introduce friction between the two layers acting at the interface. The interfacial stress, named τ, will cause equal and opposite Ekman fluxes τ/f in the two layers. Equations (1.1) and (1.2) become

$$-fv_E = \frac{1}{\rho}\frac{\partial \tau_x}{\partial z} \tag{1.6}$$

$$fu_E = \frac{1}{\rho}\frac{\partial \tau_y}{\partial z} \tag{1.7}$$

where u_E and v_E are the Ekman velocities and (τ_x, τ_y) the stresses in the x and y directions respectively.

Integrating the equations (1.6) and (1.7) with respect to z and taking into account that outside the internal Ekman layer the stresses vanish.

$$\rho f V_E = \tau_x \tag{1.8}$$

$$\rho f U_E = -\tau_y \tag{1.9}$$

where $(U_E, V_E) = \int (u_E, v_E) dz$ are the Ekman volume transports of the internal boundary layer.

Neglecting stresses in the cross-frontal direction and allowing only stresses parallel to the jet. The stresses above and below the interface are the same but with opposite signs,

upper layer $\rho f U_E = -\tau_y$ (1.10)

lower layer $\rho f U_E = \tau_y$ (1.11)

This balance predicts a secondary circulation perpendicular to the front. The lighter layer spreads over the denser one. This results in a two-celled circulation with upwelling in the mixed water close to the front and downwelling on the baroclinic zone (Garrett and Loder, 1981), diagram shown in Figure 1.4.

Considering a more realistic situation with a continuously stratified frontal region, where density ρ now becomes a continuous function of x and z. If variations in the along-front direction are ignored, and friction is neglected, then the along-frontal velocity satisfies the thermal wind equation

$$\frac{\partial v}{\partial z} = -\frac{g}{\rho f}\frac{\partial \rho}{\partial x} \tag{1.12}$$

i.e. the vertical velocity shear is proportional to the horizontal density gradient across the front.

If the external forces F_x and F_y (from eq. 1.1 and 1.2) now represent the turbulent transfer of momentum in the x and y directions respectively, given by

$$F_x = \frac{\partial}{\partial x}\left[K_H \frac{\partial u}{\partial x}\right] + \frac{\partial}{\partial z}\left[A_V \frac{\partial u}{\partial z}\right] \tag{1.13}$$

$$F_y = \frac{\partial}{\partial y}\left[K_H \frac{\partial v}{\partial y}\right] + \frac{\partial}{\partial z}\left[A_V \frac{\partial v}{\partial z}\right] \tag{1.14}$$

where K_H and A_V are the horizontal and vertical eddy viscosity coefficients.

Assuming that the ageostrophic velocity is smaller than geostrophic velocity (small Rossby number, $Ro=V/fL$ <<1), and friction is negligible compared to Coriolis acceleration (small Ekman number, $E=A_V/fH^2$ << 1). Neglecting horizontal diffusion of momentum ($K_H = 0$), equations (1.1) and (1.2) become

$$-fv + \frac{1}{\rho}\frac{\partial P}{\partial x} = \frac{\partial}{\partial z}\left[A_V \frac{\partial u}{\partial z}\right] \tag{1.15}$$

$$fu = \frac{\partial}{\partial z}\left[A_V \frac{\partial v}{\partial z}\right] \tag{1.16}$$

Substitution of (1.12) onto (1.16) leads to

$$u = -\frac{g}{\rho f^2}\frac{\partial}{\partial z}\left[A_V \frac{\partial \rho}{\partial x}\right] \tag{1.17}$$

The vertical velocity is given by the continuity equation (1.3)

$$w = \frac{g}{\rho f^2}\frac{\partial}{\partial x}\left[A_V \frac{\partial \rho}{\partial x}\right] + L(x) \tag{1.18}$$

where $L(x)$ is an arbitrary function of x (Garrett and Horne, 1978).
Garrett and Loder (1981) assert that (1.17) and (1.18) with $L(x) = 0$ are valid solutions in the fluid interior, outside the surface and bottom Ekman Layers. Thus, the result of including turbulent momentum transport parameterized in terms of a variable eddy viscosity also introduces a horizontal component of the flow in the cross frontal direction.

Garrett and Loder (1981) in their semi-analytic model applied (1.15) and (1.16) for typical frontal structures and for different values of the Ekman numbers. The cross-frontal structures were defined as

$$\frac{\partial \rho}{\partial x} = \frac{1}{2}\frac{\partial \Delta\rho(x)}{\partial x}\left\{ s - \cos\left[\frac{\pi z}{h(x)}\right]\right\} \tag{1.19}$$

where $0 \leq s \geq 1$, and $s = 0$ is a case of a forked frontal shape and $s = 1$ is a pure bottom frontal structure.

Their results using different values for the Ekman number to obtain across-front (u) and along-front (v) velocity profiles for $s = 1$ and $s = 0$ cases are shown in Figure 1.5. The vertical coordinate has been non-dimensionalized by the depth and velocity by the along-front speed that would be achieved at the surface in the frictionless case (E=0). The cross-frontal flow, u, is small if the Ekman number is small and the flow is essentially along-front (i.e. purely geostrophic). When the Ekman number is increased the frictional effects dampen the along-front velocity and the cross-frontal flows become important. In a forked-type front increasing the Ekman number implies near-surface and near-bottom flows towards the well-mixed side, whilst at mid-depth, a compensating opposite flow is developed along the pycnocline. For the bottom-front case, larger frictional effects imply also a reduction of the along-front velocity and the waters flowing from the mixed region towards the stratified on the surface and in the opposite direction near the seabed.

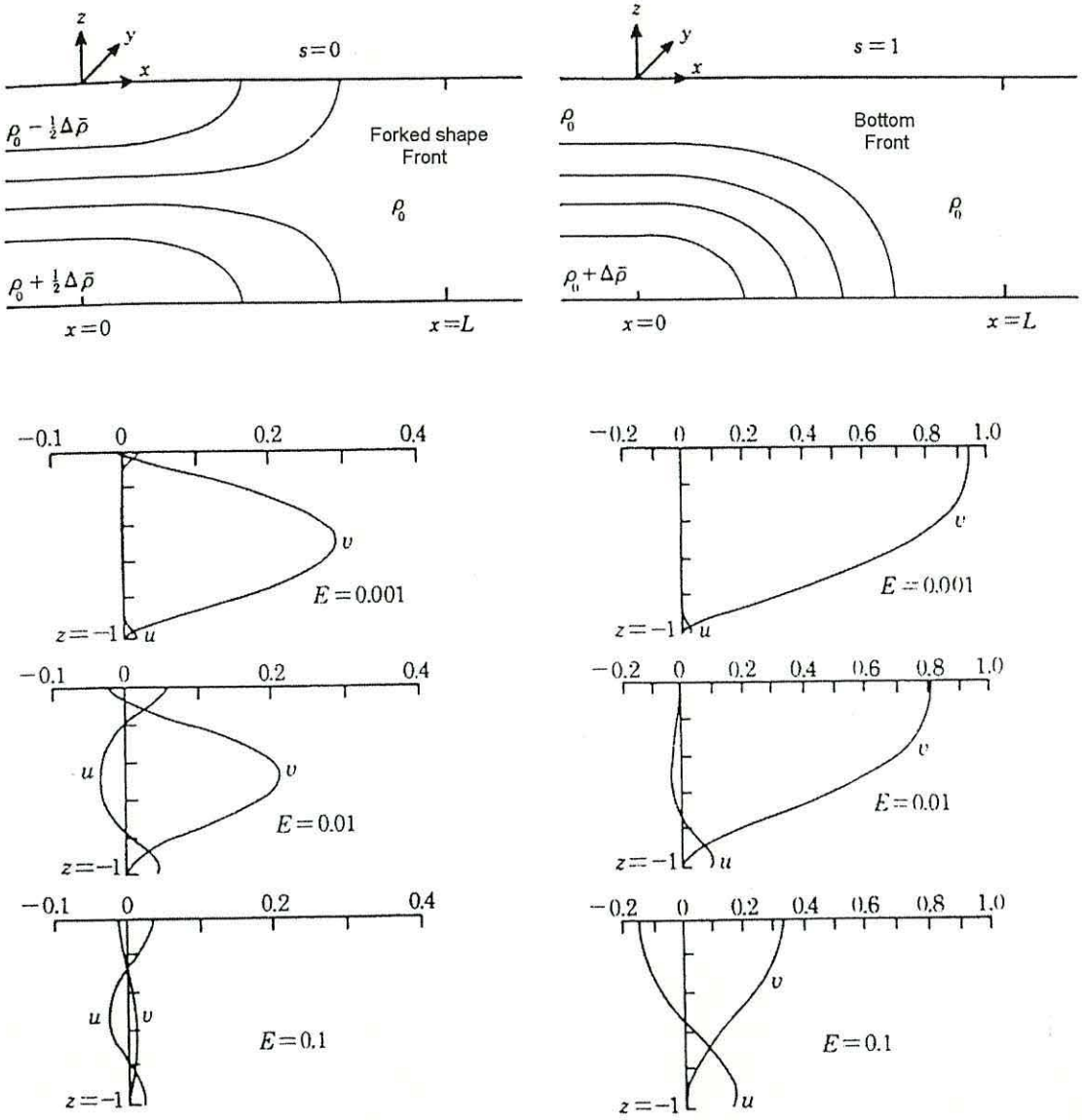

Figure 1.5 Two typical cross-frontal density structures used by Garrett and Loder (1981) showing velocity profiles of the across velocity (u) and along-front velocity (v) related to different Ekman numbers. (From Garrett and Loder, 1981).

However, the most outstanding results derived from the semi-analytical model of Garrett and Loder (1981), with dynamical significance to the study of flow field related to bottom fronts are:

- Relative strong along-front near-surface flows are associated with bottom fronts.

- For the same vertical density gradient, $\Delta\rho$, a bottom-only front will lead to a stronger horizontal density gradient and therefore bottom fronts showed stronger along-front velocity (v) than forked shape fronts using the same Ekman number.

- The cross-frontal density gradients and the sea surface slope are adjusted to give zero net cross-frontal volume flux. This has significant implications since it provides a physical basis on which to justify a level of no motion close to the seabed in geostrophic calculations for shelf sea fronts (Hill, 1993).

- Friction's role is to reduce the along-front geostrophic current, to produce a secondary cross-front circulation. Friction also stabilizes the bottom front structures (James, 1989).

It is important to consider that although the secondary cross-frontal circulation has important implications to the biomass production, because they permit the re-distribution of nutrients in the euphotic layer (Pingree *et al.*, 1975; Pingree *et al.*, 1976; Mann and Lazier, 1991), their velocities are extremely small, at least three times smaller than along front velocities (Lwiza *et al.*, 1991). Thus, in terms of organized regional circulation, the along-front flow is expected to have relatively more significance than the secondary cross-front circulation.

There is a growing body of direct evidence of frontal organized jet-like flows (*i.e.* along-front flows) in the European shelf sea associated with bottom fronts. Evidence of these jet-like flows using three extensively observed tidal mixing front systems in the North Sea and the Irish Sea is documented in the next section.

1.3 Tidal mixing fronts in the European shelf seas

In the past decade, the North Sea and the Irish Sea were extensively observed. The observational surveys included tidal mixing frontal areas such as the Flamborough front, the bottom front in the central North Sea and the western Irish Sea front (Fig 1.6). The obtained results have contributed to a better picture of the regional circulation. These have changed the perspective towards tidal mixing fronts, portraying bottom frontal areas as dynamical systems capable of maintaining organized jet-like flows. A review of the major results is briefly outlined below.

The Flamborough front and the bottom front in the central North Sea form part of a series of tidal mixing fronts in the North Sea which separate well-mixed water of the English coast, the southern shallow North Sea and Dogger Bank from stratified water in the deeper northern and central area of the North Sea (see Fig 1.6a). Salinity is almost constant in the region and the surface layer of the sea is usually well-mixed by wind, therefore, surface frontal regions can only rarely be observed by infrared satellite imagery (van Aken *et al.*, 1987). Nevertheless, though a sharp (thermal) transition between stratified and well-mixed areas is not visible at the sea surface, sharp fronts occur near the sea bottom (Fig 1.7) (van Aken *et al.*, 1987; Durazo-Arvizu, 1993; Hill *et al.*, 1993; Brown *et al.*, 1999a). Therefore, these tidal mixing fronts are predominantly bottom features with associated *cold pools* (Durazo-Arvizu, 1993; Hill *et al.*, 1993, Brown *et al.*, 1999a).

Narrow, near surface along-front flows (Fig 1.7) confined within a distance of 3-5 km (Flamborough front case) or 15 km (the bottom front in the central North Sea case), have been corroborated using ADCP, mooring and limited drifter observations (van Aken *et al.*, 1987; Lwiza *et al.*, 1991; Durazo-Arvizu, 1993; Hill *et al.*, 1993; Brown *et al.*, 1999a). These jet-like flows, with velocities up to 15 cm s^{-1}, were located above the margin of the cold pools, *i.e.* where the most steeply sloping part of the bottom front were related to the region, showing a good agreement with geostrophic calculations (van Aken *et al.*, 1987; Durazo-Arvizu, 1993; Hill *et al.*, 1993; Brown *et al.*, 1999a).

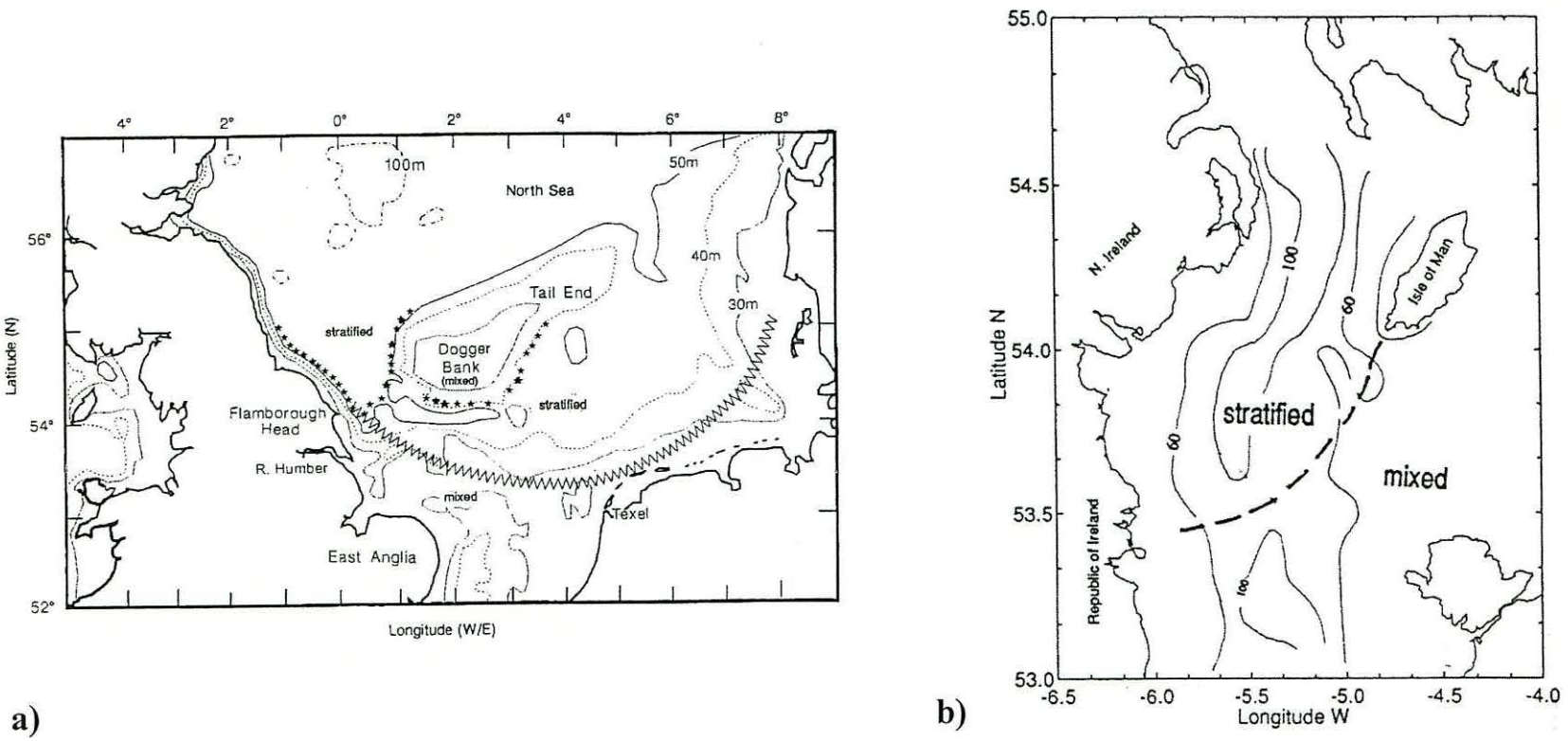

Figure 1.6 Location of frontal areas: a) North Sea: Flamborough front (stars symbols) and central North Sea front locations (denoted by zig-zag line) (From Brown *et al.*, 1999a) and b) The western Irish Sea front (denoted by broken line) (From Durazo-Arvizu, 1993).

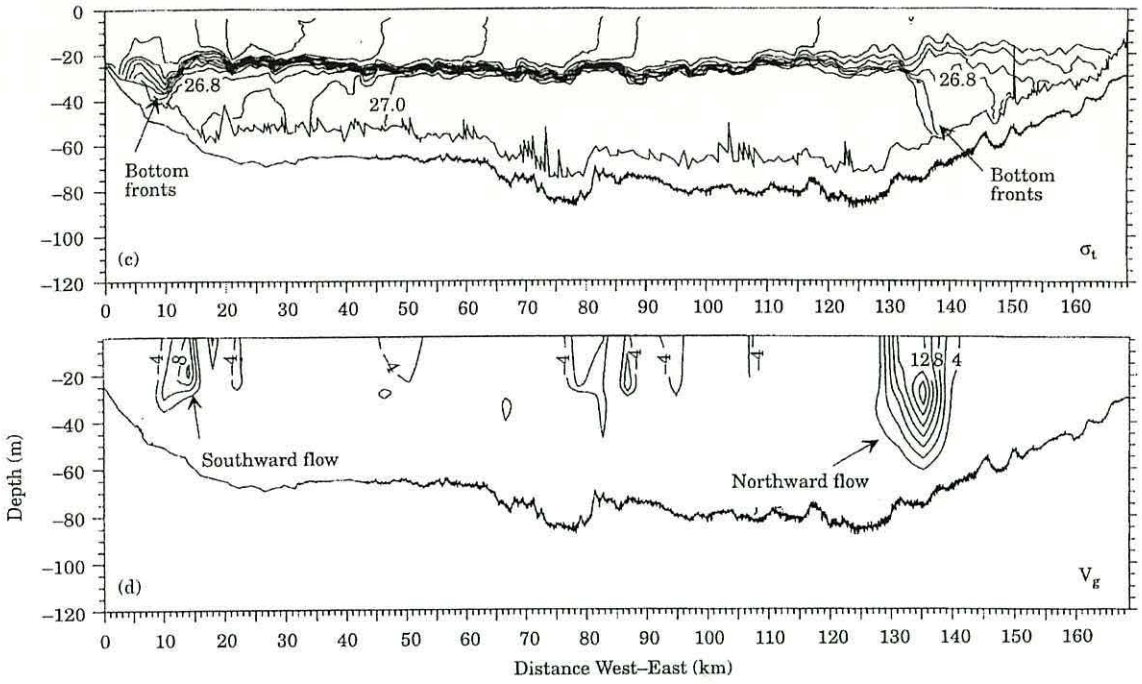

Figure 1.7 Density field and geostrophic velocities associated from a transect through the central North Sea front (From Brown *et al.*, 1999a).

In contrast to the tidal mixing fronts in the North Sea, the Western Irish Sea front shows a strong surface thermal front, with maximum temperature gradients of 1 °C/km clearly visible from I-R imagery (Fig 1.6b) (Durazo-Arvizu, 1993; Hill *et al.*, 1994; Horsburgh *et al.*, 2000). However, the temperature gradients are generally stronger at the seabed (Horsburgh *et al.*, 2000). The Western Irish Sea front can be considered a special case of tidal mixing front, where the regional characteristics make it a cold pool structure of an enclosed nature, i.e. the cold dense pool is bounded by strong bottom fronts forming a dome-shaped structure isolated on the bottom of the deepest basin of the western Irish Sea (Fig 1.8) (Horsburgh *et al.*, 2000). This dome-shaped cold pool structure induces a large-scale cyclonic near-surface gyre on the stratified side of the front. The velocities were concentrated in narrow (~10 km wide) jet-like flows up to 20 cm s^{-1} above the margin of bottom fronts at a depth consistent with the base of the thermocline (Durazo-Arvizu, 1993; Hill *et al.*, 1994; Horsburgh *et al.*, 2000). This seasonal circulation, revealed by an extensive cruise program, lasted from May to October, i.e. until the stratification conditions were suppressed by vertical turbulent mixing (Horsburgh *et al.*, 2000).

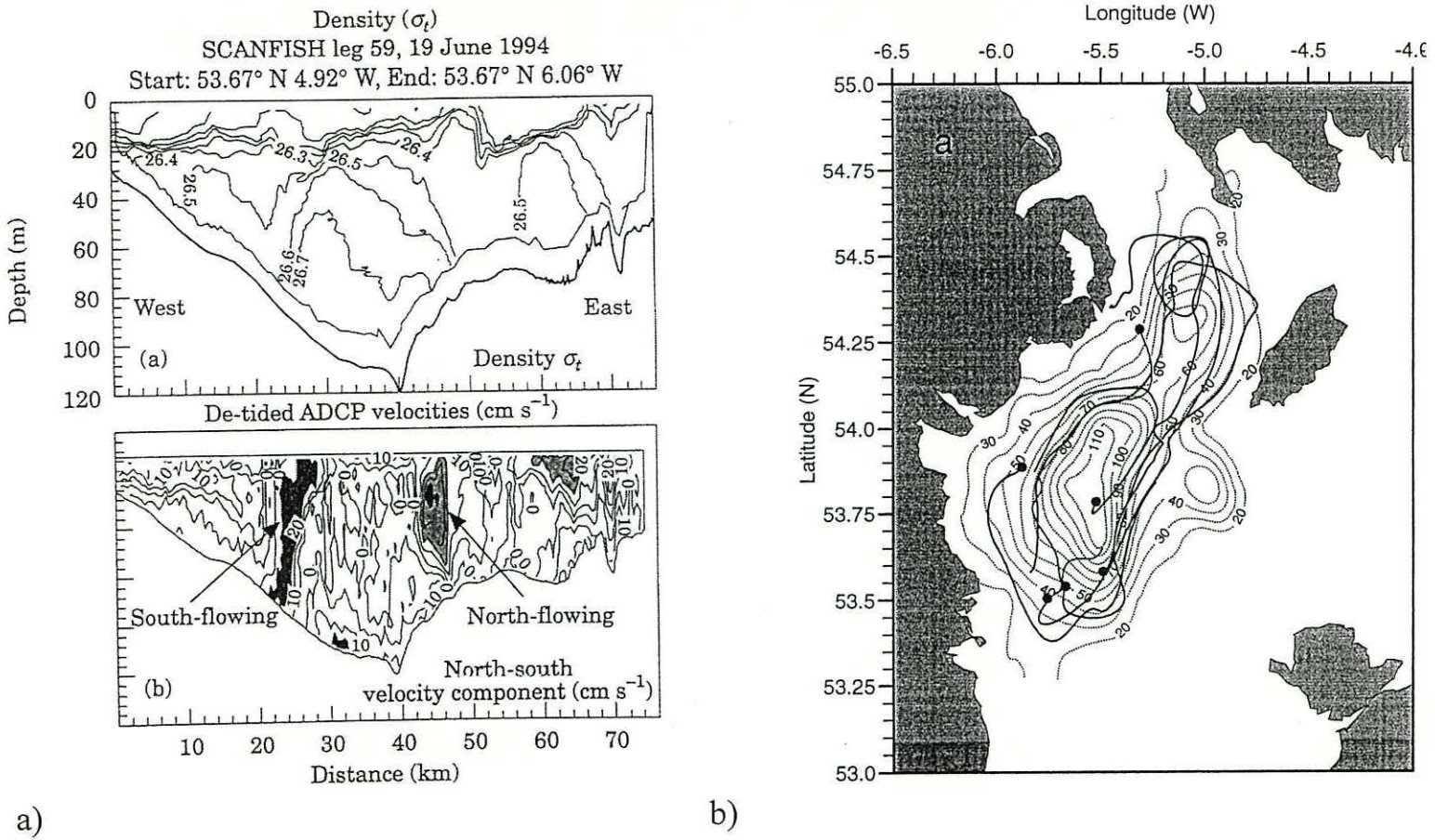

Figure 1.8 a) A cross-section through the Western Irish Sea front density field showing a dome-like structure in the bottom of the basin and the ADCP residuals agree showing a cyclonic circulation (From Hill *et al.*, 1994). b) drifters released in this frontal area defining a cyclonic gyre and following the contours of potential energy anomaly (from Horsburgh *et al.*, 2000).

It has been previously shown that some differences between tidal mixing fronts, due to the bathymetry and other regional characteristics (*i.e.* fresh water sources) can be expected. However, most of them have a common feature, namely, existence of strong horizontal density gradients near the seabed (bottom front separating mixed water from a cold pool) driving narrow and surface jet-like flows. Thus, persistent bottom fronts or cold pools are structures dynamical significant and capable of driving near surface fast pathways of circulation. In the particular case of the Western Irish Sea front, a re-circulation path with a high degree of retention for larvae and contaminants is produced (Horsburgh *et al.*, 2000).

As in other European shelf sea areas, in most of the Celtic Sea a high degree of stratification is developed during summer. The boundary between stratified and permanent mixed water conditions takes place at the entrance to the Irish Sea (St. George's Channel) and Bristol Channel, which is known as the Celtic Sea tidal mixing front (Fig 1.9). This tidal mixing front has a forked shape (not shown). In addition, there is a pool of dense and cold water beneath the thermocline separated from the adjacent tidally mixed waters by bottom fronts (Horsburgh *et al.*, 1998).

As described in this section, cold pools have been observed to have important implications for the long-term circulation in other well-observed shelf sea regions, *i.e.* North Sea and Irish Sea. However, an extensive observational survey, similar to the North Sea and Irish Sea, has not until now been conducted in the Celtic Sea. Only, a compilation of non-orientated studies, in terms of density driven currents, form the actual knowledge of the summer regional circulation in the Celtic Sea, a review of these studies is described next.

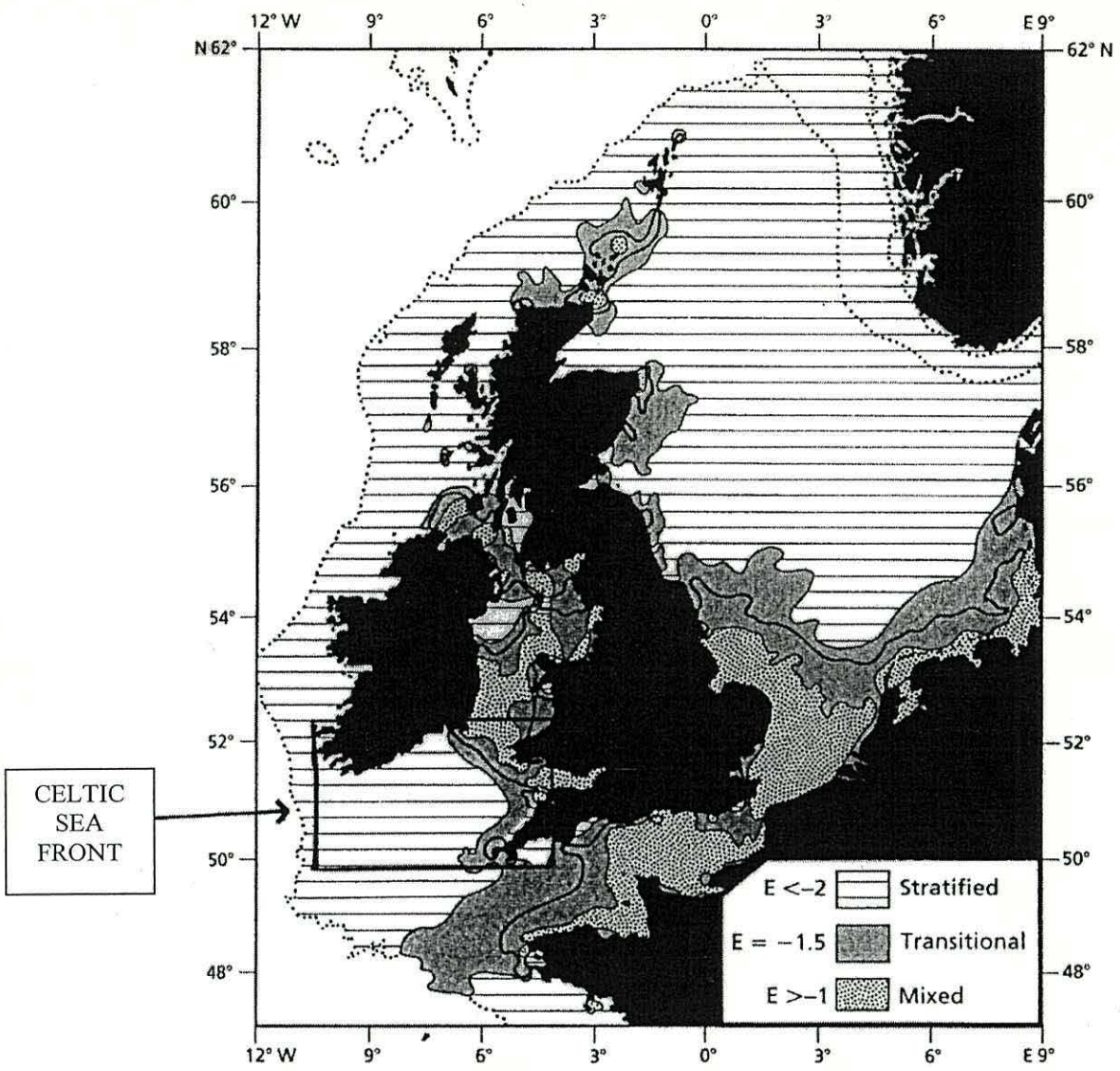

Figure 1.9 Contours of S=1.5 (marked with a heavy line) indicate the predicted positions of tidal mixing fronts from numerical model used by Pingree and Griffiths (1978). The location of the Celtic Sea tidal mixing front is indicated.

1.4 Circulation studies in the Celtic Sea

A fisheries study from the early 20th century, which was carried out by Matthews (1913), represents the first contribution to circulation studies in the Celtic Sea. He inferred from charts of salinity distribution that saltier water from the Atlantic moves cyclonically in the Celtic Sea falling continually in salinity, as a result of mixture with the surrounding fresher water (changing from 35.2 to 34.65) (Fig 1.10a). Also, he proposed that in the St. George's Channel area, the flow divides into two parts, one flows northward through the channel and the other flows in a cyclonic sense south of the St. George's Channel. However, the first hydrodynamical estimate of the summer circulation in the Celtic Sea was applied by Harvey (1929), who also inferred a cyclonic circulation using geostrophic calculations in the upper 60 meters with data collected in the area during the June-July period (Fig 1.10b).

Throughout the 1950's and 1960's, there was a (largely intuitive) attempt to rationalize an overall picture of the circulation in the Celtic Sea. Sparse hydrographic observations together with some current information, obtained mainly from light vessels and drift bottles, supported semi-empirical hypotheses suggesting a mainly wind driven cyclonic circulation in the Celtic Sea (Bowden, 1950; Cooper 1961a; 1961b). During this period, evidence of this circulation came mostly from geopotential topographies and analysis of the distribution of temperature, salinity and nutrients obtained by Cooper (1961a; 1961b, 1967) (Fig 1.10c).

The prediction of a tidal mixing front in the Celtic Sea using the stratification parameter h/u^3 by Simpson and Hunter (1974), led to a more specific approach to the Celtic Sea circulation, namely density driven currents due to the strong baroclinicity as expected in frontal areas. This new dynamical approach was carried out by Simpson (1976) investigating the density field and residual velocities in the Celtic Sea tidal mixing front. Combining the results obtained from two hydrographic cross-frontal sections and some radio tracked parachute drogues, it was possible to confirm the existence of along-front residuals associated with the baroclinicity of frontal areas estimated up to 0.3 m s^{-1} (Fig 1.11). James (1977; 1978 and 1984) approached the dynamics of the Celtic Sea tidal mixing front using numerical models obtaining strong surface currents flows (up to 0.35 m s^{-1}) along the front in the sense predicted by geostrophic balance.

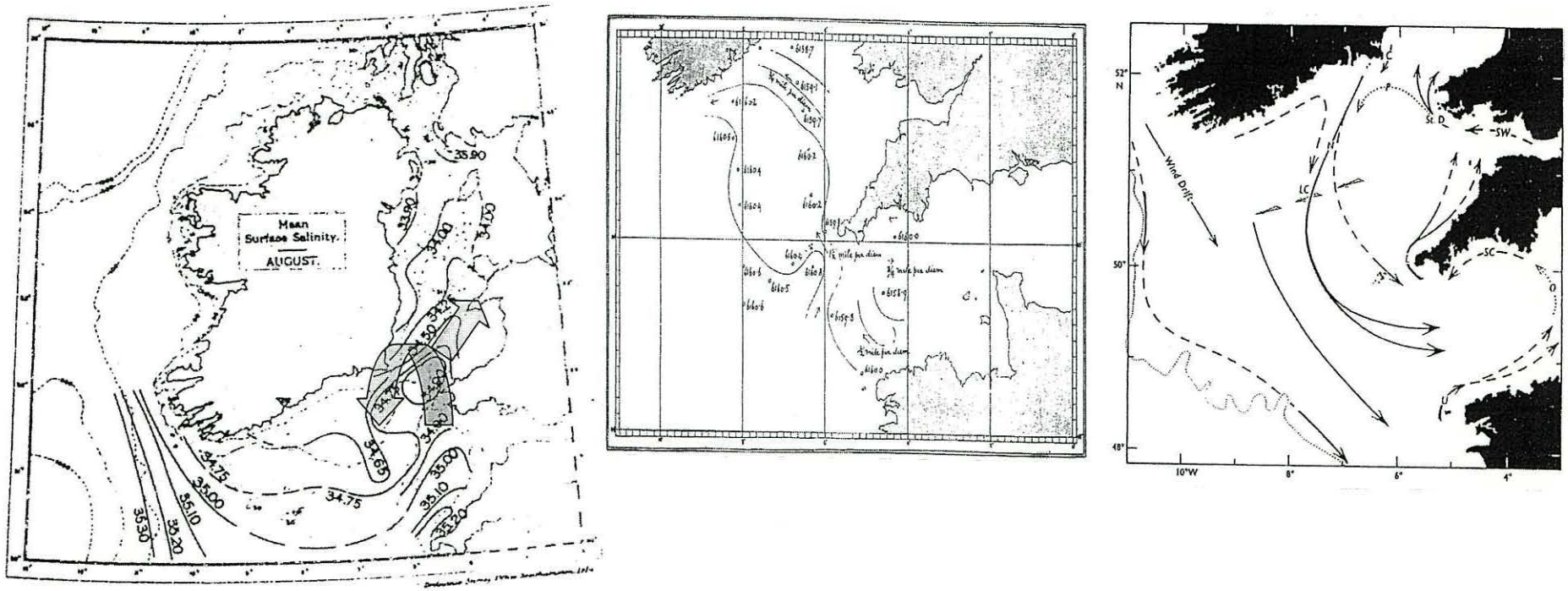

a) b) c)

Figure 1.10 Early circulation studies in the Celtic Sea: a) Mean surface salinity distribution for August used by Matthews (1913) and cyclonic circulation suggested; b) Lines of equal hydrostatic pressure at 60m depth defining a nearly a cyclonic circulation by Harvey (1929) and c) pattern of circulation suggested by Cooper (1967).

61

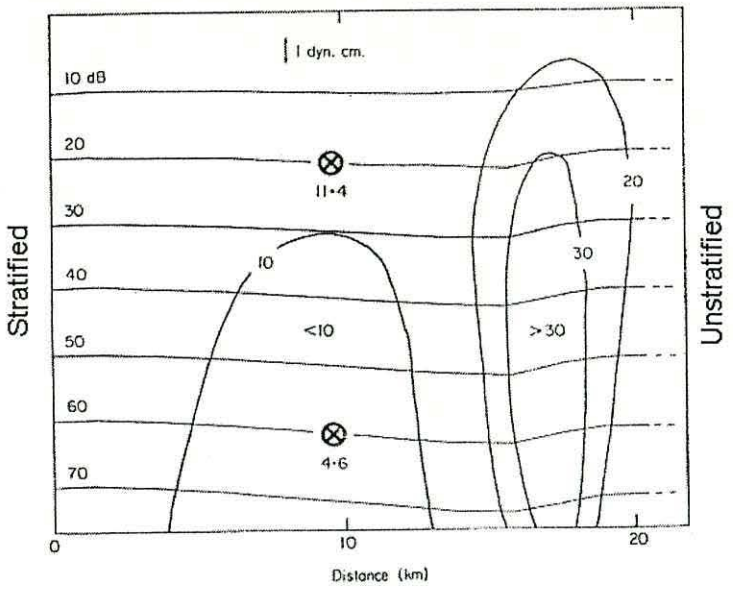

Figure 1.11 Velocity field of the frontal region from dynamic height anomalies and the 20 db drogue vector obtained by Simpson (1976). Velocities in cm s^{-1}.

However, this baroclinic perspective of the circulation was obscured by the results obtained by Thompson and Pugh (1986) and Pingree and Le Cann (1989) together with the perspective that came from the application of the available barotropic-only models to the region. Thomson and Pugh (1986) have suggested, on the basis of mooring arrays maintained for more than one month, that the low-frequency currents (residuals) are predominantly barotropic, about 1-2 cm s^{-1} and are spatially coherent over the Celtic Sea area. Additionally, Pingree and Le Cann (1989) modelled the circulation in the Celtic Sea using a barotropic model with emphasis on the barotropic response to the wind. Their numerical results and some direct observations showed weak barotropic wind driven residual currents in the central Celtic Sea, but with an important coastal response such as near the Scilly Isles (Fig 1.12). Other numerical efforts using wind and tide as forcing mechanisms also concluded a weak residual circulation in the Celtic Sea (Davies and Jones, 1992a; Young *et al.*, 2001). Thus, the long-term circulation in the Celtic Sea was portrayed as wind driven, weak and barotropic (Fig 1.13).

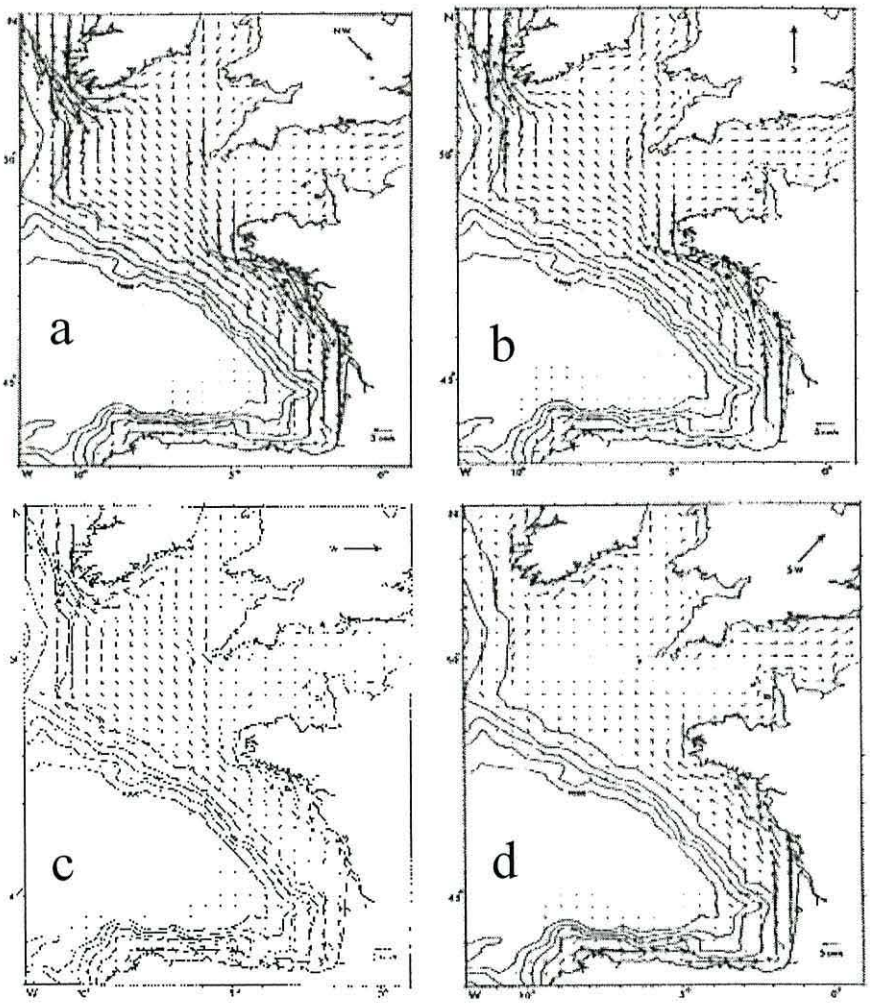

Figure 1.12 Wind driven currents from a numerical model forcing with a uniform wind stress from: a) NW, b) S, c) W and d) SW. (From Pingree and Le Cann, 1991).

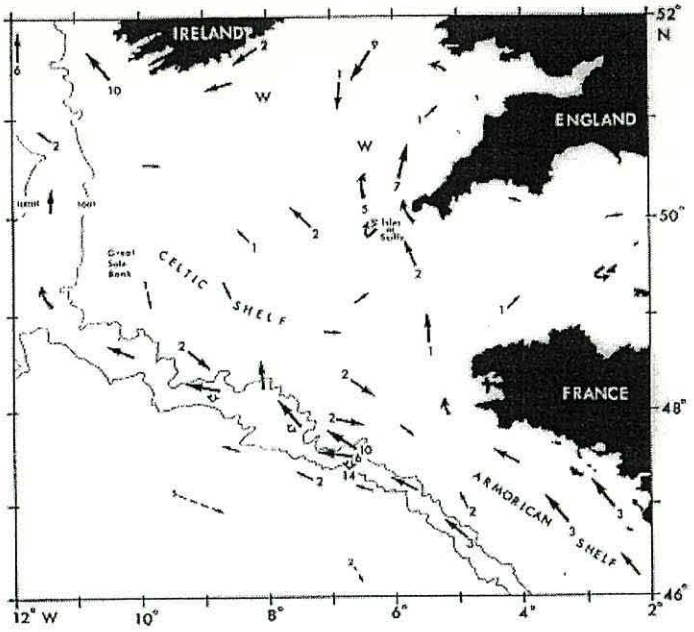

Figure 1.13 Residual currents on the Celtic Sea and Armorican region obtained by Pingree and Le Cann (1991). Numbers alongside the arrows are the values in cm s^{-1}.

Recently, encouraged by the results obtained in other tidal mixing front studies (section 1.3), Horsburgh *et al.* (1998) took back the point of view of the baroclinicity of the frontal areas as potentially important forcing mechanism and revisited the Celtic Sea tidal mixing front. The study was based on a short experiment but orientated to density-driven flows. Only three satellite-tracked drifting buoys were used and CTD stations in two cross-frontal sections were undertaken. The drifters were drogued at 30 m and deployed at the frontal areas. The drifter trajectories were associated with filaments observed in SST images of the Celtic Sea front (Fig 1.14) (Horsburgh *et al.*, 1998). These observations showed a jet-like flow with speeds of 10-25 cm s^{-1} in good agreement with geostrophic calculations (Fig 1.15). As observed in other tidal mixing fronts and accordingly with the theory of frontal systems, these baroclinic flows can be attributed to the bottom front rather than the surface front (Horsburgh *et al.*, 1998). Additionally, these results showed a northward flow on the Eastern side of Saint George's Channel and a weak southward current on the western side of the channel (Horsburgh *et al.*, 1998), as in the early work of Matthews (1913).

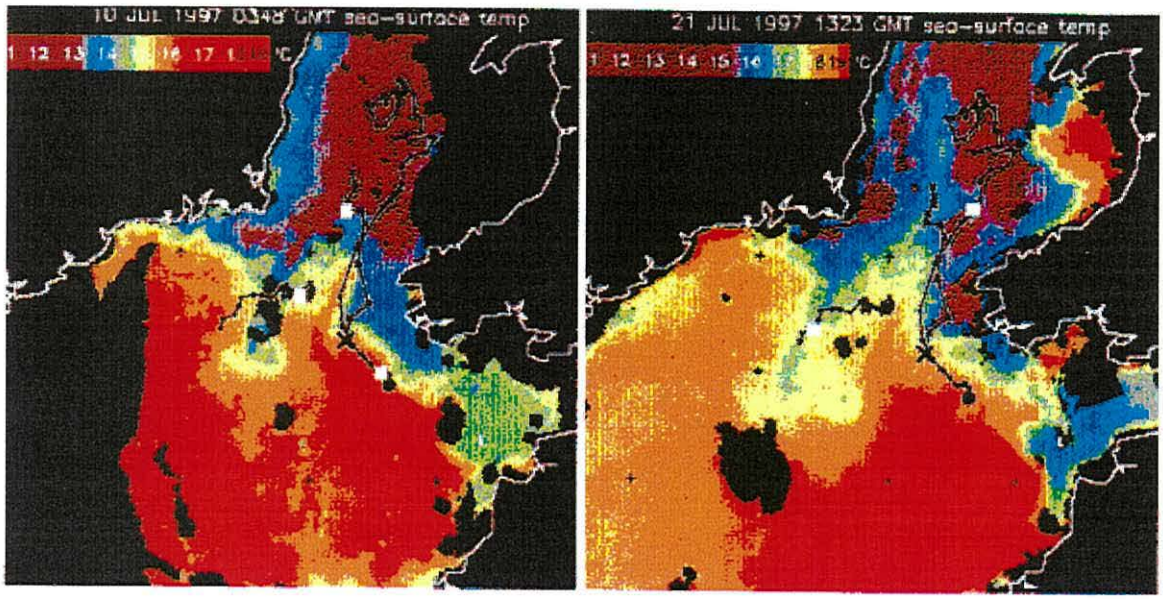

Figure 1.14 SST at the Saint George's Channel and drifter positions during July 1997 (from Horsburgh *et al.*, 1998). Their trajectories follow the contours of the surface thermal front and agree with the intrusions observed through the channel.

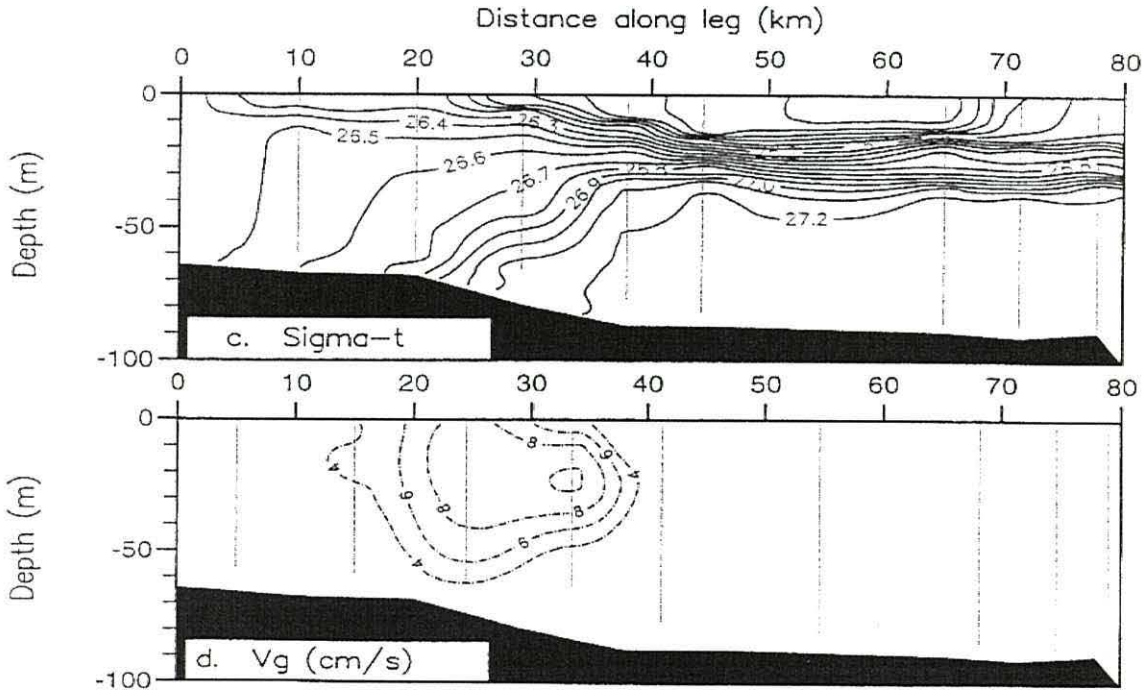

Figure 1.15 Saint George's Channel section during June 1995 showing the vertical structure of density and geostrophic calculations derived. A jet-like flow is observed above the bottom front. (From Horsburgh *et al.*, 1998)

As a whole, the long-term circulation in the Celtic Sea is still vaguely defined. A large-scale pattern of circulation is only supported by measurements at a few locations in the Celtic Sea and the numerical models lacked the baroclinic effects, the long-term circulation has conventionally been accepted as weak and barotropic wind driven (*i.e.* density was generally considered a small contributor). Nevertheless, there have been a couple of attempts to measure the effect of the baroclinicity of the frontal areas in the residual velocity field. However, the possibility that the tidal mixing front generates organized density driven flows and its effect on the whole circulation is still largely unexplored.

1.5 Aims of the thesis

By virtue of its location, the shelf sea of the Celtic Sea is affected by impacts from the traffic of tankers of the oil industry, commercial fisheries, sand and gravel extractions. At the same time, the waste includes discharge of radioactive material from nuclear installations. Several species of fish and shellfish of commercial importance (*e.g.* herring, plaice, sole and *Nephrops norvegicus*) spawn in the area (Mackie *et al.*, 1995). Additionally, the Celtic Sea is often taken as the location of boundary conditions for numerical models of the Irish Sea.

Moreover, in January 1993, an oil spill occurred off west Wales (Milford Haven, St. George's Channel). A coarse resolution model was used to forecast the oil movement and there was a lack of direct observations (Elliott and Jones, 2000). Fortunately, this incident occurred in the winter period when no strong density driven currents are expected, but if this oil incident occurred in the summer period, based on the approach outlined here, this incident could require a different plan to predict the movement of the slick and to determine the impact of the spill in the surrounding areas.

Hence, direct current measurements to support a long-term pattern of circulation in the Celtic Sea were necessary.

As in other European shelf sea areas, the Celtic Sea tidal mixing front could also provide the necessary baroclinic conditions for the formation and maintenance of jet-like flows. However, the Celtic Sea system has previously been subject to very little measurement in relation to the question of density driven frontal circulation. This provides us with the motivation to refine the understanding about the circulation during summer in the Celtic Sea, in particular, in terms of organized density driven currents.

With this in mind, during the summer of 1998, two oceanographic campaigns were conducted in the shelf sea area of the Celtic Sea. The study applied a combination of observational techniques including high-resolution towed undulating CTD's (Scanfish), ship board acoustic Doppler current profiler (ADCP), satellite tracked drifters and bottom-mounted ADCP moored in the area. In addition, cloud-free satellite images of the sea surface temperature, as well as meteorological information were also available for the

study period. Additionally, a preliminary comparison with emerging baroclinic three-dimensional model results was possible.

The main aim of this thesis, through the analysis of the extensive data set obtained during the oceanographic campaigns of summer 1998, is to draw a circulation picture for the shelf sea area of the Celtic Sea during the summer and to assess the responsible processes. The following specific objectives are defined:

- To obtain a three-dimensional characterization of the frontal areas and geostrophic flows of the shelf area of the Celtic Sea during the summer.

- To determine the Lagrangian velocity field using satellite tracked drifters and to perform an analysis of the possible responsible forcing mechanisms of the circulation observed.

- To resolve an independent picture of the residual velocity field from the ship mounted ADCP measurements.

- To obtain the non-tidal currents from two bottom-mounted ADCPs moored in the study area and to perform a complex correlation with the wind field.

- To compare the hydrographic and flow fields with a baroclinic 3D numerical model applied over the study area.

1.6 Thesis structure

The thesis contains the analysis of the results obtained from two oceanographic campaigns in the shelf sea area of the Celtic Sea during the summer of 1998. This study was developed with a similar approach to that of the pioneering descriptive works in the Celtic Sea (Matthews, 1913; Harvey, 1929; Bowden, 1950; Cooper, 1961a; Cooper, 1961b). However, in a novel fashion, it uses new instrumentation technology and the recent maturity reached in bottom frontal circulation studies in the North Sea and the Irish Sea.

This thesis is organized as follows:

Chapter 1. An introduction to the concepts of bottom fronts and cold, dense pools is given. This follows a brief examination of the theoretical background of frontal dynamics. Tidal mixing fronts in the European shelf sea area are exemplified, and the Celtic Sea tidal mixing front is introduced. Also, a review of previous circulation studies in the study area is addressed. Additionally, the aims of the thesis are presented.

Chapter 2. In this chapter the regional characteristics of the Celtic Sea such as bathymetry, tides, stratification and winds are presented. It begins with a brief description of the location and seabed topography and then considers the tidal regime of the region. A detailed description of the stratification and the tidal mixing front in the Celtic Sea is presented. Finally, some characteristics of the wind field in the study area are described.

Chapter 3. A description of the observational methods is provided including an account of the two oceanographic campaigns and the performance, quality control and calibration of the different instruments used in this thesis.

Chapter 4 The hydrographic data are presented with a three-dimensional view of the frontal areas. In addition, an indirect flow field estimate was obtained from geostrophic calculations using the density field and the bottom as a level of no motion.

Chapter 5. The Lagrangian field from the drifter observations is shown and a comparison of this field with satellite images of SST and correlation with local wind are performed. A broad analysis of the possible responsible forcing mechanisms is considered.

Chapter 6. The removal of tidal signal from the ADCP data is presented in this chapter. An analysis of two detiding methods of ship-mounted ADCP data is discussed. One of the methods consists of using a barotropic numerical model (Davies and Jones, 1992b) and the second, using a least square and polynomial interpolation (Candela *et al.*, 1992). In addition, an exploration of a new detiding technique is developed. The residuals from ship-mounted and bottom-mounted ADCP are presented. Drifter filtering was performed and harmonic analysis was applied to the observations from the bottom-mounted ADCP moorings. Also, results from the correlation between mooring data and local wind are shown.

Chapter 7. Here, the hydrographic and flow observations are compared with the results from a baroclinic numerical three-dimensional model performed for the European shelf sea area by the Proudman Oceanographic Laboratory.

Chapter 8. A discussion integrating all the observations and model results is presented describing and explaining the circulation in the shelf sea area of the Celtic Sea during the summer.

Chapter 2

Regional characteristics of the continental Shelf of the Celtic Sea

2.1 Location and Bathymetry

The study area is located in a continental shelf sea of the eastern North Atlantic, named in 1921 as the Celtic Sea (Clark, 1977), an appropriate name for a sea surrounded by the *Celtic Lands* of Ireland, Wales, Cornwall and Brittany (Fig 2.1a). This region is connected to the tidally energetic Bristol Channel and southern Irish Sea, the latter through the St. George's Channel. In the south, it maintains an open communication with the North Atlantic Ocean, where the shelf break is located at approximately 200 m depth. The southernmost limit in this study was set at ~50° N, *i.e.* the shelf break is not included. However, the Bristol Channel is contained within the study area which topographically can be considered as an extension or strip of the shelf of the Celtic Sea with depths < 40 m.

The shelf sea area of the Celtic Sea is a shallow embayment with depth range between 30 to 120 m (Fig 2.1b). Its bottom topography is characterized by an elongated basin of ~100-110 m named the Celtic Deep, which extends from the St. George's Channel towards the central Celtic Sea along a north-south line inclined approximately 25° from the geographic north.

In general, the isobaths show a gradual topographic change, mostly on the eastern side of the shelf rather than on the western side (Irish coast), which generally shows a steeper seabed slope when approaching the shoreline (except for the region of the Nymphe Bank). The latter area is an extensive (approximately an area of 14000 km^2) and relative shallow bank located in the north-west corner of the Celtic Sea with depths ranging from 25 to 75 m. Additionally, there is a shoal area known as The Smalls, distinguished by a series of tiny and rocky isles. Pronounced steep seabed slopes form the coastal borders of the St. George's Channel where the steepest bottom topography of the Celtic Sea is found.

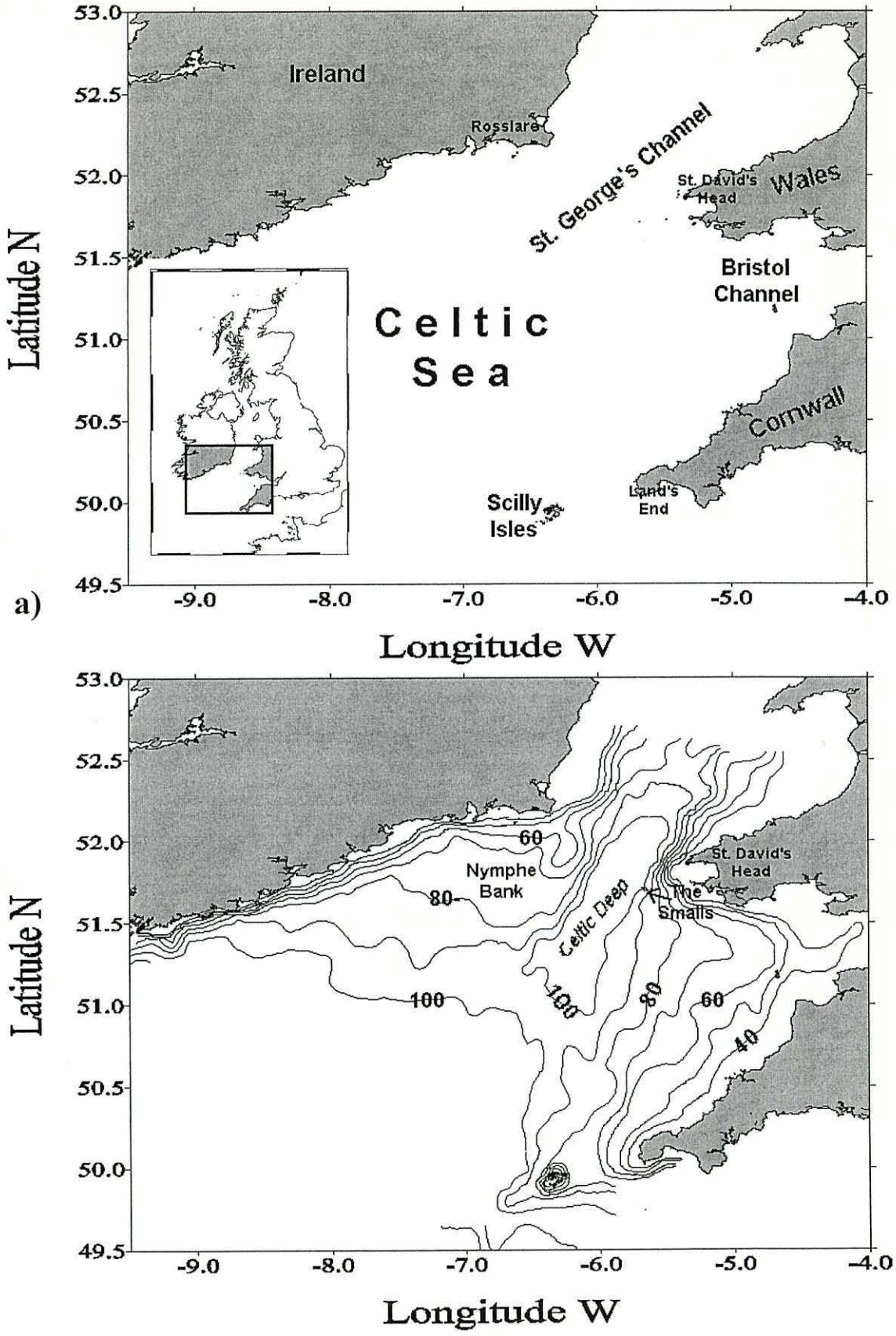

Figure 2.1 a) Study area and name of places referred in the work. b) Bathymetry of the study area and name of the main bottom topographic features used throughout the text.

2.2 Tides

Tides represent important forcing in the continental shelf sea area, because their rise and fall are frequently accompanied by strong horizontal currents. These tidal currents dominate the dynamics of the European shelf sea areas. In the Celtic Sea, the semi-diurnal tidal constituents M_2 and S_2 comprise 90 % of the total kinetic energy of currents (Pingree, 1980). However, M_2 constitutes 75 % of this total, thus M_2 represents the most important constituent.

Cotidal maps of M_2 (Fig 2.2) show that the incoming progressive tidal wave propagates in a northeastward direction, taking ~ 2 hours to travel from the shelf break to the St. George's Channel. Also, an amphidromic system lying to the north of Rosslare (Northeast of the St. George's Channel) is observed. The tidal amplitude range varies from about 11 m at the head of the Bristol Channel (not shown) to < 1 m near the amphidromic region (Pingree, 1980).

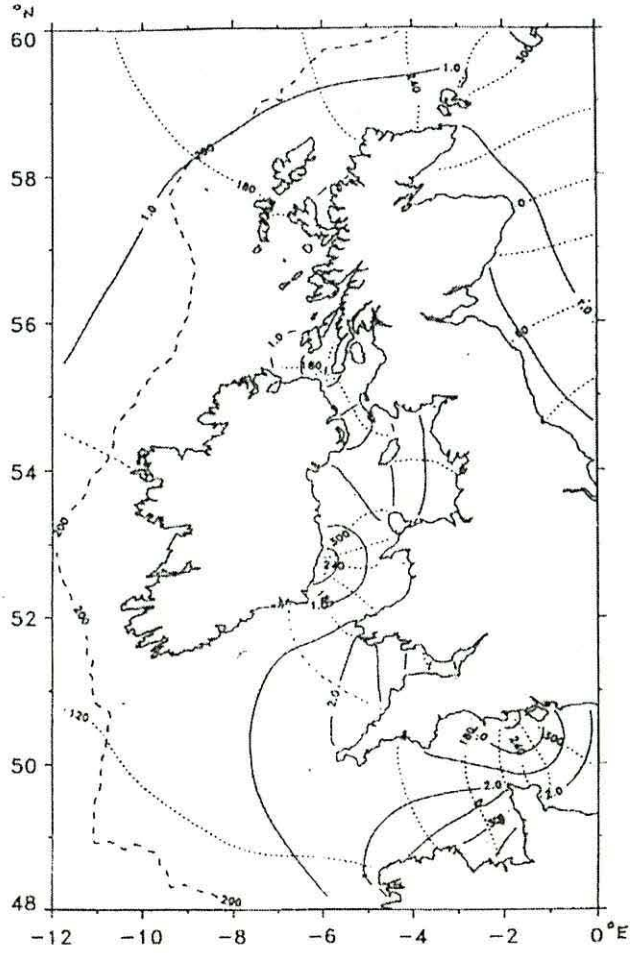

Figure 2.2 M_2 cotidal map. Solid lines represent amplitude (meters) and dashed lines phase (degrees). (From Simpson, 1998).

Over the region there is considerable variability in tidal stream amplitude. In the vicinity of Nymphe Bank spring speeds are approximately 0.3 m s^{-1}, whereas, in the St. George's Channel, tidal currents exceed 1 m s^{-1}, and in surrounding areas such as the English Channel and Bristol Channel, tidal currents are even stronger (Fig 2.3) (Pingree, 1980). However, only weak (< 0.02 m s^{-1}) tidally induced residual velocities are predicted (Fig 2.4) (Prandle, 1984).

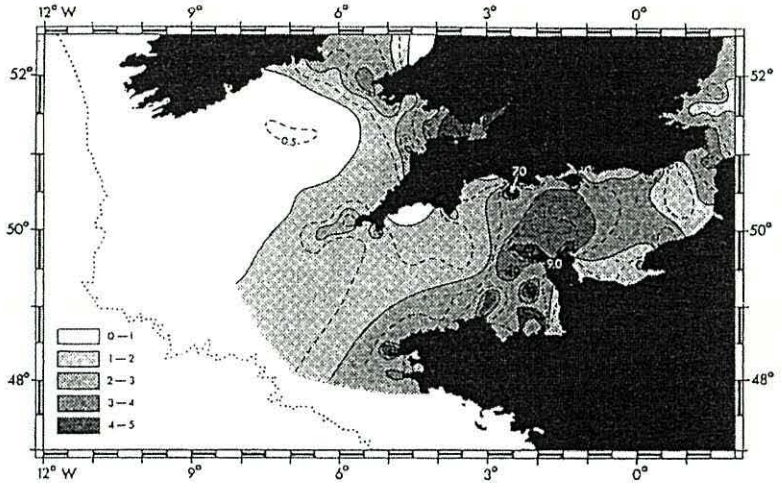

Figure 2.3 Tidal stream amplitude for M_2 (major axis of the ellipse) at spring tides. Tidal stream in knots. (From Pingree, 1980)

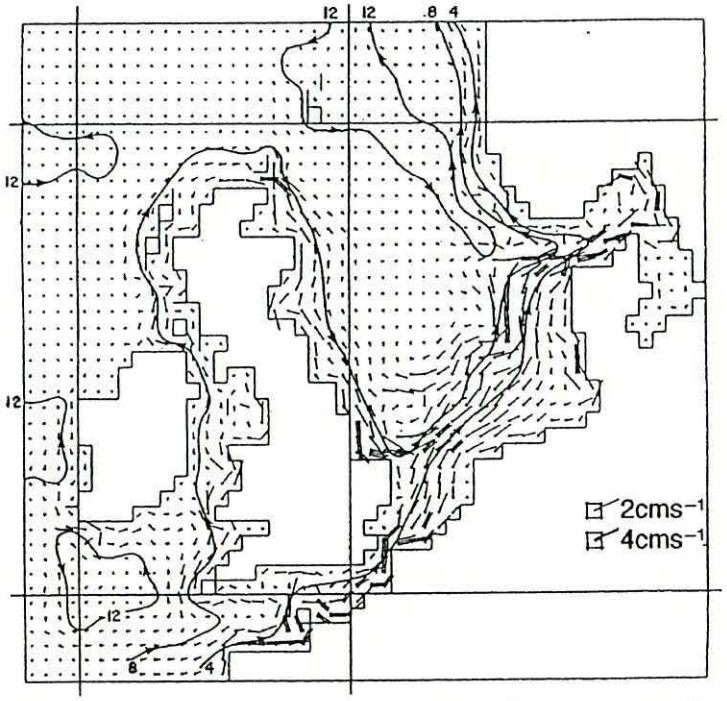

Figure 2.4 Eulerian tidally induced residual currents for M_2 (From Prandle, 1984).

In most of the Celtic Sea area, the M_2 tidal ellipses (Fig 2.5) rotate clockwise but they become strongly anti-clockwise in the northwestern region of the Celtic Sea near the entrance of the Bristol Channel. The Celtic Sea area is a less restricted area in comparison with the Bristol Channel, Irish Sea and English Channel, so it exhibits more circular tidal ellipse, with the minor axis 20-25% of the major axis. The ellipse becomes more elongated and almost rectilinear (the ratio of minor to major axes is less than 10%), toward more laterally constricted areas such as the Bristol Channel, Irish Sea and English Channel (Robinson, 1979).

The principal solar semi-diurnal (S_2) appears to be very similar to M_2, except that S_2 is only about the 33% of the tidal amplitude of M_2 (Robinson, 1979; Pingree, 1980). However, the combination of these two constituents in spring (neap) tides results in an amplitude 1.33 (0.67) times the values for M_2 only (Pingree, 1980).

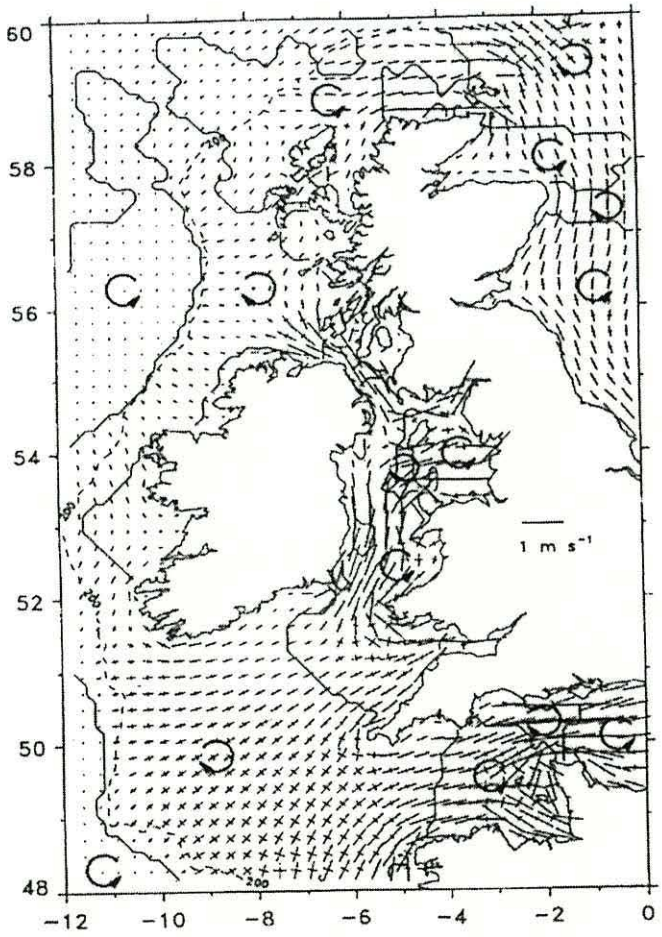

Figure 2.5 Tidal ellipses for M_2, the sense of rotation of the tidal current ellipse is indicated (From Simpson, 1998).

2.3 Stratification

In most of the Celtic Sea, a high degree of stratification is developed during the summer. Since density structure is mainly controlled by temperature (Simpson, 1976; James, 1977), the seasonal evolution of the stratification and its distribution is described in this section in terms of its thermal structure.

The heating period in the Celtic Sea lasts from March to September (Fig 2.6) but the seasonal formation and erosion of the thermocline in the Celtic Sea is quite dephased from the seasonal heating. In March, the water column is isothermal over most of the shelf with temperature ~ 8 °C, and even in April these vertically mixed conditions are still present (Pingree *et al.*, 1976; Williams and Conway, 1984; Elliott *et al.*, 1991). By the end of April and early May, as a result of heating and mixing events the stabilization of the water column takes place and thermocline forms at approximately 15-20 m depth (James, 1980; Pingree, 1980).

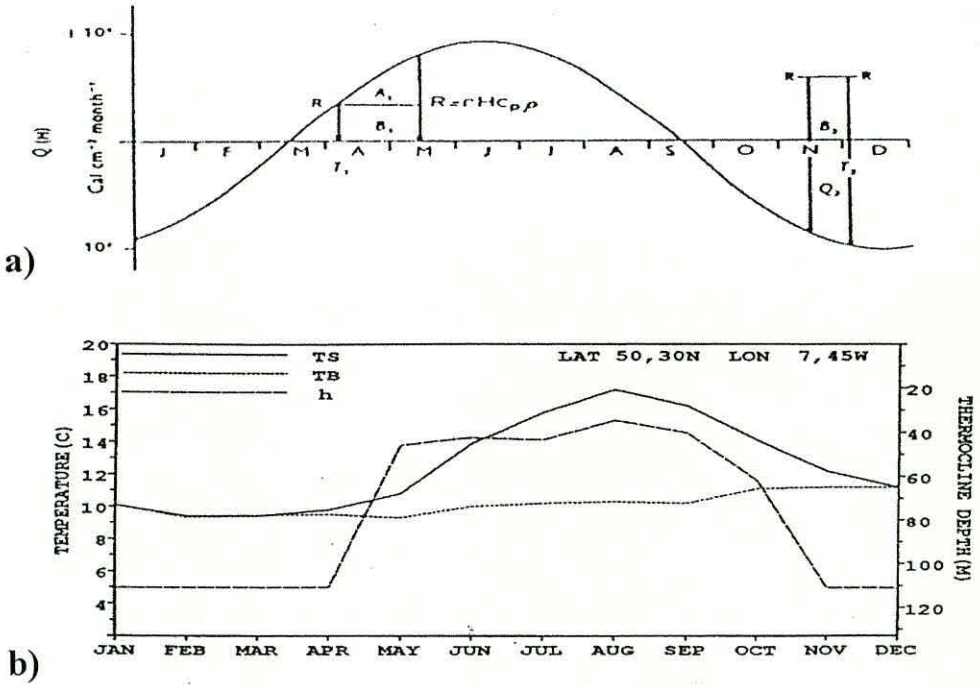

Figure 2.6 a) Annual net heating cycle at the sea surface, Q(H) per month. (From Pingree, 1980). b) Annual cycle of surface and bottom temprature and thermocline depth in the Celtic Sea (From Elliott and Li, 1991).

The development of the thermocline starts in the western region of the Celtic Sea (near Nymphe Bank), where relatively weak tidal currents are found (Fig 2.7). It spreads quickly across, at more than 30 km day^{-1} towards the shallower regions (Pingree, 1980; Elliott and Clarke, 1991; Elliott *et al.*, 1991). By the middle of June, the surface temperature has reached 14 °C (Williams, 1985) and the fronts have reached their summer positions (Elliott *et al.*, 1991). In regions where the surface tidal streams exceed 1.0 m s^{-1}, no pronounced thermocline development occurs and consequently conditions around the Bristol Channel, the southern Irish Sea (St. George's Channel), and some other shallow coastal regions (without freshwater input) remain well mixed throughout the summer (Matthews, 1913; Simpson, 1976; Pingree, 1980).

Vertical temperature contrasts continue increasing in the stratified regions through the summer season. Then, in August (near the end of the cycle heating), fully developed stratified conditions in the Celtic Sea are observed with a thermocline located at 30-40 m depth (Pingree, 1980). In this month, the maximum annual value of the sea surface temperature occurs (about 16 - 17 C°) and the top to bottom temperature difference could be as large as 6 °C (Pingree, 1980; Williams and Conway, 1984; Elliott *et al.*, 1991).

Although the surface temperature changes dramatically during the heating season, the bottom temperature in contrast increases steadily by only about 1.0-1.5 °C (Elliott *et al.*, 1991). Also, an examination of the bottom waters by Bowden (1950) observed that in the region of weak vertical mixing, the bottom waters increased in salinity during the summer months.

When net heat loss occurs, buoyancy, which has been stored at the surface during the heating period, is eroded by tidal/wind mixing and cooling at the surface. Thus, the break down of the seasonal stratification occurs in October (Elliott *et al.*, 1991). While the thermocline persists, the surface is always warmer than the bottom, and so the bottom mixed layer reaches its maximum temperature only when the thermocline has been completely eroded (Pingree, 1980). The vertical contrast is weak during November and by the end of this month stratification is completely overturned (Matthews, 1913; Elliott *et al.*, 1991).

In contrast to the rapid onset of the stratification, the breakdown and retreat of the fronts occur more slowly and towards deeper water with a mean speed of around 5 km

day^{-1} (Fig 2.7) (Elliott *et al.*, 1991; Elliott and Clarke, 1991). Throughout the winter months, from December to April, well-mixed water conditions are present in the Celtic Sea (Elliott *et al.*, 1991). Thus, stratified conditions in the Celtic Sea persist for about 7 months.

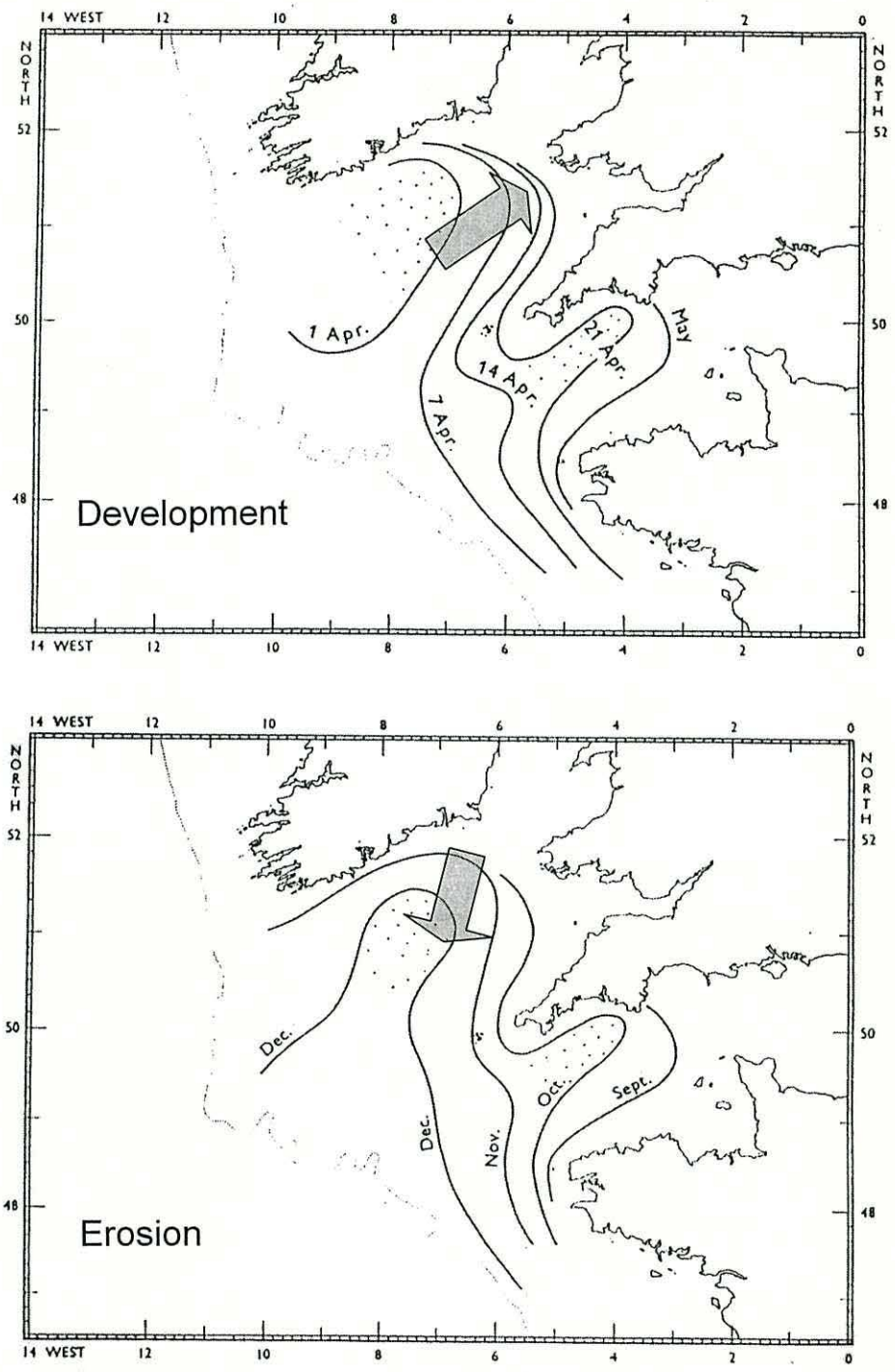

Figure 2.7 Development and erosion of the thermocline by weekly and monthly contours respectively. (From Pingree, 1980).

2.4 The Celtic Sea tidal mixing front

In the Celtic Sea, the difference in tidal regimes combined with change in depth plays an important role in the distribution of stratified and vertical mixed regions allowing the development of frontal areas. Thus, during the summer, a tidal mixing front forms in the Celtic Sea which divides the well-mixed water column of the Irish Sea and Bristol Channel from the stratified water of the Celtic Sea. This tidal mixing front has a pronounced thermal surface gradient as a signature (up to 4 °C over 20-25 km, Horsburgh *et al.*, 1998), that permits it to be observed from I-R imagery (Fig 2.8) (Pingree, 1978). Its position can be predicted with h/u^3 stratification criterion (see Fig 1.9) (Pingree and Griffiths, 1978) with important typical tidal excursion near the tidally energetic St. George's Channel estimated of ~10-20 km (Simpson *et al.*, 1978; Thompson and Pugh, 1986). This front appears to be quite variable and convoluted, as observed from I-R images (Simpson *et al.*, 1978), with some large-scale (20-25 km) instabilities with eddy-like form of a few days duration (Simpson and Pingree, 1978).

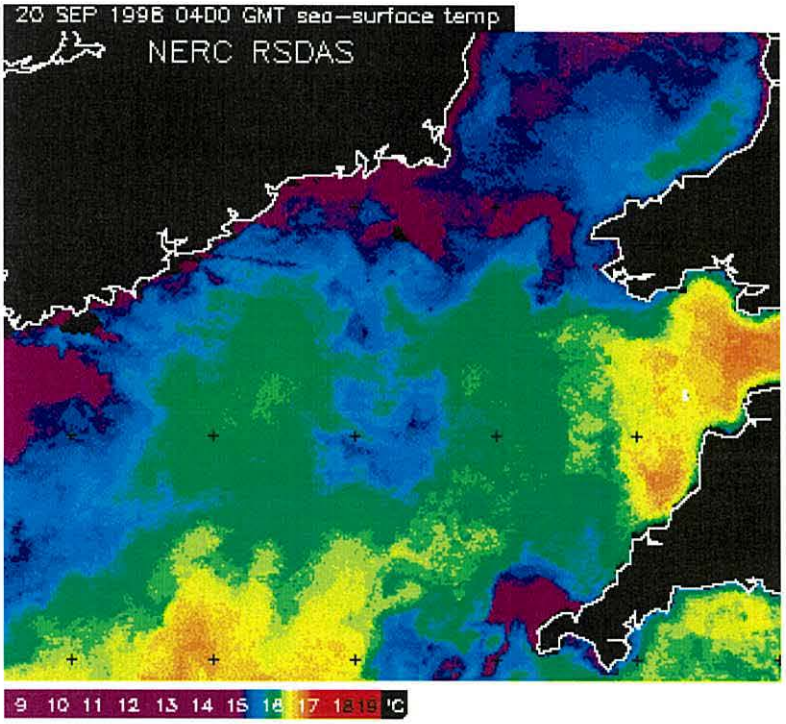

Figure 2.8 Sea surface temperature from a satellite image on September 20, 2000 showing the Celtic Sea Front, compare with the schematic diagram of this front in figure 2.10.

The vertical density structure of the tidal mixing front of the Celtic Sea comprises surface and bottom fronts (Fig 2.9) (Simpson, 1976; James, 1977). The location of the bottom front and surface fronts do not coincide along the horizontal axis (James, 1977) and the bottom front is dominant, *i.e.* the strongest horizontal density gradients are associated with the bottom rather than the surface front.

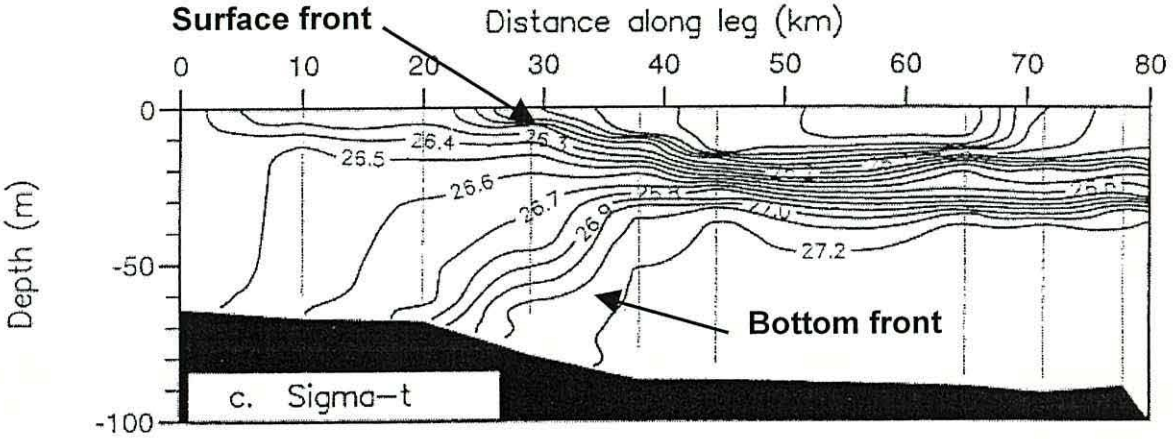

Figure 2.9 Density vertical structure of the Celtic Sea tidal mixing front obtained by Horsburgh *et al.* (1998), during summer 1997. (From Horsburgh *et al.*, 1998).

In addition, the tidal mixing front shows a persistent "tongue-like" feature (Fig 2.10), which appears to be due to the intrusion of cooler water southward from the tidally mixed regime into the stratified region of the Celtic Sea (Pingree, 1979; Horsburgh *et al.*, 1998). This intrusion is thought to represent an advective flow (as explained later) since this structure is not predicted by the stratification parameter (Pingree, 1979). Another "tongue" of relatively warmer water can be observed in the centre of the St. George's Channel (Fig 2.10). Even though this warm tongue is not as clear and persistent as the cold tongue, it can occasionally extend as much as 100 km northward (Fig 2.11) (Pingree, 1979; Horsburgh *et al.*, 1998).

The response of the Celtic Sea tidal mixing front to the wind was investigated by Wang *et al.* (1990). Their results (Fig 2.12) showed that the surface front responds to winds that blow in an approximately along-front direction. In the case of the Celtic Sea tidal mixing front in the St. George's Channel, the surface front responds to a northwesterly wind, producing a southward advection of the surface front of up to 80 km. However, the surface front does not respond to southerly winds, staying at the same position. This can be explained in terms of a coupling between horizontal advection and

vertical mixing. Thus, during a northwesterly wind the Ekman transport brings cool water across the front and the thermocline can be quickly eroded even with modest wind stirring, so an advance of the surface front is observed (Wang *et al.*, 1990). In contrast, during a southerly wind, warm water moves over cool well-mixed water being counteracted by vertical mixing, consequently a small change of surface temperature is observed (Wang *et al.*, 1990). This might explain the cold (warm) intrusions, however further work is required to explain these features.

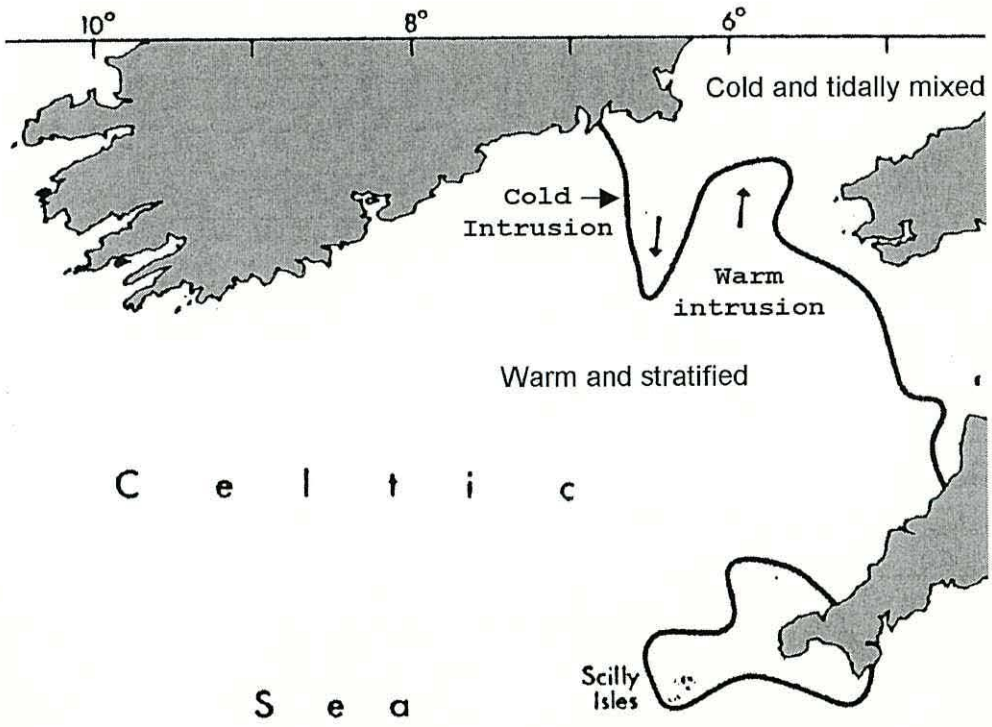

Figure 2.10 The convoluted tidal mixing front of the Celtic Sea shows a semi-permanent tongue of water from the Irish Sea which does not correspond with the stratification parameter. (From Pingree, 1979)

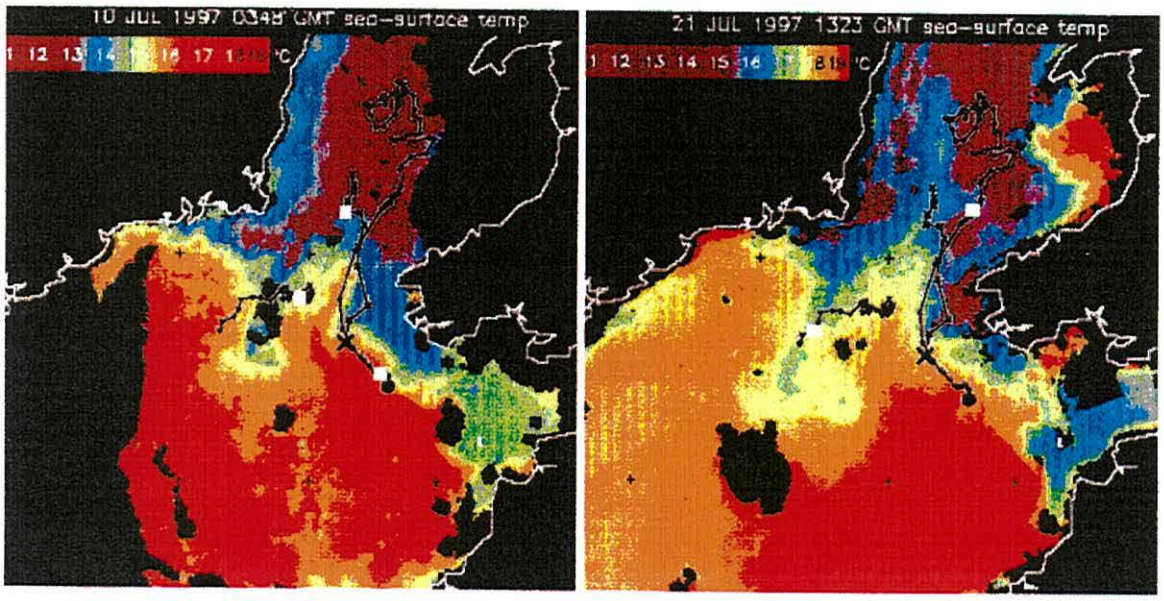

Figure 2.11 SST for the region of the Saint George's Channel and drifter positions during July 1997. Their trajectories follow the contours of the front and agree with the intrusions observed through the channel. (From Horsburgh *et al.*, 1998).

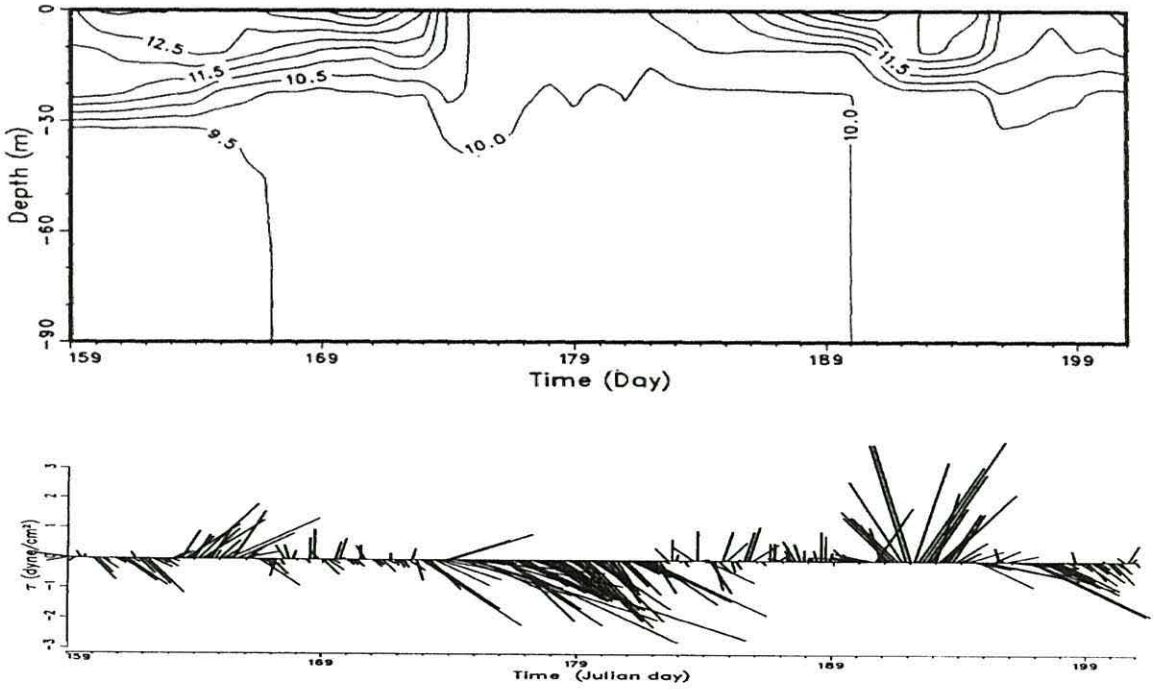

Figure 2.12 Modelled temperature at a frontal location (around St. George's Channel) and the wind stress. (From Wang *et al.*, 1990).

2.5 Wind field

In the Celtic Sea, mean winds do not have a strongly seasonal character (in contrast to the California coast where there is a drastic spring reversal in the wind direction, Badan-Dangon *et al.*, 1991), since the local air pressure distribution is affected by the continuous movement of either high or low pressure systems across the region resulting in a large variability in the wind direction (Hydrographic Department, 1970). Nevertheless, winds are more predominantly from the west-southwest, blowing occasionally from the north, with a tendency for more southwesterly direction in winter, when the pressure gradient is greater and so the prevailing winds are correspondingly stronger, whilst during the summer season they are more westerly and weaker (Cooper, 1967; Hydrographic Department, 1970). However, gales may occur in any season, and during the summer their frequency of occurrence is reduced to 1/10 of that in the winter (Cooper, 1967).

The Celtic Sea responds rapidly and uniformly to wind, in particular, to storm events (surges) which can result in surface velocities can be of 3 % of the order of the wind speed and mostly aligned with the wind direction (Davies and Jones, 1992a). However, wind-generated residual currents are mainly weak (≤ 0.02 m s^{-1}) and barotropic in the shelf area of the Celtic Sea and St. George's Channel (Fig 2.13) (Thomson and Pugh, 1986; Pingree and Le Cann, 1989; Young *et al.*, 2001); with the exception of localised shallow coastal regions with values up to 0.20 m s^{-1} in the region of the Smalls (Young *et al.*, 2001) and up to 0.05 m s^{-1} around the Isles of Scilly (Pingree and Le Cann, 1989).

Finally, apart from the local and immediate response to winds in the Celtic Sea, there is a non-local influence of the wind forcing due to storm events in adjacent seas such as the North Sea and Irish Sea (Howarth, 1975; Thompson and Pugh, 1986). Due to the fact that during a storm event, water that flows out piles up elsewhere, creating a localized pressure gradient resulting in a return flow when the driving forces relax. Thompson and Pugh (1986) explored the possible pattern of circulation expected for a constant flow of 0.10 m s^{-1} from the North Sea and from the Irish Sea (Fig 2.14). Thus, a flow from the North Sea can force a current of about 0.05 m s^{-1} around the southwestern tip of Cornwall and the Isles of Scilly (Fig 2.14a). This bifurcates and becomes weaker as it enters the Celtic Sea in a northward flow through the St. George's Channel and a westward flow around the southernmost tip of Ireland (Thompson and Pugh, 1986). In the case of a flow

from the Irish Sea (Fig 2.14b) through the St. George's Channel, the resulting circulation in the Celtic Sea consists essentially of a broad westward current of about 5 cm s^{-1} along the Irish coast; the rest of the Celtic Sea is barely affected (Thompson and Pugh, 1986).

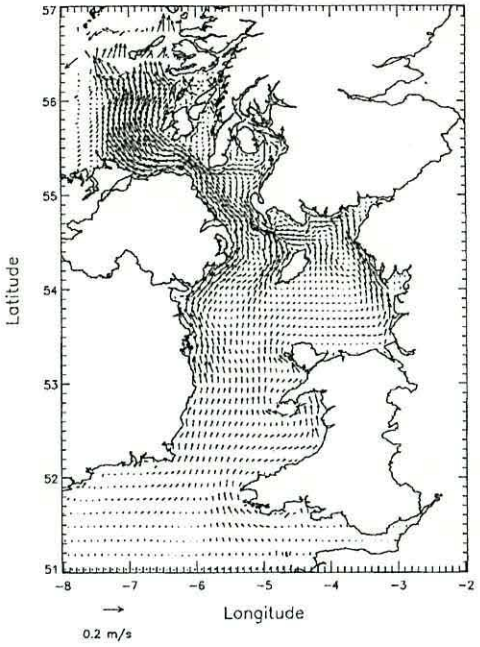

Figure 2.13 Wind induced residual velocities from a three dimensional curvilinear model. (From Young *et al.*, 2001).

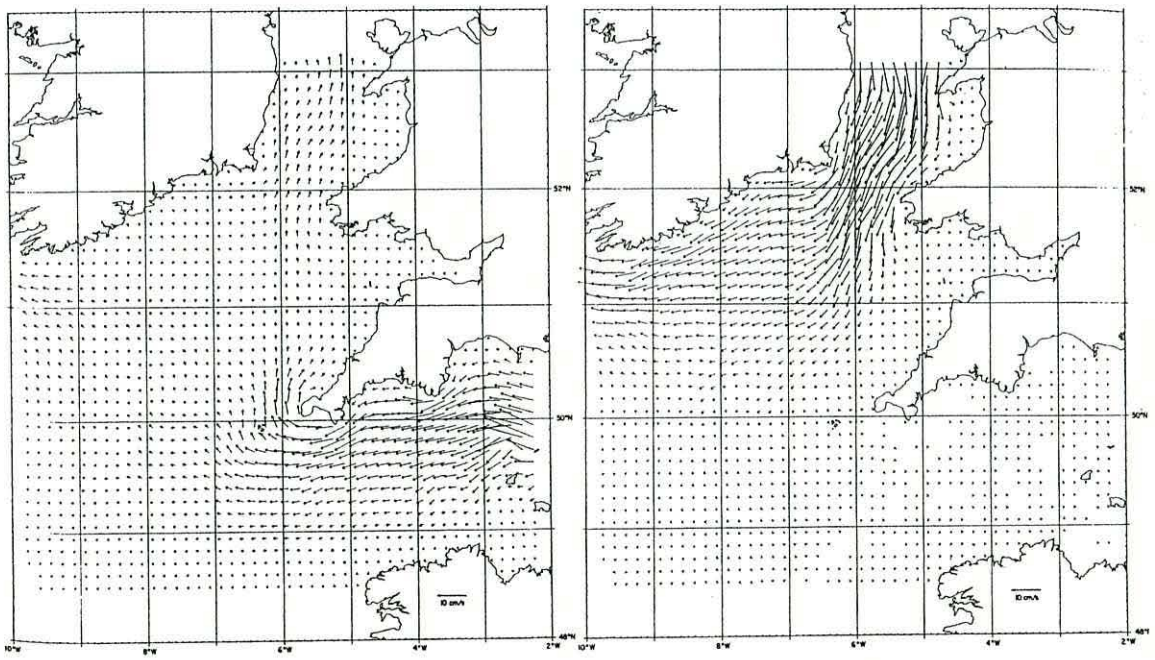

Figure 2.14 Steady circulation resulting from a flow of 10 cm s^{-1} through (a) the Dover Strait and (b) the Saint George's Channel. (From Thompson and Pugh, 1986).

Chapter 3

Instrumentation and observational methods

3.1 Introduction

Studies concerning the circulation in shelf seas demand equipment capable of rapid and simultaneous surveying of hydrographic features and velocity structure. At the present, hydrographic measurements over the continental shelf generally involve research vessels equipped with ADCP, which allow velocity measurements to be made simultaneously with hydrographic measurements. Additionally, Lagrangian devices deployed on targeted well-defined density structures can greatly contribute to understanding of the dynamics of these features (Hill *et al.*, 1994; Hill *et al.*, 1997b; Brown *et al.*, 1999a; Horsburgh *et al.*, 2000). Also, it is increasingly common to have access to some form of satellite remote sensing of sea surface temperature (SST) to help direct observations and to place the measurements into a broader context (Brink, 1998).

In this study, it was possible to use a wide range of these instruments with good spatial resolution. The purpose of this chapter is to describe the observational campaigns in the Celtic Sea during summer 1998, providing detailed information about location of the measurements and the instruments used. Each instrument and the respective calibration technique is described in successive sections of the chapter.

3.2 Two oceanographic campaigns in the Celtic Sea in 1998

In order to understand the overall circulation in the Celtic Sea during summertime with particular emphasis on the frontal areas, two observational campaigns were conducted in the Celtic Sea aboard the Centre for Environment, Fisheries and Aquaculture Science (CEFAS) Research Vessel *Corystes* during the summer of 1998. The first campaign lasted from 13 July to 24 July 1998 (hereafter referred to as CORY798). It was conducted during poor weather conditions, so the initial area of coverage planned for the Scanfish measurements was not completed. Nevertheless, 23 satellite tracked ARGOS drifting buoys, with a drogue centred at 30 m depth, were deployed. In addition, 2 bottom mounted ADCP moorings were deployed and 10 Scanfish legs with simultaneous ADCP data observations from the ship-mounted RD Instruments broadband 153.5 kHz ADCP were obtained, covering a track length of approximately 990 km (Figure 3.1). Appendix 2 provides the initial and final position of each leg. The original aim included obtaining current time series from bottom-mounted ADCP's in three locations of the Celtic Sea/St. George's Channel. However, moorings are vulnerable to damage or loss in commercially fished coastal waters and the moored ADCP deployed at the Celtic Deep was removed by a ship.

The second campaign lasted from 26 August to 6 September 1998 (hereafter referred to as CORY998). The main sampling aims of this cruise were to recover the mooring arrays, to recover the free floating satellite-tracked buoys and to undertake further Scanfish legs and ADCP measurements (Figure 3.2). The initial and final position of each leg is provided in Appendix 2. The covered cruise track length with the Scanfish was 2500 km. During this cruise, for technical reasons 3 different CTDs were used, necessitating different calibration values, as explained in section 3.3.1.

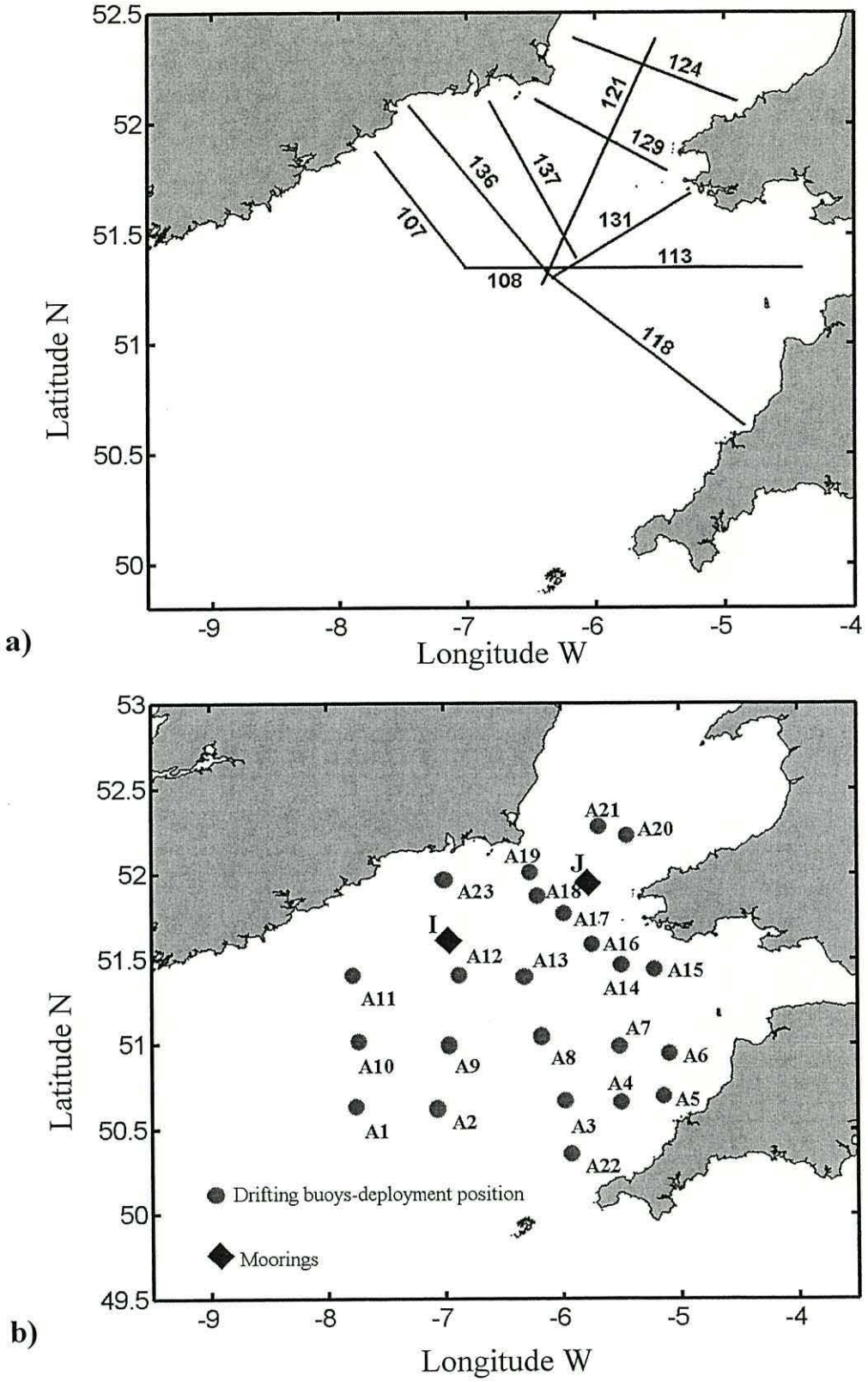

Figure 3.1 a) Location of Scanfish (and ADCP) sections during CORY798 campaign. b) Locations of Argos buoys (circles) and mooring deployments (diamonds), CORY798.

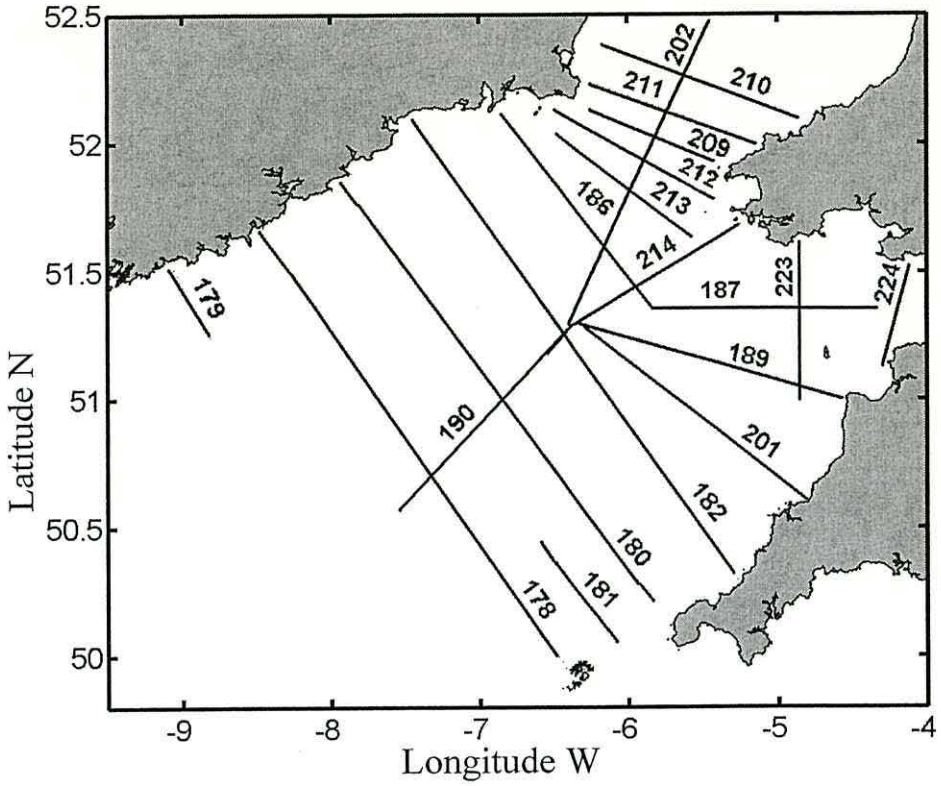

Figure 3.2 Location of Scanfish (and ADCP) sections during CORY998 campaign.

3.3 Scanfish towed undulating CTD vehicle

Towed undulating vehicles containing a CTD (Conductivity-Temperature-Depth sensor) such as the SCANFISH (Figure 3.3) allow hydrographic measurements with detailed resolution of water column structure and good spatial coverage (Brink, 1998; Brown *et al.*, 1999a). In particular, the SCANFISH has been extensively used in the frontal regions of the western Irish Sea and North Sea defining hydrographic structures with a high spatial resolution impossible to obtain using conventional CTD stations (Brown *et al.*, 1996; Brown *et al.*, 1999a; Fernand, 1999), this device was used here to collect the hydrographic information.

Manufactured by Geological & Marine Instrumentation (GMI) of Denmark and developed in conjunction with CEFAS, the Scanfish Mk II is a highly stable towed vehicle designed for the high-speed collection of oceanographic data. The body frame consists of a symmetrical wing section with dimensions of approximately 80x160x14 cm; the frame has two adjustable flaps on either side of the trailing edge for pitch and roll control. The SCANFISH is a platform on which a broad range of sensors may be mounted; here, the Scanfish was equipped with a Falmouth Scientific Inc. (FSI) CTD and a (Haardt) combined turbidity/fluorescence sensor.

The position of the towed fish in the vertical is software controlled by a PC, with information communicated via the 11.7-millimeter-diameter towing cable. Two PC's were connected to the towing cable. Through one of the PC's, the operator is able to interactively control the flight path (*i.e.* the ascent and decent rate) of the Scanfish. Even though, this can be done in an automatic mode, for safety reasons it is preferable to operate the Scanfish manually by command from the system's keyboard. Using the information from the pressure sensor, the altimeter and data displayed graphically, the operator can control the distances from the sea surface and the seabed. The second PC is used to log the information from the instruments mounted on the SCANFISH; the EG & G software package was used to collect the FSI CTD data at a rate of 17 Hz. (Brown *et al.*, 1996; Fernand, 1999).

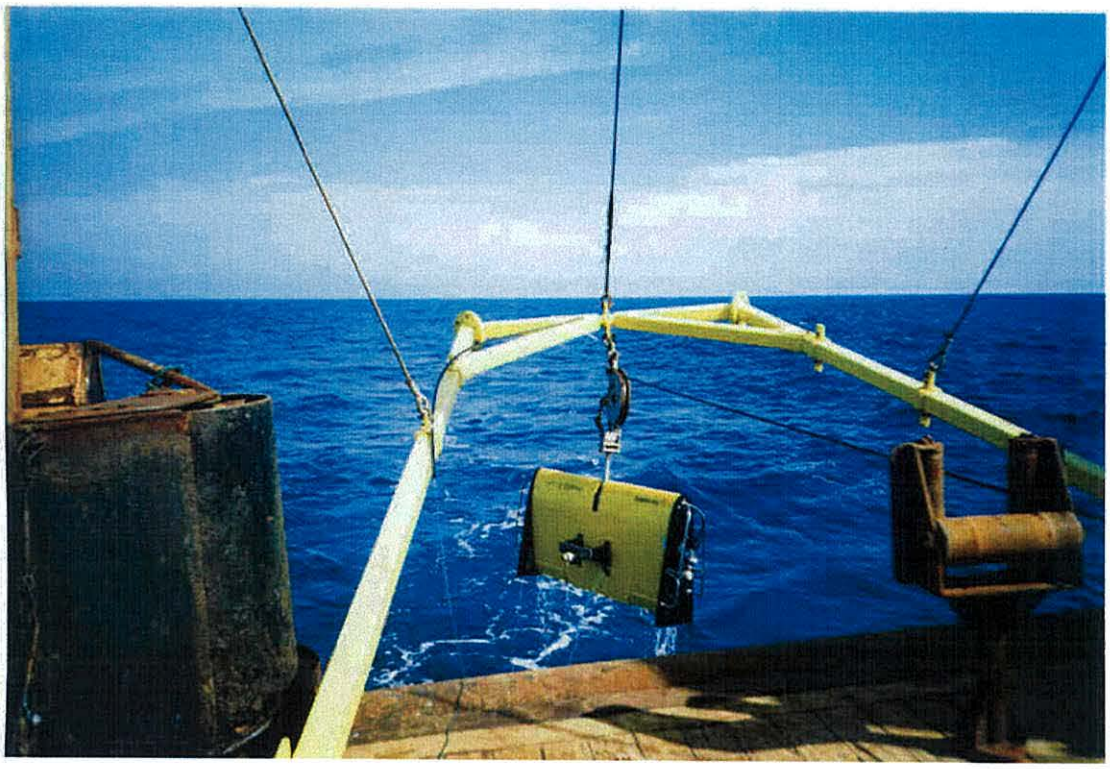

Figure 3.3 Photo of the SCANFISH during its recovering in CORY798 campaign.

The horizontal sampling resolution is a function of water depth and the towing speed (Fernand, 1999). Thus, at a ship speed of 8 knots (4.1 m s^{-1}) and a vertical flight speed of 1 m s^{-1}, the sample horizontal resolution is ~ 500 m at 125 m water depth and ~120 m at 30 m depth (Figure 3.4). In order to maintain approximately the same horizontal resolution (a uniform saw tooth profile), it is necessary, depending on the water depth, to increase or to decrease the vertical ascent speed. However, the vertical resolution tends to increase in shallower areas. For the Celtic Sea, the flight path of the Scanfish was nominally from within 4 m at the surface to 10 m above the seabed. The length of cable paid out varied between 150-450 m with vertical ascent speeds between 0.4-1 m s^{-1} depending on the water depth. Typically, the ship's operational speed was 8 knots (4.1 m s^{-1}).

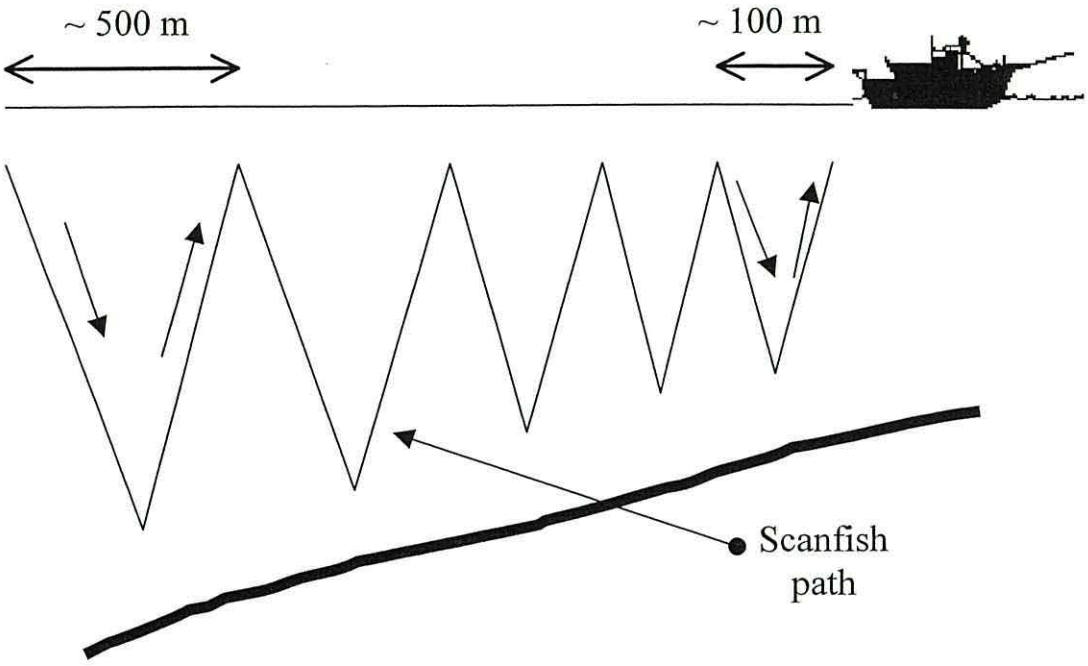

Figure 3.4 Schematic representation of the SCANFISH path and the change in the horizontal resolution using a constant ship's speed and a constant vehicle flight speed for different water depths.

3.3.1 FSI CTD Calibration

The FSI CTD used on the Scanfish was fitted with a pressure sensor, conductivity cell, platinum resistance thermometer (PRT) and fast response thermistor (FRT), the latter used in the calculation of the salinity from conductivity.

Temperature and pressure sensor calibration was performed pre-cruise (CORY798) and post-cruise (CORY998). The pressure sensor was calibrated against a Druck dead-weight tester in the range 0 - 500 dbar, at a temperature as expected *in-situ*, obtaining an accuracy of ± 0.5 dbar and resolution of ± 0.1 dbar. Calibration for the temperature sensor was determined by reference to two highly stable and long response PRT sensors using a water bath. The accuracy obtained for the temperature sensors was ± 0.001 °C. Final calibration values for pressure and temperature applied to the data were the average of pre- and post-campaign calibration values. Whereas pressure was applied as an offset (value = 0.2333 dbar), temperature calibration was applied as a simple quadratic regression; Table

3.1 shows the regression coefficient values obtained from a quadratic regression ($y = ax^2 + bx + c$) when comparing both slow and fast temperatures with the true temperature.

Table 3.1 Regression coefficients obtained from a quadratic regression of the form $y = ax^2 + bx + c$ for the slow and fast temperature sensors of the different CTDs used.

Serial Number		*a*	*b*	*c*
1366	Fast	0.00006029	-0.00190442	0.01288080
	Slow	0	-0.00035070	0.00359836
1351	Fast	0.00007564	-0.00208405	0.00811263
	Slow	0.00000268	-0.00016252	-0.00004166
1322	Fast	0.00006461	-0.00184357	0.01498167
	Slow	0.00001101	-0.00036623	0.00309023

Salinity calibration for the FSI CTD mounted on the Scanfish requires extra consideration in comparison with conventional CTD/rosette calibration alongside a water bottle sampler. In contrast, for a towed vehicle only surface water samples can be obtained whilst the ship is underway and they need to be carefully matched with the logged Scanfish data. Here, the water samples were collected hourly from the ship's pumped underway sampling system, the inlet of which is at 4-4.5 m depth. The time of sample and the length of the cable were recorded. However, one of the main limitations of this is the lag-time between the sample and the measured value once the Scanfish reached the surface. The degree of vertical variation in the near surface salinity makes it even more difficult to select the appropriate salinity value from the Scanfish data. Fernand (1999) addressed this problem proposing a salinity calibration procedure for Scanfish data, which is used here and can be summarized as follows.

Firstly, salinity values are derived from conductivity using the FRT producing a first salinity record. This record is scanned looking for data at approximately the same depth of the pump's inlet (*i.e.* between 4-5 m) and at the same time of the sample collection. Later, the salinity sample values are compared with the Scanfish data; outlying values (*i.e.* large spikes in the salinity record) give an indication of the time lag of the temperature sensor with respect to the conductivity sensor. This time lag-correction is applied to the whole time series and a new set of FSI calibration values is obtained. The

same procedure is repeated to minimize the standard deviation. Finally, the correction of the FSI salinity data is applied as a constant offset to the whole record.

During CORY998, a technical problem was detected in the fast temperature sensor near the end of completion of leg 187. Two more CTDs were installed instead, one for legs 189-190 and one more for 201. The original FSI CTD was used again from leg 202 onwards, considering the slow temperature sensor for salinity calibration however. Table 3.2 provides the calibration accuracy of the FSI salinity sensors obtained for each instrument used in both cruises.

Table 3.2 Calibration accuracy of the FSI salinity sensors for each cruise and the offset value calculated. The accuracy is represented as the 1st standard deviation of the calibration values obtained from derived fitted curves.

Cruise	Leg	Temperature Sensor	STD	Offset calculated	Number of calibration points
CORY798	All legs' cruise	Fast	± 0.005	0.0391	57
CORY998	178-187	Fast	± 0.009	0.0266	69
	189-190	Fast	± 0.008	0.0019	19
	201	Fast	± 0.010	0.0360	9
	202-224	Slow	± 0.009	0.0582	51

3.4 Argos drifters

A significant part of our present knowledge of the ocean circulation has been obtained by tracking the path of drifting objects. In the past, these objects were basically ships, waterproof cards or sealed bottles seeded in the sea. In the last 20 years, the rapid technological advance in satellite radio location has opened the possibility of accurate position fixing of Lagrangian devices such as satellite-tracked drifter buoys. These devices have succeeded in providing more insight into either oceanic or regional circulation studies with relatively high temporal and spatial resolution ranging over several scales, from studies of Global Ocean Circulation (Sombardier and Niiler, 1994), tracking of mesoscale eddies (Pingree, 1994) and coastal applications (Davies, 1985). In addition, they have helped to reveal seasonal gyre-like structures in the semi-enclosed seas of the Gulf of California (Lavin *et al.*, 1997) and the Irish Sea (Hill *et al.*, 1994; Horsburgh *et al.*, 2000); the latter had not previously been revealed by Eulerian methods.

In this study, 23 satellite tracked drifting Argos buoys manufactured by Far Horizon Marine were used. These buoys have a cylindrical surface float which is connected to a holey sock drogue by relatively thin (~ 1 cm diameter) ropes (Figure 3.5). The holey sock drogue was 5.5 m long and 1.5 m diameter and centred at 30 m depth beneath the sea surface. These drifters were designed to have a drag area ratio of 50 which restricts wind slippage to less than 1 cm s^{-1} for winds of 10 m s^{-1} (Niiler *et al.*, 1995).

The free-drifting surface buoy was equipped with an Argos Platform Transmitter Terminal (PTT) which transmits at a frequency of 401.650 MHz ± 4 kHz. The buoy uplink signal was received by the Argos data collection system on the NOAA polar orbiting satellites, and relayed by the System Argos in Toulouse to a dedicated PC in the laboratory at Lowestoft (CEFAS). At 50° N each Argos PTT can be located (fixed) at least every 5-6 hours, so about 8 position fixes per day can be expected.

The Argos processing system determines the accuracy of the position calculated using the number of messages collected and the Doppler measurements for the first and last message collected and the latest transmitted frequency. The accuracy of the position is represented by "classes". Table 3.3 shows the accuracy of the location "classes" offered for one-standard-deviation and the probable error in velocity associated using two fixes 12 hours apart from values calculated by Fernand (1999).

Table 3.3 Accuracy of the location by "classes" and the probable error in velocity associated using two fixes 12 hours apart.

Argos Location Classes	One Standard Deviation accuracy (m)	Class 1 (cm s^{-1})
Class 1	350-1000	6.5
Class 2	150-350	4
Class 3	± 150	2

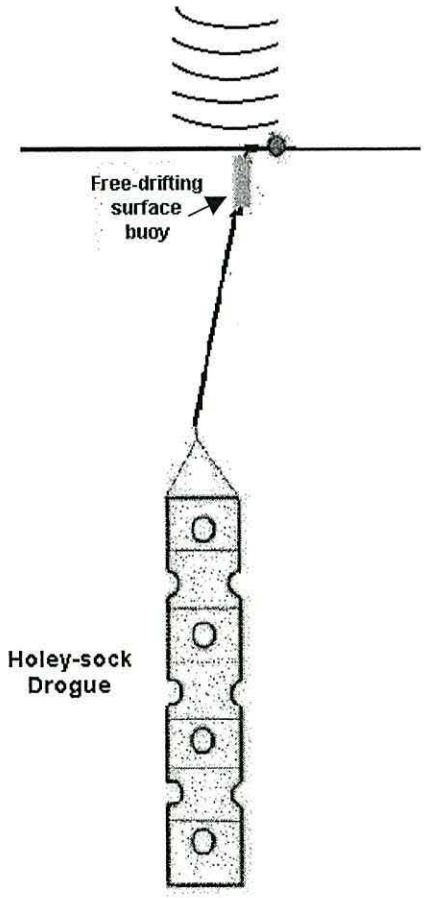

Figure 3.5 Schematic diagram of the Argos drifter used.

3.5 Acoustic Doppler Current Profiler

The capability to make measurements with high resolution (1-5 m) in the vertical makes the Acoustic Doppler Current Profiler (ADCP) an attractive current measuring technique. In particular, ship mounted ADCP allows mapping of the horizontal velocity field of large study areas. All ADCP's basically use the same operational principle. However, ADCP's which are mounted on moving platforms require extra considerations in order to separate the absolute velocity of the water from the motion of the ship. In this work, it was possible to use both vessel-mounted and bottom-mounted ADCP's. Before starting with a detailed description of the data acquisition, quality control and calibration for the ADCP, it is necessary to introduce the operational principle of the ADCP and terminology which will be used here.

3.5.1 Operational principle of ADCP

The ADCP obtains current profile measurements of the water column based on the operational principle of the Doppler effect (Figure 3.6). Minute particles suspended in the water column (*i.e.* bubbles, micro-organisms, sediment, or other solid particles), which in principle are drifting with the currents, are the "markers" scatterers user by the ADCP to register the water movement. The ADCP transmits pulses of acoustic energy from 4 beams to the water column, where they are scattered by these minute particles (scatterers). One pair of beams produces one horizontal component and the vertical velocity component. The second pair of beams produces a second, perpendicular horizontal component as well as a second vertical velocity component. Thus there are two horizontal velocities and two estimates of vertical velocity for the three components of flow. An extra estimated vertical velocity is used to have a redundancy of information and hence an estimation of the error is possible. (RDI, 1989).

A regularly spaced velocity profile is obtained by range-gating the return signal, *i.e.* breaking the return signal into successive segments to produce profiles with a number of depth cells or bins (Figure 3.7); each bin can be comparable to a single current meter (RDI, 1989). In order to reduce the measurement uncertainty, a time average of the profiles is applied obtaining time-averaged profiles or ensembles.

Typically, there are two types of ADCP's according to the emitted signal, broadband and narrow-band ADCP's. Broadband ADCP's emit a series of short pulses, which are spread over a wider frequency range, while narrow-band ADCP's emit a single pulse of a narrow frequency. Theoretically, broadband ADCP's have an accuracy of sixteen fold compared with that of the narrow-band instrument. However, due to the wider frequency, the broadband ADCP has less energy in the transmit signal than the narrow-band signal and the wider frequency is much more susceptible to acoustic interference (Fernand, 1999).

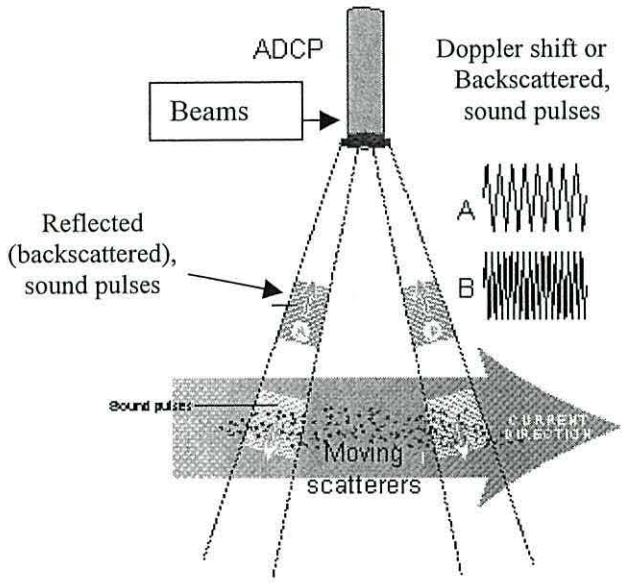

Figure 3.6. Acoustic Doppler Current Profiler (Diagram from Chereskin (2001), http://tryfan.ucsd.edu/~teri/).

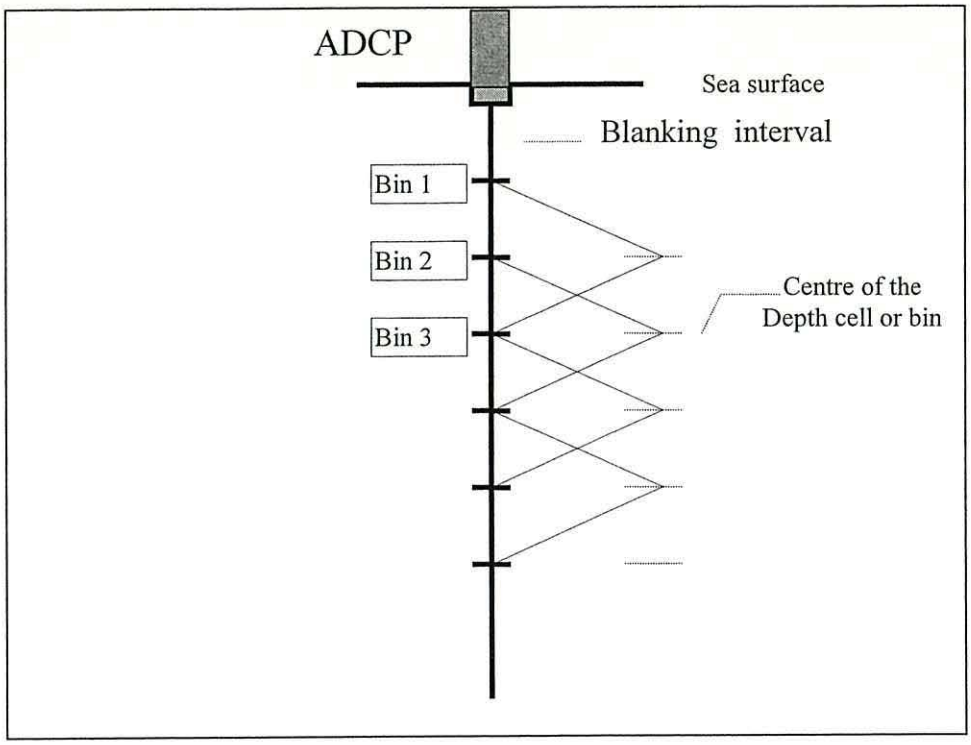

Figure 3.7 Schematic diagram showing the blanking interval and the depth cells or bins. Note that each depth cell overlaps adjacent depth cells.

In the case of vessel-mounted ADCP (Figure 3.8), there are two main modes of operation, the water tracking-mode and the bottom tracking-mode. The water tracking mode uses short transmit pulses to maintain vertical resolution and the bottom tracking mode uses short and long transmit pulses, the latter to track the seabed (RDI, 1989). If the bottom is deeper than the ADCP range it is necessary to use water tracking mode. Otherwise, if the bottom is within range the bottom tracking mode should be used, with the major advantage that errors in instrument alignment and ship heading do not contribute large errors to the current estimate as they do with independently estimated ship velocity (Kosro, 1985).

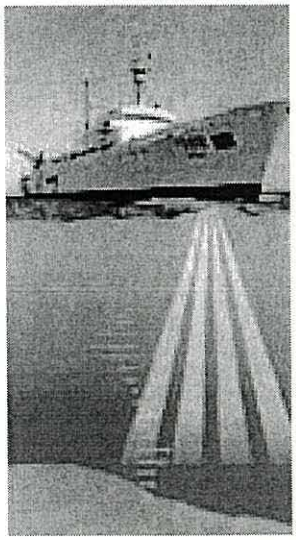

Figure 3.8. Vessel-mounted ADCP (From RDI, instruments, (2001), http://www.rdinstruments.com).

3.5.2 Vessel-mounted ADCP

The complete system to obtain velocity measurements using vessel-mounted ADCP consists of the profiler itself (ADCP), the transducer mount, a data acquisition system (computer and software), and navigation instrument including the ship compass. In this study, a vessel-mounted broadband 153.5 kHz ADCP manufactured by RD Instruments San Diego, California was used. It was mounted in the hull of the *RV Corystes* with a beam configuration of 30° concave pattern which gives a near bed shadow zone of ~ 15% of the water column due to sidelobe effects (RDI, 1989). The data were logged using the RD Instrument software package "*Transect*" which requires minimal operating effort. Table 3.4 summarizes the configuration setup of the ADCP in our cruises. The ships underway velocity was 8 knots (4.1 m s^{-1}) and the instrument operated in bottom tracking mode all the time. The navigation system consisted of a Sercel GPS with differential correction with accuracy of ± 5 m.

Table 3.4 Configuration settings for vessel-mounted ADCP for each campaign.

CORY798	All legs		
Sampling interval (min)	1		
Bin size depth (m)	2		
Bins number	45		
Tracking mode	Bottom		
First bin (m)	11.68		
Last bin (m)	98.68		
CORY998	Leg 178	Legs 179-202	Legs 209-224
Sampling interval (min)	1	1	1
Bin size depth (m)	2	2	4
Bins number	57	60	30
Tracking mode	Bottom	Bottom	Bottom
First bin (m)	8.68	8.68	14.68
Last bin (m)	120.68	126.68	130.68

3.5.3 ADCP Data Quality Control

Once the ADCP data is acquired, the next step was to proceed with a quality control of the data set, which required a range of criteria to decide upon the quality of the data. The quality of the data depends on the *navigation* during their acquisition. Optimal acquisition is achieved when the variability of both course and speed of the ship motion are minimized during the acquisition interval, *i.e.* the steaming motion of the ship is rectilinear and uniform during each profile sampling where an average of the ship motion is removed, not the actual motion (Garcia-Gorriz *et al.*, 1997). Thus, one of the first criteria applied here was to discard unreliable data when acceleration, deceleration in the ship-track and frequent station work were taking place.

The echo from a hard surface such as the seabed is much stronger than that from scatterers in the water. This strongly affects the ADCP measurement quality close to the seabed (sidelobe effect) and the percentage of the water column affected depends on beam configuration (RDI, 1989). In the case of the device used here, its beam configuration (30° concave pattern) gives a near shadow zone of 15% of the water column. Consequently, the elimination of this percentage of the profile closest to the seabed was done. Additionally, air bubbles in front of the transducer head, produced by sea state, wind and ship speed, significantly degrade the data quality as they may produce spurious current velocities over the shallower water bins and in the direction of the ship motion (Garcia-Gorriz *et al.*, 1997). Thus, the first "good" data bin in our data was selected in a depth of 12 m.

Nevertheless, unreliable data are still present, so the percent good (*i.e.* percent of the returning signal) was used as a screening criterion. Measurements with low values of the percent good indicate that the associated echoes do not have enough energy to resolve the Doppler shift (Garcia-Gorriz *et al.*, 1997). A usual threshold is 90% (Garcia-Gorriz *et al.*, 1997; Münchow *et al*, 1992; Candela *et al.*, 1992); therefore, bin depths with less than 90 % of the returning signal were discarded.

After applying the criteria described above, complementary criteria were required to reject the remaining unreliable data contained in the records. It was observed that when a bin measurement was more than three times the standard deviation of the vertically-averaged profile, the measurement might be unreliable and should be flagged. Also, correlation between neighbouring profiles was performed, and cases where the correlation was low were flagged. These flagged profiles were then examined by plotting each of

them; and suspicious ones were excluded from the data set. Where possible, subjectivity was avoided, but it was necessary to exclude some profiles, on the basis of a final visual inspection, when there were obvious spikes.

3.5.4 Calibration

Calculations of absolute velocities from ship-mounted ADCP contain inherent errors associated with rotational movements of the vessel (pitch and roll), positioning uncertainties and small deviations in the transducer orientation (transducer misalignment). Only when ADCP measurements are taken under severe sea conditions are pitch and roll errors significant (Lwiza, 1990). Several studies concluded that horizontal velocities corrected for this effect account for values $\leq$ 1 cm s^{-1} compared to non-calibrated velocities (Kosro, 1985). Positioning uncertainties depend on the navigation positioning system and could be one source of imprecision in measurements and they can be evaluated from the navigation fixes (Garcia-Gorriz *et al.*, 1997).

However, transducer misalignment leads to current errors in amplitude and orientation relative to north. These errors are constant and proportional to the ship's speed and can be removed by calibration procedures described by Kosro (1985), Joyce (1989) and Pollard and Read (1989). Here, the calibration procedure used was the bottom-tracking calibration proposed by Joyce (1989).

The ship track velocity U_s and ADCP velocity U_d are related by

$$U_s = (1+\beta)e^{i\theta}U_d \qquad 3.1$$

Where both U_s and U_d are expressed as complex vectors ($U_s = u_w + iv_s$), and θ and β represent the alignment and sensitivity errors, respectively (Figure 3.9).

To estimate the calibration values of the scale factor β and the rotation θ in 3.1, a least square fit was performed between the complex arrays of the bottom track and the ship's velocity (navigation) obtained from GPS fixes as described by Firing *et al.* (1995). All transects were used for the calibration procedure and their averaged values are shown in Table 3.5.

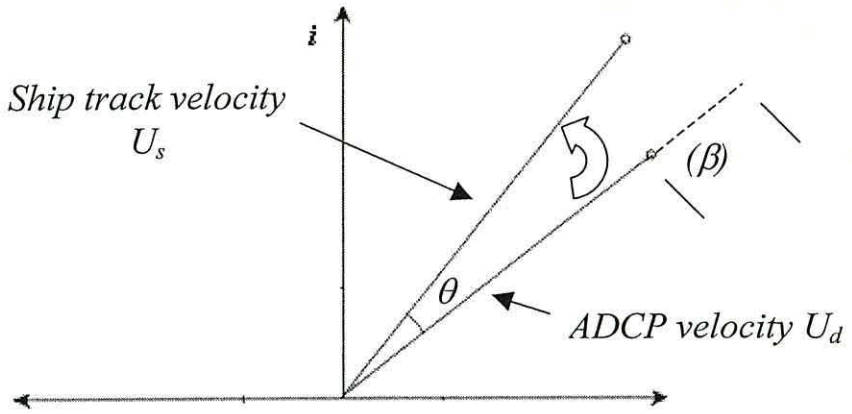

Figure 3.9 Schematic representation of the rotation and scaling of the ADCP velocity vector to obtain the corrected velocity, where θ and β represents the alignment (angle of rotation) and the sensitivity error (scaling), respectively.

Table 3.5 Calibration values of misalignment angle θ and scaling factor $(1+\beta)$ obtained for both CORY798 and CORY998 data set.

Campaign	θ	$(1+\beta)$
CORY798	2.2145° ± 2.2976°	1.0025 ± 0.0646
CORY998	2.2494° ± 1.7201°	0.9950 ± 0.0452

For the typical cruise speed (4.1 m s^{-1}) the uncertainty induced by transducer misalignment leads to a 0.019 m s^{-1} spurious speed perpendicular to steaming for both CORY798 and CORY998. The scaling factor $(1+\beta)$ values are 1.0025 and 0.9950, and thus the measurements are underestimated in modulus by 0.25% in CORY798 and overestimated in modulus by 0.5% in CORY998. Further analysis of the ship-mounted ADCP data was done after applying these corrections.

3.5.5 Bottom-mounted ADCP

Direct observations using bottom-mounted ADCP's have the advantage of resolving the time variability of local conditions giving a detailed vertical structure of currents in coastal waters. However, they are impractical in an extensive study area because a large number of these devices are needed, which implies large costs and a risk of instrument loss. Moreover, although, a considerable number of bottom-mounted ADCP deployments were possible, it would be hardly feasible to resolve narrow flows (< 10 km width). Nevertheless, bottom-mounted 306.2-kHz workhorse ADCP from RD Instruments were mounted at the bottom in two locations of the Celtic Sea and St. George's Channel (Figure 3.10). One mooring was located in 104 m depth in the centre of the Saint George's Channel operating for 45 days (see Figure 3.1b for location); the other mooring was located at 73 m depth on Nymphe Bank and operated for 41 days. At both moorings, the first bin was at 4 m from the seabed and then a bin every 2 m; and an average velocity was obtained every 10 minutes. Table IV provides the operating duration and position of the bottom mounted ADCPs.

Table IV. Operation time and position of the bottom mounted ADCPs.

Mooring ID	Dates	Longitude (W)	Latitude (N)
I	19/7/98-29/8/98	7.0000	51.6666
J	18/7/98-2/9/98	5.7980	51.9350

In contrast to the vessel-mounted ADCP, the bottom-mounted ADCP measurements did not require extensive treatment to obtain reliable data. Calibration of the instrument compasses has been performed by CEFAS (Lowestoft Laboratory) following a procedure similar to that applied to current meters. Basically, it consisted of setting the instruments on a current meter calibration table (rig), which was constructed with the purposed of allowing rotation in either direction and any angle (Jones and Read, 1993). The rig (or table) rotates in 30° steps at 3 minutes interval. The instrument (ADCP) was set to record at one minute interval. This produces 12 individual reading for calibration of the compass. The procedure is repeated to complete four circuits, two clockwise and two counter-clockwise. To be accepted, all points have to be accurate to within 2°.

Unacceptable data were observed near the surface only. Thus, data above bin 40 (~ 20 m depth) at J mooring (Fig 3.1b) and above bin 32 (~10m depth) at mooring I (Fig 3.1b) were not considered.

a)

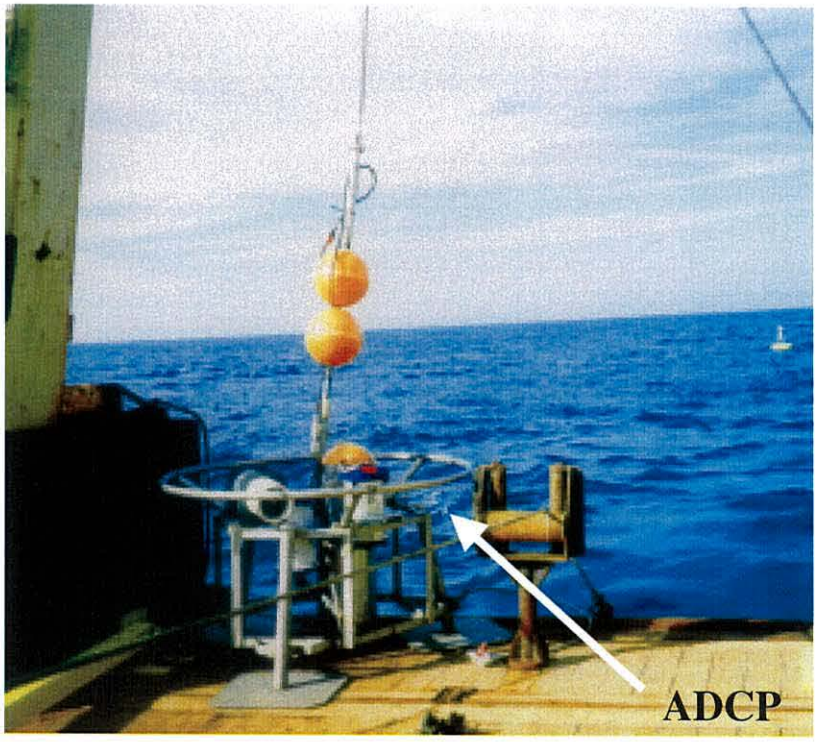

b)

Figure 3.10 a) Bottom mounted 306.2-kHz workhorse ADCP (RD Instruments, 2001; http://www.rdinstruments.com). b) Bottom-mounted ADCP on the frame before its deployment in the Celtic Sea during CORY798.

3.6 Summary

In this work a wide range of instrumentation was used to exaine the summer time circulation in the Celtic Sea and to define the importance that the density distribution could have in this circulation. This can only be achieved by obtaining a synoptic representation of the velocity field and a good resolution of the hydrographic field. The high resolution required to resolve the frontal areas was obtained using the towed undulating CTD or Scanfish, which has been demonstrated to be capable of obtaining measurements with a good spatial coverage as well as detailed measurements of the hydrographic structures (Fernand, 1999). While the hydrographic data collection was performed, ship-mounted ADCP simultaneously profiled the velocity of the water column. Synoptic coverage of the flow field was enhanced by the use of satellite tracked ARGOS drifters which operated during the summer season. Bottom-mounted ADCP moorings deliver more limited data, since they are single points in a relatively large area. However, the continuous velocity measurements can give an indication of the temporal variability of the currents in those locations.

This combination of instrumentation and observational techniques allowed us to obtain an extensive set of observations, which constitute the most comprehensive data set in this region to date. The results obtained for both the flow and the hydrographic field are showed through in the following chapters.

Chapter 4

Hydrographic Data Results

4.1 Introduction

This chapter presents the hydrographic data results obtained in the two observational campaigns in the Celtic Sea during summer 1998. This chapter has two major aims. The first is to characterize the frontal areas of the Celtic Sea and the St. George's Channel from a three-dimensional perspective (both in the vertical and horizontal spatial distribution) presenting temperature, salinity and density fields, and also the contribution of the temperature and salinity to the density field. The second aim is to establish if the density field during the summer in the Celtic Sea is suitable to maintain an organized pattern of circulation, in the context of bottom frontal dynamics derived from the shelf-sea front model of Garrett and Loder (1981), *i.e.* geostrophic calculations. The horizontal spatial distributions from both cruises are presented simultaneously highlighting the differences between them. For the vertical distributions, emphasis is placed on the second cruise (CORY998), which contains the most comprehensive coverage of the region. Although the overall vertical structure of the water column throughout the region was essentially consistent in the comparison between both cruises, a section from the first cruise (CORY798) a section is described to illustrate the vertical structure.

The chapter has been organized as follows:

- Section 4.2 presents the horizontal distribution of near bottom (~ 10 m above the bed) and near surface (10 m depth) fields of temperature, salinity, and density. Conventionally, temperature will be expressed in °C, density (σ_t) in kg m^{-3}, and salinity in practical salinity scale, which is hereafter quoted without units (UNESCO, 1978).

- Section 4.3 presents the stratification in terms of top to bottom differences in temperature, salinity and density. In addition, a brief discussion of the temperature and salinity contribution to the density field is included.

- Section 4.4 concentrates on vertical sections of temperature, salinity and density from SCANFISH legs together with the associated computed geostrophic velocity. Within the raw data the horizontal distance between equivalent points in successive 'V' shaped profiles was between 300 to 500 m (see Fig 3.4). The raw data were gridded to a resolution of 1 km in the horizontal and 1 m in the vertical using a Kriging interpolation. For the sections, the line nearest the bed marks the extent of the dive profile. Geostrophic velocities were obtained using the seabed as the no motion level in all the cross-sections. This assumption has been applied successfully elsewhere (Hill *et al.,* 1993; Brown *et al.*, 1999a; Horsburgh *et al.*, 2000) and the theoretical justification can be derived from the results obtained by Garrett and Loder (1981) as shown in section 1.2 of this thesis. The geostrophic velocity field was obtained from data gridded at 4 km horizontal resolution. As a convention, in the diagrams of velocity, solid lines represent water moving into the page and dashed lines represent water coming out of the page. In addition, to aid the visualization of the geostrophic velocity field, only velocities > 0.04 m s^{-1} are presented. Hydrographic results are described by regions: North-South cross-sections, St. George's Channel, Celtic Sea (Western-Central-Eastern), and Bristol Channel. Additionally, only some representative cross-sections are described, the remaining cross-sections are shown in the Appendix 3.

- In section 4.5, the predicted surface geostrophic circulation derived from the density anomaly calculations are shown.

- Finally, section 4.6 summarizes the principal results of this chapter.

4.2 Bottom and surface distribution of temperature, salinity and density

4.2.1 Near bottom distribution

The distribution of the near bottom temperature in the Celtic Sea mirrored the bathymetry (compare Figs 4.1a and b with Fig 4.2). The colder bottom waters corresponded to deeper water depths and the sharpest gradient of bottom temperature corresponded with the most steeply sloping parts of the seabed. The eastern Celtic Sea exhibited a stronger thermal gradient than the western side (Fig 4.1a,b). However, this thermal gradient was weak in comparison with the strongest thermal gradient (up to 2 °C/10 km) located at the St. George's Channel area. It is clear that a thermal bottom front can be defined between 60 and 100 m depth (compare Figs 4.1a and b and Figs 4.2b). In general, temperature increased toward the coast, and the western side was cooler (up to 4 °C) than the eastern side. The coldest bottom temperature (≤ 11 °C, hereafter called the "*cold pool*") was located at depths at approximately >80 m for the first cruise (CORY798) (Fig 4.1a) and >90 m for the second cruise (CORY998) (Fig 4.1b).

The bottom salinity distribution followed a different pattern from that of temperature (Figs 4.1c and d). The bottom salinity distribution did not match well with the bathymetry, *i.e.* the salinity gradient did not follow the gradient of the seabed. The strongest salinity gradient (up to 0.5 /10 km) was observed in the Bristol Channel because there was a source of fresh water from local rivers. Strong salinity gradients were also observed in the St. George's Channel (0.3 /10 km). Outside these two areas, the salinity decreased gradually from the central Celtic Sea toward the coast (Figs 4.1c and d). In general, the western side of the Celtic Sea was saltier than the eastern side because the influence of the Bristol Channel; however, this is not evident at The Smalls. The cold pool did not show the saltiest water; its salinity ranged from 35.1 to < 35.4. The saltiest water (35.4-35.45) was observed on the eastern side of the cold pool in both cruises as a tongue-like feature, which suggests a saline intrusion of more oceanic origin. However, in CORY998, this tongue-like feature ended at the centre of the Saint George's Channel (~ at 52° N and 5.8° W) (Fig 4.1d).

Overall, the bottom density distribution (Figs 4.1e and f) was well matched with the contours of the temperature field. The densest water ($\geq$ 27 kg m^{-3}) corresponded to the cold pool. The strongest density gradients were located at the St. George's Channel (0.7 kg m^{-3}/10 km). It is interesting to note that the (σ_t = 27.0) isopycnal did not lie exactly at the eastern border of the cold pool (within temperature of $\leq$ 11 °C). Due to the combination of relatively warmer temperature (12 °C) and saltier water (35.4), the 27.0 isopycnal was displaced slightly eastward from the position of the cold pool.

From July to August, there was a rise in temperature (up to 2 °C), principally in areas < 70 m depth (Fig 4.1a and b) and the densest water seemed restricted laterally in a west-east direction towards the deepest region (Fig 4.1e and f). However, the frontal zone extended ~ 25 km northwards furthest into the southern Irish Sea. Additionally, the bottom front became stronger (Fig 4.1e and f).

4.2.2 Near surface distribution

From July to August, the surface temperature and salinity increased over the entire area by almost 1.5 °C and up to 0.2 respectively (Figs 4.3a-d). In general, the western side of the Celtic Sea was colder than the eastern side (~ 1 °C), with the exception of the region in the vicinity of Scilly Isles and Land's End (see Fig 2.1a for names location map) with the coldest surface temperature (< 15 °C) (Figs 4.3b), also strong temperature gradients were observed.

One of the most pronounced features in the surface temperature distribution (Figs 4.3a and b) was a surface thermal front (~ 1 °C/15 km), principally in the St. George's Channel. This thermal surface front separated the warmer water of the Celtic Sea from the colder water of the Irish Sea. The convoluted form of this front seems to show an intrusion of cold water southwards at the western side of the St. George's Channel and movement of warm water northwards in the eastern side of the channel. The "intrusion" of colder water extended to the centre of the Celtic Sea (~ 51° N and 6.6° W, Fig 4.3a and b). This was also observed in Sea Surface Temperature (SST) images, which were contemporaneous to these data (Fig 4.4a and b). The intrusion terminated in an eddy shaped feature (~ 51° N and 7° W, Fig 4.4a and b). On the other hand, the warm intrusion did not extended further

northwards (~ 52.2° N and 5.5° W, Fig 4.3b, 4.4a and 4.4b) (only 1/4 of the distance of the cold intrusion).

Salinity did not show a clear intrusion as did temperature (Figs 4.3c and d). On the other hand, following the isohaline of 35 (35.1) in the first (second) cruise, which is consistent with a cyclonic circulation. The arrows in Fig 4.3c and Fig 4.3d help to show this pattern. In general, however, the saltiest water (35.3) was located on the eastern side of the Celtic Sea, near the coast of Cornwall and the Scilly Isles; the western Celtic Sea was fresher (up to 0.3). The freshest water corresponds to that of the Bristol Channel (< 33.6), which forms a strong gradient with the salty water of the Celtic Sea. On the eastern side of the St. George's Channel, a tongue of salty water (35.0) was present contrasting with the fresher (34.8) water of the southern Irish Sea. The other areas with strong salinity gradients were near the Scilly Isles where the saltiest surface water (35.35) was observed (Fig 4.3d).

The surface density fields (Figs 4.3e and f) suggest an intrusion of denser water from the Irish Sea towards the centre of the Celtic Sea. It is clear that the surface distribution followed the contours of temperature except for an area between the centre of the Celtic Sea and the Bristol Channel, where the density distribution seems to be controlled by the strong salinity gradient (up to 0.5 /10 km). In addition, the Scilly Isles presented strong density gradients as expected from the strong gradients of temperature observed (Fig 4.3b and d).

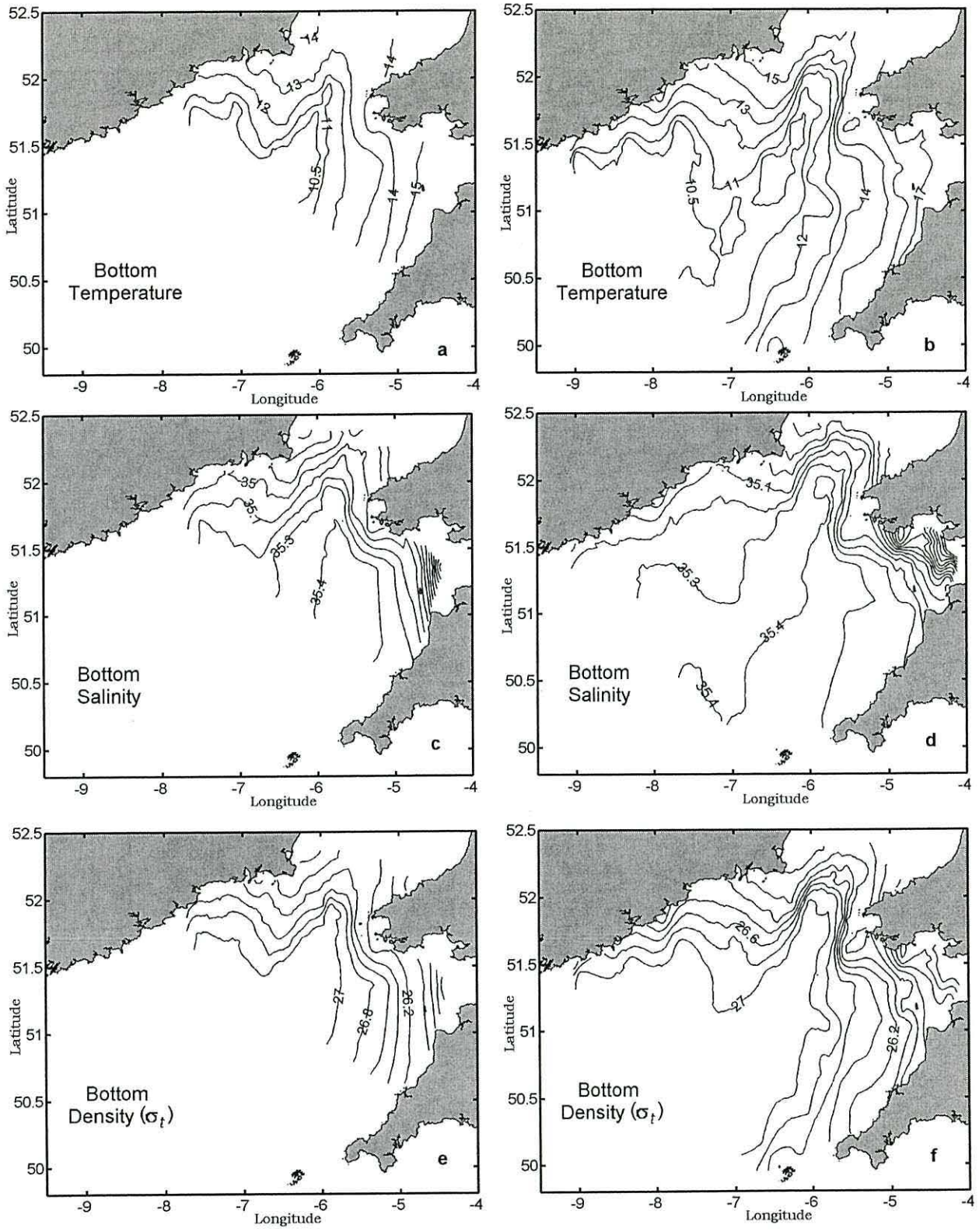

Figure 4.1 Spatial distribution of hydrographic properties at the bottom. Temperature (°C) for (a) CORY798 and (b) CORY998, salinity for (c) CORY798 and (d) CORY998, and density (σ_t) in kg/m^3 for (e) CORY798 and (f) CORY998.

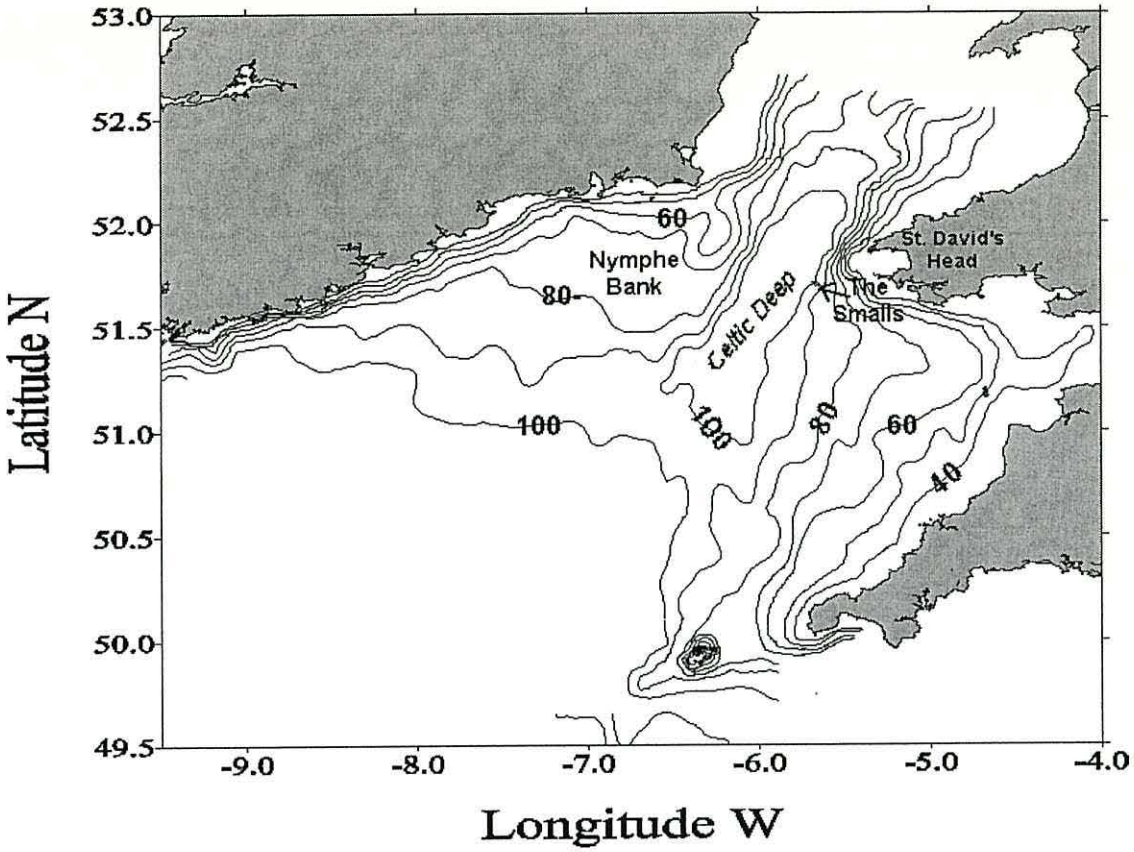

Figure 4.2 Bathymetry of the study area and name of topographic features referred in the text. Depth in metres.

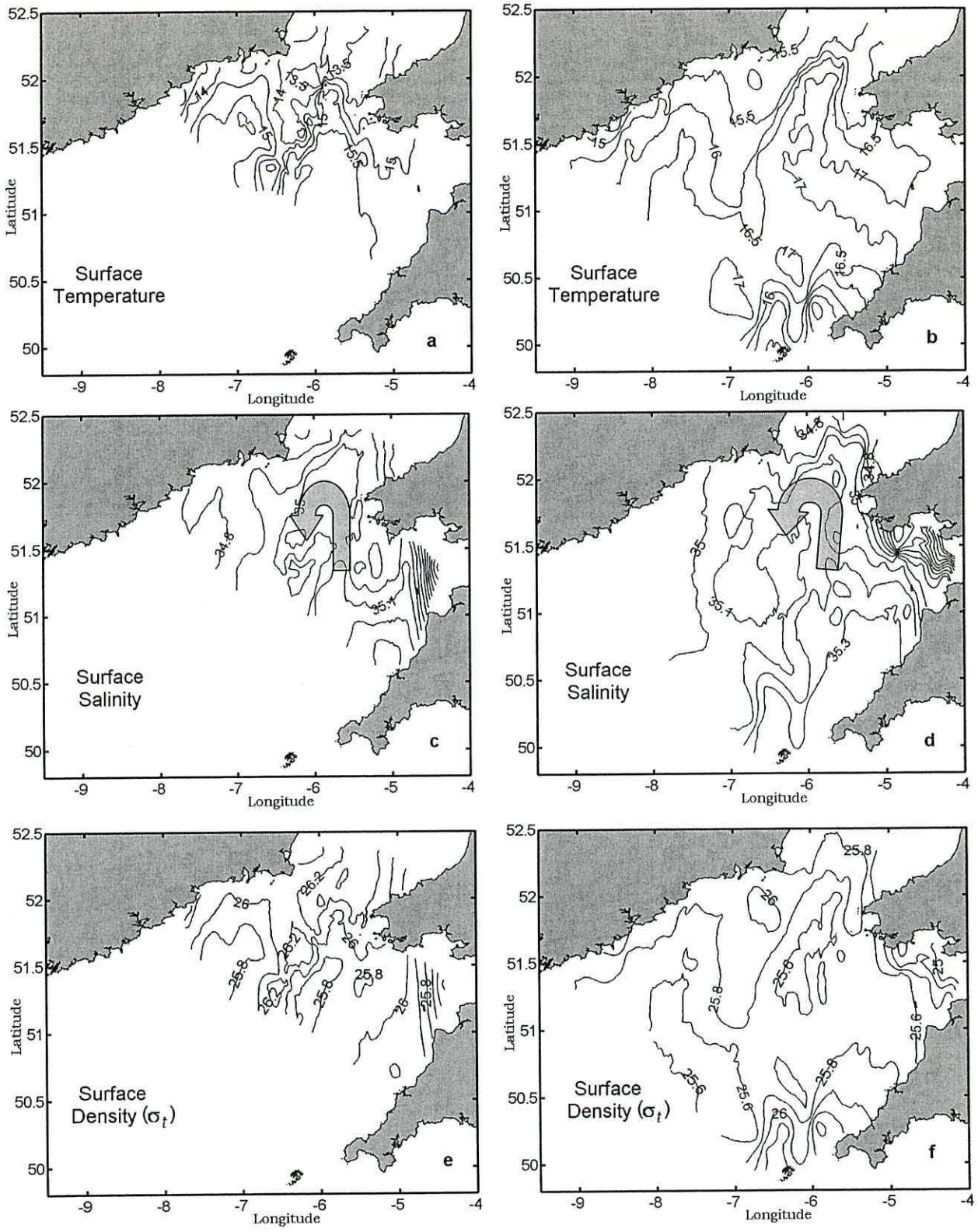

Figure 4.3 Spatial distribution of hydrographic properties at surface. Temperature (°C) for (a) CORY798 and (b) CORY998, salinity for (c) CORY798 and (d) CORY998, and density (σ_t) in kg/m^3 for (e) CORY798 and (f) CORY998. The gray arrows in (c) and (d) indicate the suggested cyclonic distribution of the salinity.

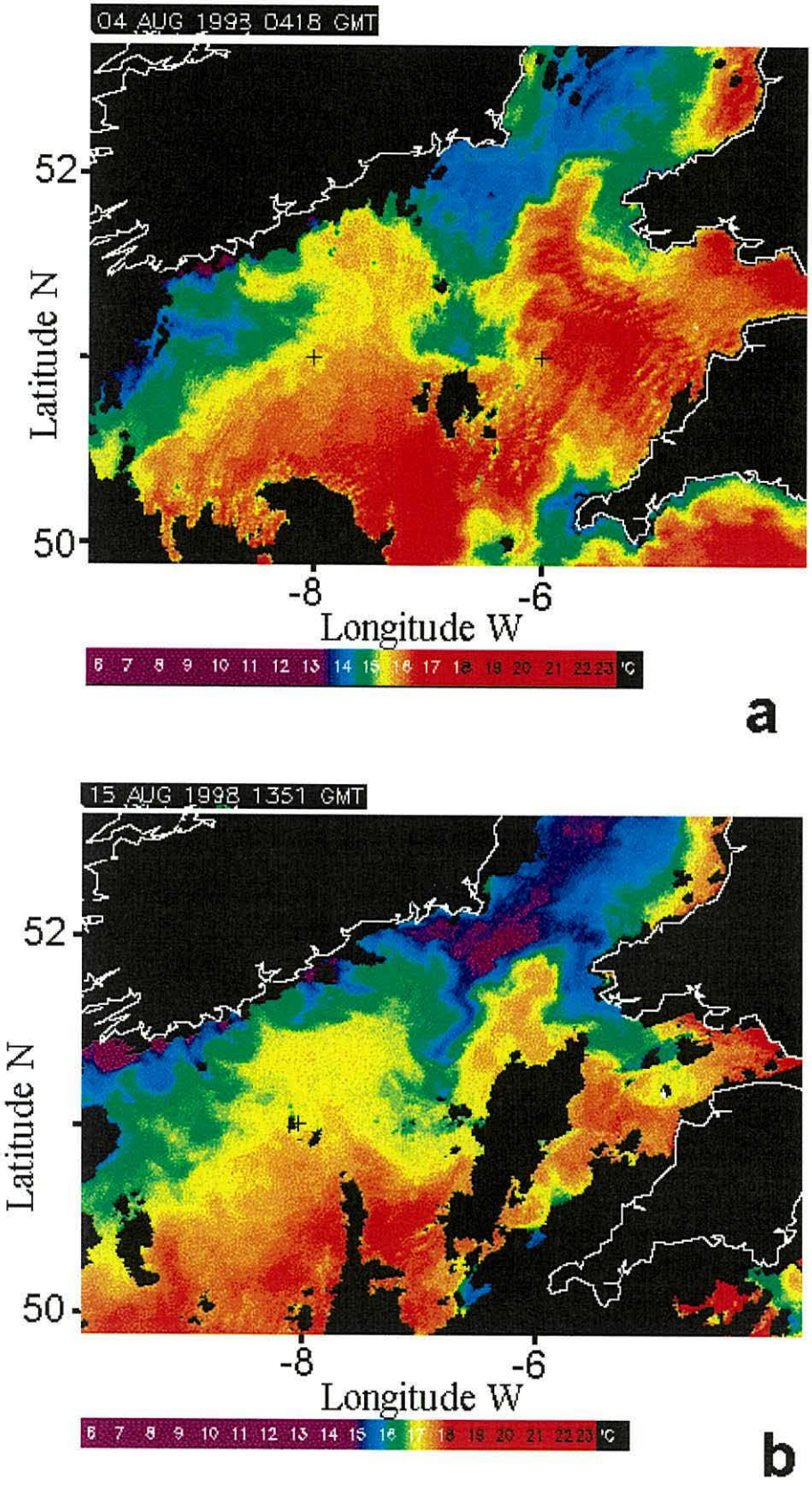

Figure 4.4 Sea surface temperature (SST) imagery for the region of the Celtic Sea and St. George's Channel. (a) 4 August 1998 and (b) 15 August 1998. Land areas and cloud are shown as black.

4.3 Spatial stratification distribution and temperature and salinity contribution to the density field

Stratification can be estimated by means of the potential energy anomaly Φ, which is the average energy required to vertically mix the water column per unit volume (Simpson, 1981). This is defined as:

$$\Phi = \frac{1}{h}\int_{-h}^{0}(\overline{\rho} - \rho)gzdz, \qquad \text{where } \overline{\rho} = \frac{1}{h}\int_{-h}^{0}\rho dz\ ;$$

and h is the total water depth, ρ is the *in-situ* density and g is the gravitational acceleration.

Figure 4.5 shows maps of Φ in the Celtic Sea during July (CORY798) and August (CORY998). The stratification increased from July to August (Fig 4.6), advancing ~ 25 km northward and eastward about the same (Figs 4.5a and b). On the other hand, on the western side of the St. George's Channel the coastal mixed conditions advanced southwestward. Broadly, the Celtic Sea was completely stratified, whilst the Bristol Channel and the shallower regions of the St. George's Channel were vertically homogeneous (Figs 4.5a and b). In general, these distributions followed the bathymetry (compare with Fig 4.2) *i.e.* stratification was strongest in the deepest areas and weaker or null in the shallowest areas. The transition from mixed to stratified regions (*i.e.* tidal mixing front) was clearly observed following the contour of Φ = 20 J m^{-3} (Figs 4.5a and b). The strongest horizontal gradient (*i.e.* relatively close contours) was observed at the St. George's Channel; outside this area the contours were widely spaced. The highest stratification values (Φ ≥ 100 J m^{-3} for CORY798 and Φ ≥ 140 J m^{-3}) were around the Celtic Deep (Figs 4.5a and b), in the case of CORY998 the value of Φ = 140 J m^{-3} was an elongated closed contour resembling the Celtic Deep basin (Fig 4.5b).

The extent of thermal stratification in the Celtic Sea and St. George's Channel can be seen from the distribution of the surface to bottom temperature difference ΔT (Figs 4.6a and b). The largest vertical temperature difference was observed at the Celtic Deep (up to ΔT ≥ 4 °C and ΔT ≥ 6 °C during CORY798 and CORY998 respectively; Figs 4.6a and b), apparent as an elongated pool clearly shown by the closed contour ΔT = 6 °C in CORY998 (Fig 4.6b), which closely agreed with the closed contour of Φ = 140 J m^{-3} (Fig 4.5b). The distribution of the vertical surface to bottom salinity difference ΔS (Figs 4.6c and d) did

not show a strong frontal area as did ΔT. Nevertheless, the ΔS contours between 0.1 and 0.2 roughly indicate the location of the frontal area (Figs 4.6c and d), however, there were not closed ΔS contours around the Celtic Deep as noted in ΔT and Φ fields (Figs 4.5b and 4.6b).

In most of the Celtic Sea, the thermal contribution to the density field is greater than the salinity contribution as can be seen qualitatively from similarities in Figs 4.5a and b with Figs 4.6a and b. However, a quantitative measurement of the relative effect of temperature and salinity on the density field was obtained considering the percentage of density stratification attributable to temperature differences ΔT. The results (Figs 5.7a and b) showed 80% of the density stratification was due to temperature in most of the Celtic Sea area. This thermal contribution to the density field decreased towards the Bristol Channel and towards the southern Irish Sea, where the thermal contribution dropped to 20% and 50% respectively (Figs 5.7a and b). By simple inspection, in the Bristol Channel area, no thermal gradients were observed (Figs 4.1a and b and Figs 4.3a and b) but considerable horizontal density gradients (up to 0.4 kg m^{-3}/ 10 km) (Figs 4.1e and f and Figs 4.3e and f). Here salinity (Figs 4.1c and d and Figs 4.3c and d) played the main role in the spatial structure of the density field, as corroborated by the above calculations.

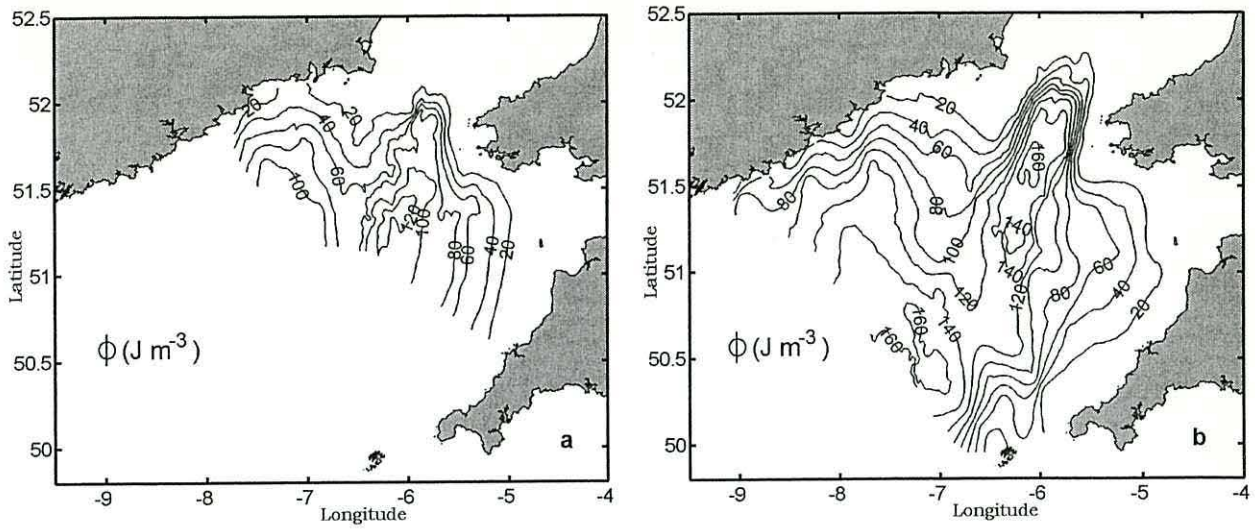

Figure 4.5 Spatial distribution of potential energy anomaly Φ (contours in J m^{-3}) for (a) CORY798 and (b) CORY998.

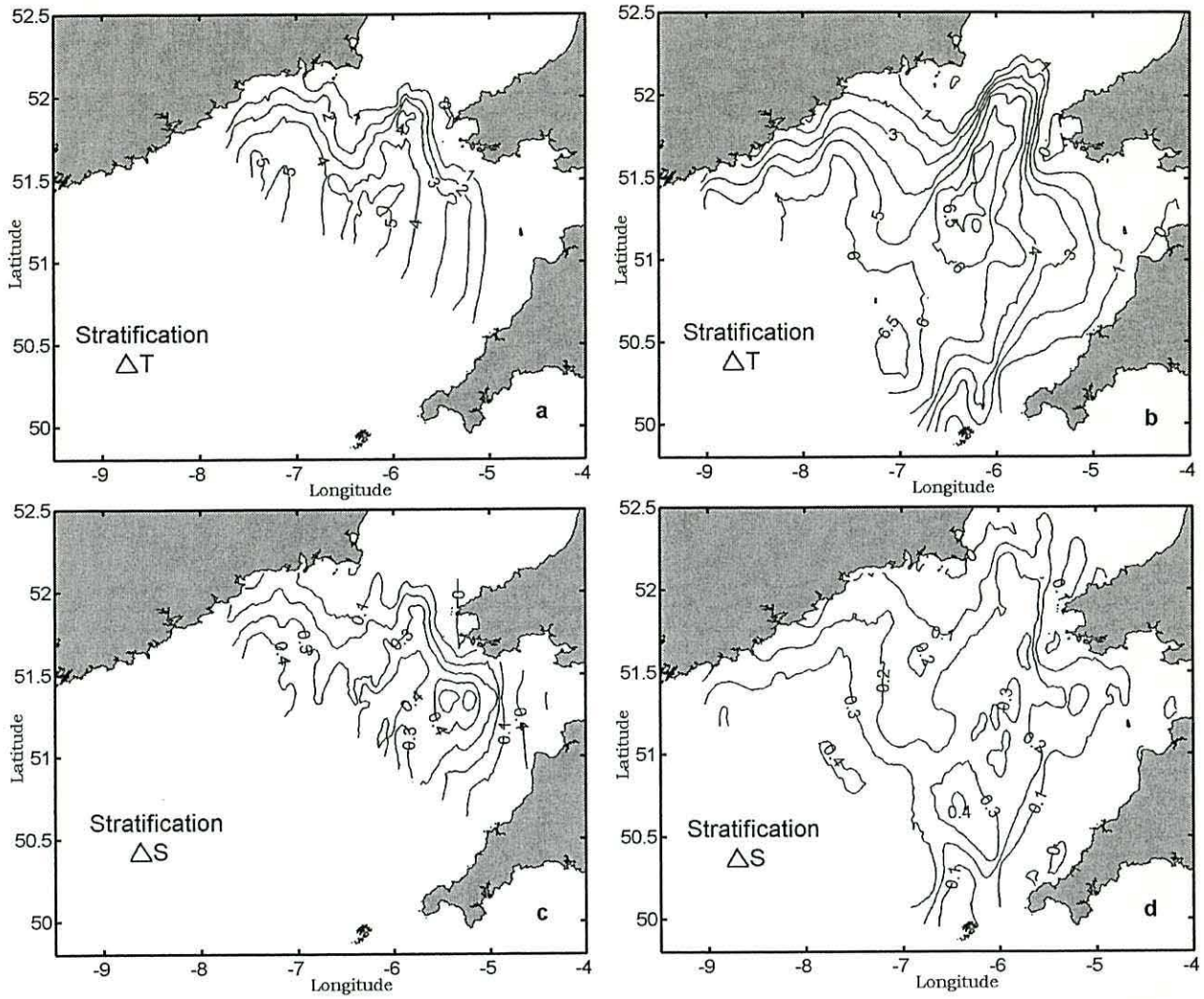

Figure 4.6 Spatial distribution of top to bottom differences: Temperature (°C) for (a) CORY798 and (b) CORY998 and salinity for (c) CORY798 and (d) CORY998.

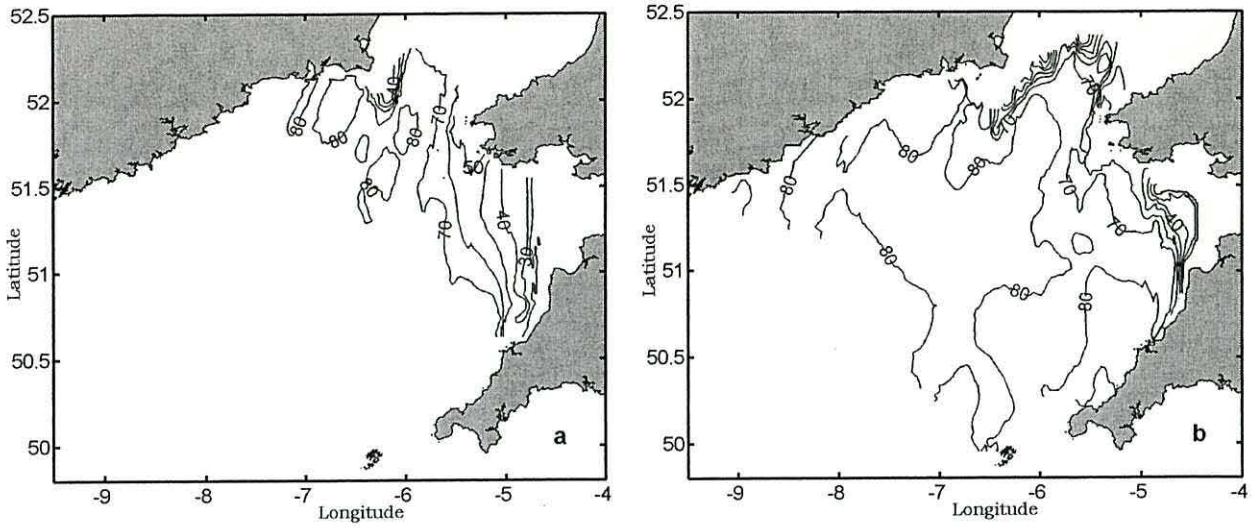

Figure 4.7 Spatial distribution of temperature control (%) on top-to-bottom density stratification for (a) CORY798 and (b) CORY998.

4.4 Vertical sections of temperature, salinity, density and derived geostrophic velocities

4.4.1 North-South cross-sections

Figures 4.8 and 4.9 show North-South cross-sections through the Celtic Sea. These sections showed vertically well mixed water in the southern Irish Sea adjacent to a frontal zone at the St. George's Channel and then stratified water in the Celtic Sea. In both cruises, a dense cold bottom water pool (> 27.0 kg m^{-3} and ≤ 11 °C) was observed in the deepest region of the Celtic Sea (Figs 4.8a,b and c and Figs 4.9a,b and c). It was isolated beneath a strong thermocline, located at 20-30 m depth during COR798 (Fig 4.8a and c) and at 30-40 m depth during CORY998 (Fig 4.9a and c). The cold pool was bounded by a series of strong bottom fronts at its northern end in the St. George's Channel, which were ~40 km wide in CORY798 (Fig 4.8c) and ~60 km wide in CORY998 (Fig 4.9c). Additionally, in the first cruise (Fig 4.8), the bottom frontal area seems separated (~20 km) approximately at the centre of the St. George's Channel (at 60-80 km along the section). Some isotherms outcrop at the surface in the St. George's Channel area forming the surface front (Fig 4.8a and Fig 4.9a). Apart from the thermal surface front, some patches of warmer and fresher water can be observed at the surface. A particular feature observed in the second cruise was an eddy-like structure of 50 km width (at 50-100 km along the section) (Fig 4.9a and c) in the central Celtic Sea. In this feature isotherms bow downwards and spread apart from the otherwise tight/sharp thermocline (Fig 4.9a).

The predicted geostrophic velocities normal to the section showed a strong westward flow (Figs 4.8c and d and Figs 4.9c and d) located immediately above the margin of the strongest horizontal density gradients near the bed (at 50-90 km and at 185-235 km along the section for CORY798 and CORY998 respectively). The jet-like flows were as wide as the frontal areas, but the strongest calculated geostrophic velocities were concentrated in narrow jet-like flows of ~10 km width, with speeds up to 0.30 m s^{-1}. The separation of the bottom fronts into two regions of sharper gradients in CORY798 (Fig 4.8c) resulted in two wide (~20 km) strong jet-like westward flows divided by a narrow (~10 km) eastward flow (Fig 4.8d). These calculated geostrophic speeds reached up to 0.32 m s^{-1} and 0.24 m s^{-1} in the westward flows and up to 0.20 m s^{-1} for the eastward one. On the other hand, geostrophic velocities associated with the eddy-like structure showed a nearly anticyclonic circulation with speeds up to 0.12 m s^{-1} (Fig 4.9d). Apart from this

feature, the central area of the Celtic Sea did not exhibit strong velocities because the absence of bottom fronts.

4.4.2 The St. George's Channel

As noted from the results of the north-south sections and from the horizontal distributions (sections 4.2 and 4.3), the St. George's Channel was the area with the strongest horizontal thermal gradients and where the transition between the stratified water of the Celtic Sea and the vertically well mixed water of the southern Irish Sea took place. Here, the vertical structure of the temperature and salinity in some cross-sections in the channel are presented (Figs 4.10-12). The description starts from the northernmost cross-sections (southern Irish Sea), passing through the channel until the transition between the southern St. George's Channel and the Celtic Sea.

The northern transect (Fig 4.10) showed the water column more or less completely mixed but the centre, having slightly cooler and saltier bottom water (Fig 4.10a and b). Negligible horizontal thermal gradients were observed (< 1 °C/ 30 km) (Fig 4.6a). However, the salinity distribution showed more structure than temperature (Fig 4.10b). The eastern coastal water was ~ 0.1 fresher than on the western coast. The saltiest water (35.10) was observed in the centre of the basin. In this area, density was mostly controlled by salinity (~50 %) as observed in Figure 4.7, and consequently the density field reflected that of salinity. Calculated geostrophic velocities (Fig 4.10d) showed speeds near the surface (above 20 m depth) of up to 0.20 m s^{-1} on the eastern side of the channel and up to 0.12 m s^{-1} on the western side.

Further southward into St. George's Channel (Fig 4.11a,b and c), the transverse sections showed a dense cold dome-like structure at the centre of the basin, which was flanked by wedges of fresher and cooler water on either side, with significant near bed density gradients at the edges of the dome (1.0 kg m^{-3}/ 12 km). Thermal bottom fronts in the St. George's Channel were pronounced with temperature changing by 3 °C in ~ 10 km (Fig 4.11a). The warmest water (> 17 °C) was located at the surface and centre of the channel, forming surface fronts with the well-mixed coastal water. The saltiest water (35.4) was located at the centre and bottom of the basin (Fig 4.11b). In contrast with the coastal salinity distribution in the northernmost line (Fig 4.10b), in this section (Fig 4.11b), the mixed coastal water on the eastern side of the St. George's Channel was saltier

than on the western side. Clearly, the density structure (Fig 4.11c) was more controlled by temperature (Fig 4.11a) than salinity (Fig 4.11b) (~ 80 % from Fig 4.7). The calculated geostrophic velocities associated with this density field (Fig 4.11d) showed a cyclonic circulation with core speeds of up to 0.28 m s^{-1} above the flanks of the bottom fronts (~ 30 m depth).

Southwards in the Celtic Sea (Fig 4.12), along the Celtic Deep, the dense cold pool was the most pronounced feature. This dense structure (> 27.0 kg m^{-3}) showed characteristic temperatures of < 11 °C (Fig 4.12a) and its salinity ranged from 35.3 to ≤ 35.35 (Fig 4.12b). Beside the eastern flank of the cold bottom water, the saltiest water (≥ 35.4) was observed. The predicted geostrophic flow field was concentrated into jet-like flows 10-20 km wide on either side of the dense pool with maximum speeds centred at ~20-30 m depth. The strong near surface velocities reached up to 0.38 m s^{-1} in the northward flow current on the eastern side of the channel and 0.30 m s^{-1} in the southward flow on the western side.

4.4.3 Western-Central-Eastern Celtic Sea

Sections across the main body of the Celtic Sea (*i.e.* legs crossing the entire Celtic Sea from northwest to southeast are presented in Figs 4.13-15.

The "northernmost" of these cross-sections (Leg 182, Fig 4.13) showed the dense cold pool located at depths > 80 m of the basin. Besides the eastern side of the cold pool, the saltiest water of Atlantic origin (≥ 35.4) was observed. The warmer surface (> 17 °C) water was patchy in salinity. The eastern side of the Celtic Sea was warmer (1 °C) and saltier (up to 0.4 of difference) than the western side (Fig 4.13a and b). The bottom frontal region was ~ 50 km in width, and sharper and better defined than the surface front (Fig 4.13a, b and c). The thermal front was not evident on the eastern side. The geostrophic velocities associated with the density field (Fig 4.12d) showed a series of surface (above 30-40 m depth) narrow flows (~ 10 km) at the centre of the section with velocity components normal to the density section of up to 0.12 m s^{-1}. However, on either side of the cold pool, associated with the bottom fronts, calculated geostrophic flows of ~20-25 km wide were observed at ~80-100 km and at 190-200 km distance along the section. The speeds of these calculated along-front flows reached 0.12 m s^{-1}.

A further southward cross-section (Leg 180, Fig 4.14), passing through the central Celtic Sea, showed a more complex temperature, salinity and density structure. Centred over the deepest Celtic Deep, the dome of the cold pool, which was bounded by a series of bottom fronts, was located (Fig 4.14a, b and c). However, fronts were not the only structures observed in the Celtic Sea. As observed in the north-south cross section (Fig 4.9), around the central Celtic Sea, a surface eddy-like structure (centred at 90 km distance along the section, Fig 4.14a and c) seems to divide the isotherms, bending them upward and downward. In addition, the cold pool seems divided where this eddy-like structure was observed (Fig 4.14a and c). Calculated geostrophic velocities showed an unclear pattern of circulation, indeed, relatively weak speeds (< 0.08 m s^{-1}) associated with the bottom fronts were observed. One of the strongest and most organized jet-like flows was that computed to flow southward at the western-central Celtic Sea (Figs 4.14d). This flow was ~25 km wide, but the maximum velocity (0.20 m s^{-1}) was concentrated in a jet less than 10 km wide. The location of this southward flow coincides with the position where the isopycnals were bending, apparently associated with the eddy structure (Compare Fig 4.14c and d).

Further south into the near open communication with the Atlantic ocean (Fig 4.15), the cold pool was an extensive feature predominating throughout almost the entire basin which mostly has depths > 80m. As was noted previously, strong bottom fronts near the coastal region bounded this cold pool. Both surface and bottom fronts showed strong horizontal gradients (up to $\sigma_t = 0.4$ kg m^{-3} /15km) (Fig 4.15e). The salinity of the cold pool ranged from < 35.4 in the central region to 35.1 towards the western coast (Fig 4.15a and b). The area of salty bottom Atlantic water (≥ 35.4) was as wide as the bottom frontal region on the eastern side (Fig 15b). Associated with the sharp bottom frontal areas on both sides of the basin, the computed geostrophic velocities normal to the section (Fig 4.15d) reached up to 0.20 m s^{-1}, in a northward flow located on the eastern side, which was concentrated within a few horizontal zone kilometres wide (< 10 km) but the total region affected by the bottom front was ~30 km (Fig 4.15c and d). On the western side, a southward flow ~ 25 km wide was calculated with speeds of up to 0.12 m s^{-1}. In general, a series of jet-like cores (~10 km wide) with speeds in the range 0.04-0.16 m s^{-1} were observed above the thermocline. However these were less organized than in the frontal region. In contrast to the sections crossing the central Celtic Sea (Fig 4.14), in this southernmost section (Fig 4.15) the structure of the temperature, salinity and density did not show complexity. However, a "slope" in the thermocline, halocline, and consequently,

in the pycnocline was observed; they were deeper on the eastern side than on the western side with a nearly constant slope of 10 m/150 km.

4.4.4 The Bristol Channel and its surrounding areas

It has already been shown in sections 4.2 and 4.3, that the Bristol Channel and its surrounding areas were regions with the strongest horizontal salinity gradients due to riverine influence. Thus, the Bristol Channel entrance was the transition zone between a region with fresh water influence and an area with more "offshore" conditions (*i.e.* Celtic Sea); Figures 4.16-20 show this transition.

The cross-section in the northern Bristol Channel entrance (Fig 4.16), which borders the St. George's Channel, showed the dense cold pool ($\geq$ 27.0 kg m^{-3} and < 11 °C) and adjacent to the eastern side of the cold pool, the saltiest water of Atlantic origin ($\geq$ 35.4) was observed. In general, the bottom frontal region was 40 km in width, with horizontal density gradients of 1.3 kg m^{-3} in ~ 40 km. The sharpest downward tilt of the isopycnals was found (Fig 4.16c) due to the completely mixed water near the coastal areas, around The Smalls. The computed geostrophic velocity (Fig 4.16d) associated with this pronounced bottom front was a narrow (~10 km) jet-like flow up to 0.40 m s^{-1}, which was concentrated in about 5 km wide zone (at 50 km distance along the section). Nevertheless, computed geostrophic velocities associated with the other bottom frontal areas, with speeds up to 0.20 m s^{-1}, were also observed.

In contrast, at the southern Bristol Channel entrance (Figs 4.17), the bottom frontal area was much broader and less pronounced than the northern entrance (changing 1.3 kg m^{-3} in 100 km vs. 1.3 kg m^{-3} in ~ 40 km). Thus, a series of bottom fronts were observed, with the sharpest bottom front (20 km distance along the section) where the cold pool was found. Associated with these bottom fronts, a calculated geostrophic strong surface flow of up to 0.22 m s^{-1} and ~ 22 km wide was observed. Towards the Cornish coast, the frontal area exhibited a weaker horizontal density gradient (Fig 4.17c). After that, the bottom front showed again a rapid change of the density, with associated velocities between 0.11-0.15 m s^{-1} in narrow flows of ~ 10 km wide (Fig 4.17d). Surface salinity was relatively fresher at the centre of the Celtic Sea (35.1) and increased in salinity further towards the coast (35.3) (Fig 4.17b). However, coastal water was fresher

(35.2) and vertically well mixed. The bottom salinity was dominated by the Atlantic salty water (≥35.4) which extended over 60 km between 70-90 m depth. The surface thermal front was not a feature observed in the whole Celtic Sea area as the bottom front was, since this was not seen in the southern Bristol Channel entrance (Fig 4.17a).

The absence of a surface thermal front was also observed in the central Bristol Channel entrance (Fig 4.18a). In this section (Fig 4.18) the transition between the stratified and more offshore conditions of the Celtic Sea and the well-mixed water column of the more inshore-estuarine conditions of the Bristol Channel was clearly evident. The thermal gradient disappeared towards the channel (Fig 4.18a). Instead a salinity gradient was observed showing an estuarine frontal area (Fig 4.18b). The warmer surface water was patchy in salinity (Fig 4.18a and b). A gradual horizontal density gradient at the bottom was observed (Fig 4.18c), changing from 26.7 to 25.8 (0.9 units) in 40km (between 25-65 km distance along the section). In contrast, the surface front was also weak except in the region where a vertically well-mixed water column was observed (90-100 km distance along the section). The computed geostrophic surface velocities (Fig 4.18d) associated with the bottom front reached 0.16 m s^{-1} and appeared as a series of narrow jets (10 km width). Velocities up to 0.20 m s^{-1} were associated with the horizontal density gradient between the vertical frontal estuarine area.

Inside the Channel (Figs 4.19 and 4.20), the cross-sections displayed more vertically mixed conditions. Some relic of cooler and saltier water (16 °C and 35.2) was observed at the bottom and centre of the section (Fig. 4.19). However, further into the Bristol Channel (Fig. 4.20a and b) vertically well mixed water conditions were displayed. In both cross-sections (Figs 4.19b and 4.20b), the northern side of the Bristol Channel was fresher (salinities as low as 33.6 in the most internal section) than on the southern side (≥ 35). Horizontal density gradients were, however, observed (Figs 4.19c and 4.20c). In general, the circulation obtained from the geostrophic calculations showed flows mostly out of the Bristol Channel (Fig 4.19d and 4.20d), with surface speeds (above 20m depth) up to 0.28 m s^{1} (Fig 4.19d) associated with the strongest horizontal density gradient (Fig 4.19c) (0.6 kg m^{-3}/10 km at ~ 20 km distance along the section). Outside this region, calculated geostrophic velocities were ≤ 0.12 m s^{-1} (Figs 4.19d and 4.20d).

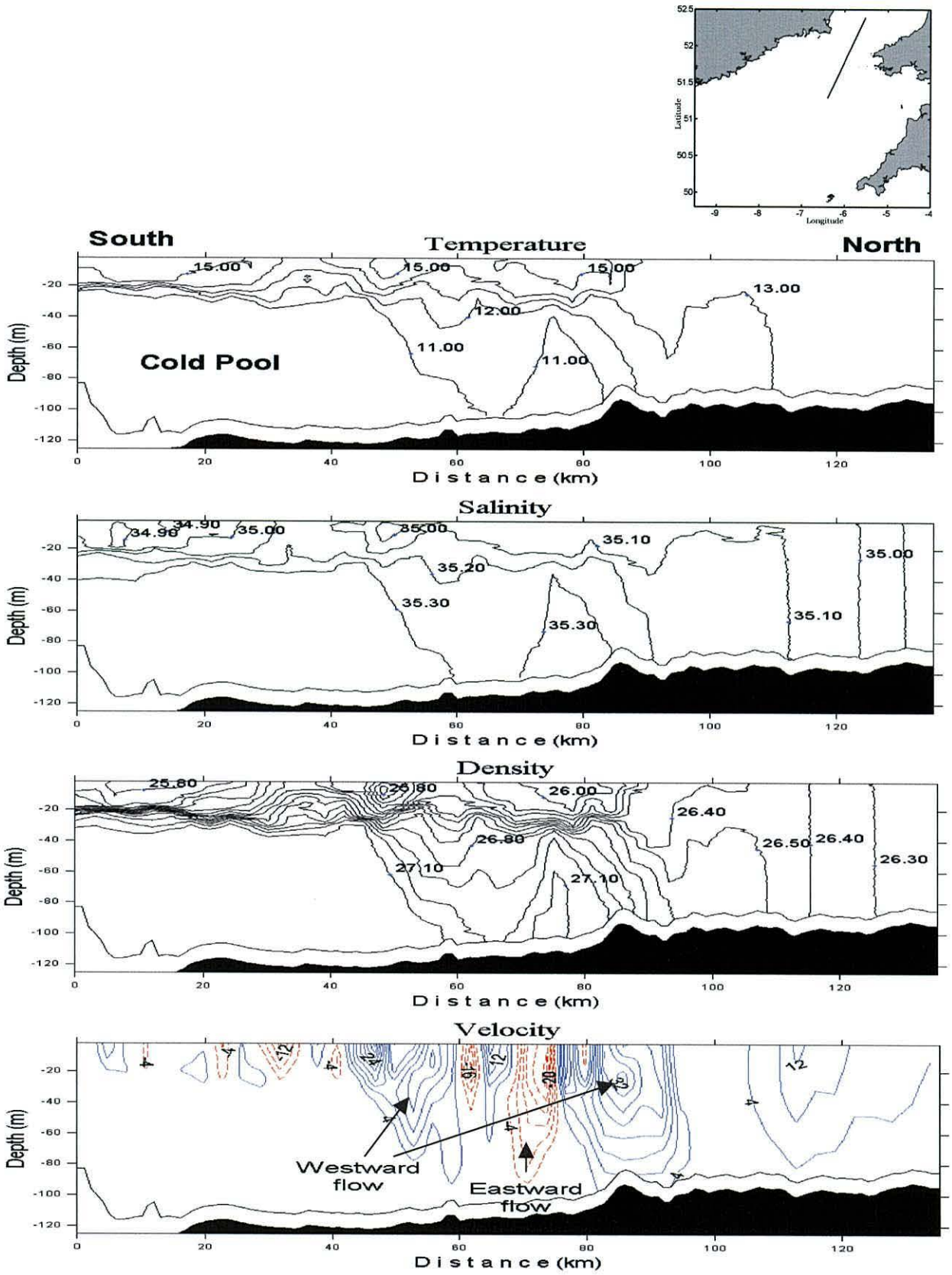

Figure 4.8 North-south cross-section from the southern Irish Sea to the centre Celtic Sea corresponding to leg 121 (CORY798) showing the vertical structure of: (a) Temperature (°C), (b) Salinity, (c) density (σ_t in kg/m^3), and (d) geostrophic velocities in cm s^{-1} derived from the density field. In the latest, continuous lines represent water going into the page, contours with dashed lines water out the page. Location of the leg can be observed in the top figure of this page.

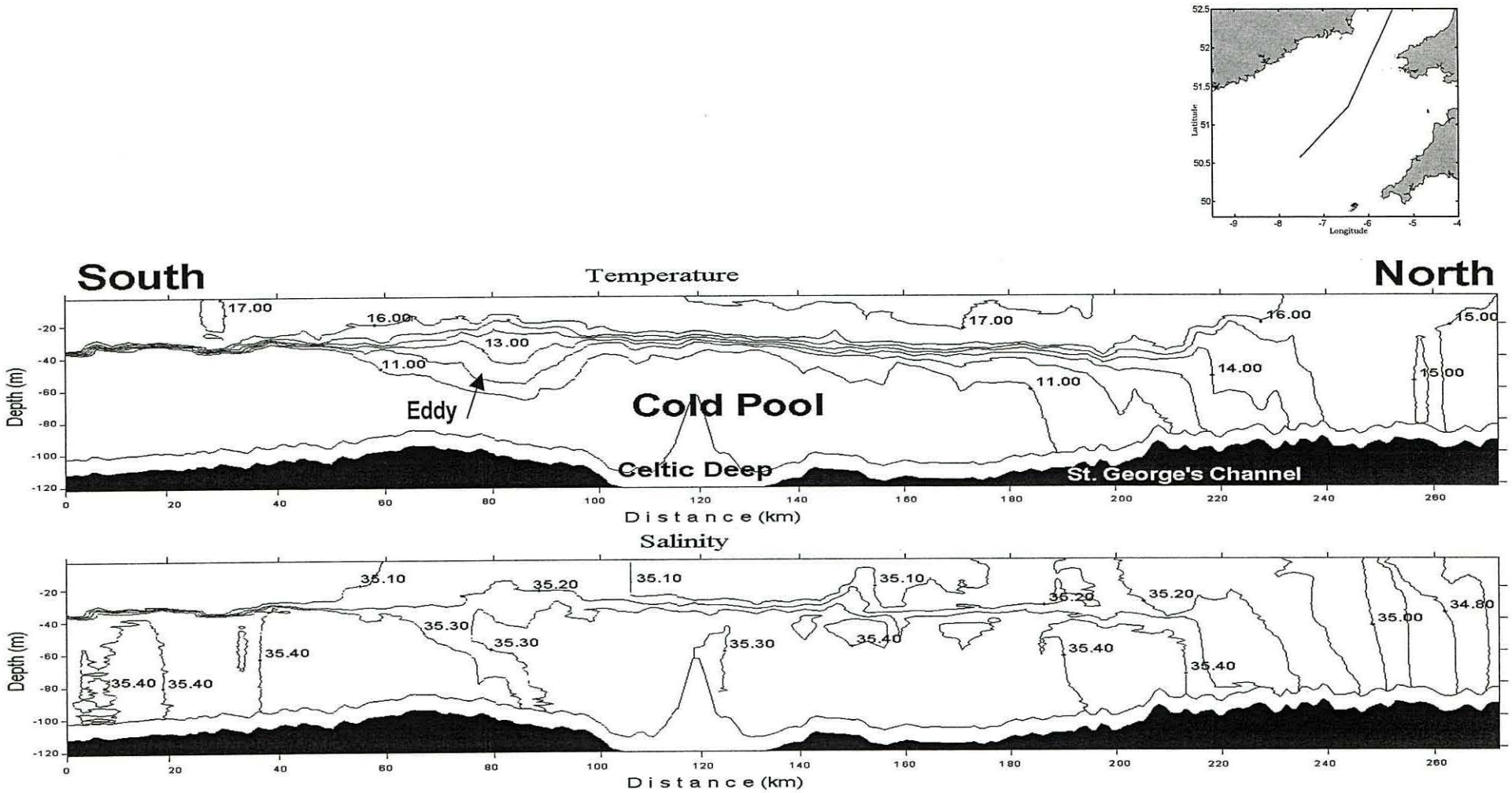

Figure 4.9 North-south cross-section from the southern Irish Sea to the entrance of the shelf sea area of the Celtic Sea, constructed with legs 190 and 202 cruise CORY998, showing the vertical structure of: (a) Temperature (°C) and (b) Salinity. The location of the cross-section is observed in the top right corner of the page. The line nearest the bed marks the extent of the dive profile.

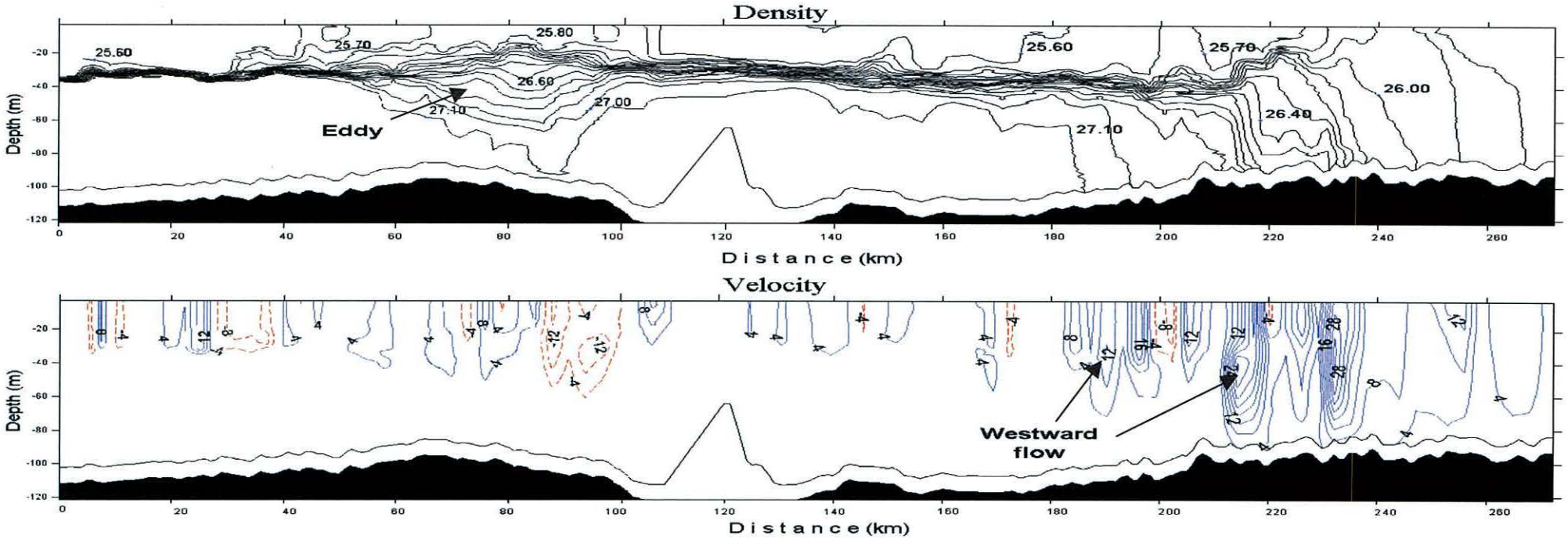

Figure 4.9 (Continued from previous page). Vertical structure of: (c) density (σ_t in kg/m^3) and (d) geostrophic velocities in cm s^{-1} derived from the density field. In the latest, continuous lines represent water going into the page, contours with dashed lines water out the page. The line nearest the bed marks the extent of the dive profile.

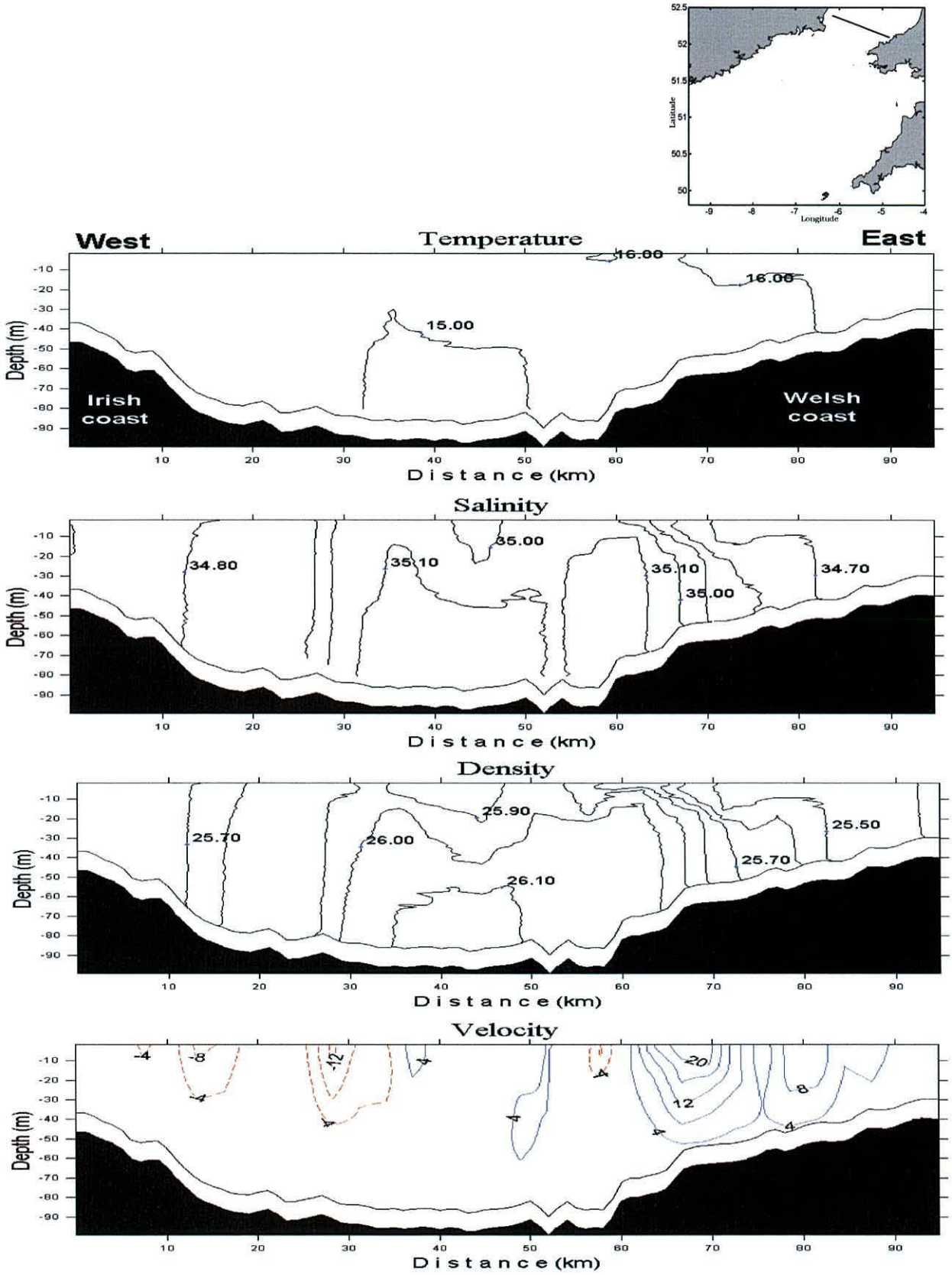

Figure 4.10 Transverse section in the St. George's Channel corresponding to leg 210 (CORY998) showing the vertical structure of: (a) Temperature (°C), (b) Salinity, (c) density (σ_t in kg/m^3), and (d) geostrophic velocities in cm s^{-1} derived from the density field. In the latest, continuous lines represent water going into the page, contours with dashed lines water out the page. The location of the cross-section is observed in the top right corner of the page.

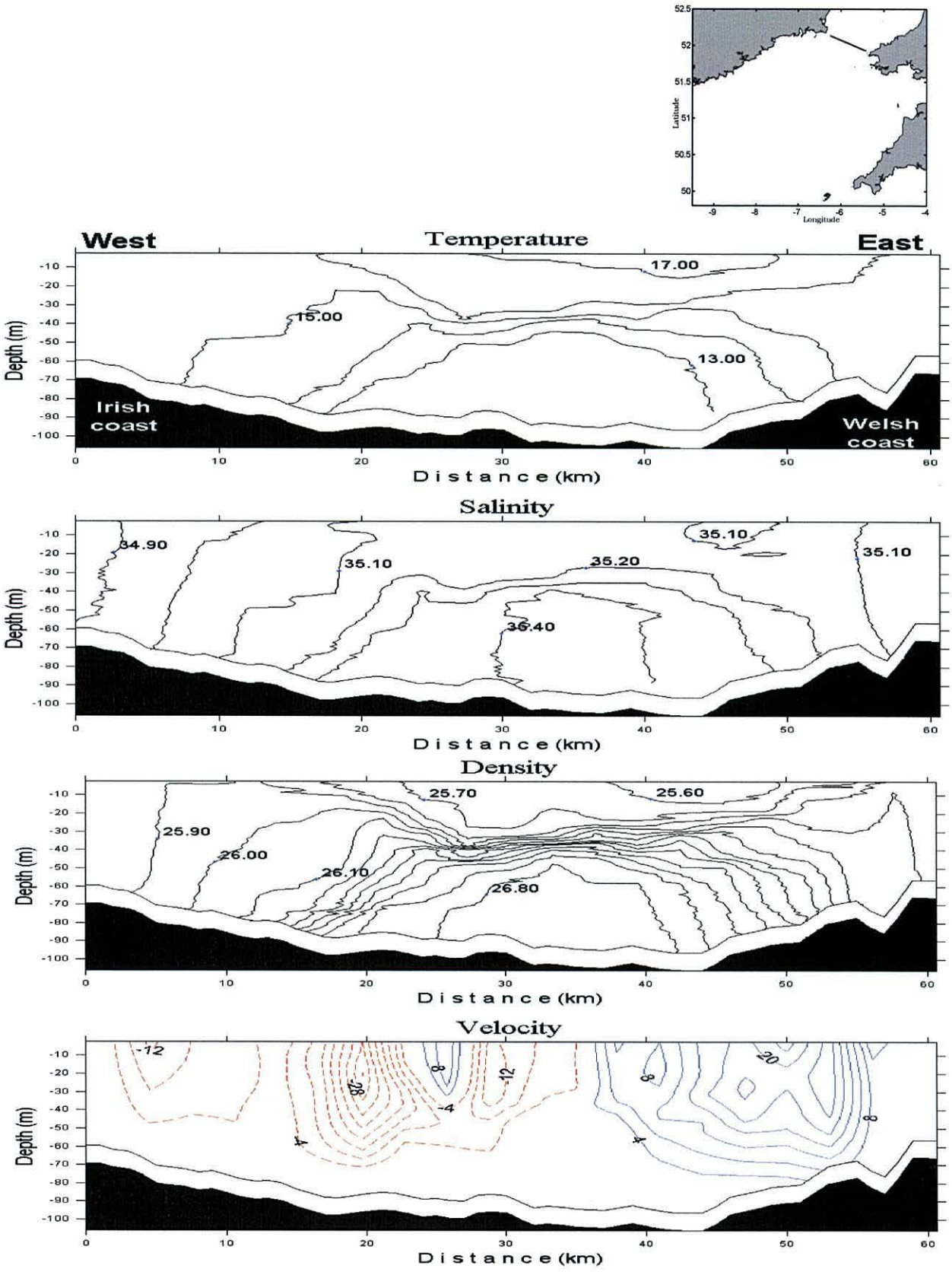

Figure 4.11 Transverse section in the Saint George's Channel corresponding to leg 209 (CORY998) showing the vertical structure of: (a) Temperature (°C), (b) Salinity, (c) density (σ_t in kg/m^3), and (d) geostrophic velocities in cm s^{-1} derived from the density field. In the latest, continuous lines represent water going into the page, contours with dashed lines water out the page. The location of the cross-section is observed in the top right corner of the page.

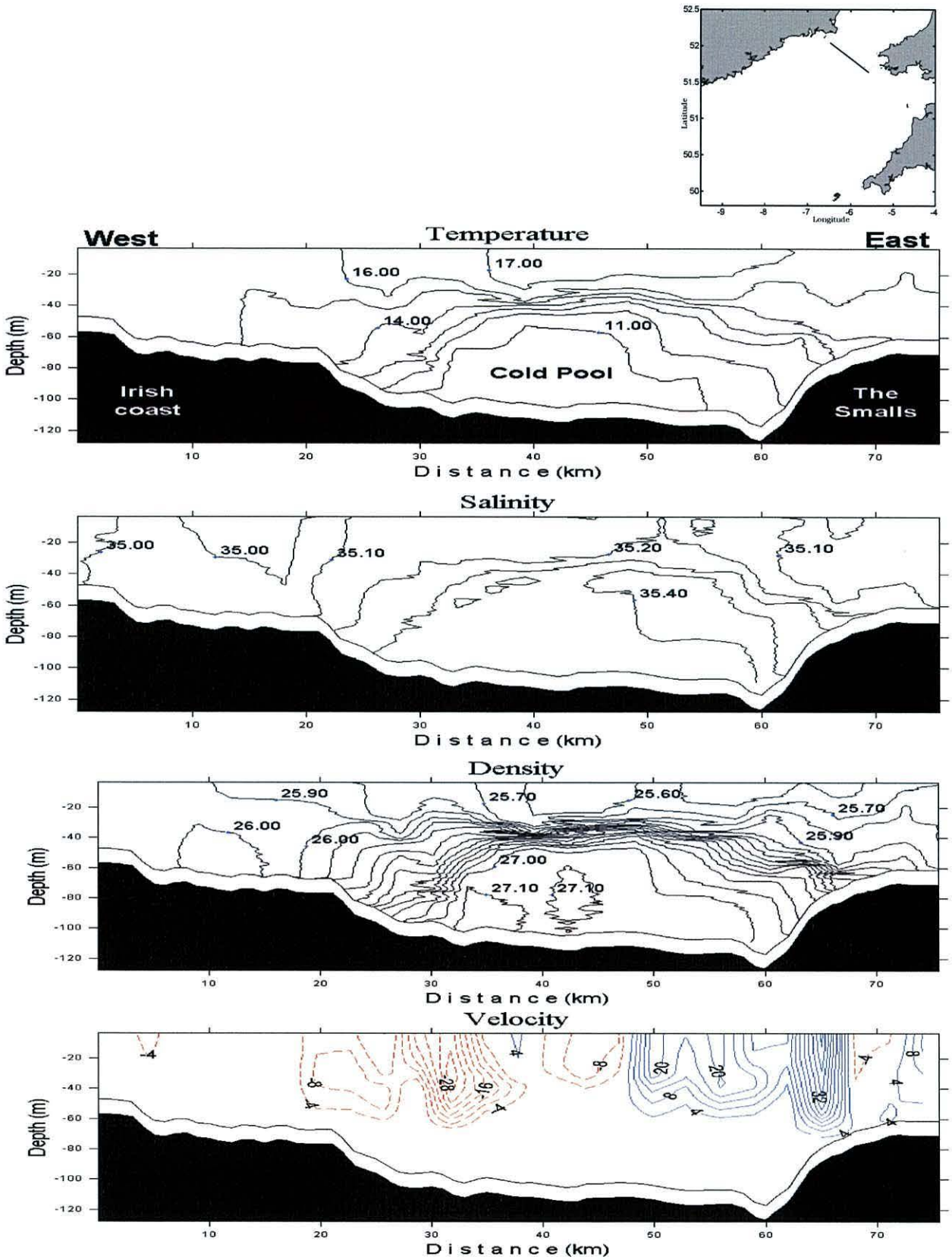

Figure 4.12 Transverse section in the Saint George's Channel corresponding to leg 213 (CORY998) showing the vertical structure of: (a) Temperature (°C), (b) Salinity, (c) density (σ_t in kg/m^3), and (d) geostrophic velocities in cm s^{-1} derived from the density field. In the latest, continuous lines represent water going into the page, contours with dashed lines water out the page. The location of the cross-section is observed in the top right corner of the page.

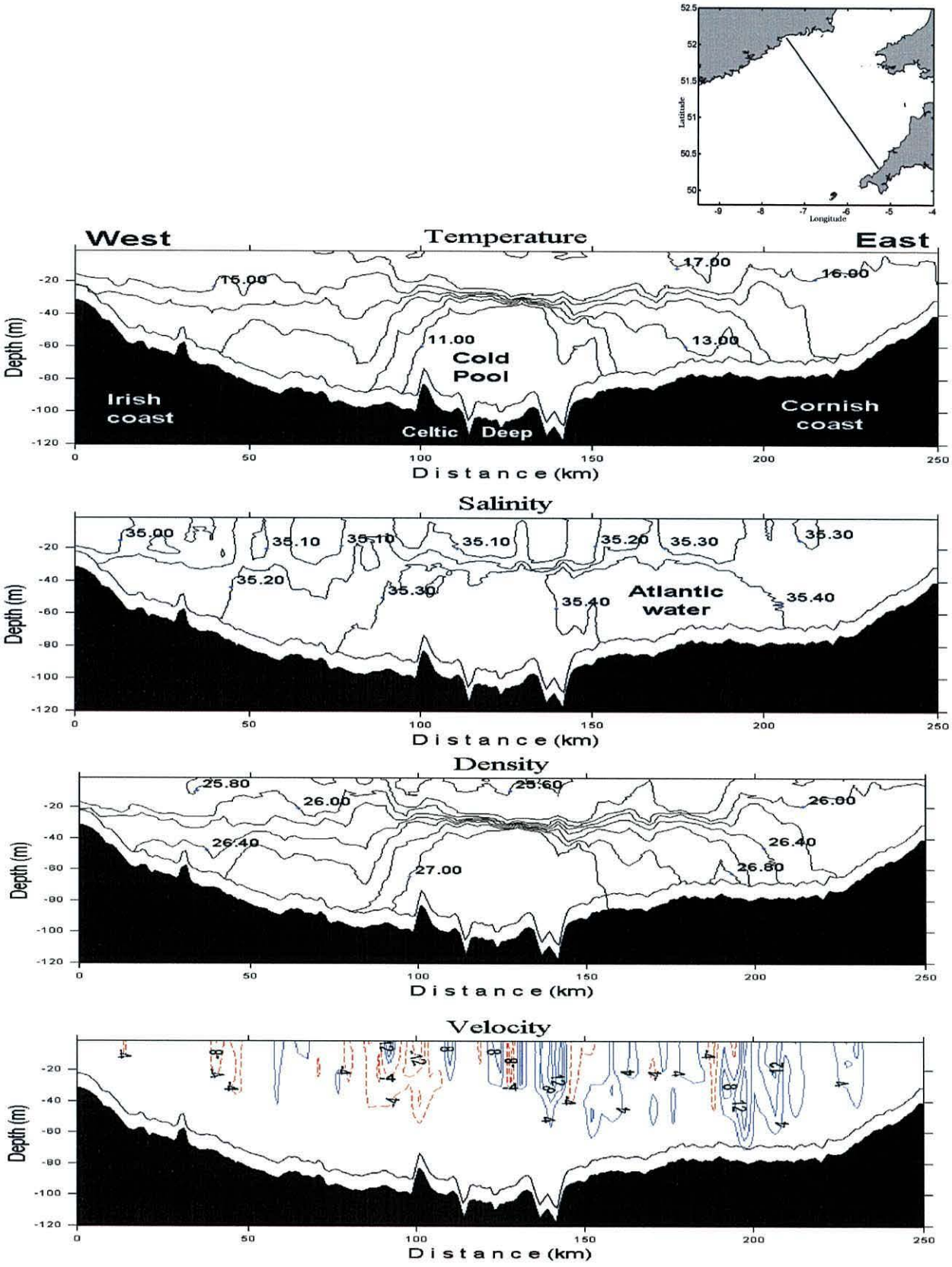

Figure 4.13 Transverse section crossing the Celtic Sea from northwest to southeast corresponding to leg 182 (CORY998) showing the vertical structure of: (a) Temperature (°C), (b) Salinity, (c) density (σ_t in kg/m^3), and (d) geostrophic velocities in cm s^{-1} derived from the density field. In the latest, continuous lines represent water going into the page, contours with dashed lines water out the page. The location of the cross-section is observed in the top right corner of the page.

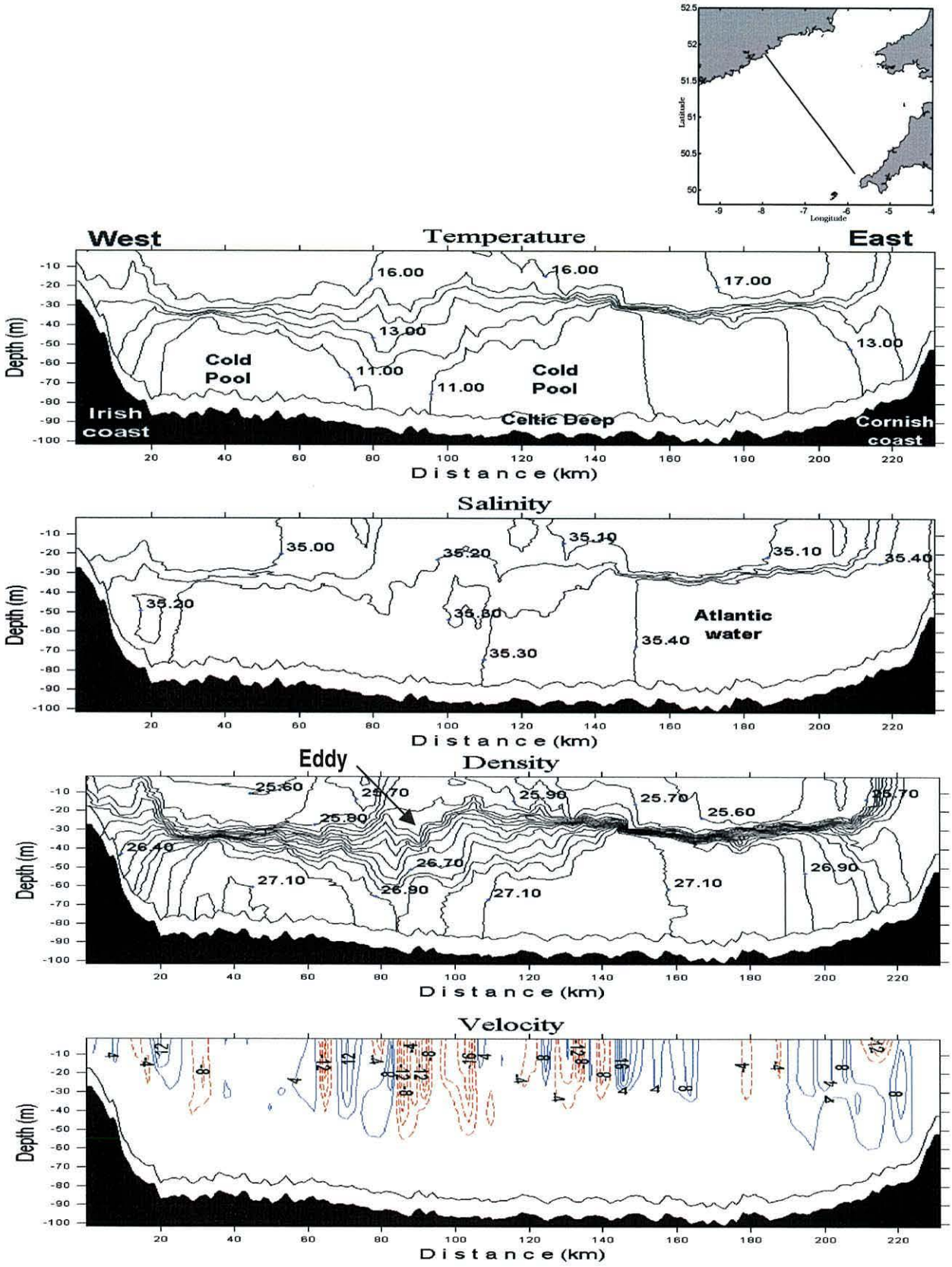

Figure 4.14 Transverse section crossing the Celtic Sea corresponding to leg 180 (CORY998) showing the vertical structure of: (a) Temperature (°C), (b) Salinity, (c) density (σ_t in kg/m^3), and (d) geostrophic velocities in cm s^{-1} derived from the density field. In the latest, continuous lines represent water going into the page, contours with dashed lines water out the page. The location of the cross-section is observed in the top right corner of the page.

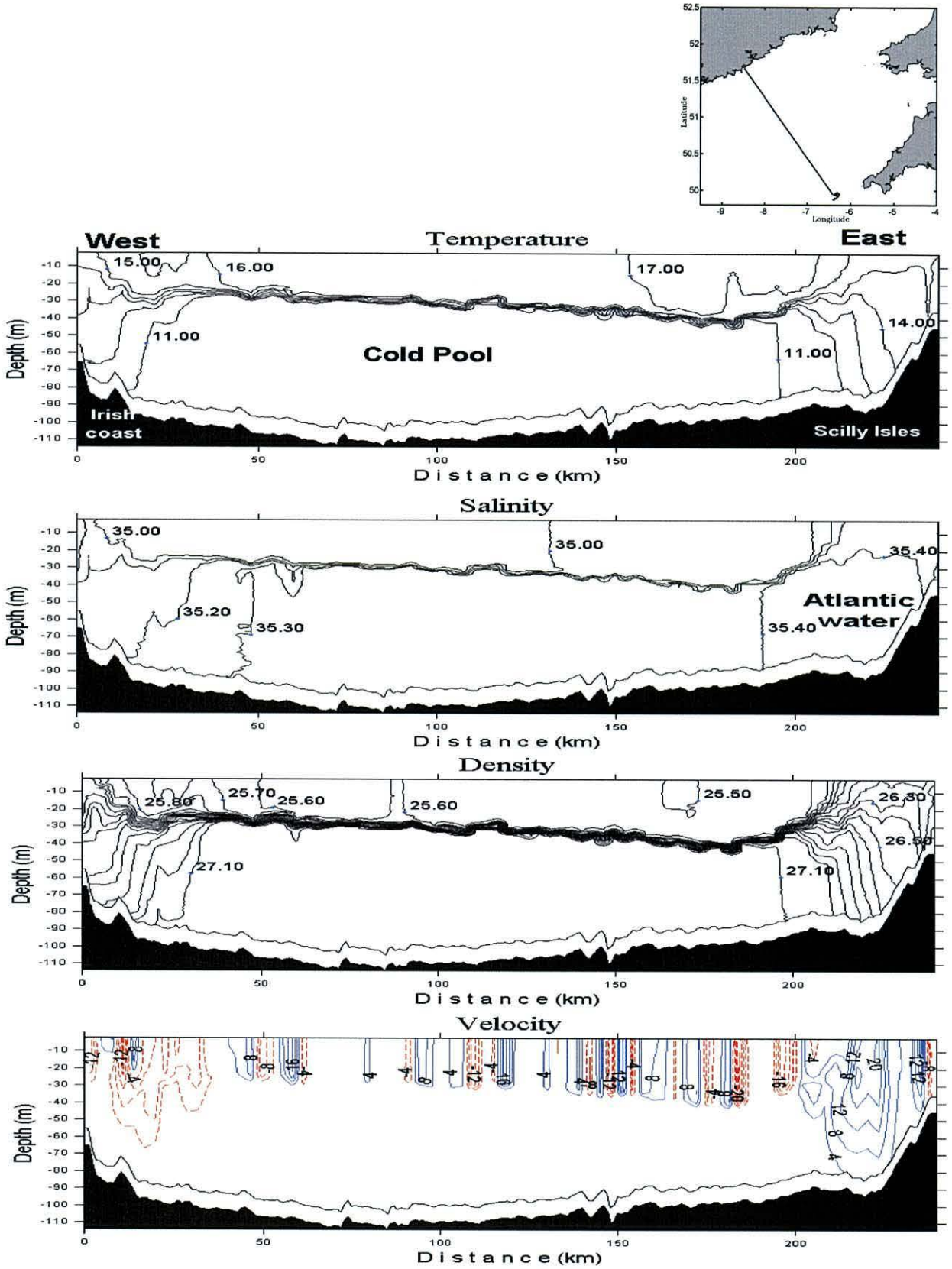

Figure 4.15 Transverse section crossing the Celtic Sea corresponding to leg 178 (CORY998) showing the vertical structure of: (a) Temperature (°C), (b) Salinity, (c) density (σ_t in kg/m^3), and (d) geostrophic velocities in cm s^{-1} derived from the density field. In the latest, continuous lines represent water going into the page, contours with dashed lines water out the page. The location of the cross-section is observed in the top right corner of the page.

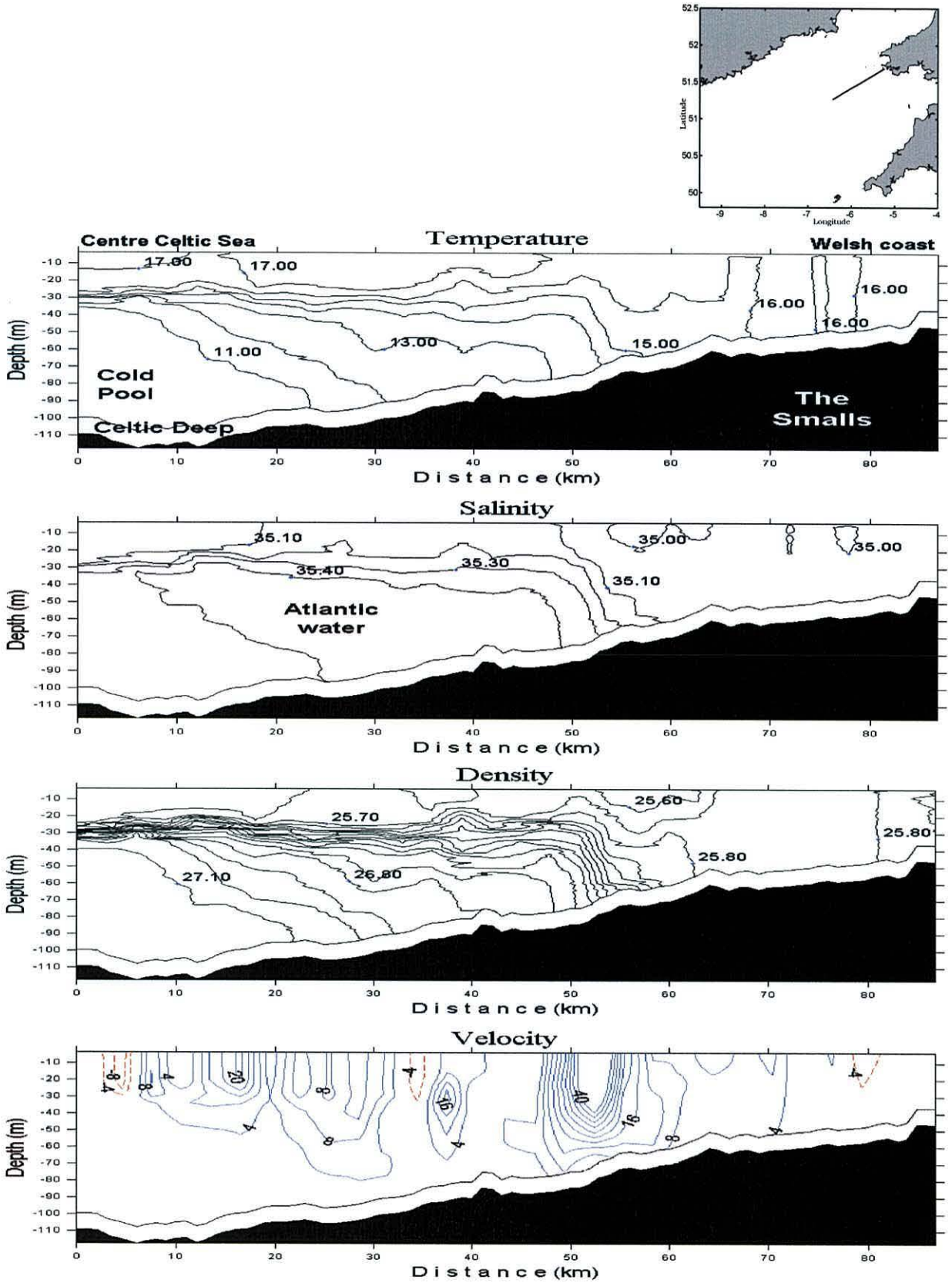

Figure 4.16 Cross-section from the Welsh coast to the centre Celtic Sea corresponding to leg 214 (CORY998) showing the vertical structure of: (a) Temperature (°C), (b) Salinity, (c) density (σ_t in kg/m^3), and (d) geostrophic velocities in cm s^{-1} derived from the density field. In the latest, continuous lines represent water going into the page, contours with dashed lines water out the page. The location of the cross-section is observed in the top right corner of the page.

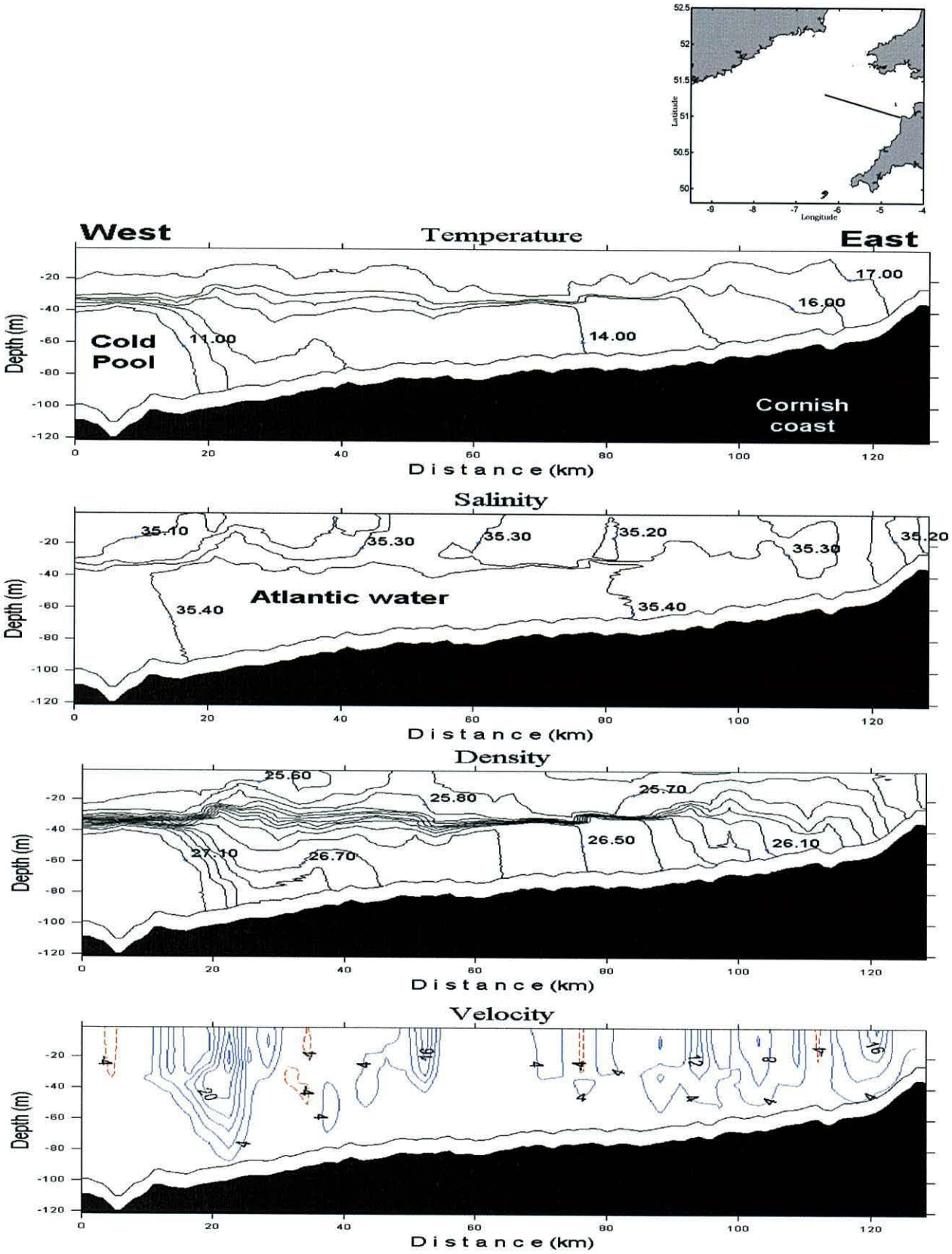

Figure 4.17 Cross-section from the centre Celtic Sea to the Cornish coast, corresponding to leg 189 (CORY998) showing the vertical structure of: (a) Temperature (°C), (b) Salinity, (c) density (σ_t in kg/m^3), and (d) geostrophic velocities in cm s^{-1} derived from the density field. In the latest, continuous lines represent water going into the page, contours with dashed lines water out the page. The location of the cross-section is observed in the top right corner of the page.

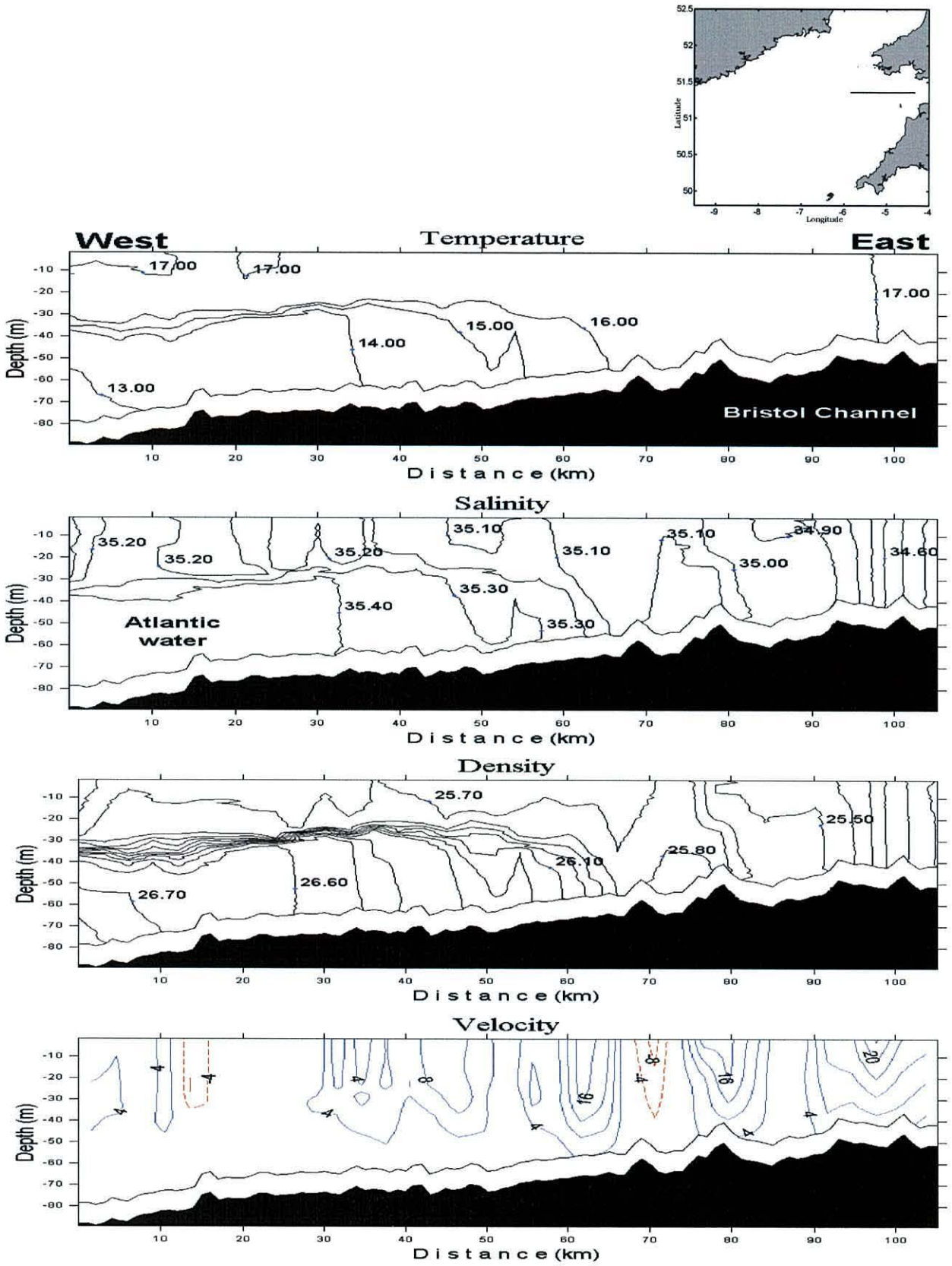

Figure 4.18 Transverse section from Bristol Channel entrance to Bristol Channel corresponding to leg 187 (CORY998) showing the vertical structure of: (a) Temperature (°C), (b) Salinity, (c) density (σ_t in kg/m^3), and (d) geostrophic velocities in cm s^{-1} derived from the density field. In the latest, continuous lines represent water going into the page, contours with dashed lines water out the page. The location of the cross-section is observed in the top right corner of the page.

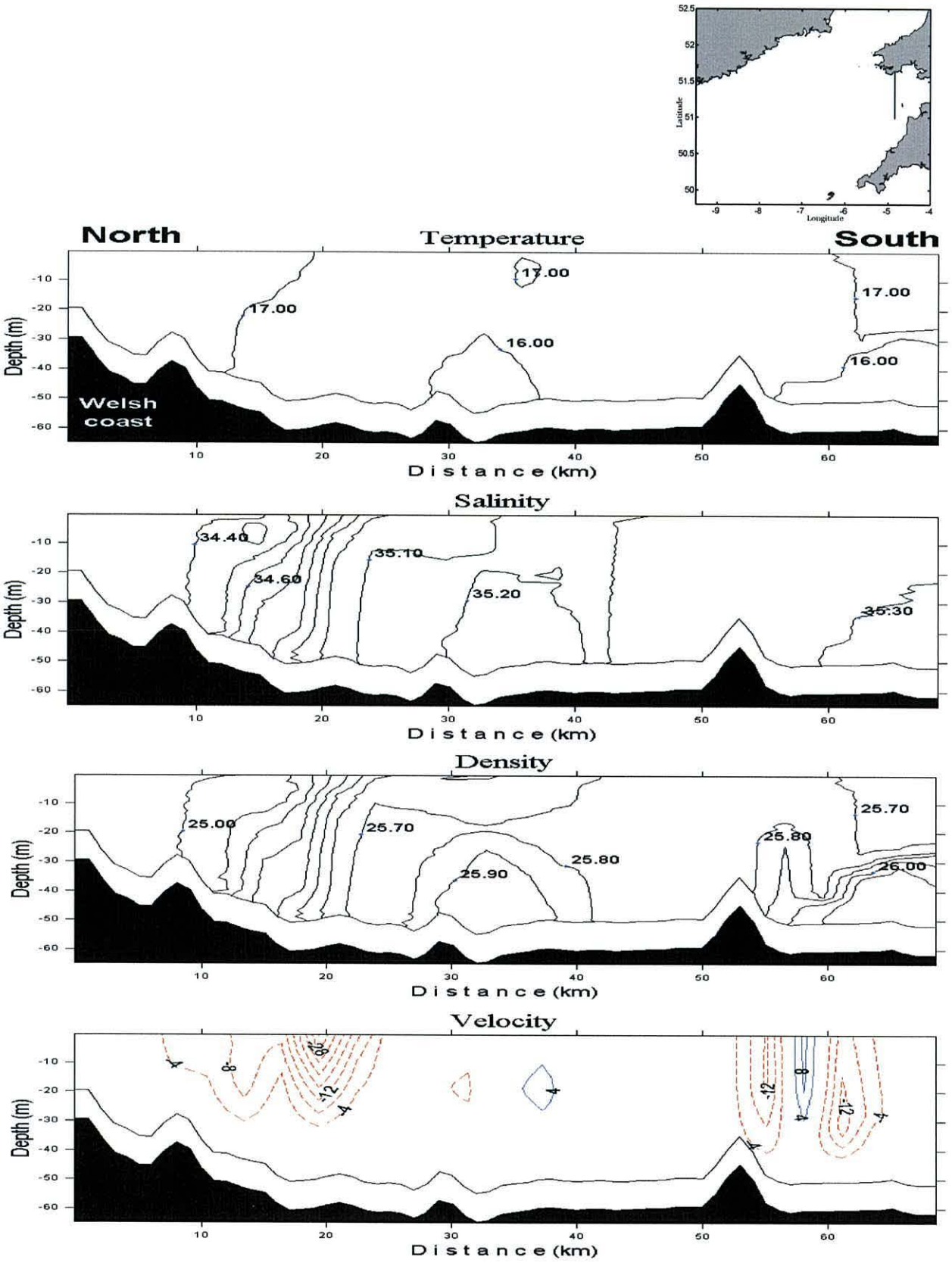

Figure 4.19 North-south cross-section inside Bristol Channel corresponding to leg 223 (CORY998) showing the vertical structure of: (a) Temperature (°C), (b) Salinity, (c) density (σ_t in kg/m^3), and (d) geostrophic velocities in cm s^{-1} derived from the density field. In the latest, continuous lines represent water going into the page, contours with dashed lines water out the page. The location of the cross-section is observed in the top right corner of the page.

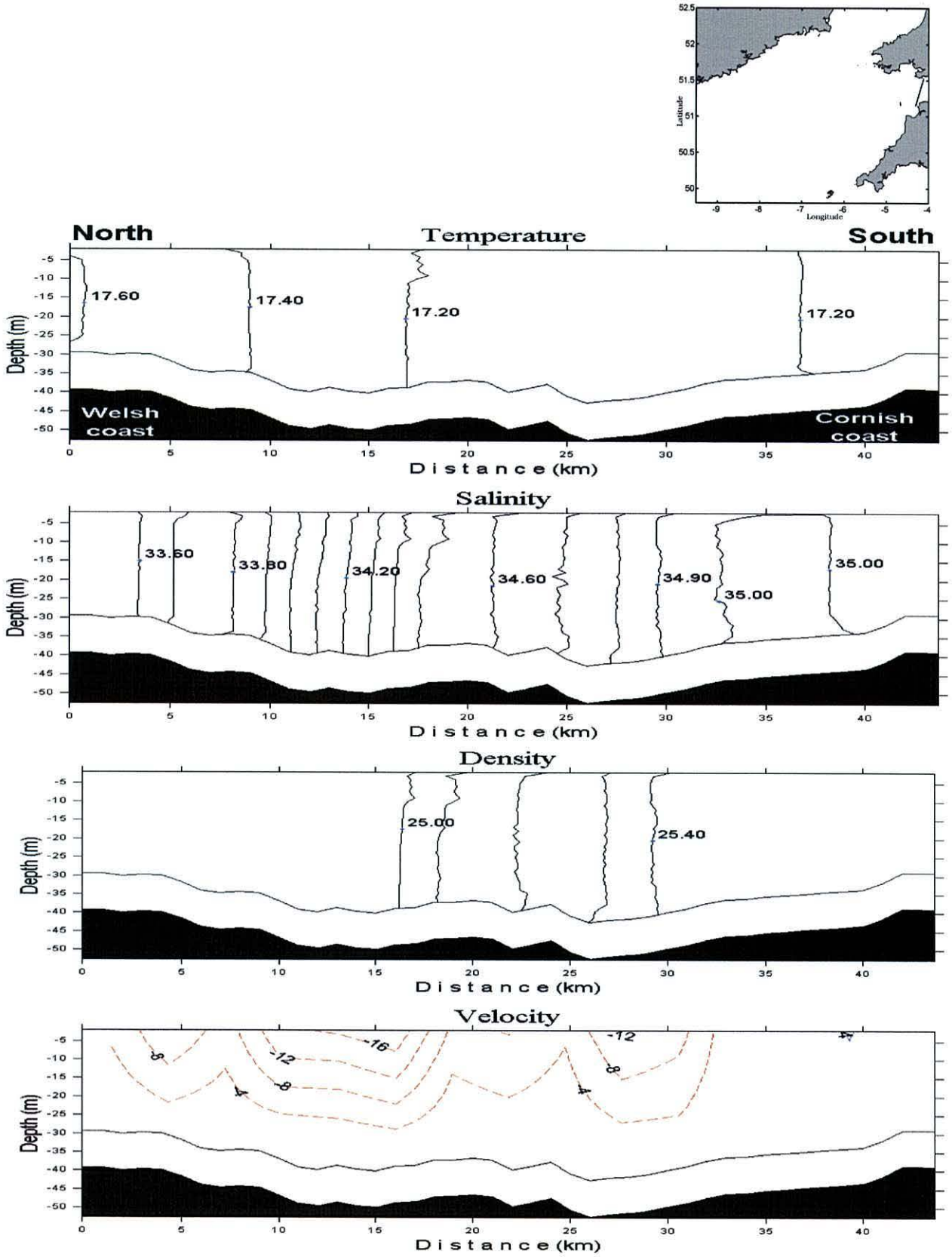

Figure 4.20 North-south cross-section inside Bristol Channel corresponding to leg 224 (CORY998) showing the vertical structure of: (a) Temperature (°C), (b) Salinity, (c) density (σ_t in kg/m^3), and (d) geostrophic velocities in cm s^{-1} derived from the density field. In the latest, continuous lines represent water going into the page, contours with dashed lines water out the page. The location of the cross-section is observed in the top right corner of the page.

4.5 Computed geostrophic surface circulation

In order to have a horizontal spatial picture of the calculated geostrophic circulation associated with the horizontal density gradients, a map with geostrophic velocities at a selected depth, can be more illustrative that calculated geostrophic velocities obtained from individual cross-sections with velocity components normal to the sections. Additionally, the maximum possible geostrophic flow can be underestimated if cross-sections cross gradients obliquely. In order to present this, geopotential anomalies were calculated as the integral of density anomalies from the bottom (*i.e.* bottom as the level of no motion) to 30 m depth from each cross-section. This depth was selected based on the previous results (section 4.4) where the strongest velocities related to bottom density gradients were found above the thermocline, which was located approximately between 30 and 40 m depth. Then, a regular grid map of geopotential anomalies was generated extracting the geopotential anomalies from each cross-section, with the proviso that a smoothing of the resulting field was obtained, *i.e.* including only large-scale aspects of the field. The regular grid map used to perform the geostrophic calculations was of 6 km horizontal resolution which was obtained using the Kriging interpolation method.

Predicted circulation of the geostrophic velocities derived from the density distribution in the Celtic Sea is shown in Figure 4.21. In both cruises, the geostrophic calculations displayed areas with organized circulation paths as jet-like flows which followed the margin of the cold pool and the bottom frontal areas (compare with Fig 4.5). This circulation could be predicted from the maps of potential energy anomaly (Φ), since the spatial distribution of potential energy anomaly is a vertically integrated measure of the horizontal density differences, thus contours of Φ can be regarded as streamlines that may provide information about the density driven flows (Horsburgh *et al.*, 2000). The calculated geostrophic flow pattern described a cyclonic circulation, with strongest velocities near the St. George's Channel area (up to 0.30 m s^{-1}). In addition, near the Scilly Isles (Fig 4.21b) a relatively organized northeastward flow with velocities of up to 0.10 m s^{-1} was shown. On the other hand, there were areas with less organized flows and relatively weak (< 0.05 m s^{-1}) speeds (Fig 4.21), mainly outside the frontal areas (Fig 4.5). The most extensive of these areas were Nymphe Bank and the Cornish coast, both having the weakest or null calculated geostrophic velocities.

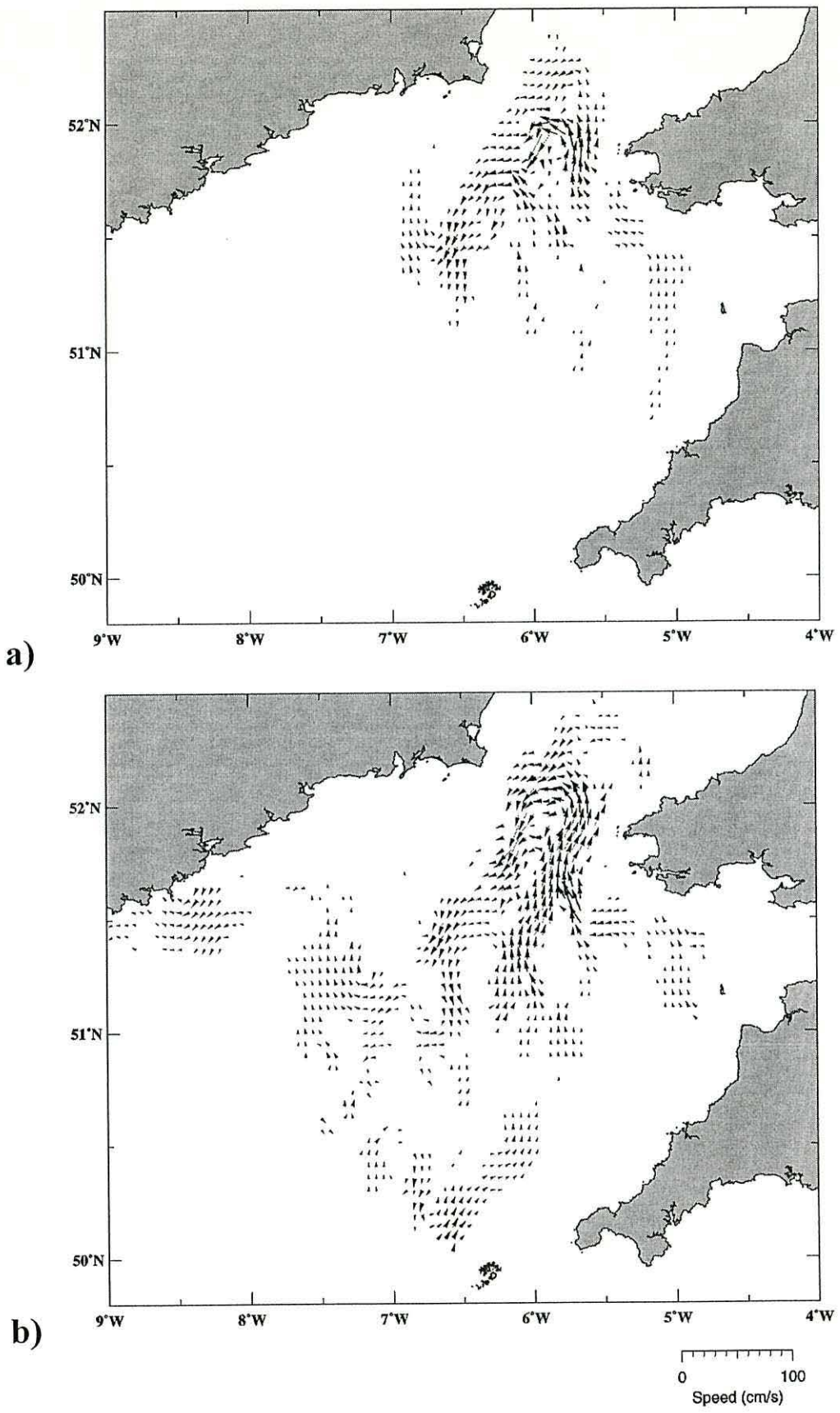

Figure 4.21 Geostrophic velocities (cm s^{-1}) at 30 m depth referred to the bottom for (a) CORY798 and (b) CORY998. Only velocities > 3 cm s^{-1} are shown.

4.6 Summary

This chapter has shown the main hydrographic results obtained from the two oceanographic campaigns undertaken during the summer of 1998 in the Celtic Sea. These results represent the first comprehensive hydrographic observations during summertime in this region to date. A characterization of the frontal areas was done; additionally, in the context of dynamics of bottom fronts (Garrett and Loder, 1981) using geostrophic calculations, it was shown that these frontal areas can provide the necessary baroclinic conditions for the formation and maintenance of jet-like flows. Moreover, organized paths of circulation could be expected in this region.

Although, the results showed a clear domination of the spatial density structure by temperature, salinity spatial distribution contributed to reinforce the density gradients in the Bristol Channel, where salinity played the predominant role in the density structure.

One of the most outstanding results was a dense cold pool structure in the Celtic Sea at depths >80 m (around the Celtic deep) which was isolated from the surface by a strong thermocline located at ~30-40 m. This cold pool structure marked the boundary of the bottom fronts in the Celtic Sea. Since the distribution of both temperature and density followed the bathymetry, their position and extent seem to be controlled by bathymetry and vertical mixing.

While bottom fronts were widely observed and well defined, this was not true for the surface fronts, in particular, the surface thermal fronts, which were weak or absent in the entrance of the Bristol Channel. In addition, bottom fronts were sharper than surface fronts. Associated with the bottom fronts, organized narrow (10-20 km) jet-like flows were calculated immediately above the flanks of the bottom fronts. The speed of these jet-like core flows reached up to 0.30 m s^{-1} at the strongest density gradients of the areas of the St. George's Channel. Calculated geostrophic velocities outside the bottom fronts did not show significant magnitudes and the flow pattern was less organized. Nevertheless, an overall cyclonic surface circulation was predicted from geostrophic calculations in this region. The surface geostrophic velocity predicted agreed well with the surface distribution of temperature and salinity, such as the intrusion of cold water from the Irish Sea towards the central Celtic Sea and the nearly cyclonic salinity surface distribution. Since the overall density structure (*i.e.* cold pool and tidal mixing fronts structures)

persisted from July to August, consequently this circulation might be expected during the summertime with important implications in the transport of larvae, pollutants and other water properties.

At first approximation, the frontal dynamics in the Celtic Sea can be explained by geostrophy (*e.g.* Rossby number << 1 for typical scales values in tidal mixing frontal regions). We acknowledge that the calculated geostrophic velocity field could only be a "frozen" and "idealized" portrait of a possible most complicated summer circulation for this region including the presence of eddy-like structures. In addition, several potentially important forcing mechanisms have been ignored, such as wind which could be an important forcing at the frontal areas (Wang *et al.*, 1990).

Thus, an important question arises: are these predicted density-driven jet-like flows observable, persistent and stable features of the summertime circulation in the Celtic Sea? This question can only be addressed by direct observations of the velocity field, which is presented in the next two chapters.

Chapter 5

Regional Lagrangian circulation

5.1 Introduction

In the context of surface density-driven currents in shelf seas, Lagrangian observations and, in particular, satellite tracked drifters targeted upon well-defined bottom density structures, have been demonstrated to provide support for organized jet-like flows (Hill *et al.*, 1994; Hill *et al.*, 1997b; Brown *et al.*, 1999a; Horsburgh *et al.*, 2000). Satellite tracked drifters have confirmed the existence of strong near-surface flows above the margins of dense-pool bottom fronts in the European shelf seas of: the Northern Sea of the Hebrides Sea (Hill *et al.*, 1997b), the North Sea (Brown *et al.*, 1999a) and the Irish Sea (Hill *et al.*, 1994; Hill *et al.*, 1997a; Horsburgh *et al.*, 2000). In addition, they can elucidate the spatial extent of these currents and have revealed the existence of oceanographic features such as the Irish Sea gyre (Hill *et al.*, 1994) and the residual circulation over the George's Bank (Limeburner and Beardsley, 1996), which were not accessible by Eulerian techniques.

Although limited in number of Lagrangian devices (only 3 satellite tracked ARGOS drifters), Horsburgh *et al.* (1998) provided evidence of the existence of these jet-likes flows in the frontal area of the Celtic Sea and St. George's Channel. However, in order to gain a more comprehensive a picture of the regional circulation of the Celtic Sea, more Lagrangian devices are needed.

Here, a much larger number (23) satellite-tracked drifter ARGOS buoys were deployed in the summer of 1998 providing the first directly-observed description of the summer regional circulation for the Celtic Sea. This chapter deals with such a Lagrangian description of the velocity field. Additionally, an attempt has been made to assess the possible forcing mechanism of the observed circulation. In particular, the predicted geostrophic density-driven flows presented in the last chapter are compared with the observed Lagrangian field.

5.2 The Data

The Lagrangian flow field was measured using 23 ARGOS drifters released in the study area during summer 1998 (see Fig 3.1b) and drogued at 30 m depth. For instrumentation details see section 3.4. Figure 5.1 shows the trajectory of each individual drifter based on their raw position data obtained from ARGOS system. Table 5.1 summarizes the drifter deployments: initial and final position, record length and the eventual fate of each drifter such as drogue lost and where either the drifter was grounded or recovered. Hazards to instruments were present, three drifters were removed by fishermen, two lost their drogues and four were lost for other (unknown) reasons. One of them accounted for 4 active days only. Nevertheless, most of the drifters were active for more than 30 days, and at least 10 of them for more than 40 days. Consequently, a general picture of the summer regional circulation was obtained by these measurements.

In order to simplify the picture of the Lagrangian circulation, it is desirable to remove the tidal signal from the drifter tracks. The next section, therefore, deals with the filtering treatment of the raw drifter position data.

Table 5.1. Argos drifters deployed in the Celtic Sea during summer 1998. The initial and final time and position and the fate of the drifter such as drogue lost and where either the drifter was grounded or recovered (Rec.) are given.

Drifter ID	Initial Time (GMT)		Initial Position Latitude N	Longitude W	Final Time (GMT)		Final Position Latitude N	Longitude W	Fate
A1	0134	14/7/98	50.6658	7.7482	1310	26/8/98	50.0593	6.6763	Intact
A2	2249	13/7/98	50.6495	6.9920	1002	26/8/98	49.6667	6.9200	Intact
A3	1245	22/7/98	50.6665	5.9975	1841	28/7/98	50.7767	5.8400	Lost
A4	0254	16/7/98	50.6668	5.4993	1556	2/9/98	51.8628	6.2887	Drogue ripped, been through The Smalls
A5	0438	16/7/98	50.6667	5.0858	0841	23/7/98	50.9117	4.8883	Rec. fisherman, no drogued attached
A6	2255	15/7/98	51.0022	4.9860	1741	2/9/98	51.6180	6.4153	Intact
A7	0053	16/7/98	51.0000	5.4960	1714	23/7/98	50.9467	4.9783	Fate unknown
A8	0245	19/7/98	50.9998	6.2473	1715	1/8/98	51.48	5.796	No drogue, lost in Smalls
A9	0541	14/7/98	50.9992	7.0000	0533	19/7/98	50.9900	7.0933	Rec. fisherman, no drogued returned
A10	0322	14/7/98	50.9992	7.7498	1836	20/8/98	50.6533	5.7933	Lost
A11	1055	14/7/98	51.4162	7.7498	0901	11/9/98	51.4162	7.7498	Grounded
A12	0755	14/7/98	51.4098	6.9140	0941	13/8/98	52.14	6.674	Grounded
A13	1616	16/7/98	51.4173	6.2487	1453	2/9/98	51.0217	6.3528	Tar on bottom panel of drogue
A14	0630	15/7/98	51.4165	5.5000	0553	2/9/98	52.4583	5.2830	Intact
A15	0639	16/7/98	51.4310	5.2180	0810	21/7/98	51.685	5.637	Drogue lost in Smalls
A16	0509	18/7/98	51.5883	5.7497	1700	31/8/98	51.1082	7.1765	Intact
A17	0320	18/7/98	51.7500	5.9983	1851	4/9/98	51.4940	6.2363	Intact
A18	0218	18/7/98	51.8498	6.1825	1245	12/8/98	52.115	6.678	Grounded
A19	0110	18/7/98	51.9832	6.3472	1900	31/8/98	50.8662	6.8290	Drogue shredded, but floating at surface
A20	0751	16/7/98	52.1663	5.5015	0942	22/8/98	52.0683	6.6817	Intact
A21	0628	16/7/98	52.2498	5.8500	0321	31/7/98	51.9750	6.9417	Rec. fisherman, no drogued returned
A22	1453	22/7/98	50.3337	5.9997	1932	22/8/98	51.3917	5.7850	Lost
A23	1159	19/7/98	51.9667	6.9990	0941	4/8/98	51.7550	8.0967	Ashore Ballycotton EIRE

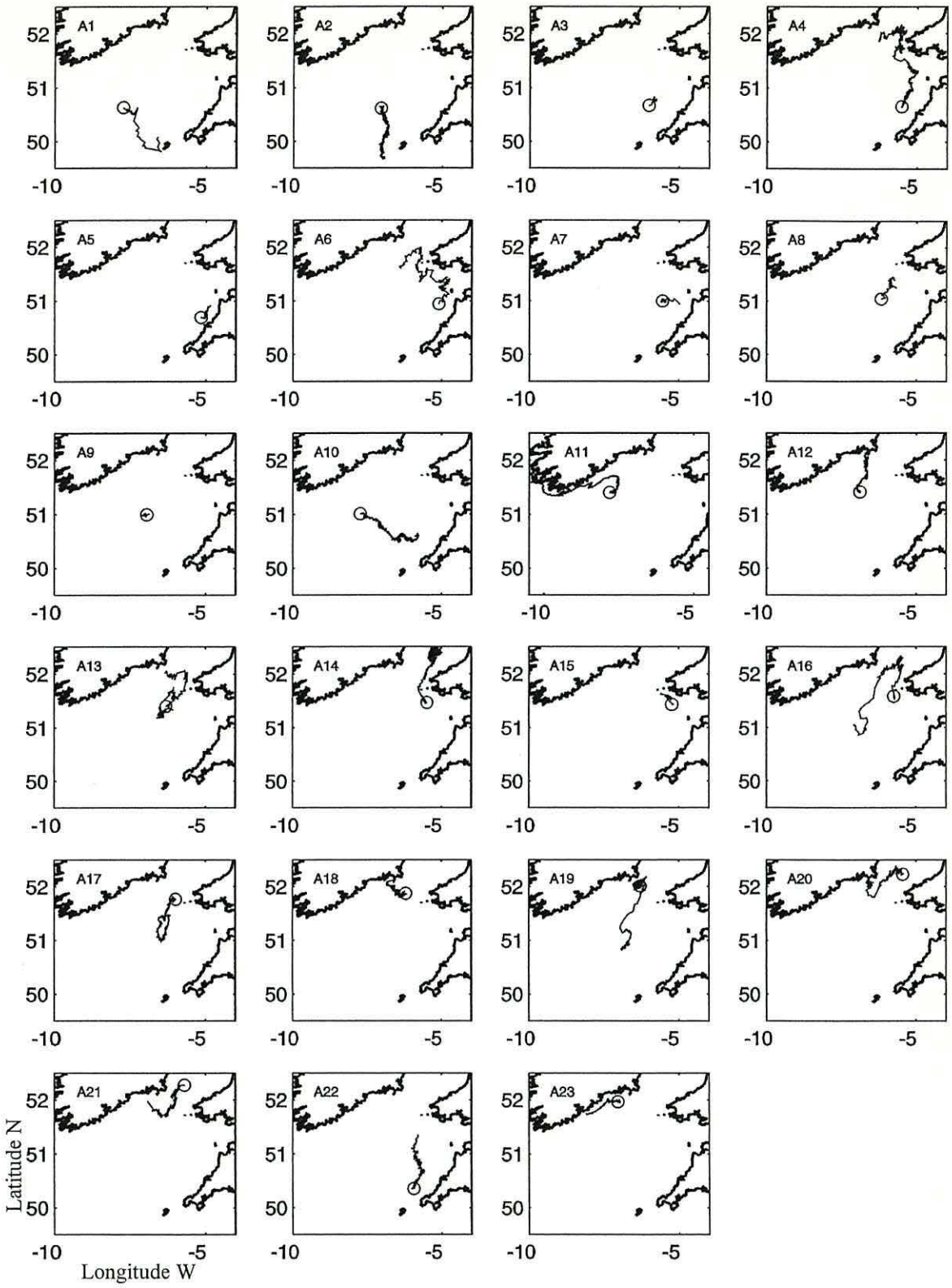

Figure 5.1 Unfiltered Argos drifter tracks of the 23 drifters deployed during summer 1998 in the Celtic Sea.

5.3 Tidal removal for Argos drifters

A common treatment for removing tidal signals from drifter data is a convolution of the data with a digital filter. Firstly, in order to apply the filter, the raw data position needs to be regularly spaced, so a linear interpolation was applied to obtain positions every 3 hours. Linear interpolation was preferred over other interpolation schemes, such as cubic spline, which can produce artificial loops in tidal regimes (Durazo-Arvizu, 1993). After this had been done, the series were low-pass filtered with a Hamming window, finite impulse response (FIR) filter designed to eliminate the tidal and inertial signals (Proakis and Manolakis, 1992).

The filter contains N = 55 coefficients given by:

$$h(n) = 2f_c(0.54+0.46\cos[2\pi n/N]) \qquad n = 0$$

$$h(n) = 2f_c\sin(n\omega_c)(0.54+0.46\cos[2\pi n/N])/ (n\omega_c) \qquad n \neq 0$$

where f_c is the cutoff frequency (normalized to the sampling frequency of 8 day^{-1}) and ω_c is its angular equivalent ($\omega_c = 2\pi/f_c$). The cutoff used ($f_c = 0.06$) filters out the semidiurnal and diurnal frequencies. Figure 5.2 shows an example of the filter's effectiveness in removal of the tidal signal from a drifter track.

The filter was applied to the uniform 3 hourly time-series. To avoid losing data at the beginning of the track dummy values were supplied by N repetitions of the start coordinates. In order to recover the N data lost at the end of the time series, due to the filtering, it was convenient to apply the filter from the end. In this way, we can obtain a whole filtered time series. The filtering cannot be performed on drifters with a number of position fixes less than the filter coefficients. In this case, instead 12 h average positions were obtained.

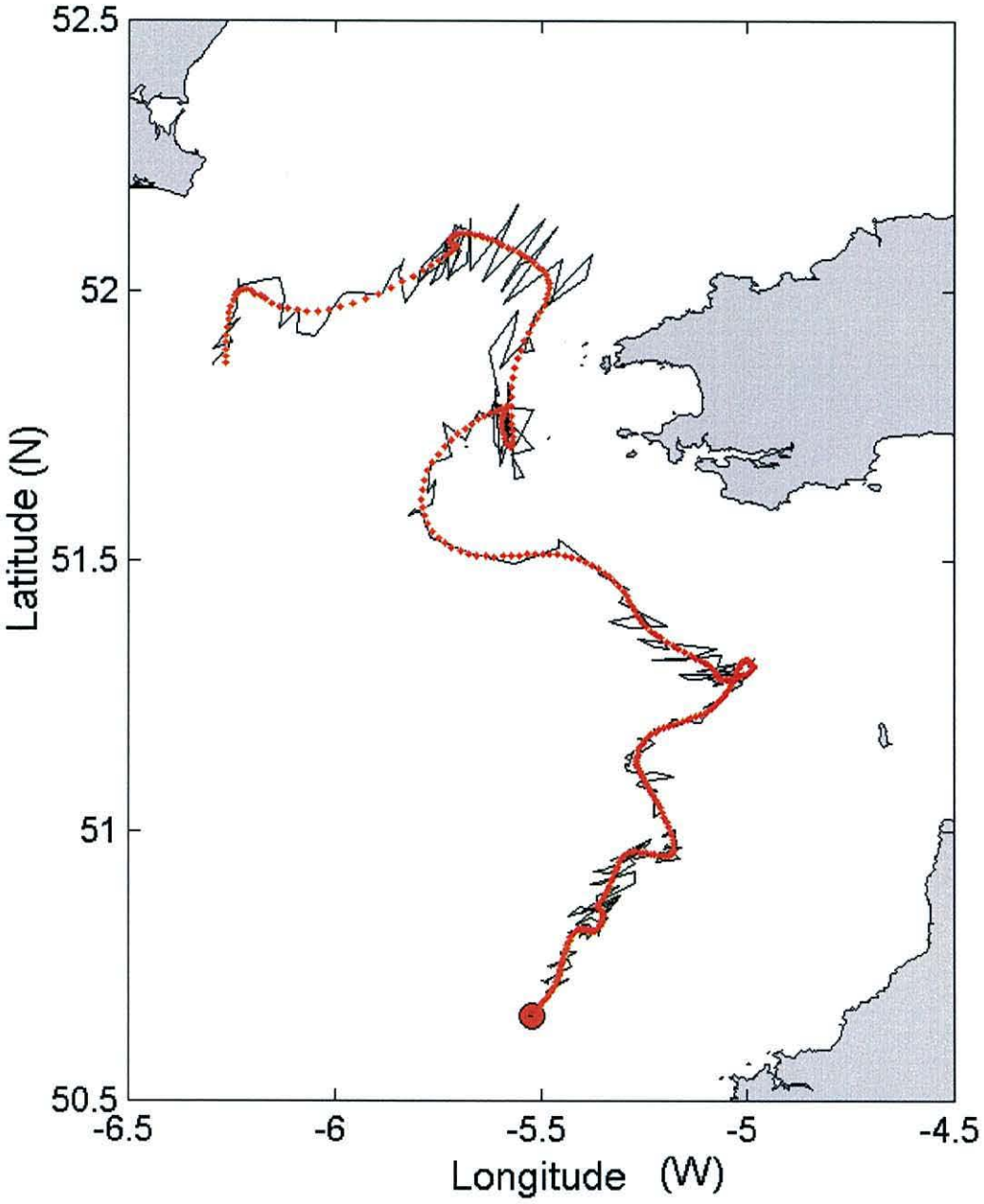

Figure 5.2 Example of filter effectiveness. Three-hour filtered data (red dots) overlaid on the raw trajectory (continuous line) of drifter A4. Initial position denoted by the red circle.

5.4 Lagrangian circulation from Argos drifters

Individual drifter trajectories (after filtering) are presented in Figure 5.3. Dots represent daily positions. These showed a complex Lagrangian field in the Celtic Sea with a variety of spatial structures such as eddies, jets, preferred paths and convergence zones which can be summarized as follows.

The St. George's Channel was the region into which drifters tended to converge (drifters A4, A6, A8, A13-A16, A19, A20 and A21; Figs 5.3d, f, h, n-r, u, w and x). It was noticeable that once drifters reached this area they increased their velocity up to 0.29 m s^{-1}. The general pattern was a cyclonic flow path, along the eastern side of the St. George's Channel and then westwards, approximately around the Celtic deep (compare with bathymetry from Figure 2.1). Drifters then moved southwards through the central-western side of the St. George's Channel. Only drifter A14 (Fig 5.3o) exited the St. George's Channel influence. Drifter A14 (Fig 5.3o) was deployed at the southeastern entrance of the St. George's Channel, and as with other drifters in this area, it repeated the track through the St. George's Channel with considerable speeds (up to 0.26 m s^{-1}) that allowed the drifter to cross this region in only 11 days. However, in contrast with other drifters (Figs 5.3d, f, h, n, q, r, u, w and x), this drifter (Fig 5.3o) did not turn westward. Instead, it continued northeastward and then, by day 14, turned eastward and continued in an erratic trajectory (Fig 5.3p) but remained in this latitude with a mean velocity of 0.05 m s^{-1}.

Drifter A16 (Fig 5.3r) was also deployed near the southeastern entrance of the St. George's Channel; it moved northward fast and passed through the channel with a speed of up to 0.29 m s^{-1}. However, by day 10 it moved only slowly with speed as low as 0.01 m s^{-1}, staying 10 days at approximately the same position in the central and northern entrance of the St. George's Channel (probably outside the influence of the current that flows westward at the centre of the channel). After that, it (Fig 5.3r) continued its track southwestward to the centre of the Celtic Sea crossing St. George's Channel with velocities of up to 0.24 m s^{-1}. However, the highest velocities were found outside the St. George's Channel in the form of a jet flow with maximum velocities of 0.43 m s^{-1}, reaching the centre of the Celtic Sea by day 30 where the velocities decreased to 0.07 m s^{-1}. This drifter then started to rotate in an anticyclonic sense with a mean speed of 0.09 m s^{-1} until its recovery.

The above jet feature was also captured by drifter A19 (Fig 5.3u). This drifter was initially trapped by an anticyclonic eddy (Fig 5.3v) at the southwestern entrance of the St. George's Channel, near the headland of the Irish coast. It stayed there 21 days with a typical velocity of 0.05 m s^{-1}. After that, the drifter passed the western side of the St. George's Channel with a velocity of 0.25 m s^{-1} and then followed the same trajectory as A16 (Fig 5.3v). It advanced quickly (Fig 5.3u) towards the centre of the Celtic Sea with speeds up to 0.33 m s^{-1} and then, in the centre of the Celtic Sea, it turned in an anticyclonic trajectory. Both trajectories of A16 (Fig 5.3r) and A19 (Fig 5.3u) from the St. George's Channel to the centre of the Celtic Sea were similar and approximately simultaneous.

There were two drifters that underwent a full cyclonic circuit around the central Celtic Sea (A13 and A17; Figs 5.3n and s). Drifter A13 (Fig 5.3n) deployed at the centre of the Celtic Sea made a complete cyclonic elongated gyre-like circulation for approximately 33 days with a mean velocity of 0.07 m s^{-1}. However, velocities fluctuated from 0.25 m s^{-1} at the western side of the gyre to less than 0.01 m s^{-1} in a region which seemed to be a stagnation zone at the centre of the Celtic Sea. Later, it left the centre of the Celtic Sea in a northeastward direction to St. George's Channel where it accelerated reaching velocities up to 0.26 m s^{-1}. It then travelled westward and southward in the St. George's Channel. By day 41, it turned southwestward towards the Waterford area on the Irish coast, until it was recovered after 49 days. A17 (Fig 5.3s) deployed almost at the central southern entrance of the St. George's Channel, also described an elongated cyclonic trajectory around the centre of the Celtic Sea. However, its trajectory was not closed. The mean velocity was ~ 0.05 m s^{-1} with a maximum of 0.14 m s^{-1} and minimum of 0.01 m s^{-1}. It experienced fluctuations in the speed (increasing or decreasing) approximately every 10 days, however, it moved slower on average (0.02 m s^{-1}) at the eastern flank of the gyre-like path.

In general, drifters deployed at the eastern side of the Celtic Sea, consistently travelled northward (A4-A6, A8 and A22; Figs 5.3d-f, h and y). Drifters A4 (Fig 5.3d) and A5 (Fig 5.3e) were deployed on the same day and were separated by 0.5°of longitude. They simultaneously followed almost the same path until A5 (Fig 5.3e) was recovered by a fisherman. Thus, A5 (Fig 5.3e) travelled northeastward parallel to drifter A4 (Fig 5.3d) and to the Cornish coast for 8 days with an average velocity of 0.05 m s^{-1}. Drifter A4 (Fig 5.3d) moved northward, approximately following the 60-80 m depth contours (compare with Figure 2.1). By day 40, this drifter was in the northern St. George's Channel and

turned westward and then southward until it was recovered. Initial velocities were 0.05 m s^{-1}. However, it accelerated during its northward path reaching maximum velocities of up to 0.29 m s^{-1} in the St. George's Channel. Drifter A6 (Fig 5.3f) tended to follow a similar path to A4 (Fig 5.3d) with additional turns making the path a little more convoluted. Also, it (Fig 5.3f) was deployed at a position northeast of A4 (Fig 5.3d) when after ~ 10 days A4 reached approximately the same latitude. Maximum velocities were observed, up to 0.29 m s^{-1}, in the St. George's Channel area. Drifter A8 (Fig 5.3h) travelled northeastward for 14 days with a mean velocity of 0.07 m s^{-1} until it lost its drogue at the Smalls. Drifter A15 (Fig 5.3q), which was deployed near the eastern entrance of the St. George's Channel, moved northward with a mean velocity of 0.13 m s^{-1} tending to follow the same trajectory as other drifters that passed through the same area (*e.g.* A4, A6, A8, A13-A14, A16, A19, A20 and A21; Figs 5.3d, f, h, n-p, r, u, w and x). However, this drifter track (Fig 5.3q) was of short duration (6 days) due to the fact that it lost its drogue at the Smalls.

A22 (Fig 5.3y) was deployed near the Cornish coast and followed approximately the same path as the other drifters deployed in this area (A4 and A5; Figs 5.3d and e). It started to move parallel to the coast and, by day 11, moved consistently northward (Fig 5.3y). The mean velocity was 0.06 m s^{-1} with a maximum of 0.14 m s^{-1}. Only drifter A7 (Fig 5.3g) deployed at the eastern area showed an irregular and unusual path when compared with drifters deployed on the eastern side of the Celtic Sea. This drifter was deployed approximately at the same latitude as A6 (Fig 5.3f) but 0.5° to the west of it. It unexpectedly travelled eastward (Fig 5.3g) with a mean speed of 0.09 m s^{-1}, when all other drifters at the same area took a northward path (*e.g.* A4-A6, A8 and A22; Figs 5.3d-f, h and y).

A flow along the Irish south coast was revealed by drifters A11 (Fig 5.3k) and A23 (Fig 5.3z). Drifter A11 (Fig 5.3k) was the one with the longest duration (60 days), and initially moved northward from its deployment position at 0.10 m s^{-1} average velocity. Then, by day 12, it turned westward and continued along the Irish coast with velocities up to 0.33 m s^{-1}. It left the survey area by day 37 and continued its trajectory around the Irish coast until it was trapped by an eddy of diameter 10-15 km on day 49 (Fig 5.3l), rotating for 11 days with a mean velocity 0.12 m s^{-1} until it grounded. Drifter A23 (Fig 5.3z) was active for 17 days travelling relatively fast (mean velocity 10 m s^{-1} and maximum speed of 0.25 m s^{-1}) along the Irish coast until it was grounded.

There was a tendency for some drifters to go aground and to concentrate in the Waterford area (A12, A18, A20 and A21; Fig 5.3m, t, w and x). The most unexpected behaviour was from drifter A12 (Fig 5.3m), deployed near the centre of the Celtic Sea. It moved northwestward with a velocity of 0.10 m s^{-1}. On day 9 it travelled southward for 2 days and then moved northward, decreasing its speed to 0.03 m s^{-1}. On days 22-23 it stayed almost at the same location and then again moved northward until it grounded in the Waterford Head area. Drifter A18 (Fig 5.3t) was deployed near the central and southern entrance of the St. George's Channel. It travelled northwestward in a convoluted path until it grounded on day 26 in the Waterford area where A12 (Fig 5.3m) had also grounded. The mean velocity of A18 (Fig 5.3t) was 0.05 m s^{-1} with a maximum speed of 0.13 m s^{-1}. A20 (Fig 5.3w) deployed in the central northern St. George's Channel, moved westward for about 7 days (at 0.07 m s^{-1}) and then took a southwestern path, passing through the St. George's Channel with velocities up to 0.13 m s^{-1}. By day 21 it had turned west and travelled about 10 days towards the region of Waterford where A12 (Fig 5.3m) and A18 (Fig 5.3t) had grounded. However, A20 (Fig 5.3w) did not ground, probably due to the fact that it moved westward avoiding shallower areas. Another drifter that passed close to the Waterford area was A21 (Fig 5.3x). After its deployment it (Fig 5.3x) moved fast southward, crossing the central St. George's Channel with velocities up to 0.18 m s^{-1}. After 10 days it turned to a slightly northwestern direction, although it did not travel in the shallower area.

Drifters deployed near the southern entrance of the Celtic Sea basin (A1 and A2; Fig 5.3a and b) tended to leave the area southwestwardly around the Scilly Isles. Drifter A1 (Fig 5.3a) moved southeastward with a mean velocity of 0.07 m s^{-1}. It moved initially with an average velocity of 0.04 m s^{-1} during the first 12 days and then started to accelerate reaching a velocity of 0.13 m s^{-1} by day 16 and then returned to a velocity of 0.04 m s^{-1}. From day 26 it slowly accelerated reaching a maximum of 0.20 m s^{-1} 10 days later. Before it reached the Scilly Isles it changed direction (day 38) travelling northward. Drifter A2 (Fig 5.3b) moved consistently southward with an approximately constant velocity of 0.04 m s^{-1}, with higher velocities (up to 0.09 m s^{-1}) during the last week of operation (days 38-44). Drifter A10 (Fig 5.3j), also deployed in the southern entrance of the Celtic Sea basin, did not exit the area. Instead it moved eastward and slightly to the south with a mean velocity of 0.08 m s^{-1}. During the first 11 days it moved at 0.07 m s^{-1}, then accelerated until it reached a velocity of up to 0.15 m s^{-1}. By day 21, it decreased its

velocity and 10 days later it accelerated to 0.15 m s^{-1} starting to move parallel to the Cornish coast when it was lost.

Drifters with a very short time duration (A3, A9, A15; Figs 5.3c, i and q), ~ 6 days, give little information about the circulation. However, they at least gave an indication of their mean velocity which was typically ~ 0.05 m s^{-1}.

Despite the complexity of the Lagrangian circulation depicted by the ARGOS drifters, a consistent pattern emerges when a composite picture of the flow field is presented (Fig 5.4). Thus, collectively drifters define an overall cyclonic circulation in the Celtic Sea, as can be seen from the spaghetti diagram (Fig 5.4). Although two drifters underwent almost closed trajectories around the central Celtic Sea, the overall circulation is not a closed gyre-like cyclonic circulation as occurs in the western Irish Sea. On the other hand, from the collection of drifter trajectories around the St. George's Channel, a well-defined cyclonic flow path emerged, which was relatively narrower on the eastern side of the St. George's Channel than on the western side. Additionally, a southward flow along the Irish coast was observed.

The observed Lagrangian field shows similarities with the density driven currents obtained in Chapter 4. In order to examine the effect of the wind, the residual tidal currents and the horizontal density gradients upon the Lagrangian observations, an analysis is presented in next section of the possible driving mechanisms.

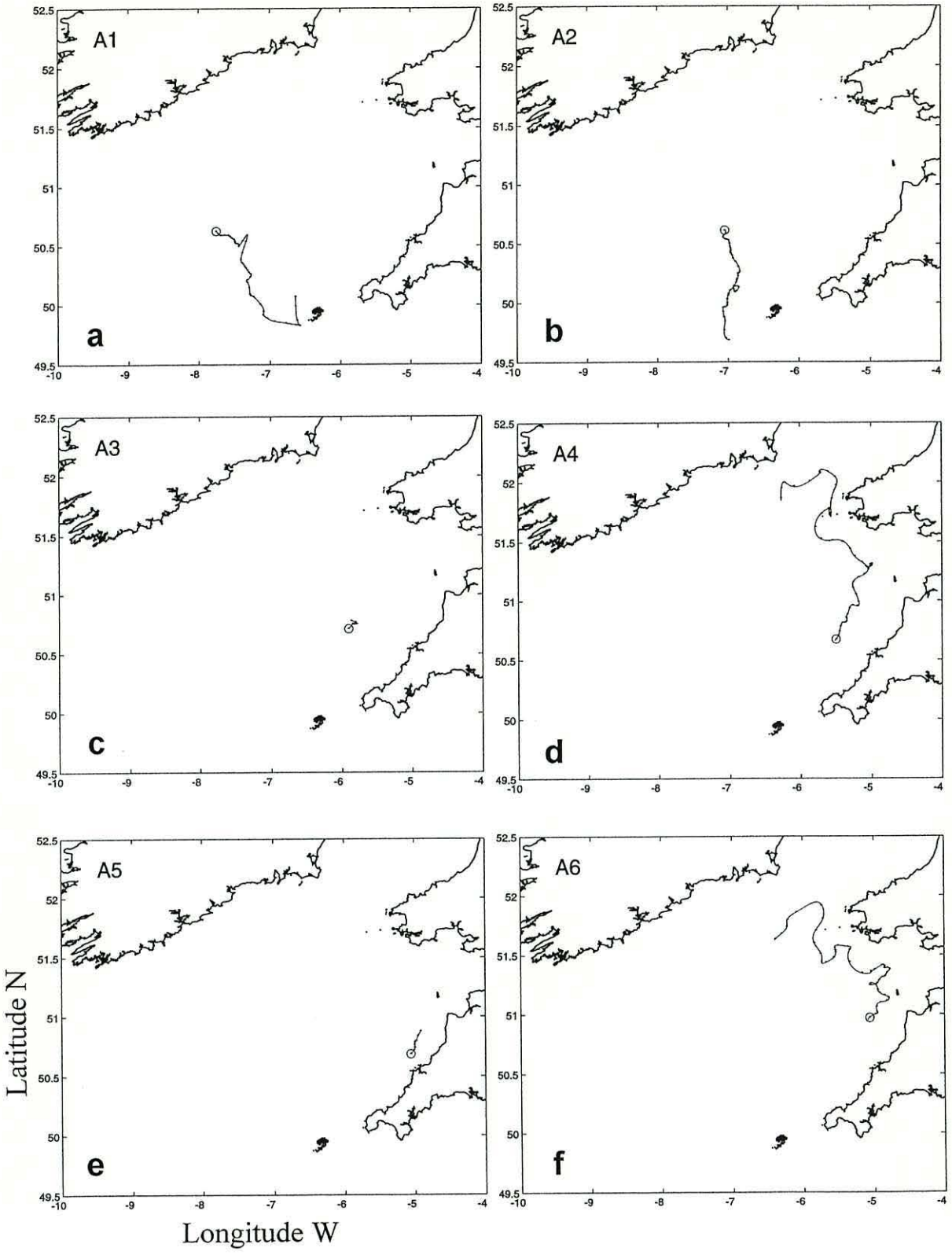

Figure 5.3 Filtered Argos drifter trajectories deployed at the Celtic Sea during summer 1998. The initial position is denoted by a circle symbol. Dots represent daily position. Initial position denoted by a circle. Drifter's ID is shown at the top-left corner of each panel.

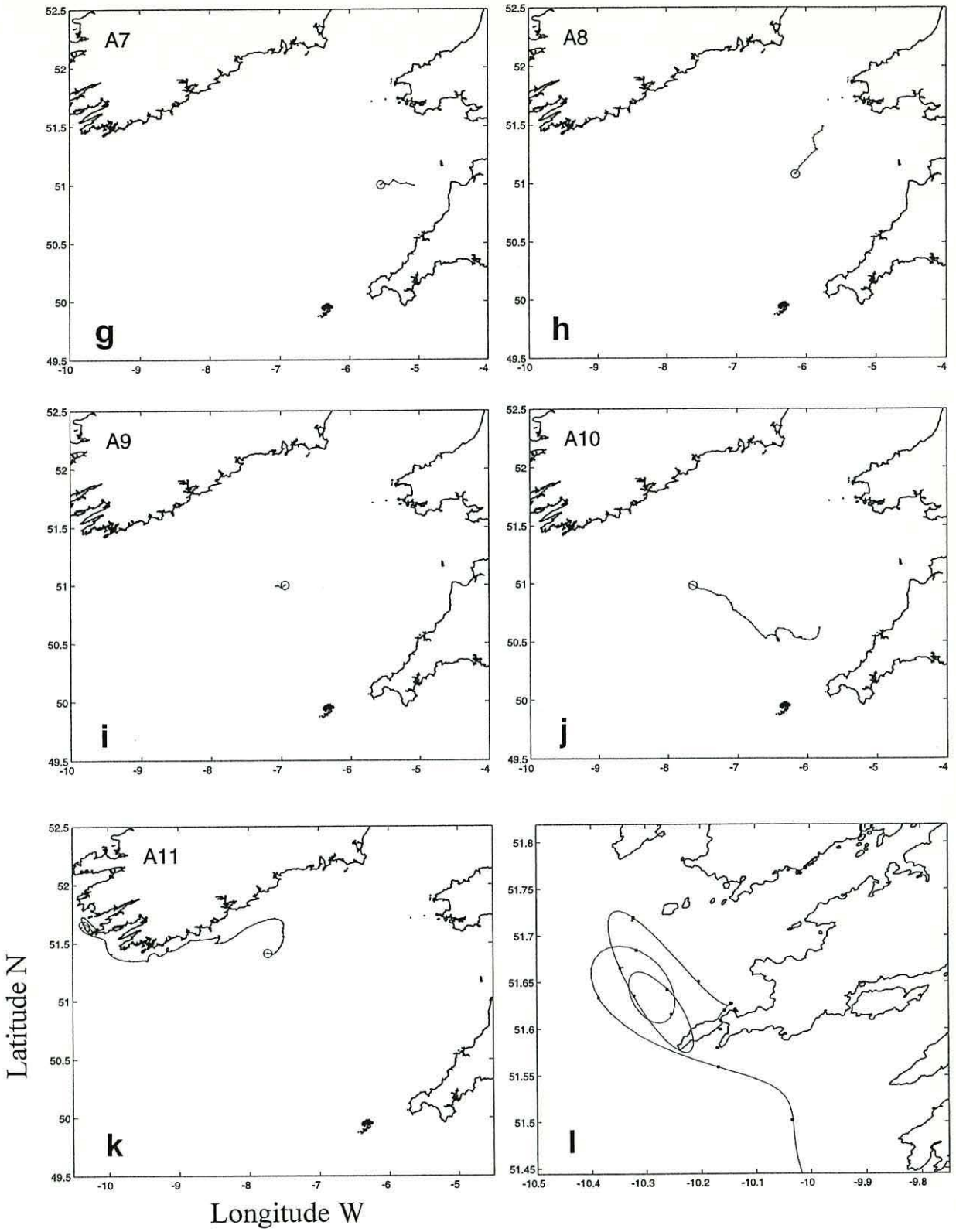

Figure 5.3 Continued from previous page. A close-up of the eddy feature observed in drifter A11 is shown (bottom-right panel).

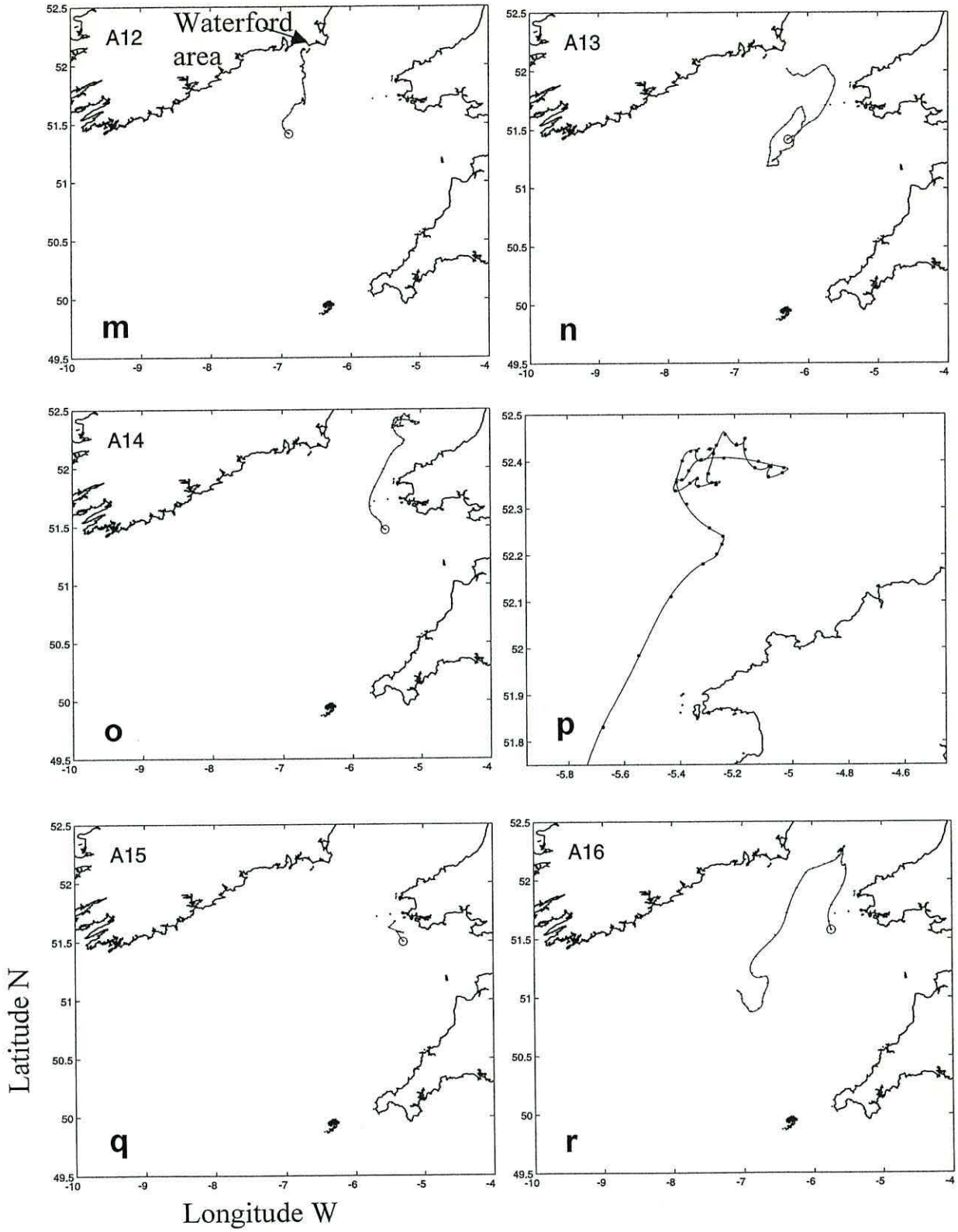

Figure 5.3 Continued from previous page. A close-up of the erratic behaviour observed in drifter A14 is shown (central-right panel).

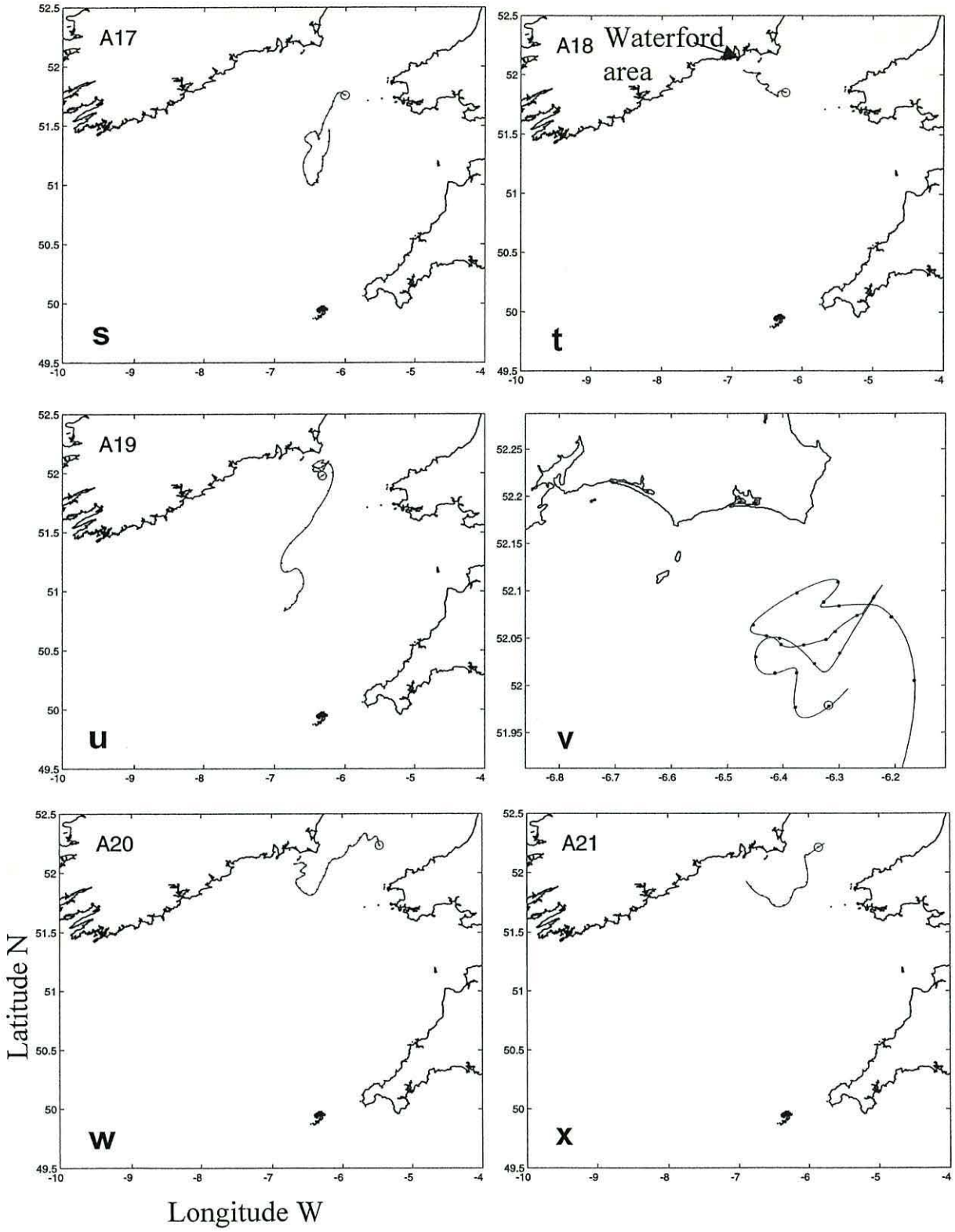

Figure 5.3 Continued from previous page. A close-up of the eddy feature observed in drifter A19 is shown (bottom-right panel).

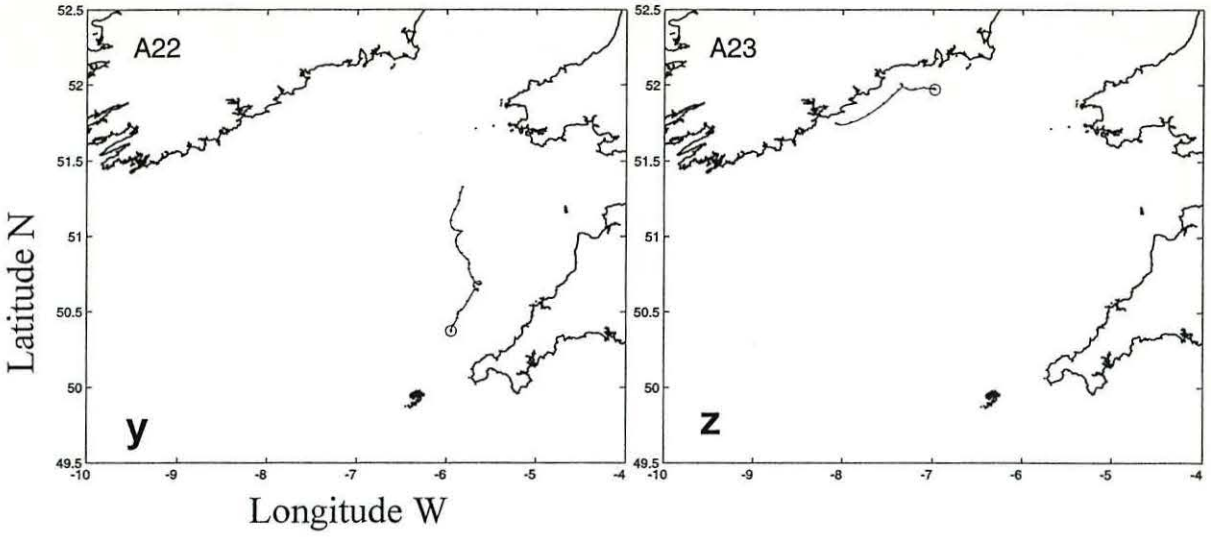

Figure 5.3 Continued from previous page.

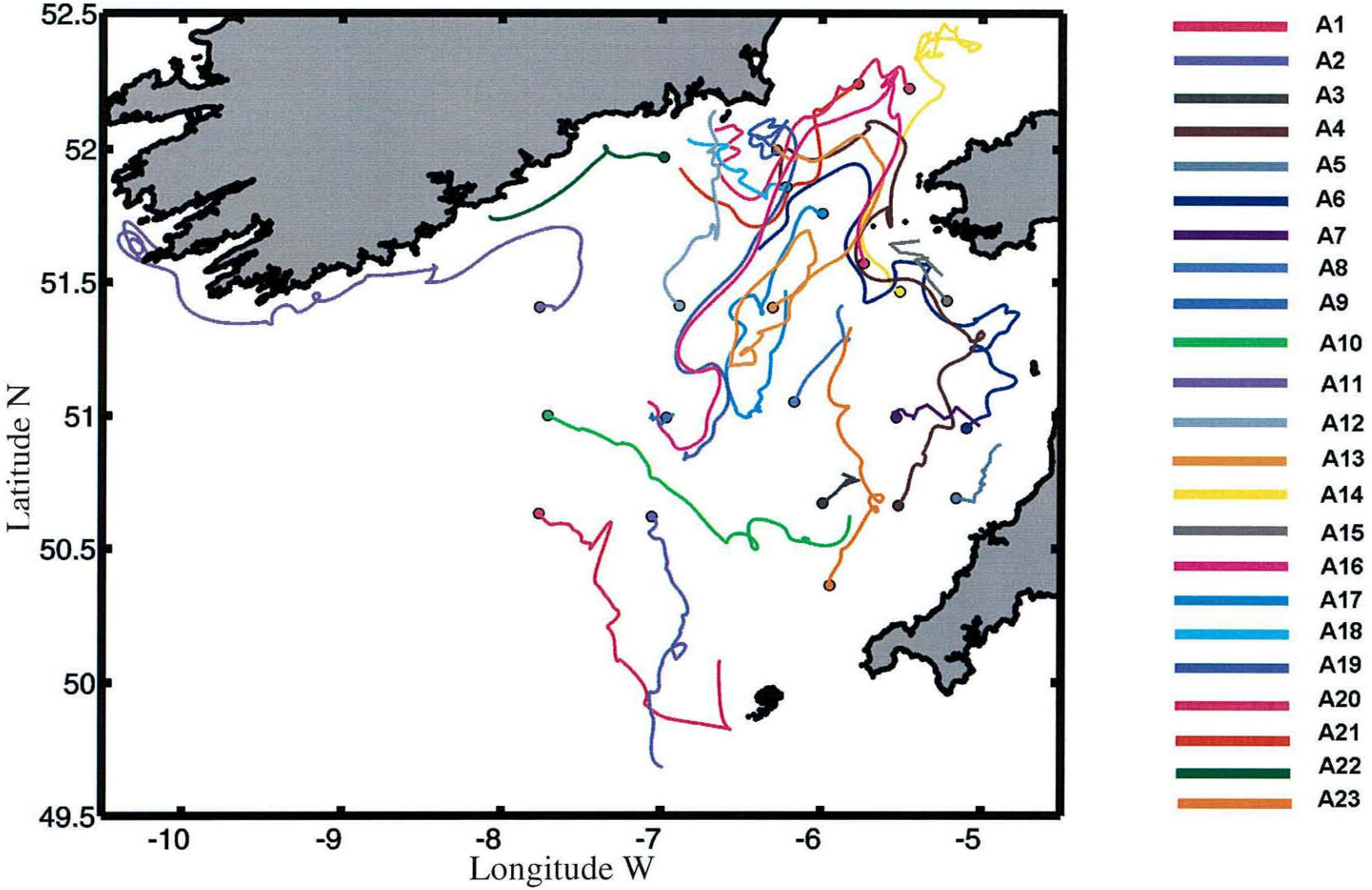

Figure 5.4 Spaghetti diagram showing the filtered trajectories of the 23 drifters deployed during summer 1998 in the Celtic Sea.

5.5 Analysis of the possible forcing mechanisms for the flow

5.5.1 Wind

The most obvious forcing that might be expected to influence the drifter trajectories is the wind. As shown in section 2.5, a uniform response to the local wind can be expected in the shelf area of the Celtic Sea (of ~ 30-120 m) because the wind field scale is generally larger than that of the Celtic Sea region (Thompson and Pugh, 1986; Davies and Jones, 1992a). However, a simple inspection of the difference in the shape of the trajectories suggests the wind field was not the direct forcing mechanism. In order to investigate whether the drifter trajectories were governed by the wind, hourly wind information during the observation period was obtained from the UK Meteorological Office from the St. Mary's Saws station located on the Isles of Scilly. Figure 5.5 shows the wind vector diagram after applying a 72-hour low-passed filter to hourly values to eliminate diurnal and higher frequencies. The 72-hour filter is a good compromise between maximizing the sharpness of the cut-off at frequencies just below the diurnal band and minimizing the loss of data at the beginning and end of each record (Pugh, 1987), although the latter was not a problem in the record. In general, wind was variable with mean speeds < 7 m s^{-1} and maximum up to 11.5 m s^{-1}. Winds from the south were more frequent and stronger than the northerly winds. Assuming that a constant wind of 10 m s^{-1} is blowing in the area, a broad estimation of the surface current driven gives us a value of 0.14 m s^{-1}, which is considerable. In addition, little deflection of the surface drift with respect to the wind can be expected (between 0-13.2 degrees) (Brown, 1991). However, the speed of some drifters was twice of that calculated value; also, some drifters travelled against the local wind, which was not constant in strength and direction. Nevertheless, in order to estimate quantitatively the wind influence over the drifter trajectories, a complex regression between the wind and the drifter velocities can be applied using a similar procedure as Prandle and Matthews (1990) and by Souza *et al.* (1997).

Expressing the non-tidal drifter velocities as a scaled and rotated function of the wind velocity together with a steady non-wind-driven component, *i.e.*,

$$U_{nt}(t)-U_o=aW(t)$$

where $U_{nt} = u_{nt} + iv_{nt}$ is the total non-tidal velocity, $U_o = u_o + iv_o$ is the steady non-wind-forced residual and $a=|a|e^{-i\theta}$ is a complex coefficient with scaling factor $A=|a|$ and veering angle θ of the current relative to the wind and $W=W_x + iW_y$ is the wind velocity.

The values of the non-wind-driven residuals and the a-coefficients were calculated by a complex least squares regression of the wind and current velocities. Results obtained are presented in Table 5.2. In general, low correlation was found with negligible values of the scaling factor. The most outstanding scaling factors were obtained in A8 and A16 with 0.11 and 0.17 m s^{-1} respectively, however, the values of the correlation coefficients were <1 % and 6.5 %. The highest correlation coefficient values were 36 and 33 % (A5 and A21), however the value of the scaling factor was less than 0.01 m s^{-1} and 0.02 m s^{-1}. Therefore, we can say with some confidence that local wind was not responsible for the Lagrangian circulation observed.

The possibility that the observed Lagrangian circulation was due to a non-local wind forcing can be discarded, since no strong storm event was registered during the drifters lifetime. In any event (from the North Sea or from the Irish Sea as explored by Thompson and Pugh (1986), see section 2.5), the expected pattern of flow does not correspond to that observed from drifters which was a cyclonic pattern of circulation with stronger currents.

Table 5.2 Results from complex regression between wind and drifter velocities. A is the scaling factor, θ is the veering angle of the current relative to the wind, u_o and v_o are the u- and v- mean velocity component, and R^2 is the correlation coefficient.

Drifter ID	A	θ	u_o	v_o	R^2
A1	0.027	163.037	0.034	-0.017	2.995
A2	0.015	89.464	0.002	-0.028	5.549
A3	0.048	-31.932	0.009	0.015	2.570
A4	0.066	-65.622	-0.020	0.032	6.649
A5	0.007	-57.615	0.025	0.036	36.398
A6	0.028	-76.672	-0.035	0.018	1.068
A7	0.004	-80.028	0.088	-0.001	1.630
A8	0.110	-80.878	0.023	0.031	0.048
A9	0.004	-67.365	-0.056	-0.004	5.961
A10	0.022	99.725	0.063	-0.013	7.257
A11	0.070	132.820	-0.054	0.005	0.254
A12	0.025	71.126	0.007	0.020	10.892
A13	0.051	-123.475	0.000	0.016	6.942
A14	0.052	-108.168	0.006	0.026	1.276
A15	0.005	-48.723	-0.002	0.078	11.971
A16	0.174	-146.687	-0.040	-0.016	6.506
A17	0.007	-137.769	-0.006	-0.008	2.842
A18	0.033	-62.751	-0.013	0.008	0.335
A19	0.012	-164.190	-0.015	-0.033	3.915
A20	0.042	145.968	-0.044	-0.006	2.250
A21	0.020	71.492	-0.096	-0.033	33.168
A22	0.022	24.645	0.005	0.041	17.313
A23	0.039	134.531	-0.094	-0.019	21.512

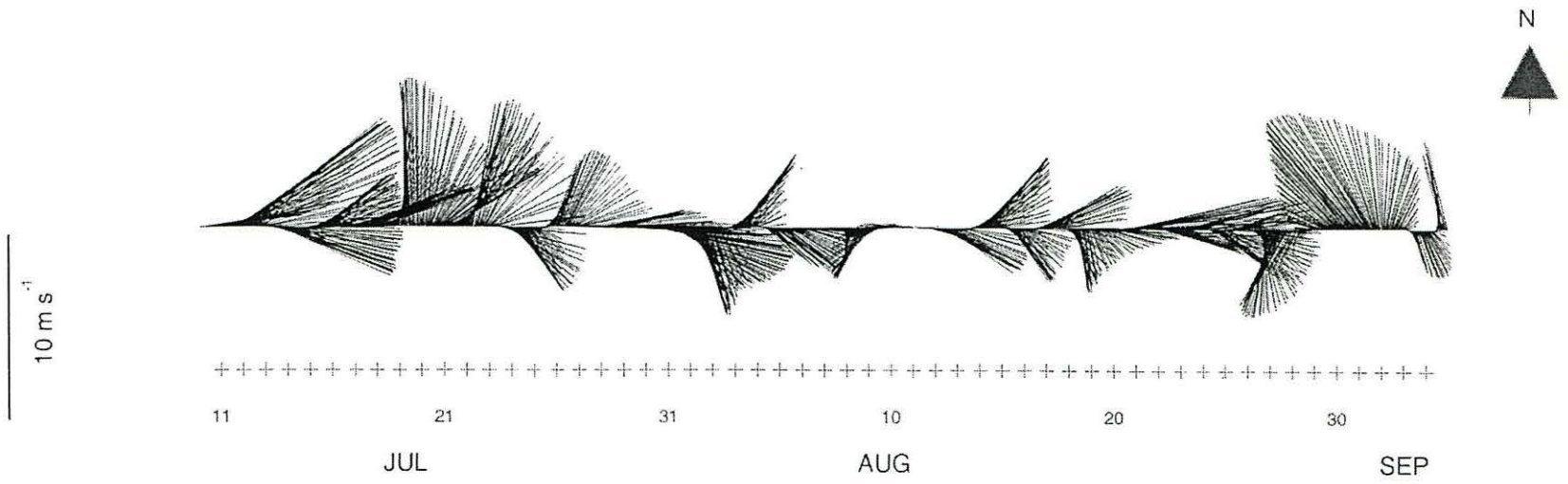

Figure 5.5 Low-passed filtered hourly wind vectors during summer 1998 in the Celtic Sea from the St. Mary's Saws station located in Isle of Scilly (data provided by UK Meteorological Office).

5.5.2 Tides

The total Lagrangian flow (*i.e.* movement of a particle originating at a point) is the sum of the Eulerian residual flow (the mean velocity measured at a fixed point) plus the movement of a particle due to its interaction with the time varying, space varying (mostly tidal) flow field (Longuet-Higgins, 1969). Thus, the tidal Lagrangian velocity is given by:

$$u_L = u_E + u_s \qquad 5.1$$

where u_L is the Lagrangian velocity, u_E is the Eulerian velocity at a point and u_s is the Stokes drift velocity due to the passage of the tidal wave known as Stokes drift (Longuet-Higgins, 1969). At any given point x, u_s can be obtained from:

$$u_s = < \int u_E dt \frac{\partial u_E}{\partial x} > \qquad 5.2$$

(Longuet-Higgins, 1969) where $u_E(x,t)$ is the Eulerian velocity at the point x averaged over a tidal cycle.

The influence of the tidal Eulerian flow and Stokes drift in the drifter trajectories is analyzed here.

When barotropic tidal currents interact with the irregularities of the basin geometry, *i.e.* irregular sidewalls (headlands) and changes in the bottom topography (such as sand banks and bottom slope), over a tidal cycle, they can generate Eulerian residual currents due to the nonlinear effect of friction, rotation and/or advection (Huthnance, 1973; Zimmerman, 1978; Loder, 1980). The case of the interaction of tidal currents with bottom topography, is called tidal rectification (Loder, 1980). The most outstanding topographic features are the Celtic Deep and Nymphe Bank, and in the latter, tidal currents were observed to be weak (section 2.2). Therefore, tidal rectification cannot be expected in the Celtic Sea, at least at the spatial scale of the circulation pattern portrayed by the drifters. Moreover, numerical models do not predict significant tidally induced Eulerian residual currents in the shelf area of the Celtic Sea (in general < 0.02 m s^{-1}; Prandle, 1984). Considerable tidal residuals can only be expected around the headlands of the St. George's Channel, where strong tidal currents are observed (> 1.5 m s^{-1}) (Fig 5.6a). In particular, due to the vorticity generated by the headland with the oscillatory tidal currents, transient eddy features can be expected (Zimmerman, 1978; Signell and Geyer, 1991). The

determination of the magnitude of these tidal residuals is out of the scope of our limited data. However, a qualitative comparison is made. Eddy formation has been observed at the Saint David's Head every tidal cycle, in a high resolution (1 km) tidal numerical model developed by Elliott and Jones (2000); an example is presented in Figure 5.6. Thus, similar structures might be occurring at the opposite headland (Irish coast). This might be the cause of the eddy-like feature observed in drifter A19 during the first 20 days since its deployment (see Fig 5.3v). However, more studies related to the eddy generated by tidal currents in the headlands area of the St. George's Channel need to be undertaken in order to examine the evolution of these eddies and the possible interaction with the frontal areas and so their effect on the overall circulation.

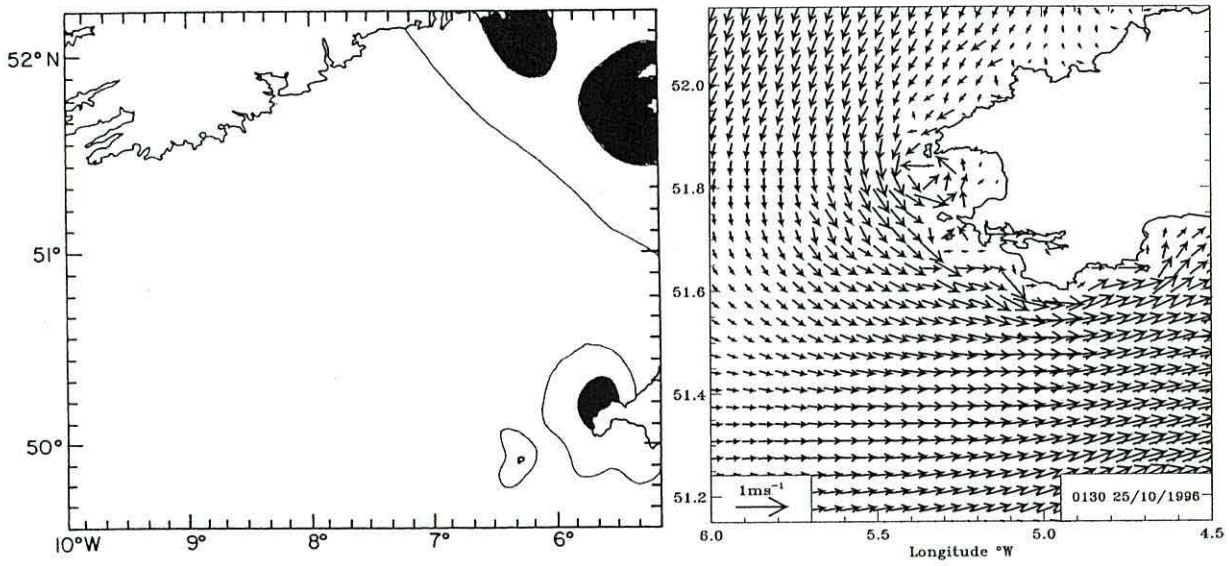

Figure 5.6 a) zones with high tidal currents (> 1.5 m s^{-1}) in the Celtic Sea and b) Model simulation of the tidal currents around Saint David's Head showing a eddy-like feature generated every tidal cycle from model of Elliott and Jones (2000). Model resolution of 1km.

From Eq. 5.1, it follows that when the Eulerian mean is zero, the Lagrangian mean may in general not be zero, *i.e.* a contribution to the Lagrangian velocity can be expected due to the net flow in the direction of the tidal wave *i.e.* Stokes drift (Longuet-Higgins, 1969). Thus, even when the Eulerian velocities are negligible over most of the Celtic Sea area (*i.e.* tidal residuals < 0.02 m s^{-1}), a contribution to the Lagrangian velocity can be

expected due to the Stokes Drift in the direction of the surface tidal wave. The Stokes drift velocity can alternatively be estimated as $u_s = U^2/2c$ (Longuet-Higgins, 1969) where U is the tidal current amplitude and c is the phase speed of a long progressive wave given by $c = \sqrt{gh}$ where g is gravitational acceleration and h is the water depth (Zimmerman, 1979). The Celtic Sea presents a variety of tidal regimes with tidal currents oscillate between 0.3-1.2 m s^{-1}. Taking mean tidal values of U = 0.5 m s^{-1} and c = 20 m s^{-1} (for a mean water depth of 40 m) gives values of u_s less than 0.01 m s^{-1}. Even when U takes values of the maximum tidal current velocity of 1.2 m s^{-1} (*e.g.* near the St. George's Channel) and using the same value of c = 20 m s^{-1}, the u_s is only as much as 0.04 m s^{-1}. These velocities are far smaller than the observed drifter velocities. Therefore, this forcing mechanism is discarded as a principal driver of the measured circulation.

5.5.3 Density gradients

The remaining forcing is the horizontal density gradients which, from the results presented in chapter 4, seem to be the most likely candidate to drive the observed circulation.

A comparison of the drifter tracks with the potential energy anomaly Φ distribution (*i.e.* with the stratification field) is presented in Figure 5.7. In general, drifters consistently travelled following the Φ contours, particularly, in the frontal areas. They only exhibited unusual tracks when they passed weak frontal areas or passed through vertically mixed areas. The shape of the frontal area in the St. George's Channel was described by trajectories of drifters that passed through the area. However, there was one drifter A14 (Fig 5.7) that did not follow the same path as the other 9 drifters and left the St. George's Channel to enter the Irish Sea. Once this drifter was in the vertically well mixed area its track became erratic and it stayed at approximately the same latitude for 36 days (Fig 5.3p shows a close-up of its trajectory). Another drifter A16 (Fig 5.7) stayed about 10 days in the mixed area around the central and northern area of the St. George's Channel. However, it did not leave the cyclonic path, probably due to the fact that it was near the area of frontal influence and was integrated to the St. George's Channel path. The complete and partial circuits observed in the drifters at the central Celtic Sea (drifters A13 and A17) partly following the contours of maximum stratification. However, not all the drifters that passed the central Celtic Sea followed the same pattern. It seems that horizontal gradients are not strong enough to *trap* all the drifters that pass near this area. Apparently, two

drifters (A16 and A16) were brought to the central area by a jet-like feature (see later). There were some drifters that crossed frontal areas. An example is the unusual path of the drifter A12 from the central Celtic Sea going to the Waterford area. For these few drifters an explanation for their behavior cannot be given solely in terms of density gradients.

A clearer qualitative picture of the density gradients, as the driver of the surface observed circulation, emerges when the drifter tracks are compared with the bottom density distribution (Fig 5.8). Clear agreement between the drifter tracks and the bottom density distribution, in particular with the location of the bottom fronts, was observed. As mentioned before, the St. George's Channel was the area where drifters tended to converge defining a cyclonic flow path, a location which corresponds with the strongest bottom density gradients. Figure 5.9 shows drifter trajectories superimposed on contours of surface density distribution. The agreement was good but not as close as with the bottom density distribution. However, some of the drifter tracks that crossed the bottom isopycnals in Figure 5.8 and some others underwent a closed circuit similar to a cyclonic gyre at the centre of the Celtic Sea, even when the bottom density contours were not closed. These drifters more likely followed the surface density distribution (Fig 5.9), which indicates whether some of the surface circulation is not directly correlated with the bottom density field (*i.e.* see drifter track of A12 ; Fig 5.8) or that small variability in the surface circulation existed in the Celtic Sea. In addition, the surface density distribution (Fig 5.9) showed an intrusion of heavier and cold surface water from the Irish Sea in comparison with the relatively lighter and warmer surface water of the Celtic Sea. This intrusion was captured by two drifters, which showed jet-like characteristics. This intrusion can be observed in Sea Surface Temperature (SST) satellite images. For example, Figure 5.10 shows one of these two drifter trajectories overlaid on SST during summer of 1998. Notably, the correspondence is close as the drifter followed the contours of the thermal front, including the track of an anticyclonic eddy-like feature in the southern limit of the drifter trajectory contrary to the overall pattern of bottom density in the central Celtic Sea (see Fig 5.8).

Although some spatial and temporal variability in the surface circulation and surface density field was certainly exhibited by the trajectory of the drifters, bottom density fronts seem (to first order) to be responsible for most of the surface Lagrangian circulation observed. However, in order to clarify the relation between bottom and surface circulation, a closer quantitative comparison is made in the next section.

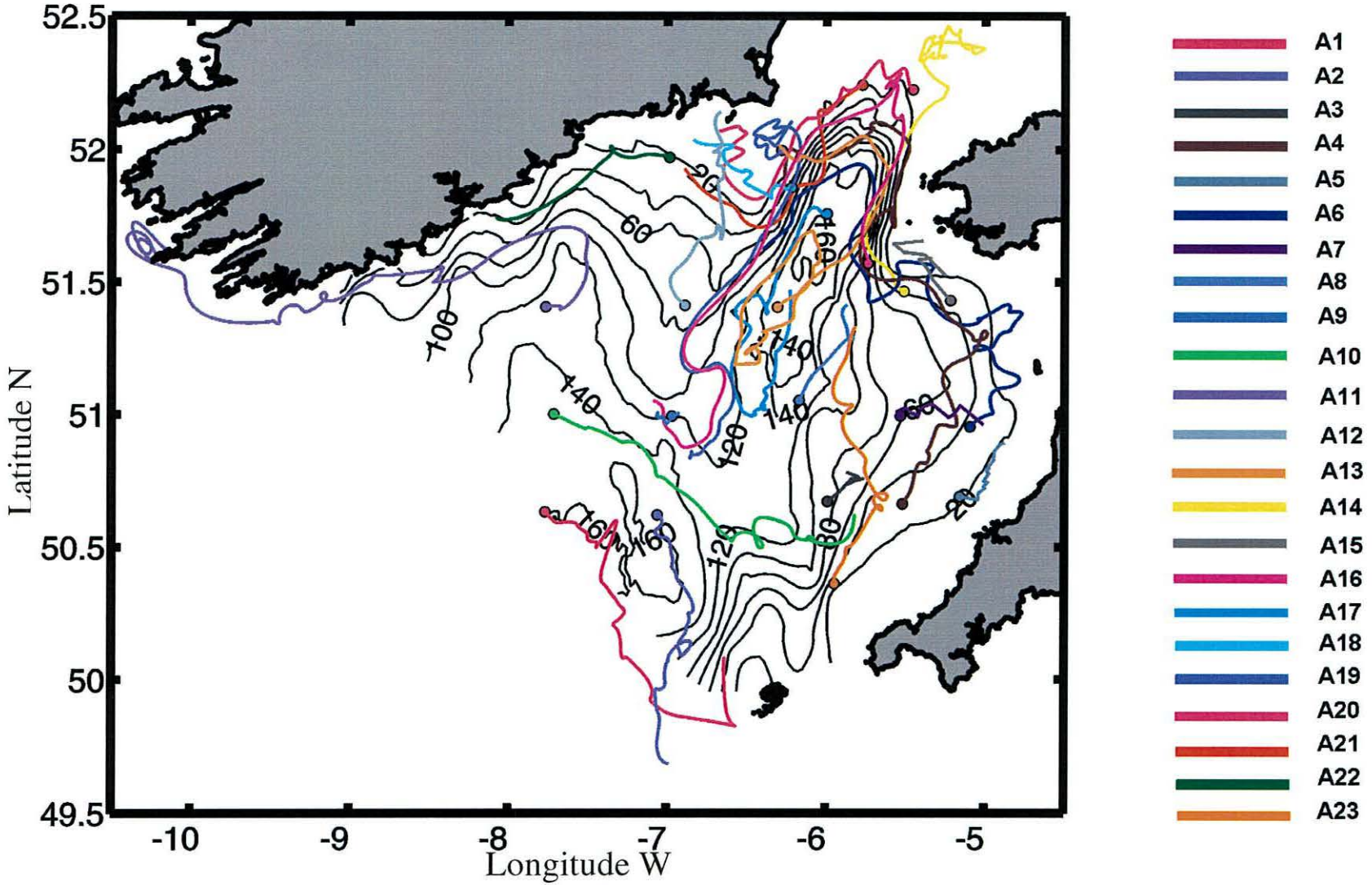

Figure 5.7 Drifter trajectories overlaid on the spatial distribution of potential energy anomaly (contours in J m^{-3}) during summer 1998 in the Celtic Sea. Drifter ID and corresponding colour are shown on the right.

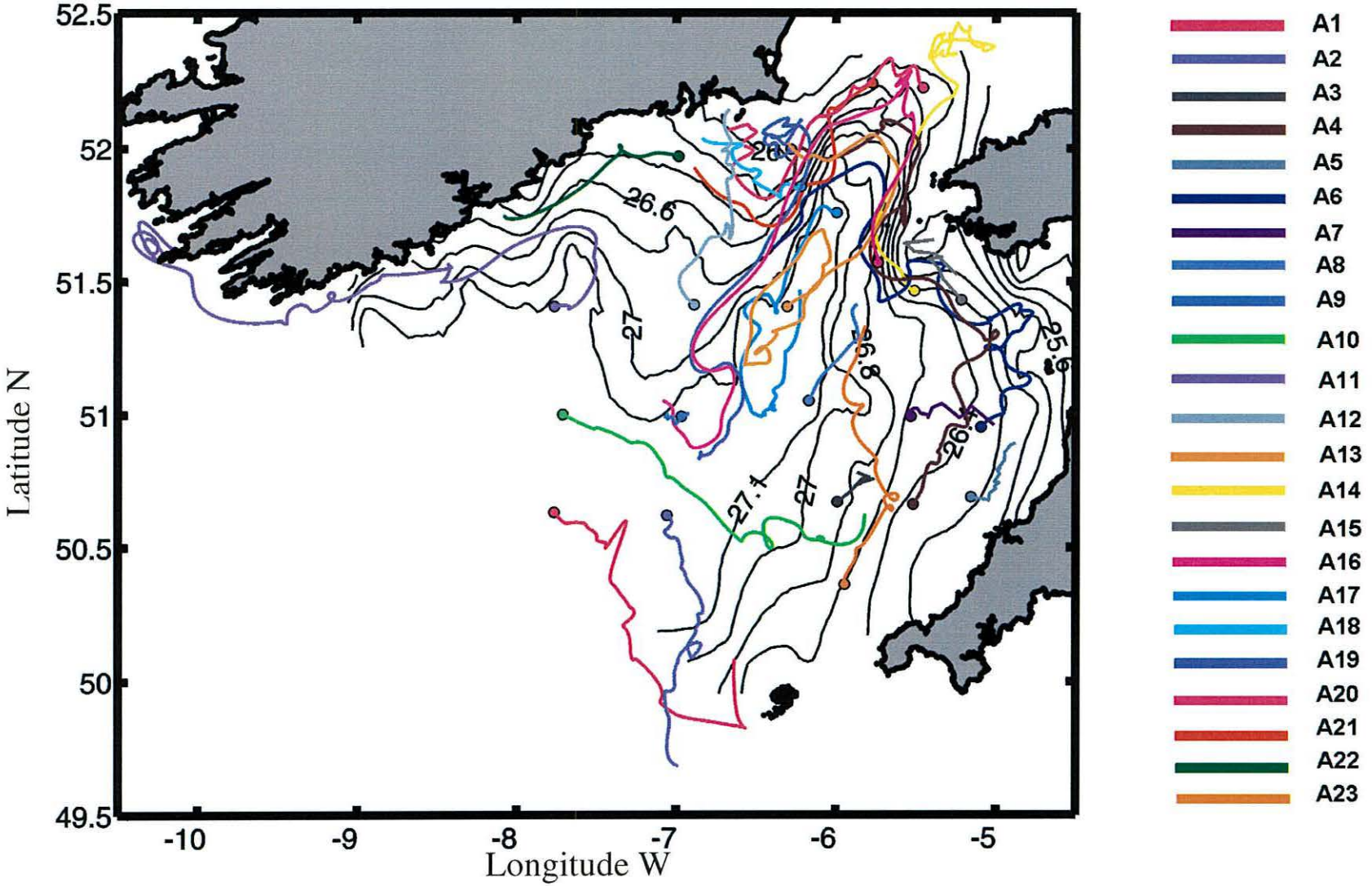

Figure 5.8 Bottom density distribution and drifter trajectories during summer 1998 in the Celtic Sea. Drifter ID and corresponding colour are shown on the right.

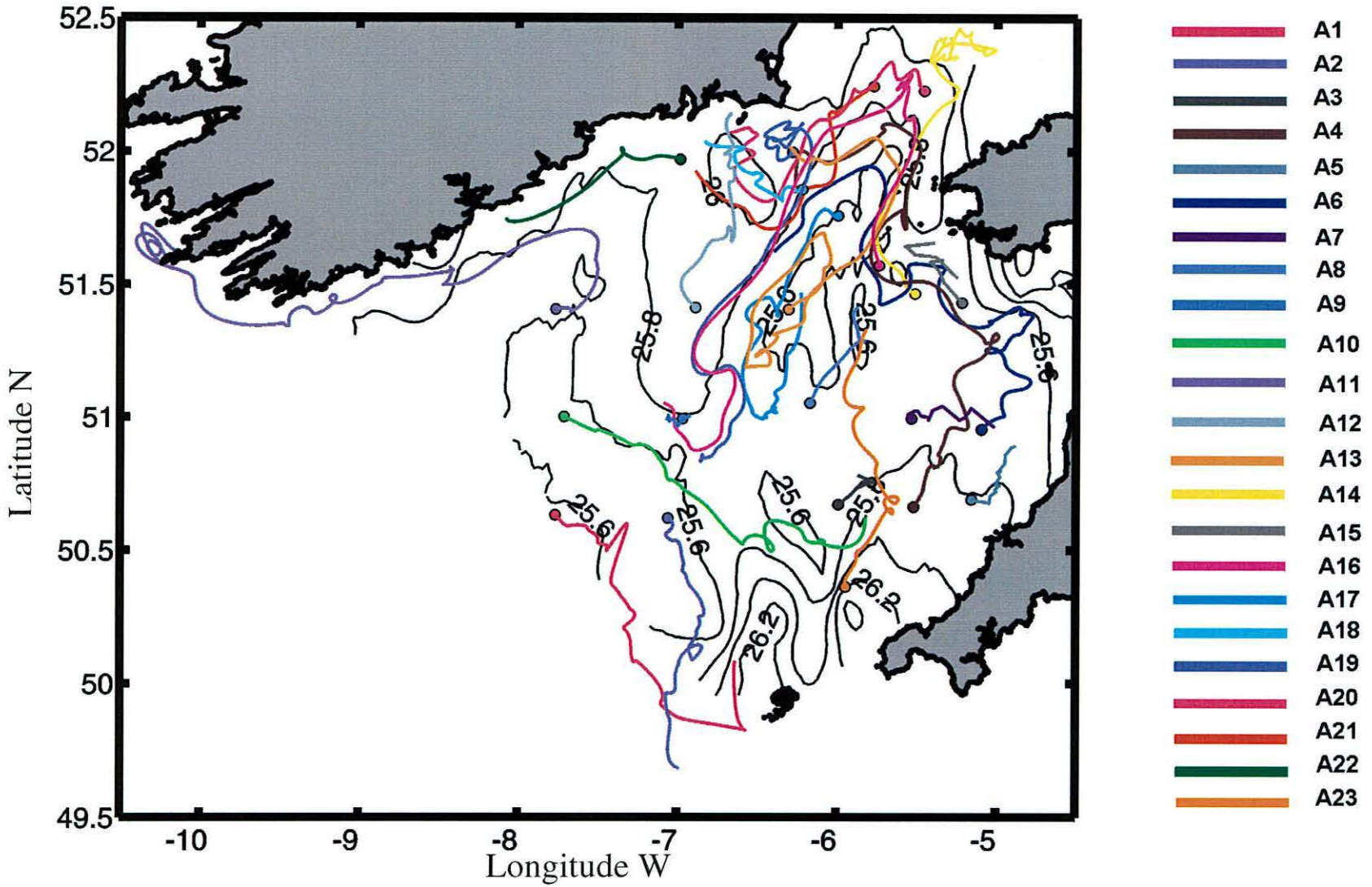

Figure 5.9 Surface density distribution and drifter's trajectories during summer 1998 in the Celtic Sea. Drifter ID and corresponding colour are shown on the right.

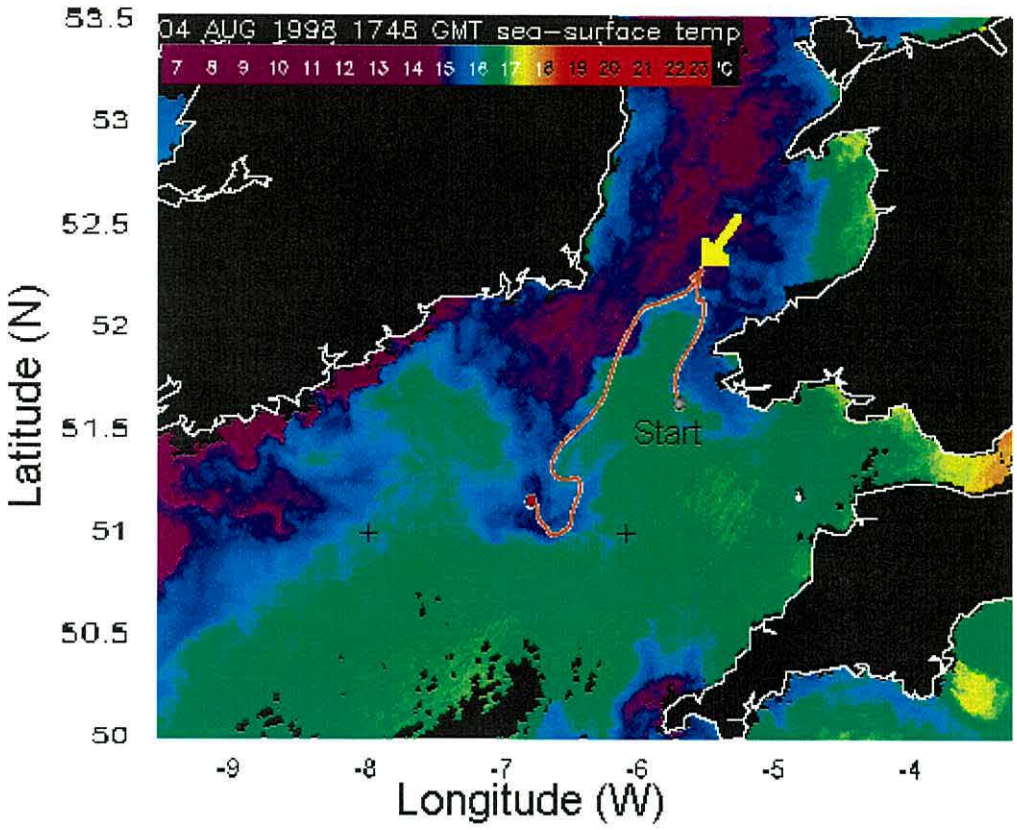

Figure 5.10 Drifter trajectory of drifter A16 overlaid in a SST image corresponding to 4 August 1998. Yellow arrow indicates the position of the drifter at the time of the image was captured.

5.6 Comparison of the quasi-Eulerian velocity field from drifter observations and calculated geostrophic velocities

A further indication of the bottom fronts as underlying the forcing mechanism of the surface circulation from drifter observations can be obtained when a direct comparison between the magnitude of the drifter velocities and the calculated geostrophic velocities is performed. Such comparison was carried out as follows. Using all the drifters, the drift velocity component normal to a section was estimated when one crossed a transverse section of the cruise CORY998. Then, the corresponding calculated geostrophic velocities (normal to the section) were extracted. The results are shown in Table 5.3; positive values denote an approximately northward flow (eastward flow in the North-South sections 202, 190 and 223). A good agreement in magnitude and direction between both drifter velocities and geostrophic calculations was observed. This consistency is not true for the larger legs 180 and 178, which were located near the southern entrance of the Celtic Sea (see Fig 3.2 for location) with more oceanic conditions. In general, they differed in magnitude with a standard deviation of ± 9 cm s^{-1}. A scatter plot of the values from drifters and from geostrophic calculations (Fig 5.11) helps to visualize the comparison of the values, shown in Table 5.3. The scatter plot revealed a roughly rectilinear relationship between the drifter velocities and geostrophic calculations (Fig 5.11). The best linear fit to the data was obtained from linear regression values of $a = 0.6330$ and $b = 0.4484$, for $y = ax + b$ (Fig 5.11). In general, a positive correlation between both drifter velocities and geostrophic calculations with a modest correlation coefficient value of 0.71.

Consistency in the predicted calculated geostrophic velocities in relatively strong bottom frontal areas is clearly illustrated in Fig 5.12, which shows a section across the St. George's Channel indicating where the drifters passed through it. Even when the transect was not contemporaneous with the crossing of the drifters, it is remarkable how they agree with the position and depth of the core of jets derived by geostrophic calculations and associated with bottom density fronts (Fig 5.12). This is consistent, however with the expectation that the location of bottom fronts will be relatively stable over time (as demonstrated in chapter 1). A perfect match cannot be expected, since the geostrophic calculations were normal to the cross-section and the maximum velocities could be underestimated because the strongest density horizontal gradients are slightly oblique to the section. In addition, drifters are merely *snapshots* of the circulation and some

variability could be included in their trajectories or in the density field when they passed through the section, thus this comparison can only be used in a qualitatively way.

In order to obtain a more suitable presentation of the Lagrangian field that allows us to make comparisons with other estimated velocity fields, *i.e.* the surface geostrophic velocities, a map of the quasi-Eulerian circulation was constructed from the filtered drifter velocities. Thus, residual velocity components were assigned to a grid of ~ 4 km (1/28° of latitude by 1/28° of longitude) and averaged. Figure 5.13 shows the resulting vector plot of the mean velocities representing the 1/28° x 1/28° box averages. Although spatial data is sparse, a cyclonic pattern of the circulation can still be seen. Comparisons with the geostrophic calculations obtained in chapter 4 (see Fig 4.21) shows a good agreement between the few drifter velocities and the geostrophic calculations. In particular, there was a good match in the St. George's Channel. The agreement is qualitative only; in some areas, the surface geostrophic velocities were weaker (~ 50%) than drifter velocities. However as mentioned before, drifter velocities are only a snapshot and some variability at the flow is likely to be present.

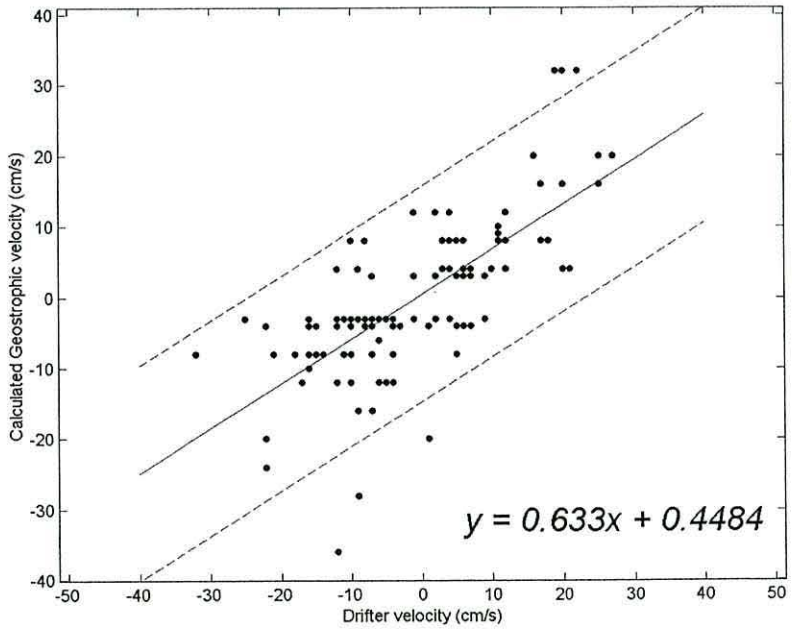

Figure 5.11 Scatter plot showing calculated geostrophic velocities versus drifter velocities from values in Table 5.3. A regression line is shown (values of the regression analysis are presented in the right-bottom corner of the plot). Dashed lines represent the 95% confidence zone.

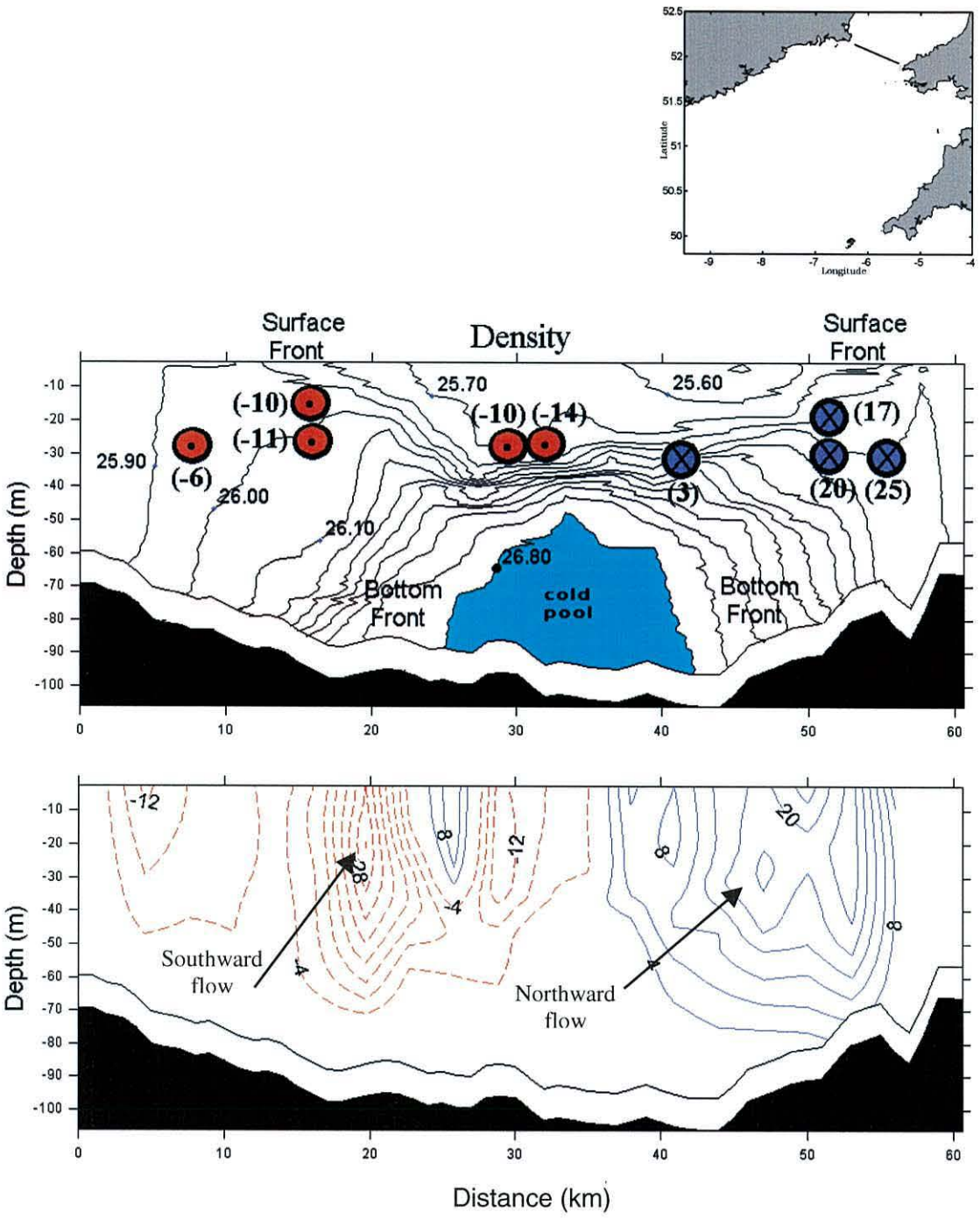

Figure 5.12 Cross-section at the Saint George's Channel corresponding to leg 209 CORY998 showing: the vertical structure of density, geostrophic velocities (cm s^{-1}) and drifter position where the drifters crossed the section (denoted by the symbols ⊗ and ⊙, into and out the page respectively). All drifters were drogued at 30 m depth, dual symbols represent multiple crossing. Number into parenthesis represents the drifter velocity normal to the section in cm s^{-1}. Position of the cross-section is shown in the right-corner panel.

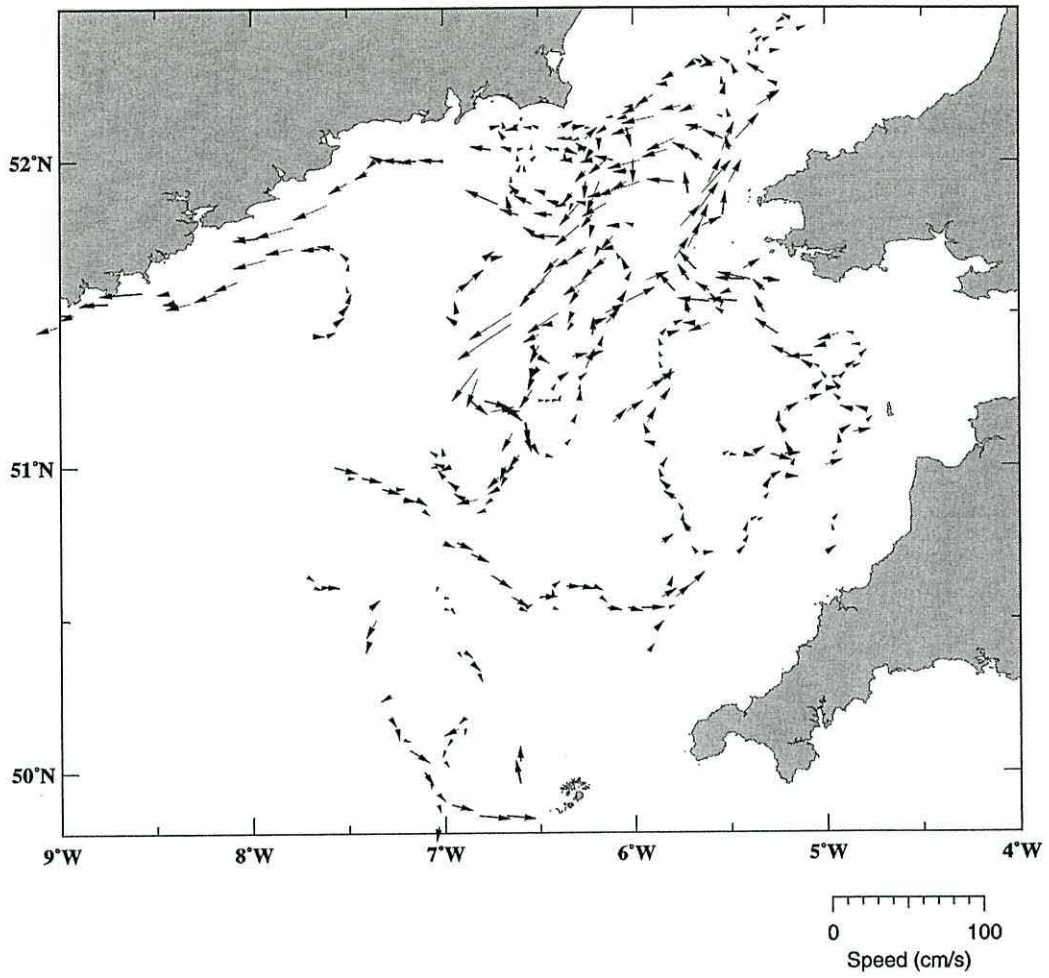

Figure 5.13 Quasi-Eulerian field obtained from drifter velocities averaged in 1/28° longitude x 1/28° latitude boxes.

Table 5.3 Comparison of drifter and calculated geostrophic velocities. The velocities represent the component normal to the section at 30 m depth obtained from the drifter velocity when crossing the transverse section for cruise CORY998. The estimated geostrophic velocity at the same position of the drifter is shown. Time difference in days between drifter crossing the section in comparison with geostrophic velocities is given.

Leg Number	Drifter ID	Drifter Velocity (cm s^{-1})	Geostrophic Velocity (cm s^{-1})	Time difference (days)	Position: Longitude (°W)-Latitude (°N)	
202	A13	-5	-3	40	-6.08	51.69
	A17	-5	-3	45	-6.03	51.76
	A6	-17	- 12	6	-5.89	51.92
	A4	-22	-24	3	-5.82	52.02
	A13	-12	-12	8	-5.80	52.05
	A16	-7	-16	23	-5.71	52.15
	A20	-7	-8	44	-5.61	52.27
	A13	-1	-3	20	-6.38	51.31
190	A10	6	-4	40	-7.11	50.83
	A16	-7	-4	10	-6.95	50.92
	A16	8	8	4	-6.64	51.12
	A19	11	9	11	-6.60	51.15
	A17	11	10	20	-6.60	51.15
	A13	2	12	22	-6.52	51.19
	A13	-4	-3	28	-6.44	51.25
179	A11	-16	-10	13	-9.01	51.45
178	A11	-15	-8	24	-8.31	51.52
	A10	9	3	42	-7.68	50.99
	A2	1	-20	28	-6.92	50.36
180	A23	-6	-3	37	-7.83	51.77
	A11	-16	-3	30	-7.74	51.70
	A11	5	-4	38	-7.52	51.52
	A16	-10	8	4	-6.74	50.92
	A19	-8	8	3	-6.72	50.90
	A10	6	3	18	-6.35	50.61
181	NONE					
182	A23	-4	-3	34	-7.32	51.98
	A12	11	8	41	-6.86	51.61
	A19	-14	-8	13	-6.70	51.46
	A16	-4	-12	12	-6.66	51.44
	A13	-6	-12	31	-6.53	51.33
	A17	-8	-3	20	-6.49	51.30
	A13	9	-3	18	-6.44	51.26
	A17	5	-8	1	-6.33	51.16
	A3	2	3	36	-5.83	50.75
	A22	3	4	27	-5.70	50.64

Table 5.3 Continued.

Leg Number	Drifter ID	Drifter Velocity (cm s^{-1})	Geostrophic Velocity (cm s^{-1})	Time difference (days)	Position: Longitude (°W)-Latitude (°N)	
186	A18	-9	-3	25	-6.72	52.02
	A20	4	-3	20	-6.63	51.95
	A20	-8	-3	23	-6.45	51.81
	A16	-1	-3	14	-6.35	51.74
	A19	-25	-3	17	-6.34	51.73
	A21	-11	-3	35	-6.34	51.72
	A6	-12	-4	1	-6.28	51.69
	A17	-4	-4	38	-6.22	51.64
	A13	-18	-8	36	-6.21	51.63
	A13	4	8	42	-6.08	51.53
	A13	21	4	22	-6.07	51.52
	A8	-12	4	32	-5.90	51.40
	A12	2	-3	38	-6.68	51.97
187	A4	6	8	20	-5.19	51.35
	A6	12	8	19	-5.19	51.35
	A6	-1	12	21	-5.05	51.35
	A6	4	12	28	-4.82	51.35
189	A17	5	-4	2	-6.26	51.29
	A8	10	4	42	-5.95	51.23
	A22	9	-3	12	-5.88	51.23
	A4	6	4	30	-5.27	51.12
	A6	7	4	43	-4.96	51.07
209	A20	-6	-6	33	-6.15	52.11
	A16	-10	-8	21	-6.04	52.08
	A21	-11	-8	45	-6.04	52.08
	A13	-10	-12	7	-5.85	52.03
	A13	3	8	10	-5.69	51.99
	A4	-14	-8	4	-5.82	52.02
	A4	17	8	11	-5.56	51.96
	A16	20	16	43	-5.56	51.96
	A14	25	16	44	-5.51	51.95
210	A14	20	4	44	-5.29	52.19
	A20	-3	-4	43	-5.74	52.29
	A16	-1	3	38	-5.56	52.25
211	A20	-10	-3	38	-5.95	52.17
	A21	-12	-3	49	-5.96	52.17
	A16	-7	-3	24	-5.80	52.14
	A16	4	4	43	-5.52	52.08
	A14	5	8	42	-5.48	52.07

Table 5.3 Continued.

Leg Number	Drifter ID	Drifter Velocity (cm s^{-1})	Geostrophic Velocity (cm s^{-1})	Time difference (days)	Position: Longitude (°W)-Latitude (°N)	
212	A19	-7	-4	24	-6.17	52.02
	A20	-9	4	32	-6.22	52.03
	A16	-22	-4	21	-6.15	52.01
	A16	27	20	45	-5.66	51.85
	A14	25	20	45	-5.66	51.85
	A21	-14	-8	45	-6.02	51.97
	A4	-16	-8	5	-6.01	51.97
	A13	-4	-8	7	-6.01	51.97
	A4	16	20	13	-5.57	51.82
	A13	25	20	13	-5.64	51.85
	A6	-5	-12	8	-5.89	51.93
	A6	12	4	9	-5.70	51.87
213	A19	-21	-8	24	-6.19	51.91
	A20	-10	-3	33	-6.28	51.95
	A4	-10	-4	3	-6.26	51.94
	A16	-32	-8	27	-6.23	51.92
	A21	-9	-28	44	-6.12	51.87
	A6	-22	-20	9	-6.09	51.86
	A6	17	16	11	-5.79	51.73
	A16	18	8	47	-5.77	51.72
	A4	19	32	20	-5.75	51.71
	A13	20	32	15	-5.75	51.71
	A14	22	32	47	-5.74	51.70
214	A17	-8	-4	3	-6.24	51.33
	A6	-16	-4	14	-5.74	51.50
	A4	-12	-36	22	-5.72	51.52
	A14	-9	-16	50	-5.62	51.55
	A15	-15	-4	48	-5.45	51.61
201	A17	6	8	0	-6.27	51.27
	A8	12	4	43	-6.05	51.17
	A22	12	4	15	-5.95	51.12
	A4	4	4	39	-5.36	50.86
	A5	7	3	47	-5.03	50.71
224	NONE					
223	A6	-12	–12	36	-4.85	51.41
	A6	7	3	48	-4.85	51.10
	A6	-5	3	46	-4.85	51.16
	A6	1	-4	31	-4.85	51.31

5.7 Summary of the main findings

The Lagrangian observations during the summer of 1998 showed a surface circulation in the Celtic Sea with a variety of spatial structures such as eddies, jets, preferred paths and convergence zones. Therefore, the Lagrangian observations in the Celtic Sea revealed a picture more complex than in other European shelf sea areas such as the Irish Sea and North Sea. In spite of this complexity, they primarily revealed a cyclonic circulation along with an intrusion of cold water from the Irish Sea to the central Celtic Sea with a jet-like characteristic.

An analysis was performed of the possible driving mechanisms of the observed circulation. The results of this analysis strongly suggest a density driven circulation associated with bottom fronts in most of the Celtic Sea. In addition, once the drifters reached strong bottom density frontal areas their velocities increased in magnitude to be comparable with that obtained by geostrophic calculations. However, there exists an intrinsic variability in the surface circulation and consequently in the surface density distribution. Eddy-like features were observed that seem to be the product of the baroclinic instability of the frontal areas and due to the interaction of tidal flows with headlands, to assess these dynamics, however, is out the scope of our data.

With few data in some areas (*i.e.* only one pass of the drifters) and considering that drifter trajectories cannot be taken as streamlines, the results cannot be completely conclusive. Still more direct measurements need to be conducted to give extra support to the theoretical approach of a surface circulation driven by bottom density fronts and to clarify the variability observed in the circulation. This additional information about the velocity field can be obtained from the ship-mounted ADCP measurements that covered most of the study area during the cruises (CORY798 and CORY998) providing a good spatial resolution both in the horizontal and in the vertical structure. The next chapter deals with these ADCP measurements.

Chapter 6

ADCP data analysis

6.1 Introduction

ADCP measurements can reveal low-frequency (subtidal) currents once the tidal signal is removed. In most of the northwest European shelf, tides account for 90% of the variability of measured currents (Howarth and Proctor, 1992). Since this "masking" of the subtidal signal by tidal currents severely limits the ability to interpret ADCP data, the removal of tidal currents (or detiding) from ADCP data is the main challenge. Any efficient method for filtering tidal currents from vessel-mounted ADCP data must take into account the spatial and temporal tidal variability, particularly in coastal regions where both tidal currents and spatial gradients can be large (Münchow, 2000).

One such approach is to obtain a map of the tidal constituents when enough moored observations are available in the surveyed area. However, this method still fails to describe tidal currents spatially in areas with considerable spatial tidal current changes (Münchow *et al.*, 1992). Another approach to detiding ship-mounted ADCP data consists of repeating the track over one or more tidal cycles obtaining a number of ADCP observations at specific locations (Fig 6.1a and b) (Geyer and Signell, 1990; Simpson *et al.*, 1990). Once that has been done, a harmonic analysis is applied to remove the tidal signal from fixed points along the repeated track. Although this method has been shown to obtain good results, it is an inefficient use of ship time if the only reason to repeat the survey track is to account for the tides, particularly if a large area is under study.

Another approach, originally proposed by Candela *et al.* (1992), allows a description of tidal and subtidal currents to be obtained from a single survey of an area (Fig 6.1c). This method is based on a spatial interpolation scheme using arbitrary functions (least square polynomials or biharmonic splines) to fit the ADCP data, in order to determine the horizontal spatial structure of the tidal and subtidal currents. In addition, this method also allows available nearby measured currents to be combined with the ADCP observations, improving the detiding analysis. Some improvements in the accuracy of the subtidal currents could be expected if a more dynamical approach is used in the spatial

base functions (Candela *et al.*, 1992). Additionally, Candela *et al.* (1992) only applied the method to depth-averaged tidal currents. To extend the detiding to a three-dimensional space requires inclusion of the vertical structure of tidal currents. This structure, for instance, is influenced by bottom friction causing the maximum tidal currents to occur earlier near the bottom than they do near the surface (Prandle 1982; Maas and van Haren, 1987). An attempt at this was made by Münchow *et al.* (1992) using first order polynomials to model the horizontal variations and Ekman layer solutions in the vertical. Although applied only to a single cross-section, Münchow *et al.* (1992) included the frictional dynamics in the vertical using an Ekman layer depth modified by an oscillatory current, which depends upon a vertical eddy viscosity (Maas and van Haren, 1987).

An extension of the method of Candela *et al.* (1992) to three dimensions has also been explored by Steger *et al.* (1998) using a large current meter data set (over 254,651 observations) and ADCP observations (over 450,129 observations) in the Gulf of Farallones, a continental shelf area off San Francisco. They prescribed the tidal velocity field as varying linearly in the horizontal and the depth as a variable in the tidal model to include the effects of baroclinic tides. Recently, Münchow (2000) also extended the spatial interpolation scheme to three spatial dimensions using biharmonic splines. This statistical method revealed consistent tidal velocity fields by fitting the functions to ADCP data obtained from repeated surveys of ship-mounted ADCP, mooring and surface current data and weighting the velocity data from different sources by their relative error. However, the vertical dimension was still unresolved and the inaccuracy in the vertical was estimated to be about 30% of the true signal (Münchow, 2000). As pointed out by Münchow (2000), some experimentation with tidal fields is necessary in order to obtain an accurate and stable solution. Whilst deciding the appropriate number of nodes and their position constitutes the main disadvantage of the method, its simple algebraic expression for predicting tidal currents in space and time is its main advantage (Münchow, 2000).

One of the most dynamically-based approaches for detiding ship-mounted ADCP data is predicting tidal currents from a hydrodynamic numerical model whose domain includes the region of measurements (fig 6.1d). However, its use is restricted to regions where the observed tidal currents are well simulated by an existing numerical model. Foreman and Freeland (1991) used a barotropic numerical model, in the region off British Columbia, Canada. This area, however, was strongly baroclinic which meant that it was difficult to obtain an accurate representation of tidal currents, even though they tried to

correct the tidal currents for baroclinicity in accordance with historical observations from stationary current meters in the region, with little success. Howarth and Proctor (1992) used a two-dimensional numerical tidal model in the North Sea and compared the results with depth-averaged currents calculated from ADCP observations from 14 cruises at monthly intervals. They found that the numerical model predicted velocities that were too high and for tidal comparison the spatial variation was more significant than temporal variations. They also contended that although the model was unbiased for elevations the same is not necessarily true for currents (Howarth and Proctor, 1992).

Some other dynamical approaches have addressed the problem of detiding ship-mounted ADCP data as an inverse problem. Dowd and Thompson (1996) obtained encouraging results by using the shallow water equations to create a simple barotropic tidal model and solving the boundary conditions by fitting the model to ADCP observations. Bogden and O'Donnell (1998) incorporated dynamics into statistical framework of minimum-variance estimation. A reduction of the model-data misfit was obtained by using interior dynamics and open-boundary conditions as weak constraints (Bogden and O'Donnell, 1998). However, the detiding inverse method was strictly two-dimensional.

In the case of the shelf sea area of the Celtic Sea, there were not enough moored observations to map the tidal current properties and our sampling strategy did not include repeated transects. Therefore, different techniques from (a) and (b) in Figure 6.1 were needed. With the advantages of the development of numerical tidal models on the European continental shelf sea area, in particular around the British Isles, it was possible to detide the ship-mounted ADCP data collected in the study area using the model POLPRED developed by the Proudman Oceanographic Laboratory. However, in addition to the numerical model, the method of Candela *et al.* (1992) was also used to explore the suitability of this detiding method in the Northwest European shelf seas. Thus, an attempt to describe the tidal and subtidal currents in the study area using this statistical method was done. However, both methods had limitations in representing the spatial variation of tides correctly. Consequently, a new approach for estimating more realistic tidal currents was considered. This method can be interpreted as the simplest form of oceanographic data assimilation, using a linear combination of data and results from a numerical model.

Since the aim of this chapter is concerned with the long-term, non-tidal circulation in the region, emphasis is placed on the residual currents derived from the ADCP observations. In addition, bottom-mounted ADCP data gives extra information about the temporal variability of the velocities measured. The chapter is organized as follows. Section 6.2 presents a brief description of the numerical model and its spatial domain from which the harmonic tidal constituents were obtained. Also, in this section, is provided the theoretical approach to detiding by the technique of least square and polynomial spatial interpolation. In the last part of this section, tidal results from these two conventional detiding techniques are presented and discussed. Section 6.3 introduces a new approach to detiding ship-mounted ADCP data, (called here the *blending* technique), derived from a blending scheme used in data assimilation. Meanwhile, section 6.4 deals with the residuals obtained after applying this detiding technique. Section 6.5 shows the results from the bottom-mounted ADCP data and a correlation of the residual velocities with the wind field is performed. Finally, section 6.6 summarizes the main findings of this chapter.

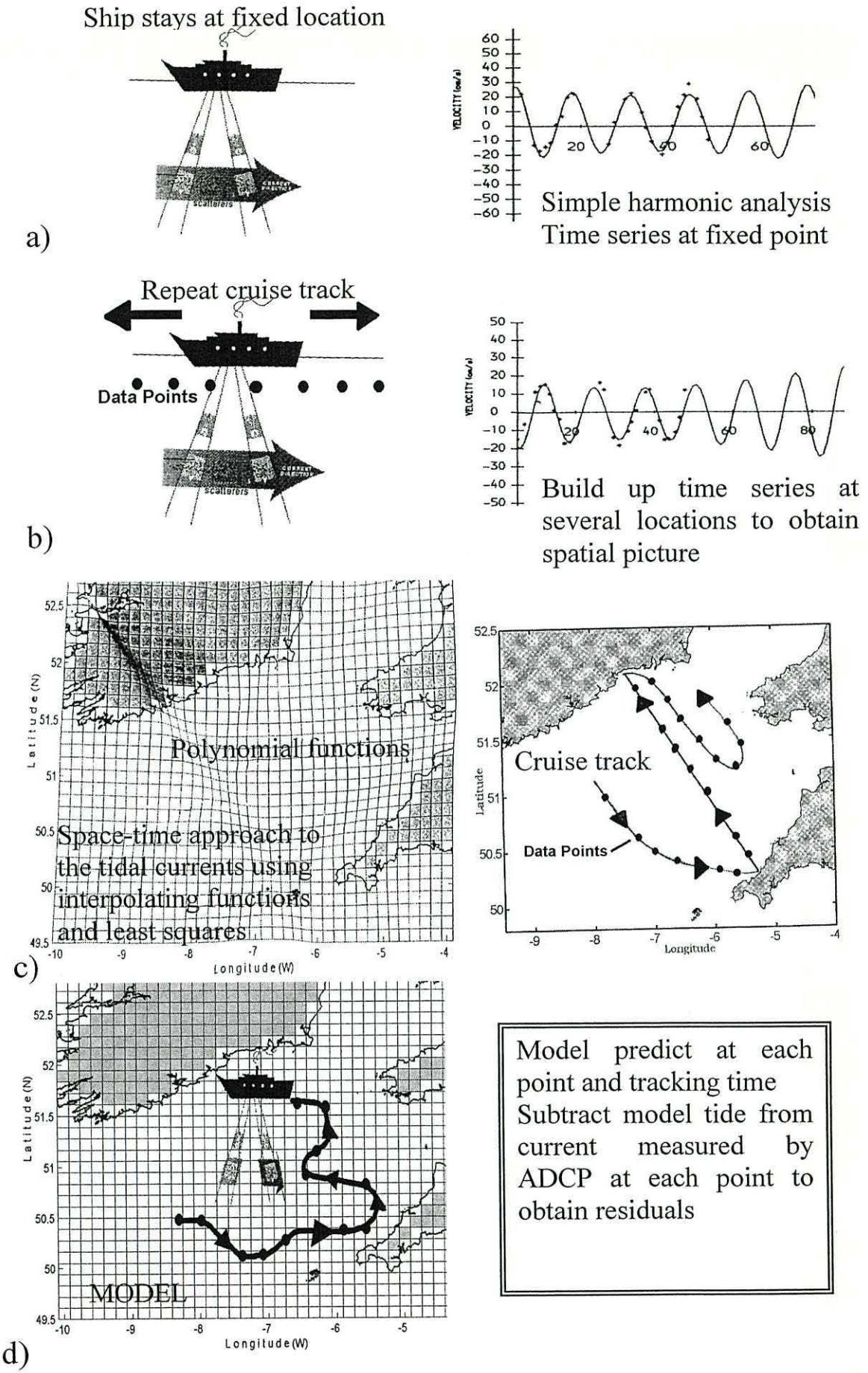

Figure 6.1 Different detiding approaches to ship-mounted ADCP data. a) measurements at fixed location, b) repeating cruise track, c) using spatial functions and least squares and d) using a numerical model.

6.2 Removing the tidal signal from ship-mounted ADCP data

6.2.1 Detiding technique using a numerical tidal model

The numerical model that was used to provide the harmonic constituents to detide the ship-mounted ADCP data was developed by Davies and Jones (1992b). It is a three-dimensional numerical model of the Celtic Sea and Irish Sea region based upon a regular finite difference grid, with horizontal spatial resolution of 4' latitude and 6' longitude, that is ~ 7km grid size (Fig 6.2). The model was based on the three-dimensional nonlinear hydrodynamic equations, including the advective terms, but neglecting the horizontal viscous terms. The boundary conditions were zero surface (wind) stress and quadratic law of bottom friction. Vertical eddy viscosity was computed using the parameterization given by Davies and Furnes (1980) relating the flow field to the depth mean components of velocity. More detailed model information can be found in Davies and Jones (1992b). They simulated for five of the major tidal constituents for the Celtic Sea, namely O_1, K_1, N_2, M_2 and S_2, and the model results were extensively validated against 60 current meter records and 100 (including permanent and temporary) tide gauges in the region (Fig 6.2).

Co-tidal charts were in good agreement with charts of the region based upon observations. However, the same was not true for the predicted tidal currents. In general, tidal currents were overestimated by the model of Davies and Jones (1992b). On average, the major axis of the current ellipse for the semi-diurnal constituents, M_2 and S_2, can be up to 0.05 m s^{-1} over predicted by the model, with phases agreeing to within 5° (Davies and Jones, 1992b). In the case of M_2, the u-component of velocity in the area around the St. George's Channel was smaller than observed. The magnitude of the tidal currents for the semi-diurnal tidal constituent N_2 and the diurnals K_1 and O_1 were slightly over predicted by the model. In the case of the diurnal constituents, the tidal ellipse orientation was only reproduced with an accuracy of 10-20° (Davies and Jones, 1992b). This difference in orientation is perhaps due to local effects.

Before either detiding technique (polynomial or numerical model) was applied, it was necessary to reduce the noise level that could remain in the 2 minute averaged ADCP profiles. Consequently, 10 minute averaged profiles were obtained. Using the tidal harmonics from the numerical model, a program was run to predict the tidal currents at the time/positions where ADCP profiles were obtained. Hence, the calculation of the residual currents is straightforward.

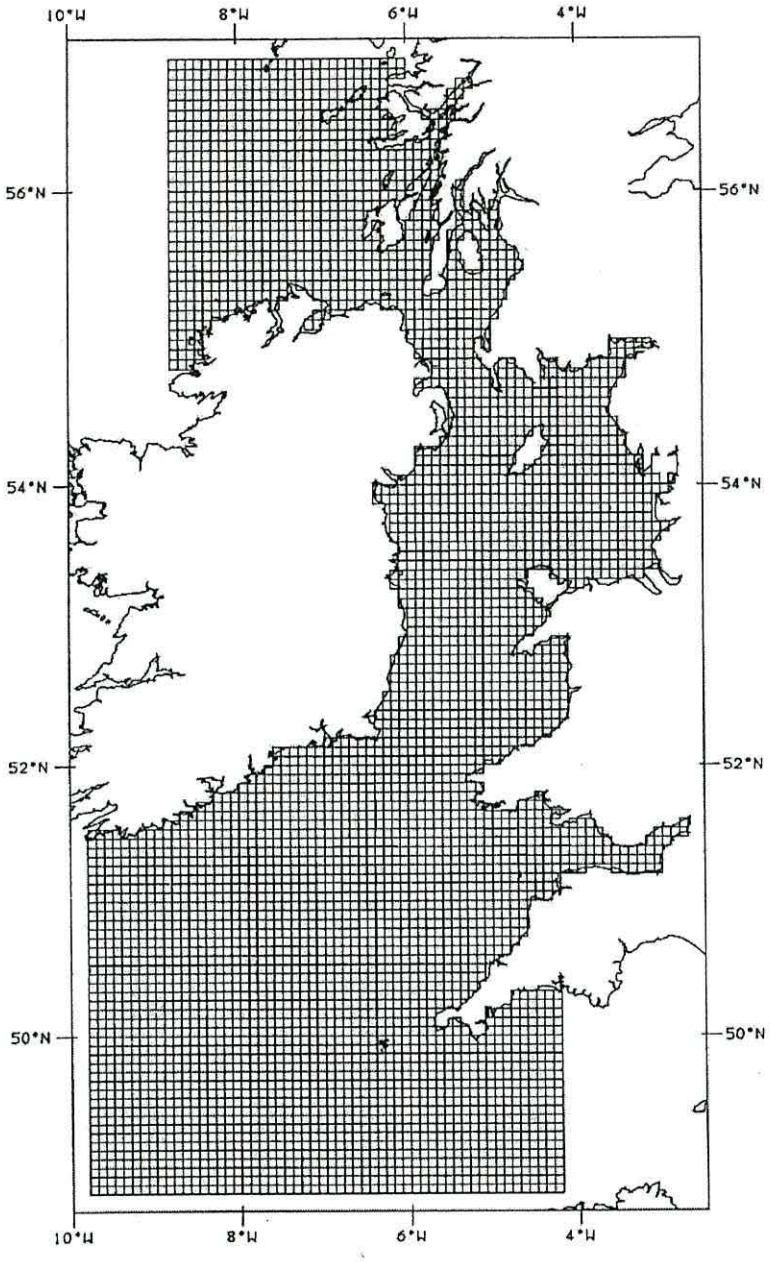

Figure 6.2 Finite difference grid of the tidal numerical model of the Celtic Sea and Irish Sea region. (From Davies and Jones, 1992b).

6.2.2 Detiding technique using least squares and polynomial spatial interpolation

In order to explain this detiding technique, it is necessary to first consider the simplest case of current observations at a fixed point. Current measurements at a fixed point can be represented as a mean (steady) current u_o, a time dependent tidal current $u_T(t)$ and time varying residuals $u'(t)$, *i.e.* $u = u_0 + u_T(t) + u'(t)$.

Since tidal currents $u_T(t)$ can be written as a linear combination of sinusoidal terms, each having a different amplitude and frequency, we can express current observations at a fixed point in the form:

$$u(t) = u_o + \sum_{k=1}^{n} a_k \cos(2\pi\omega_k t) + b_k \sin(2\pi\omega_k t) + u'(t) \qquad 6.1$$

$$v(t) = v_o + \sum_{k=1}^{n} c_k \cos(2\pi\omega_k t) + d_k \sin(2\pi\omega_k t) + v'(t) \qquad 6.2$$

where $u(t)$ and $v(t)$ are the time series of the eastward and the northward current component, respectively,

u_o and v_o are the mean steady current of the eastward and the northward current component, respectively,

$u'(t)$ and $v'(t)$ are the unresolved time varying residuals of the eastward and the northward current component, respectively.

ω_k is the tidal frequency ($1/T_k$) for the kth tidal constituent, where T_k is the tidal period for the kth tidal constituent.

a_k, b_k, c_k and d_k are the coefficients to be solved using the least square method.

n is the number of tidal constituents which depends partly in the length of the observations. The number of tidal constituents can be determined by the Rayleigh criteria, or/and in accordance with previous knowledge of the main constituents in the study area.

However, ship-mounted ADCP currents have implicit time and spatial variations. Candela *et al.* (1992) suggested that tidal spatial variability can be included in our current representation by allowing a_k, b_k, c_k and d_k to be functions of the horizontal spatial coordinates x and y.

If the normal modes of the tidal wave in a particular shelf are unknown, arbitrary interpolating functions are suggested. The simplest interpolating functions are polynomials in powers of x and y.

Using them to expand a_k

$$a_k(x,y) = \sum_{j=0}^{DP} \sum_{i=0}^{j} \lambda_l x^{j-i} y^i \qquad 6.3$$

where the values of λ are constants to be fitted to the observations, DP is the degree of the polynomial, and j and i are integers with $l=(j\text{-}1, i)$. The same treatment is applied to b_k, c_k and d_k. The mean steady field is also expected to vary with x and y. Therefore, a similar representation is possible for u_o and v_o. The unresolved subtidal temporal and spatial variability will be included in the terms u' and v', which can be referred as the noise of the estimation. However, these terms (unresolved signal) together with the mean steady field represent the subtidal signal.

In general, we seek a set of prediction equations of the form:

$$Ap = q \qquad 6.4$$

where $\boldsymbol{A}$ is a (m x n) model matrix which depends on the basis functions chosen, with m being the number of observations, and n the model order, p is an n column vector of unknown coefficients to be solved, and q is an m column vector containing the measurements. Two separated systems of equations for u and v are prescribed, with the same basis function matrix $\boldsymbol{A}$ but different coefficient column vector, p and observation column vectors, q.

Independently of either formulation of the basis functions used, the estimates of the parameters in c are chosen to minimize the sum of squared residuals. The solution of 6.4 is given by $p = (\boldsymbol{A}^T\boldsymbol{A})^{-1}\boldsymbol{A}^T q$; where $\boldsymbol{A}^T$ denotes the transpose of $\boldsymbol{A}$ and $(\boldsymbol{A}^T\boldsymbol{A})^{-1}$ the inverse matrix of $\boldsymbol{A}^T\boldsymbol{A}$. However, the direct calculation of $\boldsymbol{A}^T\boldsymbol{A}$ and its inverse may lead to large inaccuracies due to rounding errors (Candela *et al.*, 1992). Of the many methods to solve 6.4 for p, one of the most stable procedures is by obtaining the singular value decomposition (SVD) factorization of the matrix $\boldsymbol{A}$, *i.e.*, $\boldsymbol{A}=\boldsymbol{U}\Sigma\boldsymbol{V}^T$ where $\boldsymbol{U}$ and $\boldsymbol{V}$ are (m x m) and (n x n) orthogonal matrices respectively and Σ is a (m x n) diagonal matrix containing the singular values, *i.e.*, the positive square roots of the eigenvalues of the

product A^TA (Candela *et al.,* 1992). Therefore to find c with least squares approximation the equation 6.4 becomes: $\hat{c} = V\Sigma^{-1}U^T d$, where Σ^{-1} is the pseudo-inverse of the matrix Σ, *i.e.*, a (m x n) diagonal matrix whose elements are those of Σ to the -1 power (Candela *et al.,* 1992).

The misfit between the data set (d) and the estimated ($\hat{d}$), can be represented as $\varepsilon = d - \hat{d}$, which presents an unbiased variance of $\vartheta = \varepsilon' \varepsilon / \nu$, if and only if ν is the true degree of freedom. Since the collected data are not truly random samples from a random population, there is invariably a nonzero correlation between values (Emery and Thompson, 2001). The effective degrees of freedom must take into account the degree of correlation that exists between data points. The true degrees of freedom can be obtained based on the knowledge of the autocovariance $C(\tau)$ as a function of lag τ, by the relationship

$$\nu = N\Delta t / T \qquad 6.5$$

where Δt is the time averaging interval chosen, $N\Delta t$ is the total duration of the record and T is the integral time scale for the data record given by :

$$T = \frac{1}{C(0)} \int_0^\infty C(\tau) d\tau \qquad 6.6$$

where $d\tau$ is the time increment and $C(0)$ is the variance of the full data series (Emery and Thompson, 2001)

Assuming that observations possess an unbiased normal distribution it can be expected that estimates for $\hat{d}$, errors ε and coefficients $\hat{c}$ will also have an unbiased normal distribution (Emery and Thompson, 2001). Thus, it is possible to compute the confidence interval of the estimated value $\hat{d}$ using the expression:

$$\hat{d} - t(1-\alpha,\nu)\vartheta < d_{\substack{true \\ value}} < \hat{d} + t(1-\alpha,\nu)\vartheta, \qquad 6.7$$

where α represents the value of the desired probability for a Student's t distribution, expressed in percentage, ν is the degrees of freedom and ϑ is the variance.

Application in the Celtic Sea

The tidal extraction using least squares and polynomial interpolation technique in the Celtic Sea required additional assumptions, calculations and experimentation as set out below.

The number of possible combinations of tidal constituents and order of the polynomial functions are quite large. However, prior knowledge helps to set the model order and the important tidal constituents to be considered (Candela *et al.*, 1992). As mentioned in section 2.2, semi-diurnal frequencies are the most important signals in current observations in the study area, with M_2 and S_2, accounting for 90% of the total tidal signal. Thus, these tidal constituents (M_2 and S_2) are considered here. In order to resolve for M_2 and S_2, according with Rayleigh criterion for the separation of these tidal constituents, a record of length of 15 days is required (Pugh, 1987). However, the record length of each cruise was approximately for 8 days (CORY798) and 11 days (CORY998). So, applying Rayleigh criterion, we can just resolve for one tidal constituent. However, one of the advantages of the detiding method of least squares of Candela *et al.*, 1992 is that ADCP survey data from different cruises in the study area can be used (which effectively increases the separation time between measurements) improving the results (Candela *et al.*, 1992). Thus, in order to overcome the problem in the separation of the tidal constituents of M_2 and S_2 from the individual records, a longer record was constructed using the ADCP record from both cruises, CORY798 and CORY998, allowing the separation of M_2 and S_2 tidal signal.

In contrast, it was expected that the inclusion of the bottom-mounted ADCP data from the two mooring locations in the detiding process would improve the results, especially near the mooring sites, with an imperceptible change in the general tidal patterns (Candela *et al.*, 1992). However, using the additional bottom-mounted ADCP data from the two mooring locations degraded the fit over the whole domain and weighted preferentially the tidal predictions in the location areas of the moorings, probably due to the fact that there only were two isolated locations.

The procedure to obtain the best fit was based on some trial experimentation varying the degree of the polynomial functions. The best fit for the whole study area was obtained by using a second degree polynomial for the steady field (see Appendix 4), first degree for S_2 and fourth degree for M_2. The high degree of the polynomial function for M_2 cannot be justified purely in terms of dynamics. However, as a numerical approximation to

tidal currents in the region, this order was most appropriate because of the variety of tidal regimes observed in the study area, as will be seen later. In addition, although a spatial field for M_2 and S_2 is expected to be similar, it was not true in terms of the numerical approximation of the tidal field. However, when a higher degree in S_2 is used, small oscillations in the tidal prediction are observed, which cannot be related to the tidal signal but indicating that some noise can be numerically added. Therefore the predicted tidal results required to be critically examined before detiding.

On the other hand, the maximum order of the polynomials that can be used in each fit depends on the degrees of freedom available, *i.e.* the number of independent observations (Foreman and Freeland, 1991). The minimum number of independent observations required to determine the polynomial coefficients can be estimated as $n(m+1)(m+2)/2$, where m is the order of the polynomial and n the number of polynomial functions (Foreman and Freeland, 1991). Thus fitting a polynomial of order $m = 4$ (using the highest order) to each of the u_o, b_i and c_i functions for both semi-diurnal (M_2 and S_2) constituents ($n=5$) requires at least $5(4+1)(4+2)/2 = 75$ independent observations. Accordingly to Eq. 6.5, from the ADCP data, the number of decorrelated ADCP data (*i.e.* independent observations) was 124. Therefore, fourth order can be used given the number of available observations is larger than the minimum required.

6.2.3 A comparison of the tidal results from the detiding methods

Figures 6.3 and 6.4 show the time series of u- and v-components of depth-averaged current velocity measured with the ship-mounted ADCP and the predicted tidal currents using both the numerical model and the polynomial fitting. The observed velocities show a strong tidal signal (Figs 6.3a, 6.3d, 6.4a and 6.4d). The explained variance for the u-component (v-component) accounted for 86% (88%) respectively with the numerical model and 82 % (89%) with the polynomial method. The similarities between the tidal predictions from both methods were remarkable (Figs 6.3b-6.3f and 6.4b-6.4f), even when they were obtained from different approaches. They showed approximately the same order of magnitude and the same changes in tidal signal. However, some differences were observed near the gaps in the time series. From here, it is difficult to define which method performed better, although based on the explained variance mentioned above, the method of the polynomial showed a tidal signal slightly better correlated to the data. Differences between each of the tidal results could be due to the number of tidal constituents used in

the prediction. The polynomial technique resolved the semidiurnals M_2 and S_2 only, the numerical model resolved these two and the diurnals K_1 and O_1, along with the fortnight N_2. The latter constituent modulates the spring-neap cycle, which can cause considerable differences in the tidal currents. On the other hand, very little can be gained by the inclusion of the additional diurnal tidal coefficients in the polynomial approach because their solution requires additional degrees of freedom, which is not supported by the time series length. Therefore, we have to consider that we might be losing about 10 % of the total tidal variability with the polynomial technique.

M_2 Tidal Ellipse comparisons

The predicted spatial tidal current ellipses for M_2 with both the numerical model (Fig 6.5a) and the polynomial method (Fig 6.5b) were compared. They qualitatively showed the same spatial variability of the tidal currents in the area. Both detiding methods closely agreed in the orientation of the tidal ellipses. In the St. George's Channel, where the strongest tidal currents were located, the semi-major axis amplitude reached values up to 1.4 m s^{-1}, while the semi-minor axes were either small or vanish. Hence, M_2 tidal currents were rectilinear and the tidal ellipse was oriented along the channel (northeast-southwest). Also, in both methods, tidal ellipses became smaller and more circular near the entrance of the Bristol Channel, which makes it more difficult to determine their orientation. However, in the northern entrance of the Bristol Channel, tidal ellipses were nearly Northwest-Southeast orientated, becoming more northeast-southwest orientated towards the southern entrance. The tidal ellipse eccentricity parameter, which is defined as the ratio of the semi-minor axis to the semi-major axis, helps to define if the ellipse is nearly circular (values ~1), and its sign defines the sense of rotation of the tidal current ellipse. That is, a positive eccentricity indicates a cyclonic (anti-clockwise) rotation, a negative an anticyclonic (clockwise) rotation. Both methods displayed nearly circular ellipses in the central entrance of the Bristol Channel, as indicated by the eccentricity value of almost 0.8 (Figs 6.6a and 6.6b). Outside this area, more rectilinear tidal ellipses were found in the remainder of the Celtic Sea, with generally an eccentricity value of 0.2-0.4 (Figs 6.6a and 6.6b). The rotation of the tidal currents was cyclonic in most of the Celtic Sea, becoming anticyclonic towards more oceanic conditions. However, in the St. George's Channel, the cyclonic rotation of the tidal currents in the least squares method (Fig 6.6b) was not as clear as it was in the model (Fig 6.6a).

In general, the methods differed in their prediction of the size of the semi-major axis with a mean difference of 0.04 m s^{-1} and a maximum difference of 0.20 m s^{-1}. Differences in the semi-minor axis were up to 0.33 m s^{-1} but only 0.08 m s^{-1} on average. Model and least squares methods differed in phase by up to 50° (Figs 6.7a and 6.7b) and in orientation with a mean difference of 12°. However in some locations there was considerable disagreement in phases > 100° (Fig 6.7a and 6.7b) such as near the Irish coast and in the Bristol Channel.

In order to compare the tidal predictions with available observations, tidal information extracted from current meter records held by the British Oceanographic Data Centre (BODC) were used. Nine locations representing the different regions of the study area were selected (see Figure 6.8 for locations).

Figure 6.9 shows the tidal ellipses from the current meter at the nine selected locations (Fig 6.8) together with the predicted ellipses using the numerical model and the polynomial method. A quantitative representation of the differences is shown in Figure 6.10, where values of the difference are shown between the four tidal ellipse parameters (semi-major and semi-minor axis, orientation and phase of the tidal ellipse) from current meter measurements along with estimated currents obtained by both methods (model and polynomial fits). Both methods equally well predicted in areas 1, 2 and 3 (Figure 6.9 and 6.10). Both predicted the ellipse orientation well and were particularly good in the St. George's Channel (location 1). However, some areas were better predicted with the polynomial method, such as areas 5 and 6. Other areas were better predicted by the model such as areas 4 and 8. The worst predicted area with the polynomial was 9 (near the Irish coast) where the semi-major axis was overestimated by a factor of 3 times the model error (see Figure 6.9c and 10a). The tidal ellipse parameters worst estimated by the polynomial method were semi-minor axis and phase (Fig 6.10b and 6.10c). Estimation of the phase from the polynomial technique differed by up to 40° and the semi-minor axis was up to 0.15 m s^{-1} overestimated at location 4.

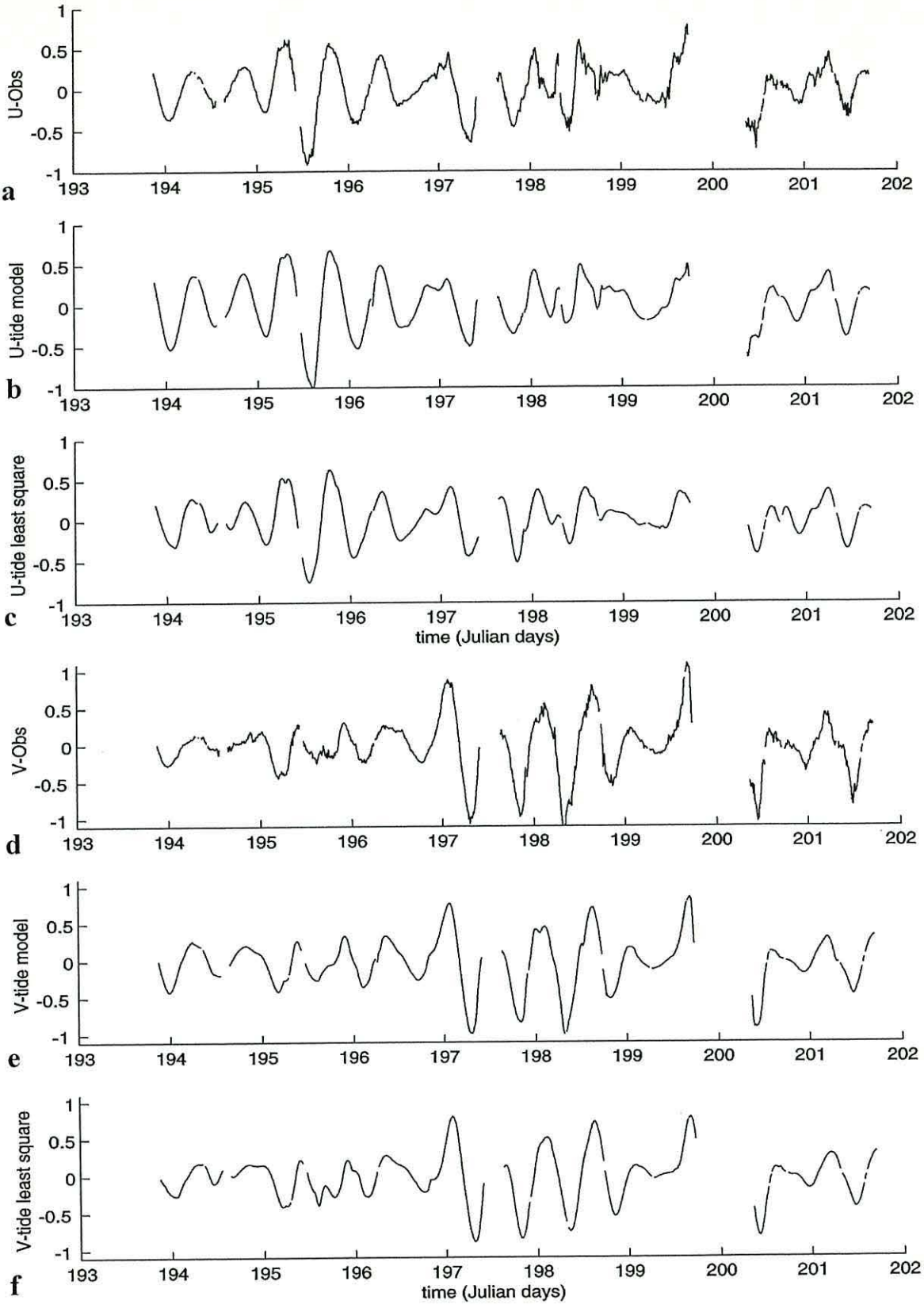

Figure 6.3 Time series plots of the east-west u and north-south v velocity components for the ship-mounted ADCP observations, tidal model prediction and tidal from polynomial and least squares approach (CORY798).

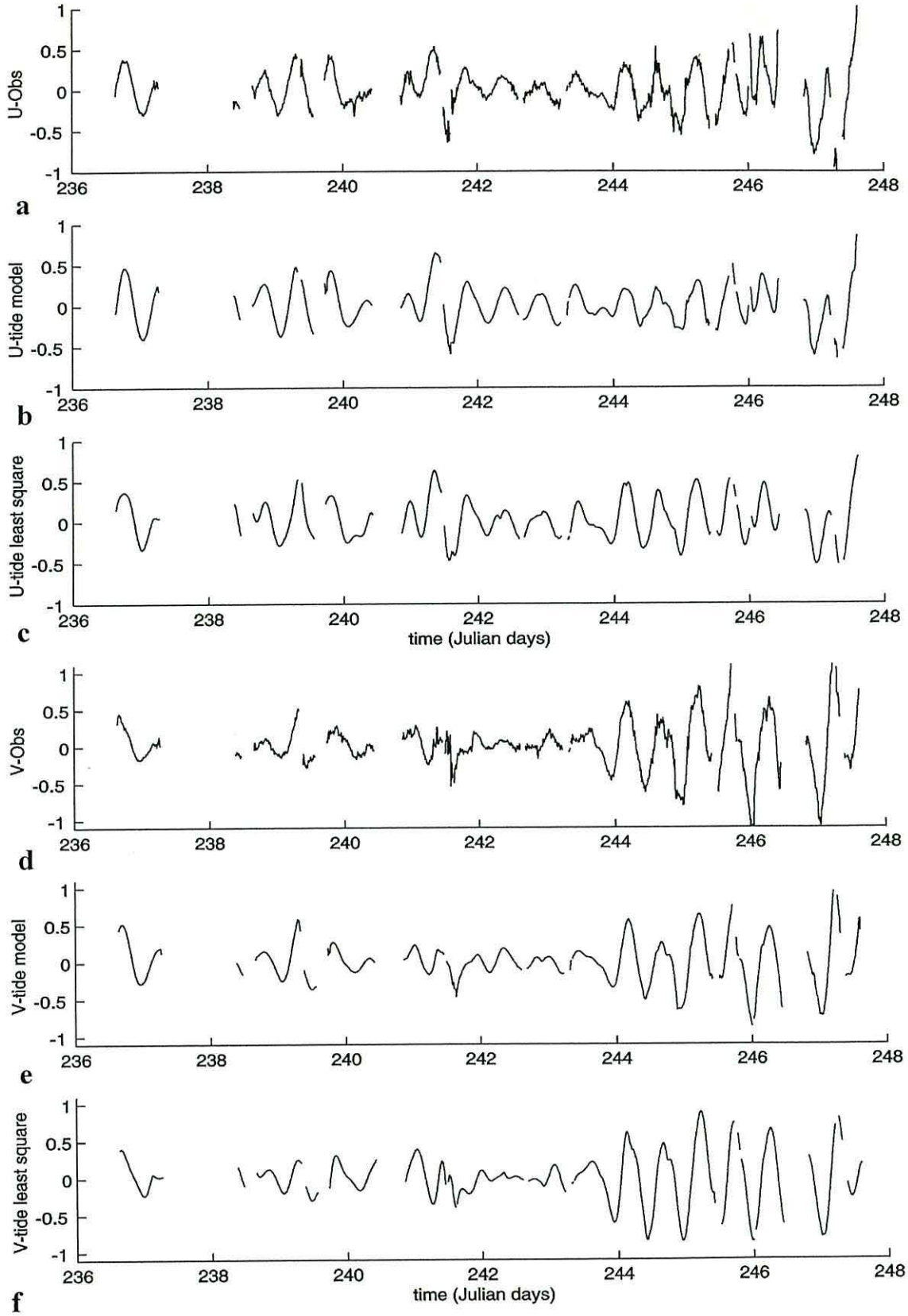

Figure 6.4 Time series plots of the east-west u and north-south v velocity components for the ship-mounted ADCP observations, tidal model prediction and tidal from polynomial and least squares approach (CORY998).

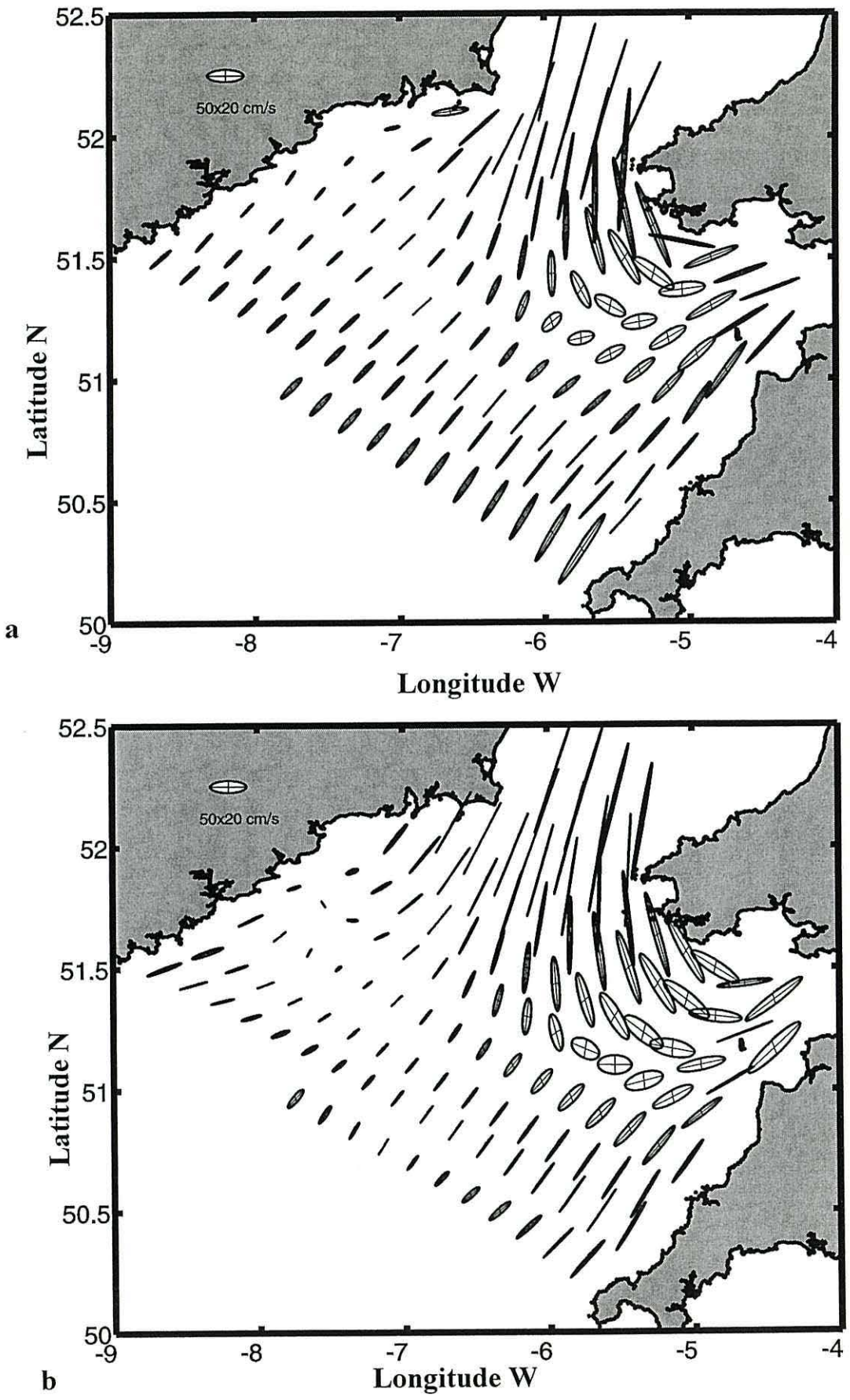

Figure 6.5 Tidal ellipse maps for M_2 estimated from the numerical model (top) and from the polynomial and least square technique (bottom). Scale appears on the top-left corner.

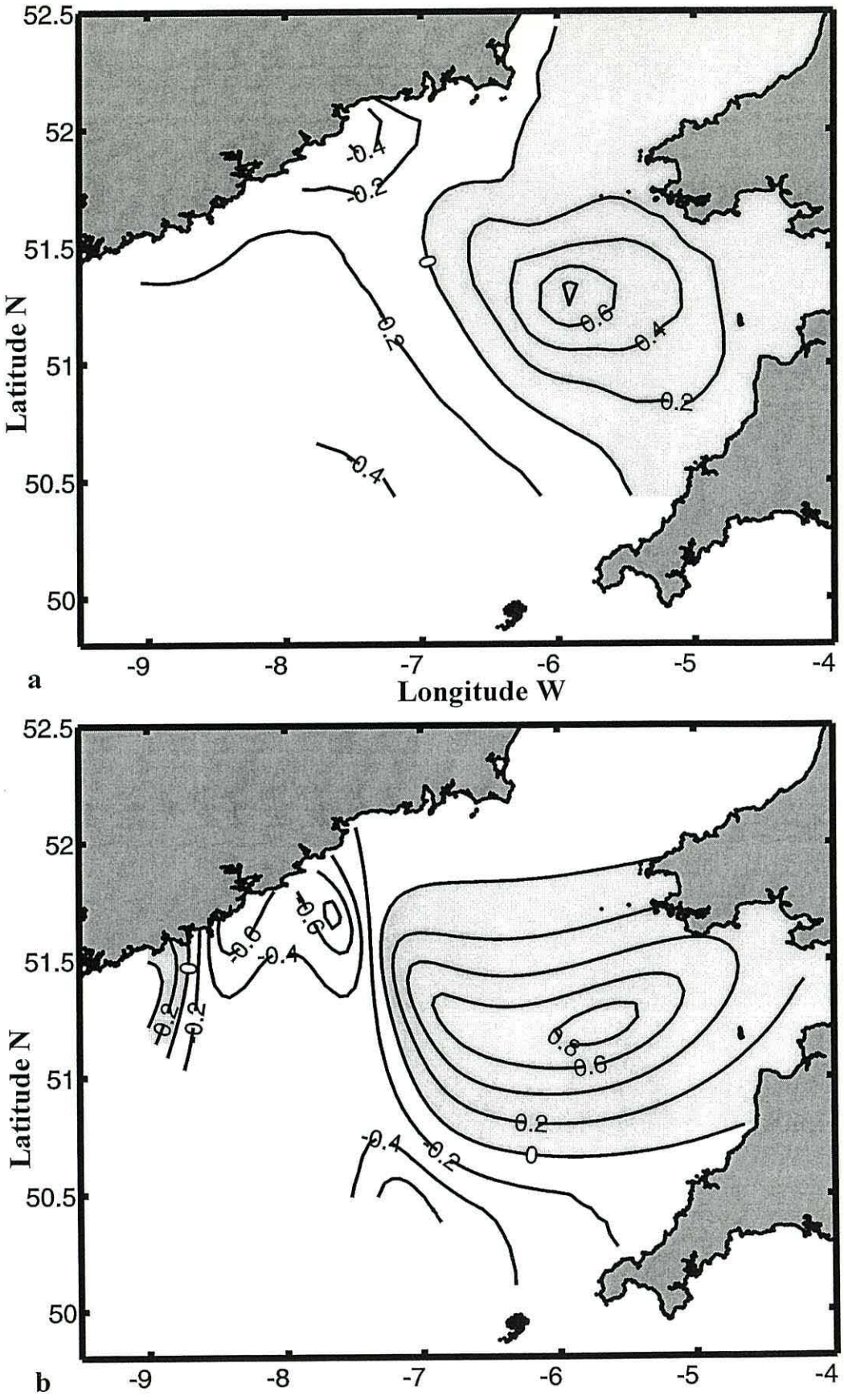

Figure 6.6 Eccentricity of the tidal ellipse maps for M_2 estimated from the numerical model (top) and from the polynomial and least squares technique (bottom). Shadowed areas represent cyclonic (anti-clockwise) tidal ellipse rotation.

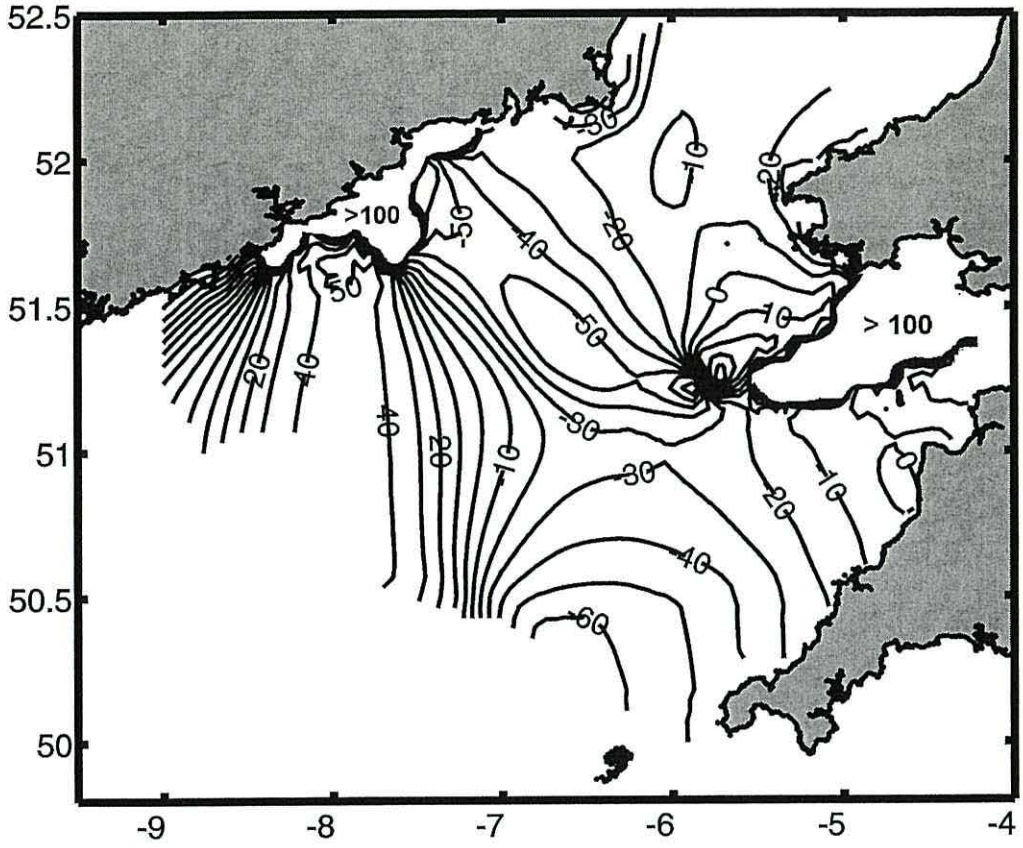

Figure 6.7 Phase differences (in degrees) between numerical model and polynomial and least squares technique for M_2.

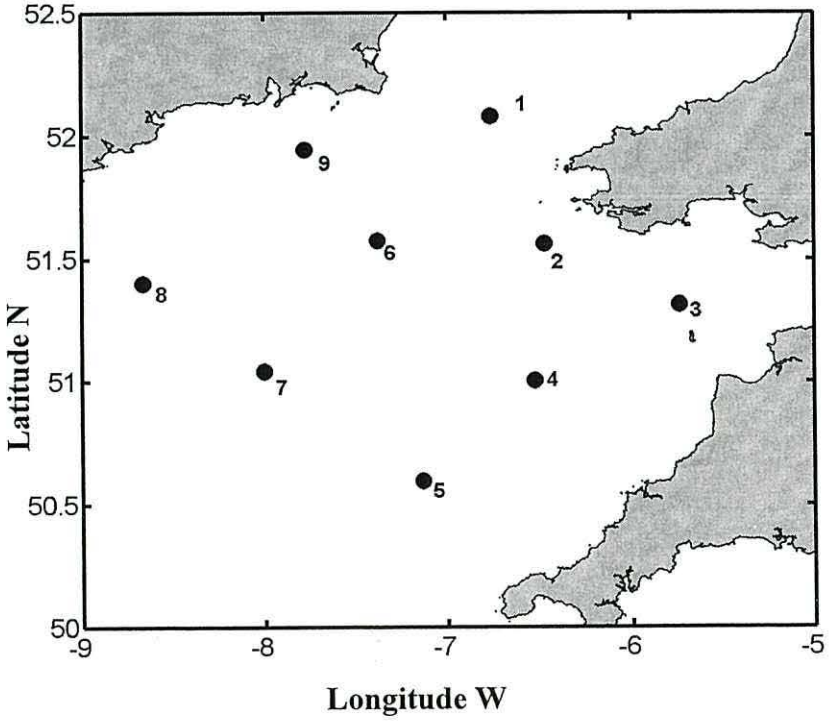

Figure 6.8 Map of the Celtic Sea showing the current meter locations selected for the comparison of the tidal ellipses parameters between observations and predictions from numerical model and polynomial method. The current meter information was obtained from the BODC database.

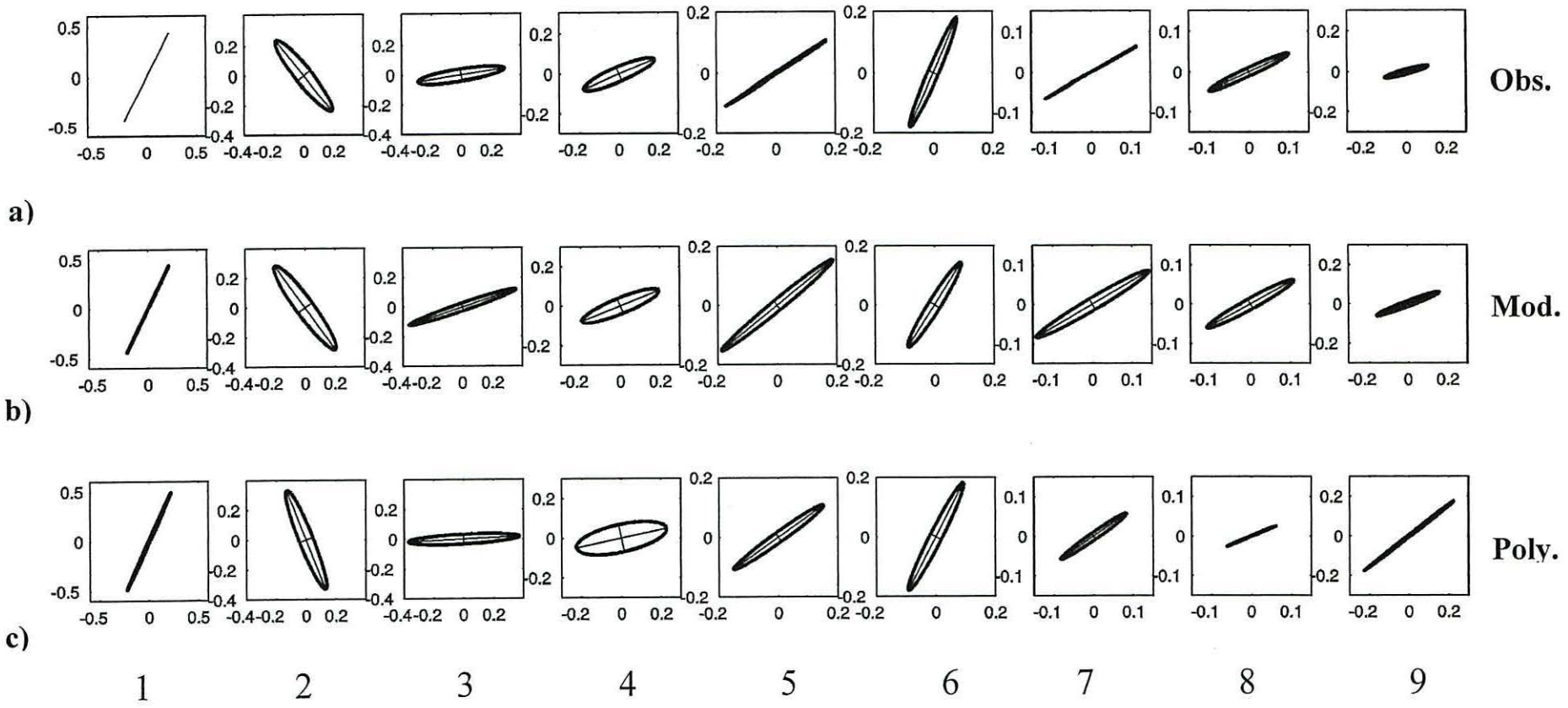

Figure 6.9 Comparison of M_2 tidal ellipses obtained from current meters from the locations selected (first row) and the tidal ellipses predicted with the numerical model (second row) and polynomial method (third row). From left to right locations 1-9.

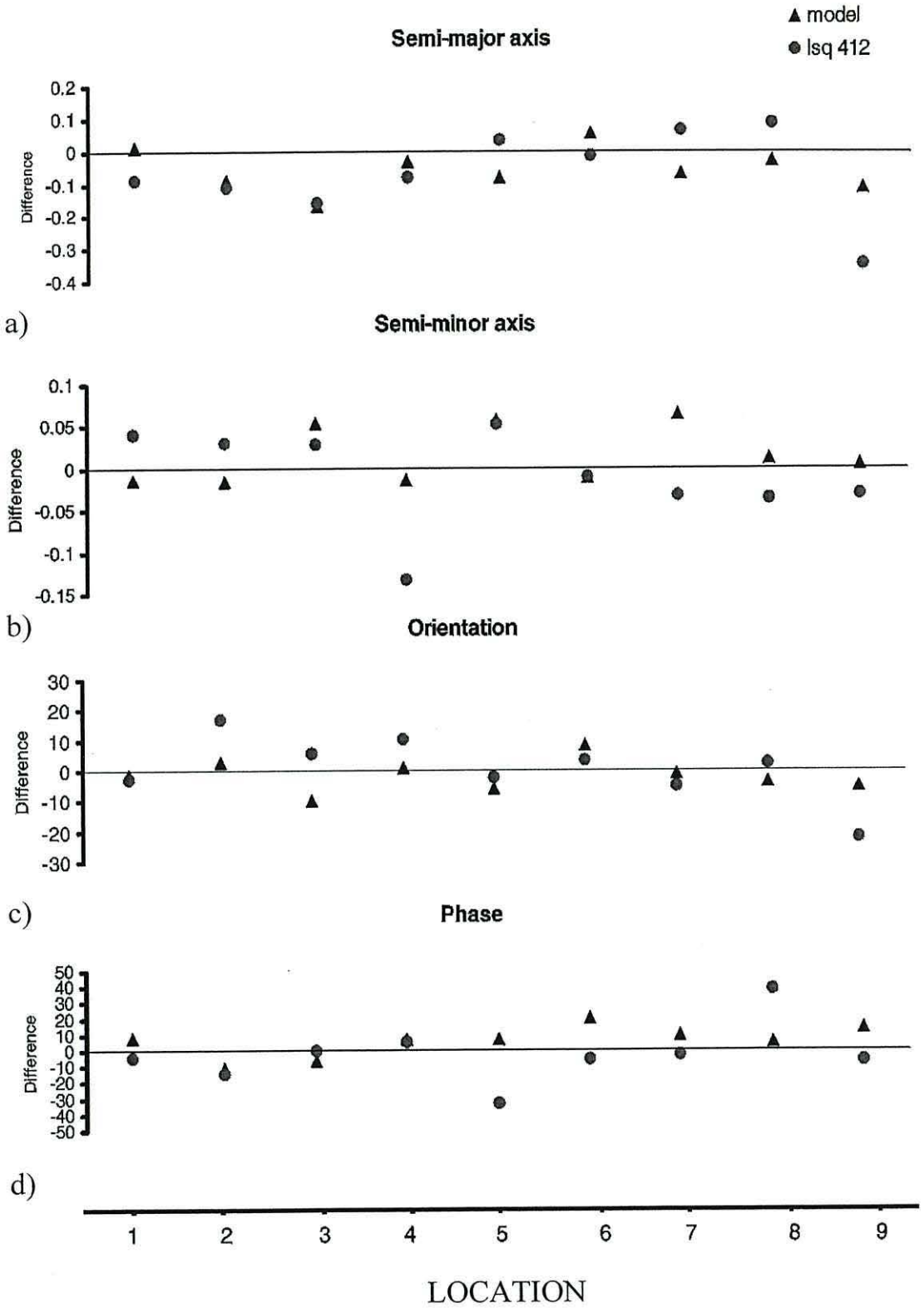

Figure 6.10 Differences of the tidal ellipses parameters (semi-major and semi-minor axis, orientation and phase) for M_2 between: current meters and the numerical model (blue triangle symbols), and current meter and polynomial method (red circle symbols). Numbers at the bottom correspond to locations 1-9. Differences in semi-major and semi-minor axis in m s^{-1} and orientation and phase in degrees.

S_2 Tidal Ellipse comparisons

S_2 tidal ellipses obtained by both methods are shown in Figure 6.11. In general, both methods agreed showing an S_2 spatial tidal distribution similar to that of M_2 (Fig 6.5). However, differences between the methods, in the case of S_2 (Fig 6.11), were larger than with M_2 (Fig 6.5). Both methods (Fig 6.11a and 6.11b) showed approximately the same tidal ellipse orientation (within 5° on average). However, differences up to 85° can be seen near St. David's Head. S_2 tidal current from the model differed considerably in magnitude compared to that from the polynomial method. The latter were almost half of the value of the numerical model results, principally in the St. George's Channel. Semi-major axis mean difference was 0.20 m s^{-1}, while the semi-minor axis differences were < 0.10 m s^{-1} with a mean of 0.05 m s^{-1}. The methods disagreed in phase (Fig 6.13) with a mean of 37° and maximum of 100°. It is important to observe that these extreme values were principally in two areas, namely the areas near the Irish coast, and near the St. David's Head and the Bristol Channel. Rotation of the S_2 tidal ellipses with respect to the numerical model (Fig 6.12a) showed a similar pattern to that of M_2 (Fig 6.6a). The polynomial method (Fig 6.12b) did not show the same pattern of the tidal ellipse rotation compared to that of the model (Fig 6.12a). Both methods showed an anticyclonic current rotation in the St. George's Channel, with cyclonic rotation in the Celtic Sea and Bristol Channel, and anticyclonic rotation towards the southern connection of the Celtic Sea with the North Atlantic ocean. However, they differed in the areas near the Irish Coast.

S_2 ellipses predicted using both methods (Fig 6.14b and 6.14c) exhibited approximately the same orientation as the observations (Fig 6.14a). The main discrepancies were in the shape of the tidal ellipses due to overestimated or/and underestimated semi-major and semi-minor axes (Fig 6.15). As observed with M_2, there were some areas that were better estimated with the polynomial method and others were better with the numerical model. The semi-major axis was underestimated by the polynomial method in location 1 and 2 accounting for 15 m s^{-1} and 0.05 m s^{-1} respectively (Figs 6.15a and 6.15b). In general, the numerical model predicted reasonably well the value of the semi-major axis with a slight overestimation < 0.05 m s^{-1} in most of the locations, only location 9 showed an overestimation of ~10 m s^{-1} (Figs 6.15a and 6.15b). The polynomial method overestimated the semi-minor axis in locations 1-4, 6 and 9, while locations 7 and 8 where underestimated. The semi-minor axis from the numerical model also differed in amplitude from observations with values < 0.05 m s^{-1}, overestimating in

locations 1, 2, 4 and 6 and underestimating in locations 3, 5, 7-9. Estimation of the phase from the polynomial technique differed by up to 90° in S_2 from current meter observations, mainly in locations 8 and 9.

Even though the closest estimation of the tidal properties was obtained with the numerical model (Figs 6.10 and 6.15), some errors still could be present. Therefore, its results need to be taken with care. The worst predictions with the polynomial method were expected near the edges of the domain of data coverage such as the coastal zone, which represents the most serious drawback of the polynomial technique (Candela *et al.*, 1992). However, even when the polynomial method is a numerical statistical approximation to the tidal field, which was captured with two surveys that were very close in time, it performed reasonably well for M_2. Despite the discrepancies between the polynomial tidal ellipse results and the current meters (Figs 6.10 and 6.15), the total estimated tidal signal (M_2 plus S_2) from this method (Fig 6.3c and 6.4c) was not significantly different from the numerical model results (Fig 6.3b and 6.4b). Perhaps, in the sum of the M_2 and S_2 signals could be a compensation of the misfit of the estimation from the individual harmonic constituents. On the other hand, the current meter data originated from different kinds of instruments and measurement duration. Consequently, these results also need to be treated with some care. In addition, current meter measurements represent single points in a region with considerable spatial tidal gradients, and errors in the comparisons with the tidal field estimated from the numerical model and the polynomial method may result.

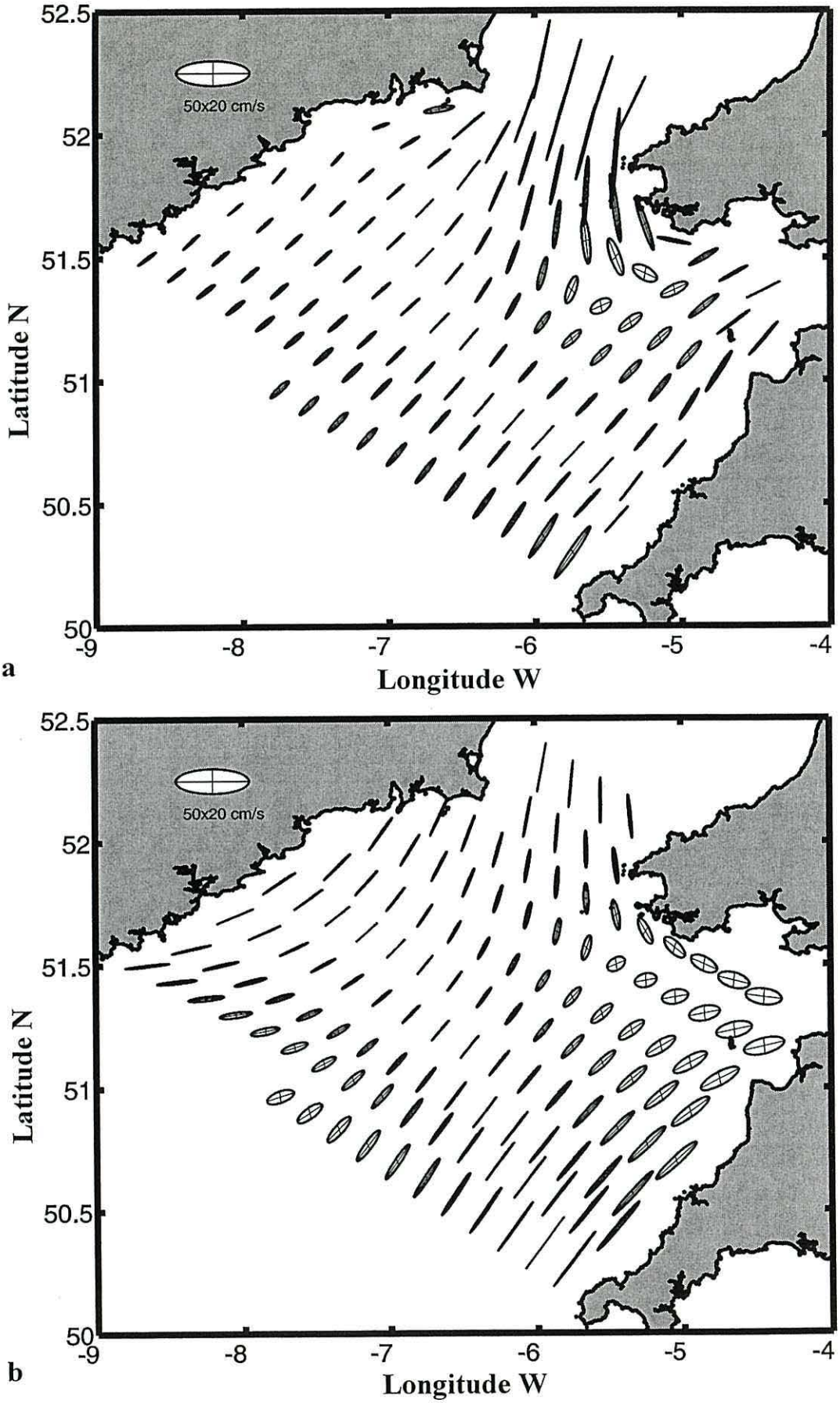

Figure 6.11 Tidal ellipse maps for S_2 estimated from the numerical model (top) and from the polynomial and least square technique (bottom). Scale appears on the top-left corner.

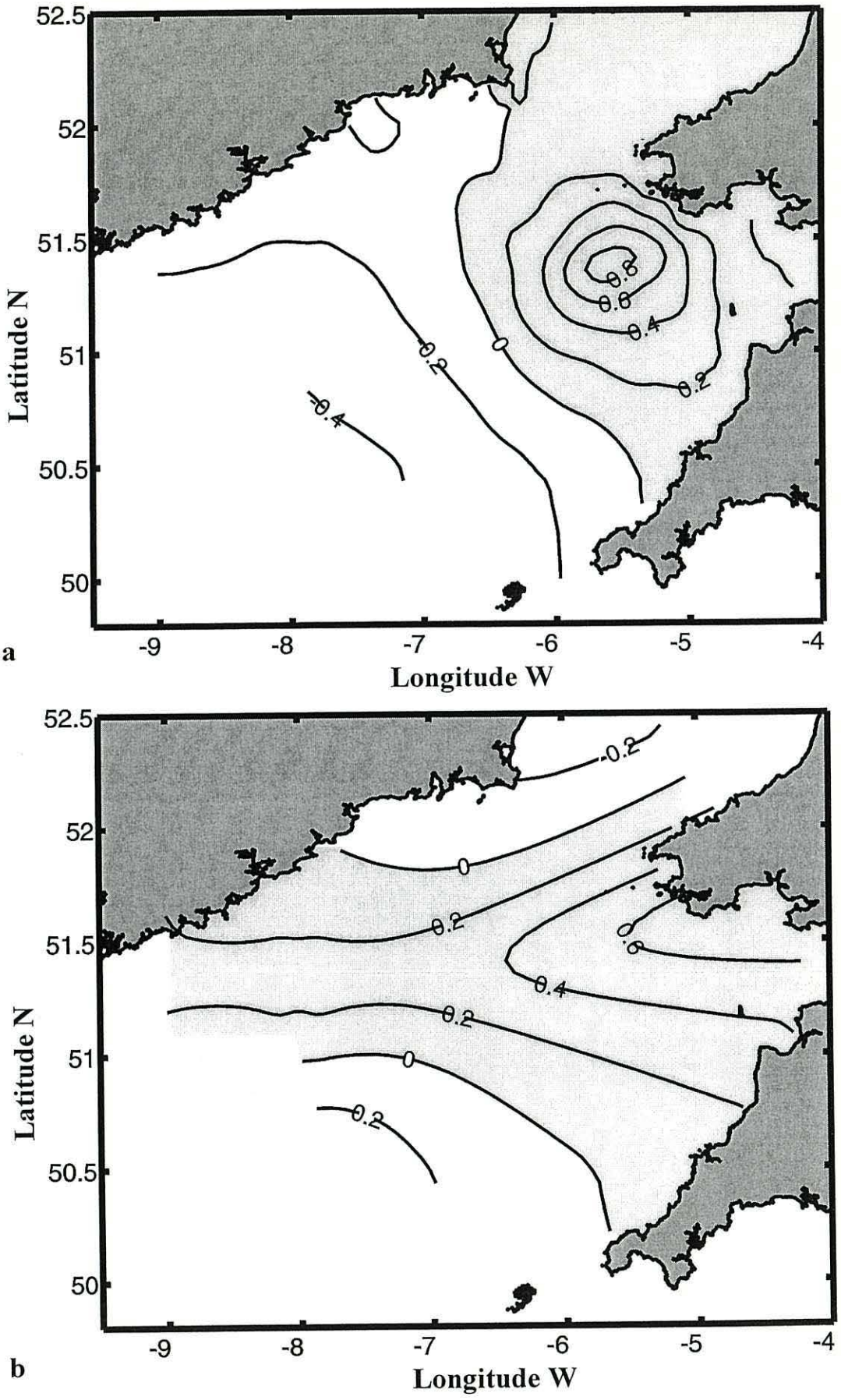

Figure 6.11 Tidal ellipse maps for S_2 estimated from the numerical model (top) and from the polynomial and least square technique (bottom). Scale appears on the top-left corner.

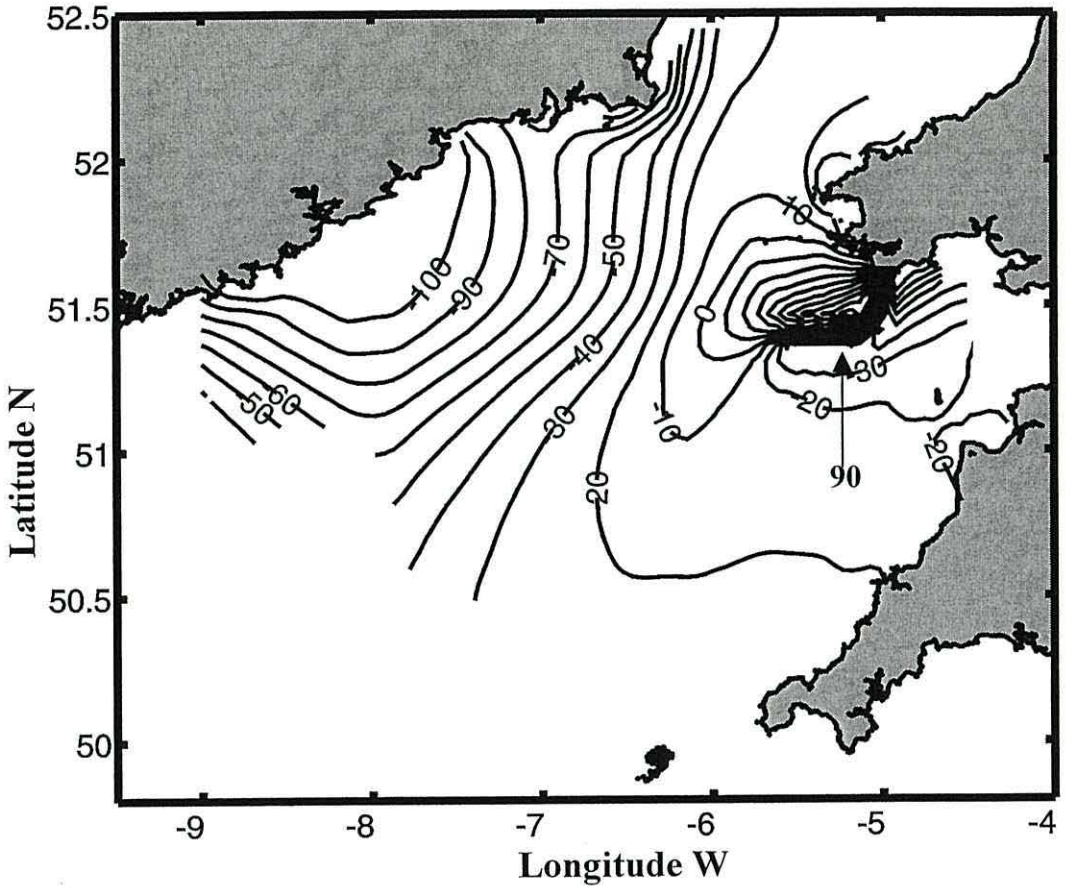

Figure 6.13 Phase differences (in degrees) between numerical model and polynomial and least squares technique for S_2.

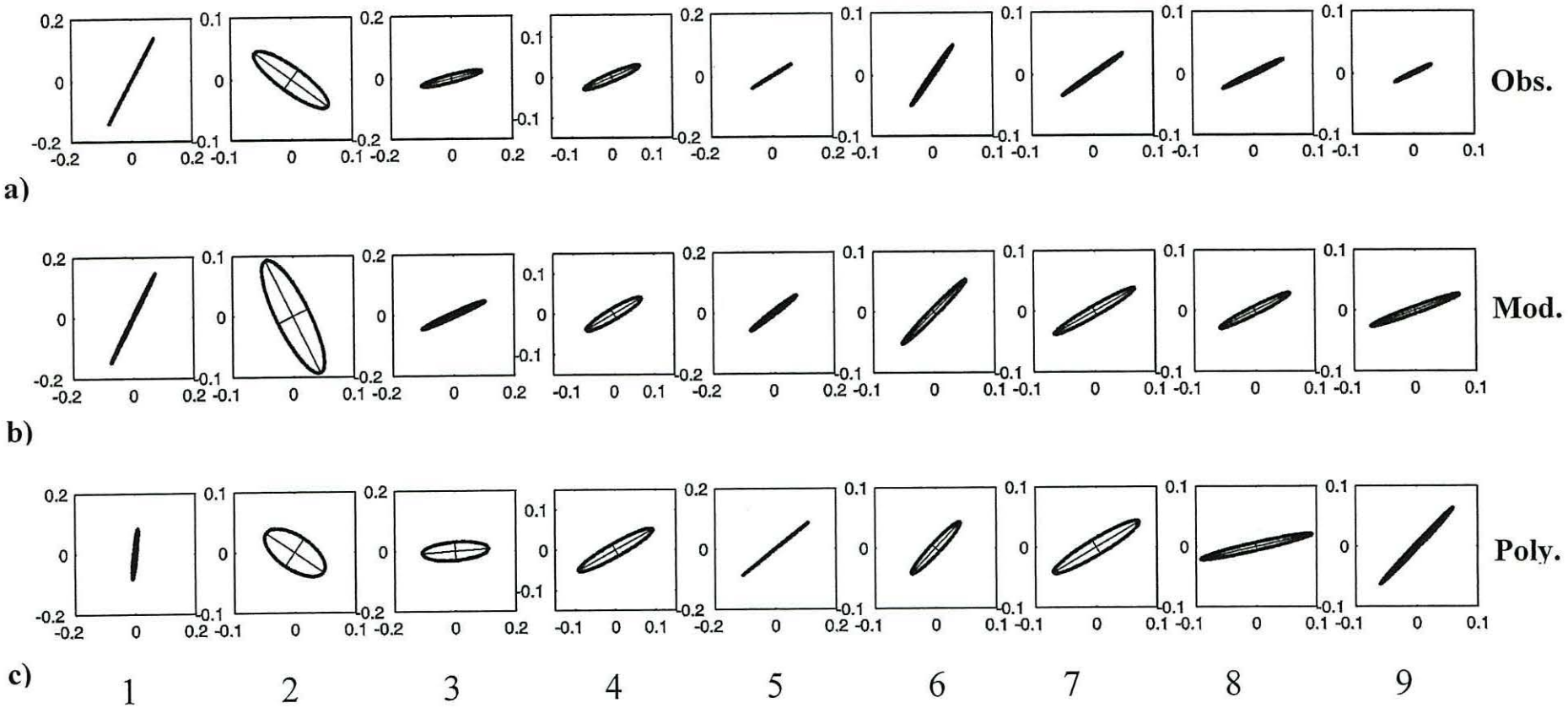

Figure 6.14 Comparison of S_2 tidal ellipses obtained from current meters from the locations selected (first row) and the tidal ellipses predicted with the numerical model (second row) and polynomial method (third row). From left to right locations 1-9.

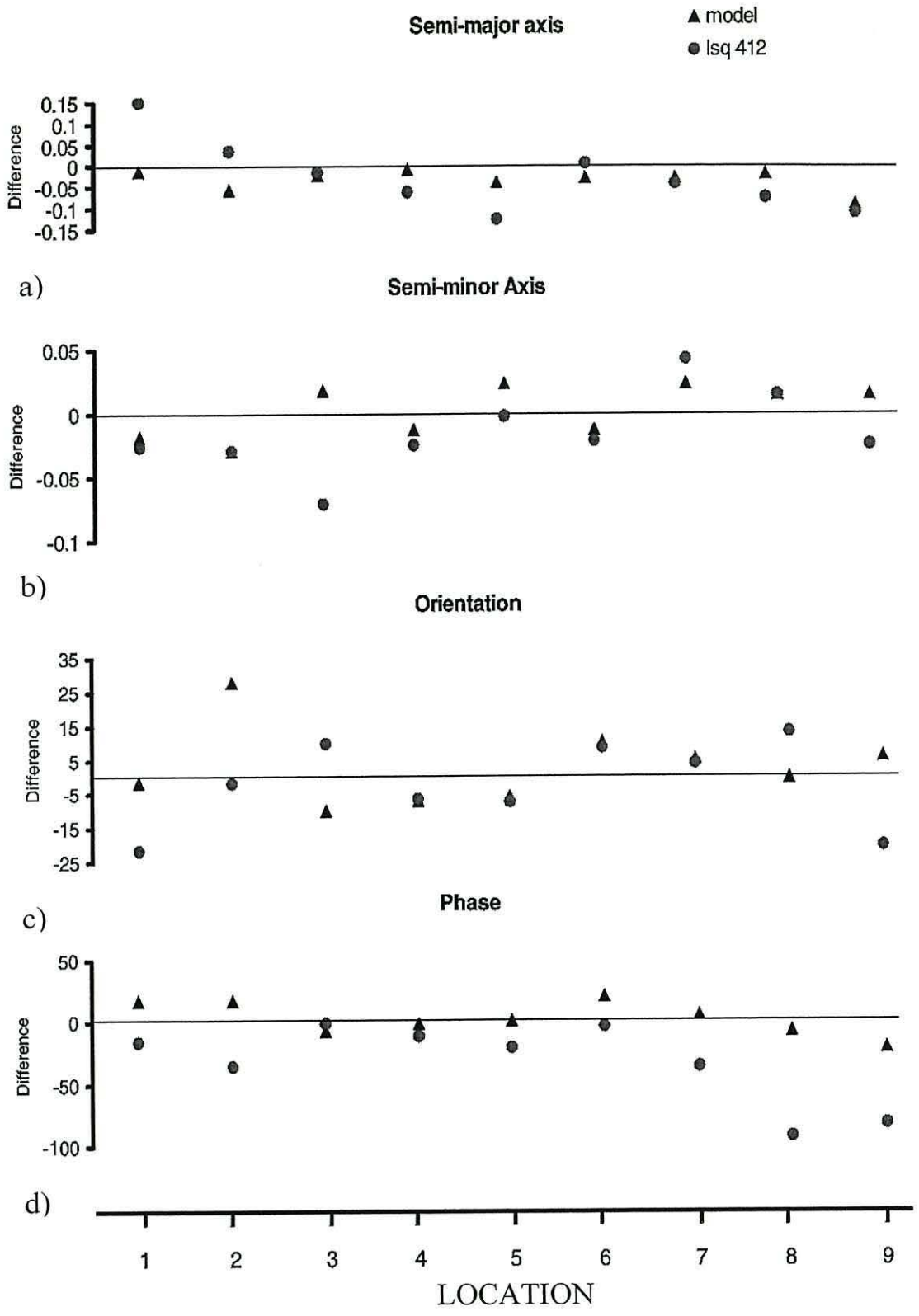

Figure 6.15 Differences of the tidal ellipses parameters (semi-major and semi-minor axis, orientation and phase) for S_2 between: current meters and the numerical model (blue triangle symbols), and current meter and polynomial method (red circle symbols). Numbers at the bottom correspond to locations 1-9. Differences in semi-major and semi-minor axis in m s^{-1} and orientation and phase in degrees.

6.3 An alternative detiding approach: Blending technique

In the preceding section, it was seen that both methods were able to predict reasonably well the main tidal signals in the whole study area. However, a closer inspection, comparing the time series of the ADCP data and the tidal signal obtained from the numerical model, shows that there were some areas where the numerical model performed better than the polynomial method and *vice versa*. Therefore, in seeking to obtain the subtidal signal from the ADCP data, both methods are likely to fail to solve the spatial variation of tides sufficiently to satisfactorily extract tidal fields. Some correction in both methods is still therefore needed. Improvements in the tidal predictions could be perhaps obtained with a better spatial resolution (in the case of the numerical model) or with an interpolation scheme that accounts for the dynamics (in the case of the least squares technique).

In an attempt to find a better technique to reduce the tidal frequency energy from the ADCP data, an alternative method is proposed. The numerical model estimated the tidal signal of the study area using a dynamical approximation. On the other hand, the polynomial method extracts the tidal signal using numerical-statistical approximation but lacks a dynamical input. However, in some way, this statistical tidal approach contains a dynamical components dictated by the data. Therefore, it seems possible that a better estimation of the tidal currents might be obtained combining the tidal information extracted using the polynomial method with the tidal results from the numerical model. This procedure resembles the methodology of data assimilation.

As established for data assimilation, the combination of observational data with the dynamical approach (model) to the system under observation makes possible a more efficient, accurate and realistic estimation, which might not otherwise be feasible (Robinson *et. al.*, 1998). Moreover, combining or melding the results of a dynamical model with observations, usually does not degrade the reliable information of the observational data, but rather enhances that information content by reducing the random noise (Robinson *et. al.*, 1998). There are several melding schemes in data assimilation. However, a linear combination of the observation data and dynamical model is usually chosen. This is known as linear melding or blending (Lermusiaux, 1997). With the idea of the blending scheme, an alternative detiding technique is attempted here.

Assuming that estimations of the tidal currents from the polynomial method and from the numerical model are unbiased and independent estimates of the true tidal currents, then, the linear combination of these two independent tidal current approaches can be possible. The detiding blending technique consists of a simple weighted average of the numerical model results with those from the polynomial method. Thus, it is assumed that at all points in the tidal blending estimate there is a scalar combination of the tidal currents from the model and from the data values (*i.e.* polynomial technique) in the form:

$$(\hat{T}_k)_b = \frac{W_1 \hat{D}_k + W_2 \hat{M}_k}{W_1 + W_2}$$

Where $(\hat{T}_k)_b$ is the blending estimate of the tidal current at the kth data point;

$\hat{D}_k$ is the estimated tidal current from the polynomial technique at the kth data point;

$\hat{M}_k$ is the estimated tidal current from the numerical model at the kth data point;

W_1 and W_2 are the weight of the average for $\hat{D}_k$ and $\hat{M}_k$ respectively.

Here, the assigned values for W_1 and W_2 were 0.9 and 1.0 respectively. The W_1 value was given considering that for D only M_2 and S_2 semi-diurnal constituents were calculated, which account 90 % of the total tidal variability. W_2 was obtained assuming a 100% of the tidal variability is due to the 5 constituents M_2, S_2, K_1, O_1 and N_2.

For illustrative purposes, Figure 6.16 shows an example of observations (raw data), the tidal current approximation from the two conventional detiding techniques of numerical model and polynomial interpolation and the blending technique. The blending procedure acted as a correction procedure for the phase and amplitudes of the total modeled tide including the five constituents. However, it was not applied to the individual harmonic constituents.

In the course of this work, this detiding technique was applied to the ship-mounted ADCP data to obtain the residual flow field, which will be presented in the next sections.

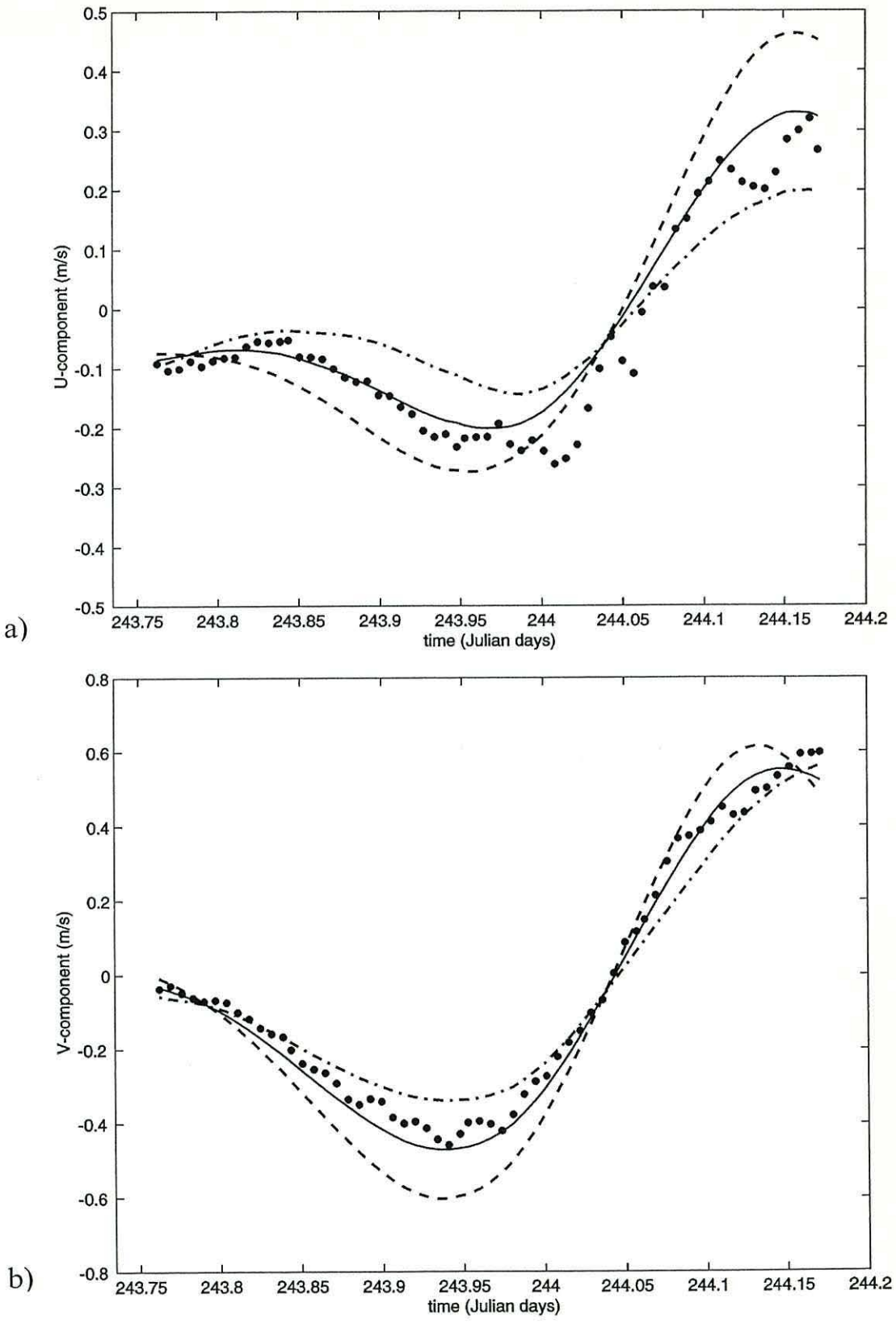

Figure 6.16 Comparison of current tidal predictions from different approaches. East-west *u* (top panel) and north-south *v* (bottom panel) tidal velocity components. Dots represent the observed velocities from ship-mounted ADCP for Leg 202, dot-dashed line is tidal current from the numerical model, broken line is the tidal current estimation from polynomial method and solid line shows the tidal prediction with the blending technique.

6.4 Subtidal currents from ship-mounted ADCP

The ultimate purpose of detiding ADCP data is to reveal the subtidal flow field in a study area. Although, subtidal currents are weaker than the instantaneous tidal currents, they are more significant in terms of describing the seasonal long-term circulation. The purpose of this section is to present the subtidal currents derived from the ship-mounted ADCP data.

6.4.1 Horizontal field of the subtidal currents

The whole subtidal velocities from the ADCP measurements (Fig 6.17) contain the steady field and the unresolved tidal currents (time variant). Subtidal currents were obtained after applying the detiding *blending* procedure (explained in last section) to depth averaged velocities. Maps of the subtidal currents from depth averaged velocities using the polynomial method and the numerical model are presented in Appendix 5.

Both campaigns showed a similar pattern in the whole area (Figs 6.17a and 6.17b), with some areas of more complex pattern presenting crossing vectors, *i.e.* convergence flows. In general, the residual field showed a cyclonic circulation in the Celtic Sea with the strongest velocities concentrated in the area of St. George's Channel, as predicted from the density driven currents. However, in this area an inconsistent pattern was observed, since this region was crossed by the ship on several occasions and the same pattern was not repeated. Even when it was expected that there would be semi-permanent jet-like flows associated with bottom fronts (as predicted by geostrophy), only some transects showed these strong flows and other transects showed weak and irregular residual velocities. In addition, flow in the reverse direction to the one predicted by geostrophy was found on both sides of the channel but mainly in the eastern side of the channel near St. David's headland. In the Bristol Channel area, subtidal velocities were noisy and irregular, however, a westward flow in the northern Bristol Channel entrance and an eastward flow at the southern side of the channel entrance can be identified.

The subtidal velocity field showed a southwesterly flow along the southeastern Irish coast (Fig 6.17b). However, north of Nymphe Bank, the pattern was unclear in cruise CORY998 (Fig 6.17b) and velocities were in the opposite direction to the density driven currents expected in CORY798 (Fig 6.17b). Unresolved tidal motion and systematic error (due to the instruments) could however be included in the residual results. Nevertheless,

they are expected to be consistent. On the other hand, it is important to consider that residuals represent the instantaneous subtidal velocity field and their behaviour could reflect a natural variability in the actual flow field responding to a different forcing than density driven forcings. An outstanding candidate of such forcing is the wind in the area. However, a closer comparison between the velocities and the prevailing wind during the measurements showed variability in the direction and strength of wind, which did not help to elucidate this apparent inconsistency in the residual velocity pattern. In addition, the analysis of possible forcings of the drifter trajectories (Chapter 5) did not show strong wind correlation.

Nevertheless, in general terms, the residual currents (Fig 6.17) agreed with density driven currents (Fig 4.21) and with drifter results (Fig 5.12), particularly in respect of a cyclonic flow pattern in the actual region of the northern Celtic Sea, away from land boundaries.

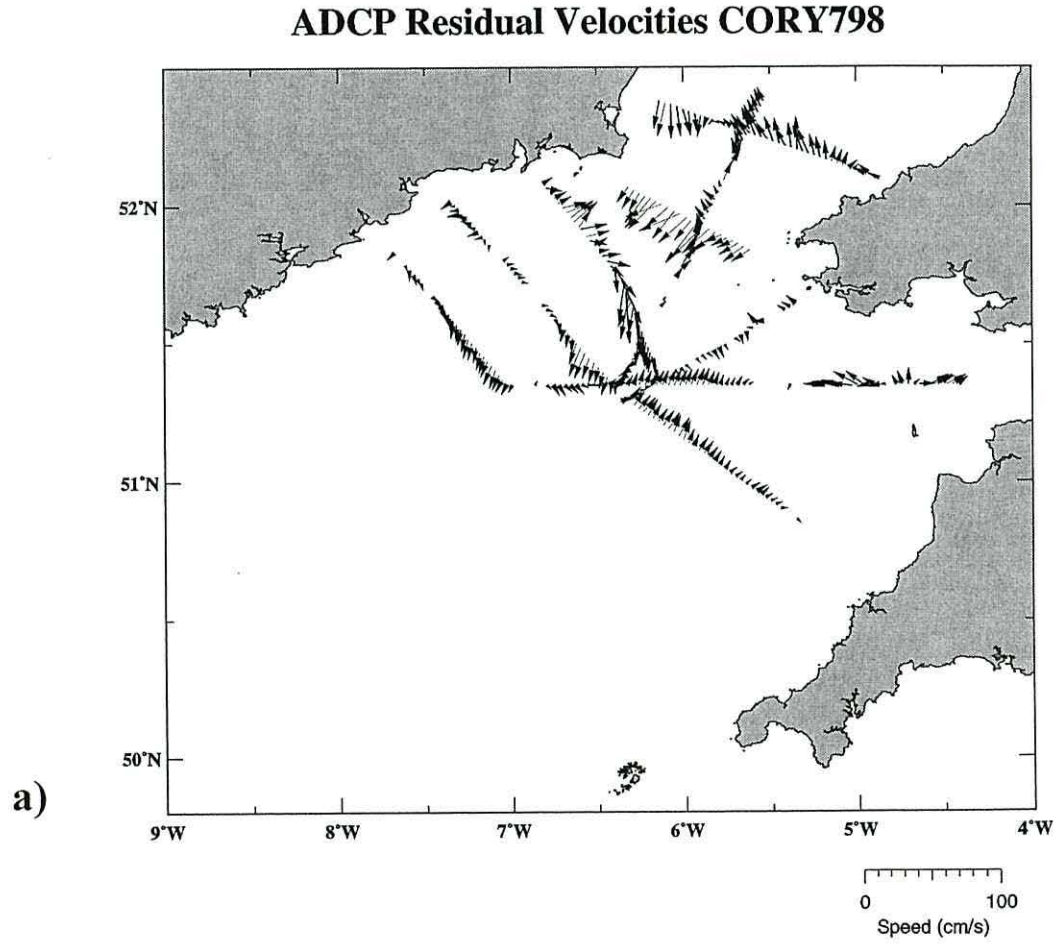

a)

Figure 6.17 Subtidal velocities obtained applying the blending technique the depth averaged velocities. a) CORY798 and b) CORY998 (next page). Scale is displayed at the bottom right of the panels.

b)

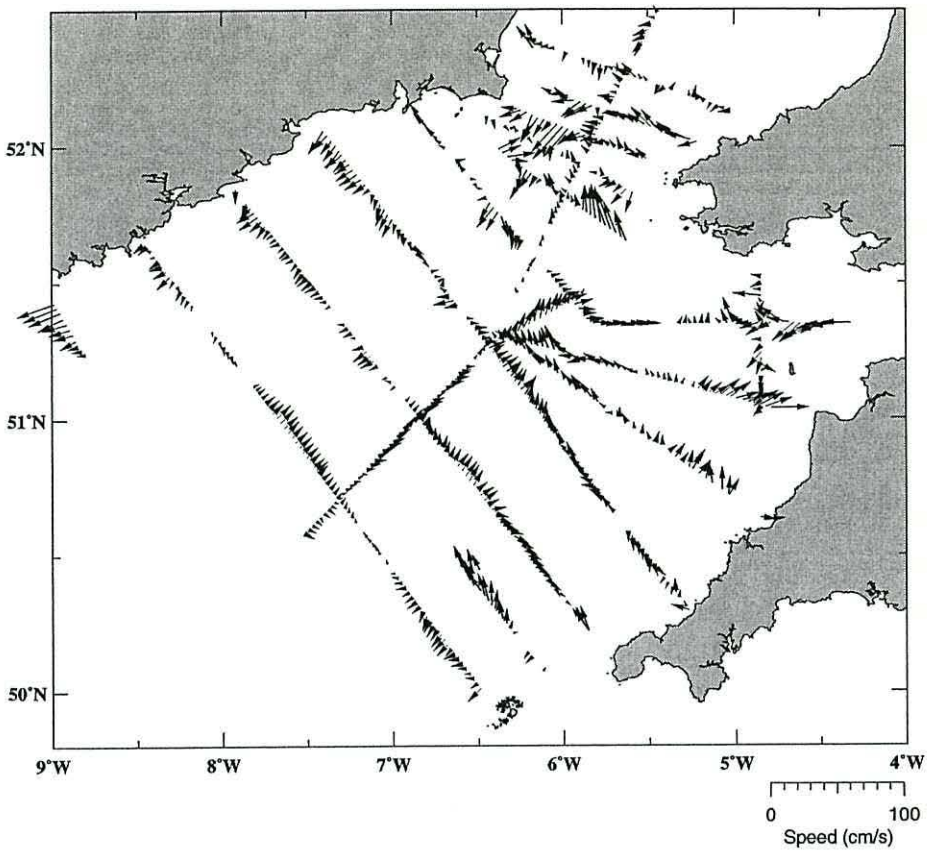

Figure 6.17 Continued.

6.4.2 Vertical structure of the residual currents

A complete three-dimensional picture of the residual field can only be obtained by applying detiding to the vertical velocity structure. Here, the vertical structure of the subtidal currents from the ship-mounted ADCP data was obtained using the linear combination of a simplified analytical tidal profile (explained later) for the model detiding technique and the numerical approach from the polynomial and least square detiding technique.

Before discussing the residual results for the cross-sections, it is useful to compare the two tidal current profile approaches (model and least squares) with the raw data. In the case of the model, the tidal current profile was derived from a theoretical analytical profile proposed by Prandle (1982) based on boundary layer theory (see Appendix 6). The numerical approach to obtaining the vertical structure of the tidal currents from the ship-mounted ADCP used here consisted of the application of the polynomial and least square approximation, as explained in section 6.2.2, to each depth cell.

Figure 6.18 shows examples of the vertical structure of the measured velocity (raw-data), the theoretical and numerical tidal profiles. In general, the tidal profiles obtained with the Prandle's theoretical approach presented a smoother curve shape than with the polynomial-least square. With the latter method a profile more similar to the observed raw data was observed because that vertical tidal structure was in principle captured from the data. However, both methods tended to present a broadly similar profile shape with some under- and over-estimations of the magnitude of the tidal current because the simplicity of the methods to approach the *real* tidal profile. The linear combination is expected to reduce the noise from each method and improve the results. On the other hand, it is important to consider that most of the measurements were performed in stratified water columns and a decoupling of the tidal currents associated with a reduction in the eddy viscosity in the pycnocline can cause abrupt changes in tidal phases across the pycnocline (Maas and van Haren, 1987; Hill, 1998b), which was not considered in the analytical profile (Prandle, 1982).

From the profiles (Fig 6.18), it can be observed that the main contribution to the magnitude of the velocities in the profile was the tidal barotropic profile, however the vertical structure of the measured currents showed high variability. Dissimilarities with the barotropic tidal profile represent the subtidal currents, which in all the cases were stronger

and more variable in the top 40 metres, above the pycnocline. This can be expected since the surface water column is more susceptible to the influence of other forcings such as wind and density gradients (*e.g.* bottom fronts as observed from the vertical structure of the velocity derived by the geostrophic calculations). Thus, the strongest velocities are expected above the bottom fronts with a strong pynocline located at approximately 40m (see Chapter 4). This can be clearly observed in the cross-sections presented next.

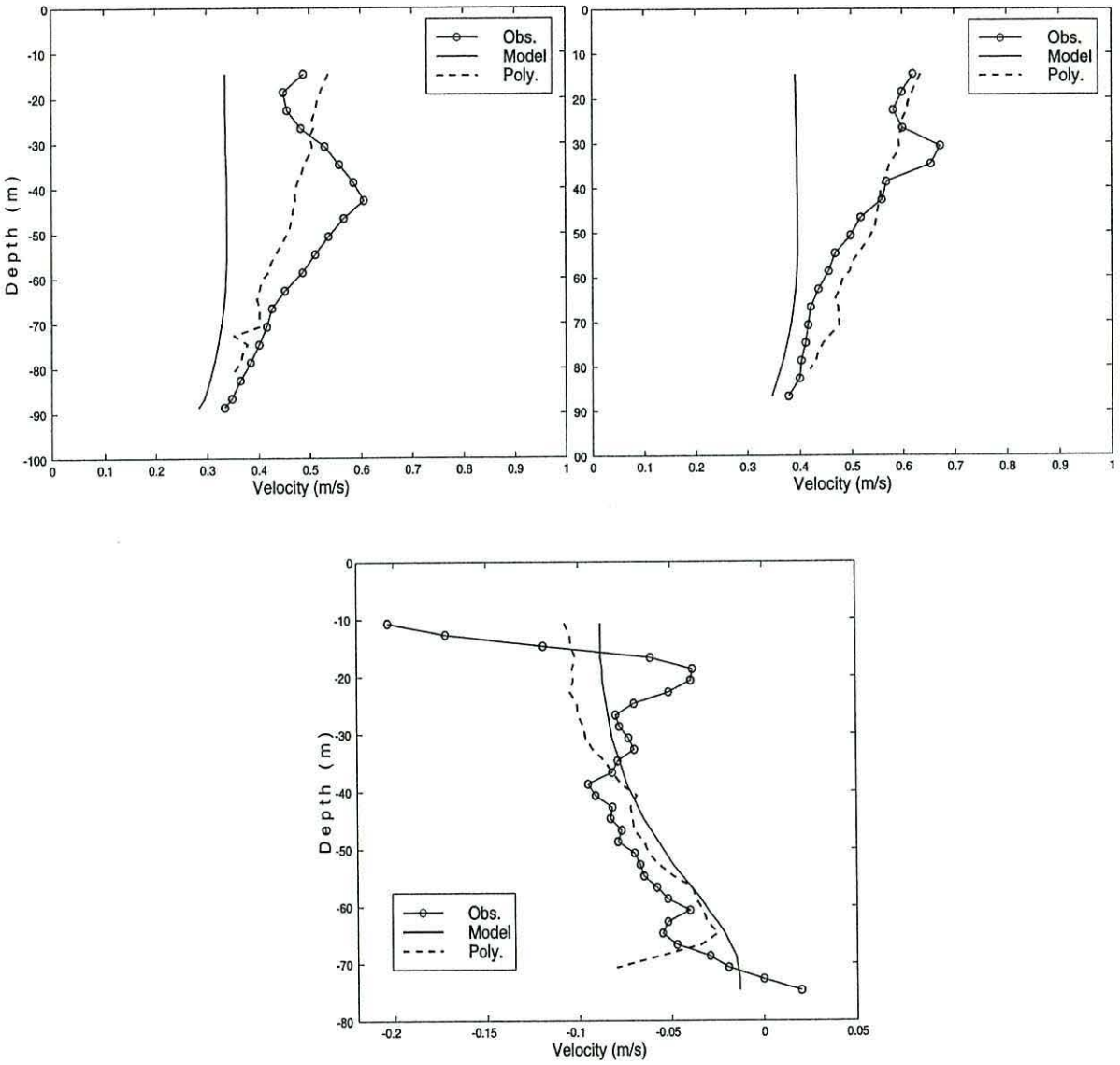

Figure 6.18 Comparison of vertical profiles of observed (circles and solid line) and predicted vertical profiles from numerical model (solid line) and polynomial method (dashed line). Only 3 examples are shown for illustrative purposes.

6.4.3 Cross-sections

Figures 6.19 to 6.23 show the vertical structure of the subtidal currents derived from the linear combination of both methods for cross-sections in the same areas of the Celtic Sea as presented in chapter 4. The cross-sections are: North-south section (Fig 6.19); central St. George's Channel section (Fig 6.20); southern entrance of the St. George's Channel (Fig 6.21); west-east cross-section passing through the centre of the Celtic Sea (Fig 6.22); and finally a transverse section at the mouth of Bristol Channel (Fig 6.23). The remaining cross-sections are shown in Appendix 7. Tidal residual currents are presented in u- and v- components (*i.e.* west-east and north-south, respectively) in order to maintain consistency with the general circulation context, instead of the traditional along- and across-frontal components, which is difficult to obtain due to most of the sections being oblique to the fronts. Additionally, the geostrophic velocities derived from the density field and the vertical structure of the density field are shown. Conventionally, in the ADCP residuals, blue solid contours represent positive values and red dashed contours represent negative values of the velocity. In the geostrophic velocities, blue solid contours represent water going into the page, red dashed contours represent water out of the page. Here only flows > 0.05 m s^{-1} are presented for clarity

In the north-south cross-section (Fig 6.19) jet-like flows can be identified in the ADCP residuals (Figs 6.19a and 6.19b). The u-component residuals (Fig 6.19a) showed a relatively strong westward flow (up to 0.20 m s^{-1}), located at 210-240 km distance from the x-axis, where the strongest bottom fronts were located and with a maximum centred at 30 m depth (Fig 6.19c). This flow showed approximately the same shape and position as the westward calculated geostrophic velocities normal to the section (Fig 6.19d), however, the observed residuals were 0.10 m s^{-1} smaller than the geostrophic calculation. The v-component residuals (Fig 6.19b), indicated a core of a northward flow with velocities up to 0.15 m s^{-1} approximately the same position as the westward flow indicated by the u-component (Fig 6.19a). Thus, a northwestward flow was captured by the ADCP at the frontal region of the St. George's Channel. Another core of strong surface residuals was located at 260 km distance from the x-axis. However, the maximum of this surface flow was confined near the surface, however, this flow was weakly obtained by the geostrophic calculations with values up to 0.12 m s^{-1} (Fig 6.19d). The bottom fronts were not observed in this location (Fig 6.19c). Outside the frontal area, considerable near surface (above 40 m depth) flows up to 0.10 m s^{-1} and 15 m s^{-1}, in the u- and v-component respectively (Figs

6.19a and b), were observed. However, between 100-140 km distance from the x-axis (central Celtic Sea), velocities were smaller than 0.05 m s^{-1}. Velocities (Figs 6.19a and b) associated with the eddy-like feature (60-100 km distance in Fig 6.19c), did not show a clear anticyclonic circulation associated (Fig 6.19d), combining u- and v-components gave a southeastward flow between 80-100 km distance and a northeastward flow between 60-80 km distance (Figs 6.19a and 6.19b). In the remaining southernmost part of the section, velocities were mostly northeastward (between 20-60 km distance) and slightly more southward direction at 0-20 km distance from x-axis. It is important to note that the highest velocities were observed near the surface above 40 m.

More direct evidence of the jet-like flows associated with the margin of bottom fronts is found in the sections crossing the frontal areas of the St. George's Channel (Figs 6.20 and 6.21). In this section, the v-component (Fig 6.20b and 6.21b) can be more directly related to the normal velocity to the section (*i.e.* as are the calculated geostrophic velocities; Figs 6.20d and 6.21d). Observed residuals and geostrophic velocities were similar. The v-component (Figs 6.20b and 6.21b) showed the same order of magnitude and nearly the same position as the calculated geostrophic velocities. Residual velocities, in particular the v-component (Figs 6.20b and 6.21b), were concentrated in jet-like flows 20 km wide with a core of maximum velocity (up to 0.40 m s^{-1}) concentrated at approximately 20-40 m depth above the pycnocline (Figs 6.20c and 6.21c). Residuals in the u-component (Figs 6.20a and 6.21a) showed westward flows in most of the cross-channel area, with a more northeastward coastal flow on the western side of the channel in the southernmost cross-section (Figs 6.20a and 6.21b).

In contrast, residual velocities in the west-east cross-sections (Figs 6.22a and b) showed a weaker and disordered structure. These residuals were more difficult to compare with the calculated geostrophic velocities (Fig 6.22d), because the u- and v-component are not directly related to the velocities normal to the section. In addition, the frontal areas (Fig 6.22c) where not as strong as in the St. George's area (Figs 6.20c and 6.21c). Nevertheless, the northwestward flow between 150-200 km distance (Figs 6.22a and b) where the series of bottom fronts were located (Fig 6.22c). A southwestward flow near the Irish coast was observed (0-50 km distance from the x-axis; Figs 6.22a and b) and probably related to the frontal area (Fig 6.22c). On the other hand, there were considerable velocities (Fig 6.22a and b), up to 0.20 m s^{-1}, that cannot be associated with the bottom density fronts (Fig 6.22c), particularly in the central area of the Celtic Sea, as seen in the

north-south section (Fig 6.19a and b). Also, in this section a northwestward narrow (~ 10 km width and ~90 km distance from the x-axis) flow (Fig 6.22a and b) was located immediately besides the right flank of the bottom front (Fig 6.22c).

In a cross-section in the Bristol Channel (Fig 6.23), the u-component represents the normal velocity to the section and can be directly compared with the calculated geostrophic velocities. The u-component residual (Fig 6.23a) agreed with the geostrophic field estimated (Fig 6.23d). Clearly, a relatively near-surface strong northwestward flow (up to 0.20 m s^{-1}) at the northern entrance of the Bristol Channel (located between 15-20 km distance from the x-axis) was observed (Fig 6.23a). Other predicted (*i.e.* geostrophy) westward flows (Fig 6.23c) at ~55-60 km distance from the x-axis with velocities up to 0.12 m s^{-1} were comparable with the u-component velocities (Fig 6.23a) in this area. The v-component (in this case along the section), (Fig 6.23b) showed that approximately at the northern entrance (0-40 km) flows were northward and towards the central and southern entrance were more southward.

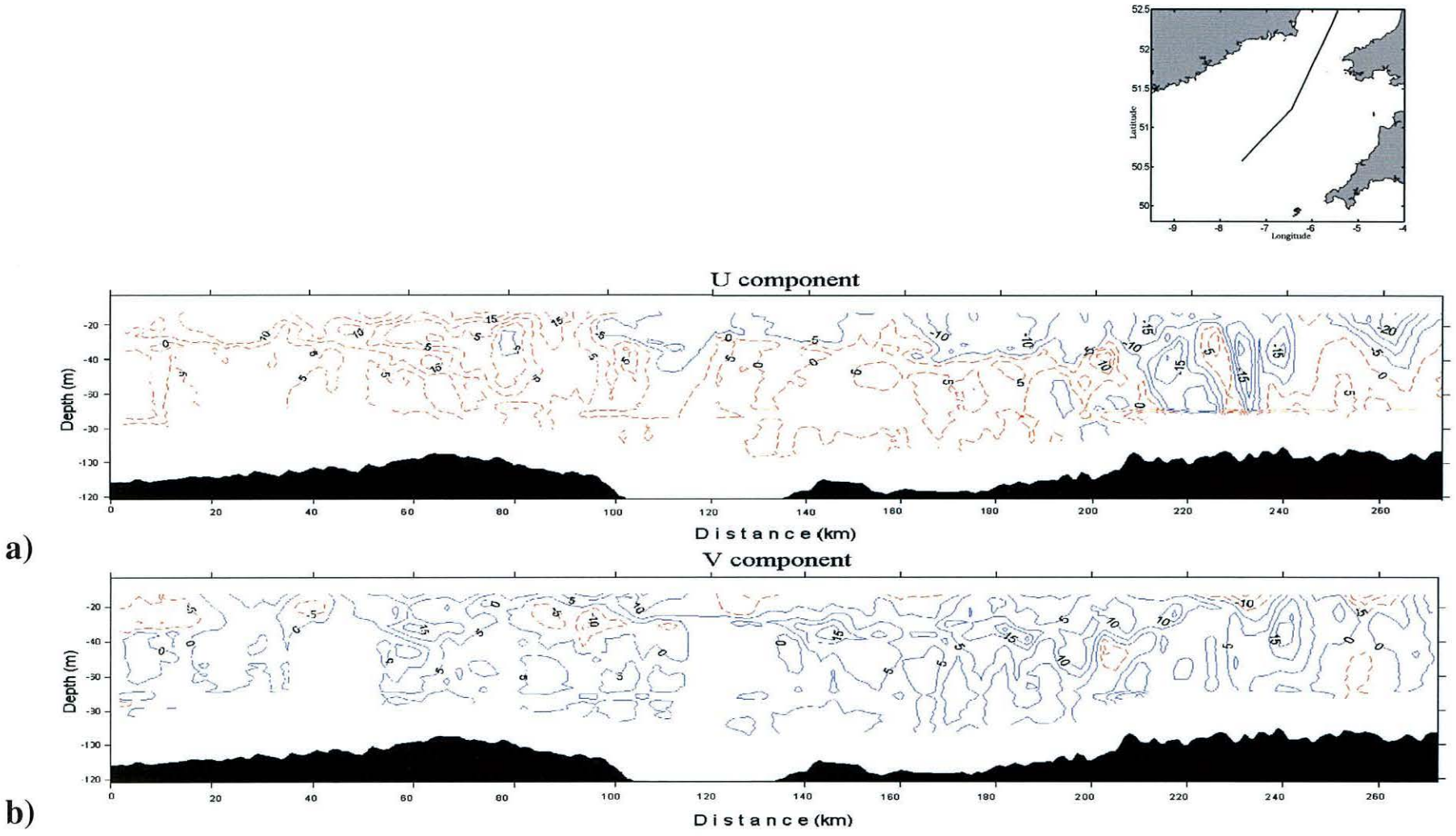

Figure 6.19 Vertical structure of the ADCP residuals for a cross-section from north to south (Leg 202 and 190) (top-right corner panel shows location). a) U-component (west-east), b) V-component (north-south). Next page: c) density (σ_t) in kg/m^3 and d) geostrophic velocities. Velocities in cm s^{-1}.

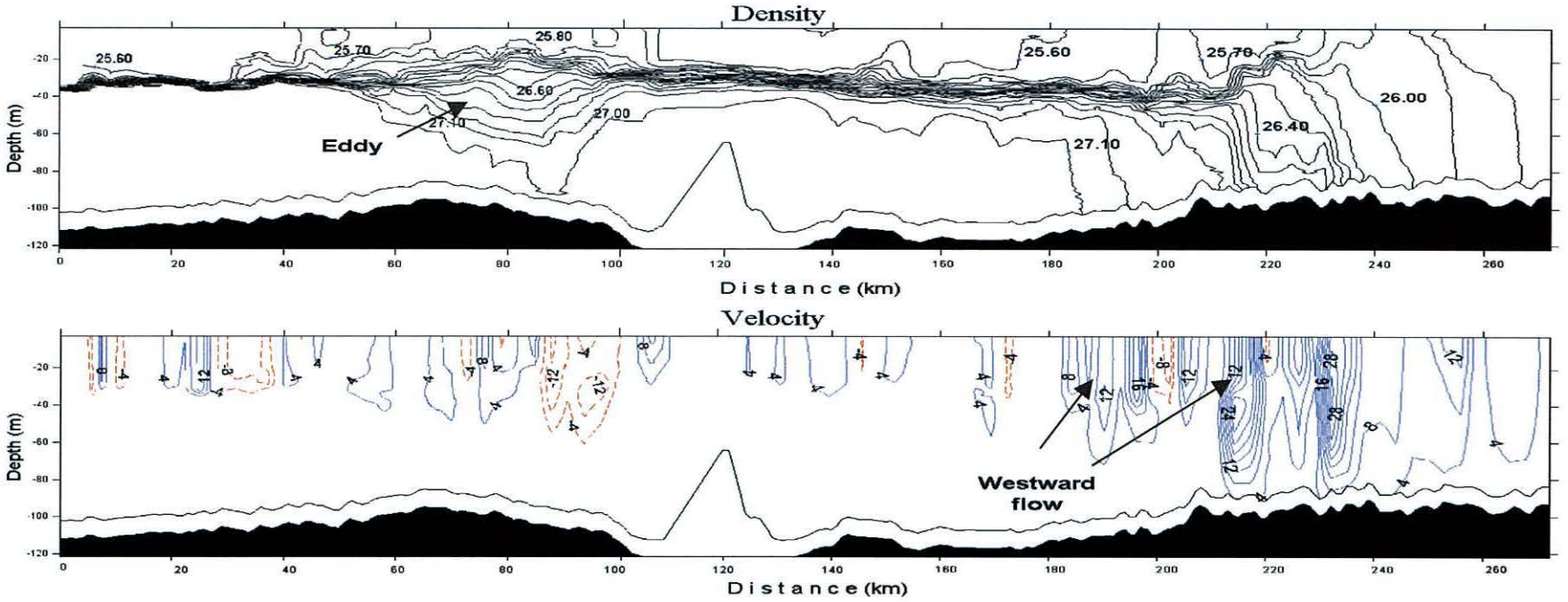

Figure 6.19 Continued from previous page.

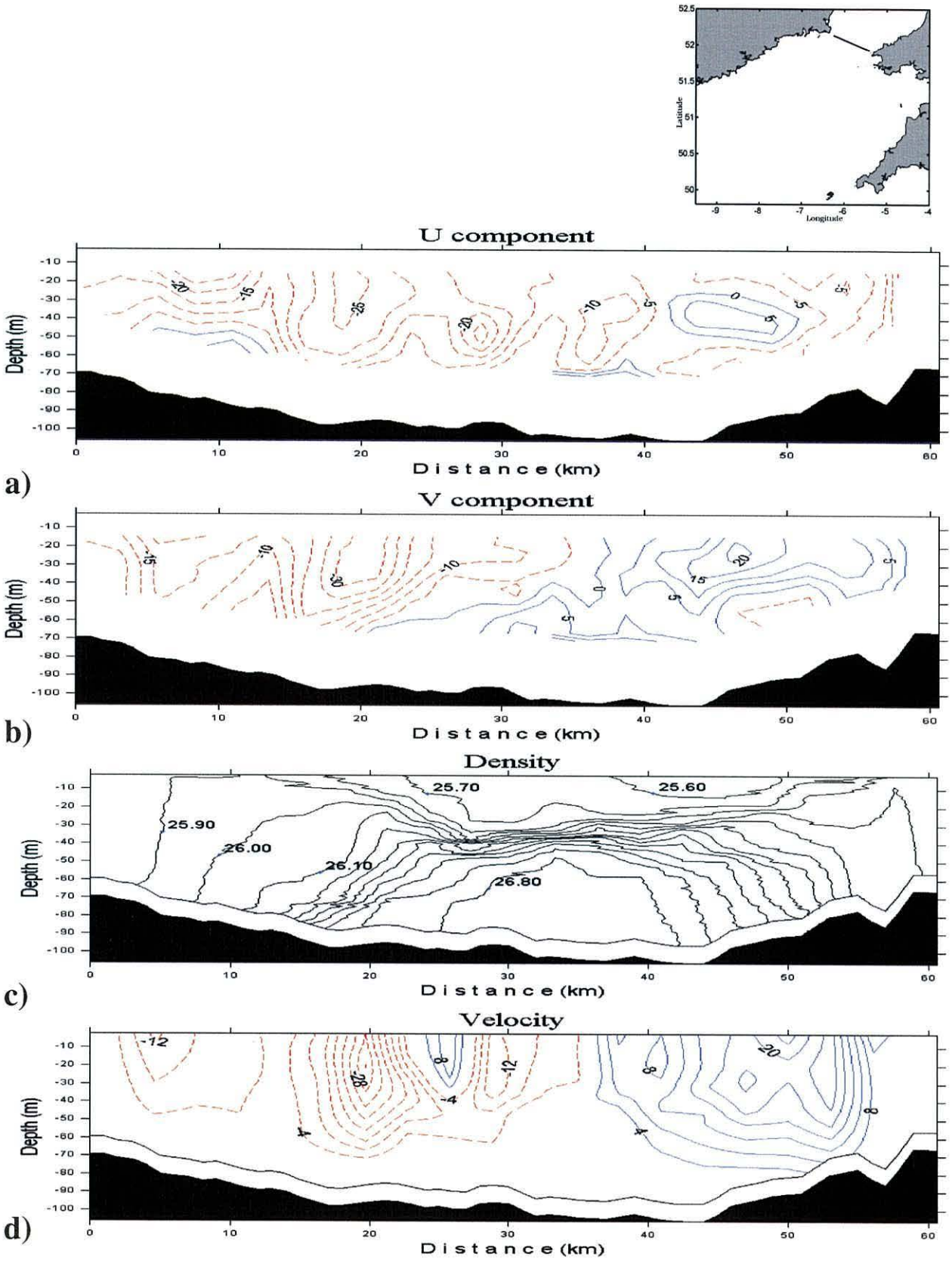

Figure 6.20 ADCP residuals for Leg 209 (top-right corner panel shows location). a) U-component (west-east), b) V-component (north-south), c) density (σ_t) in kg m^{-3} and d) geostrophic velocities. Velocities in cm s^{-1}.

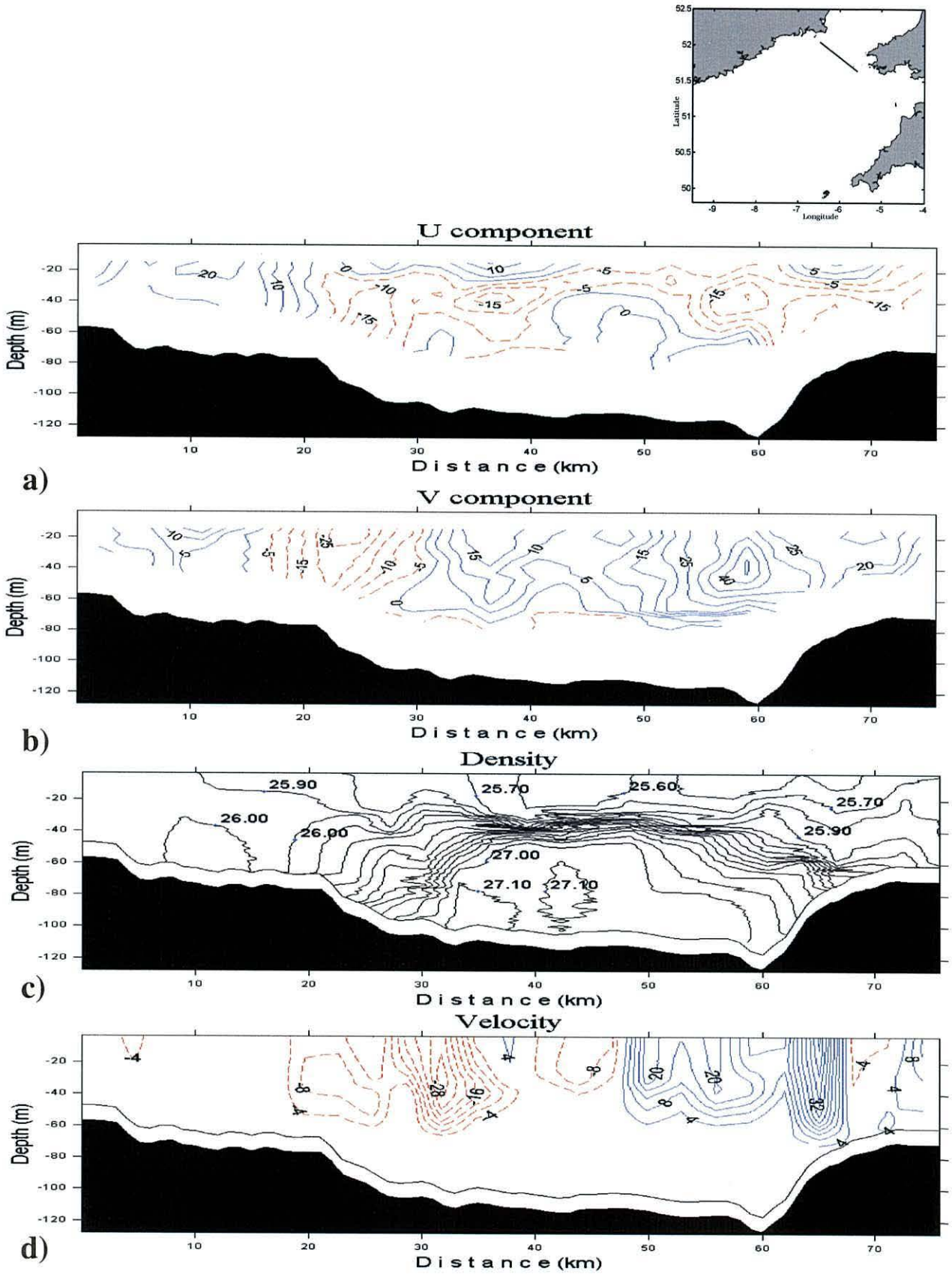

Figure 6.21 Vertical structure of the velocity residual field for Leg 213 (top-right corner panel shows location). a) U-component (west-east), b) V-component (north-south), c) density (σ_t) in kg m^{-3} and d) geostrophic velocities. Velocities in cm s^{-1}.

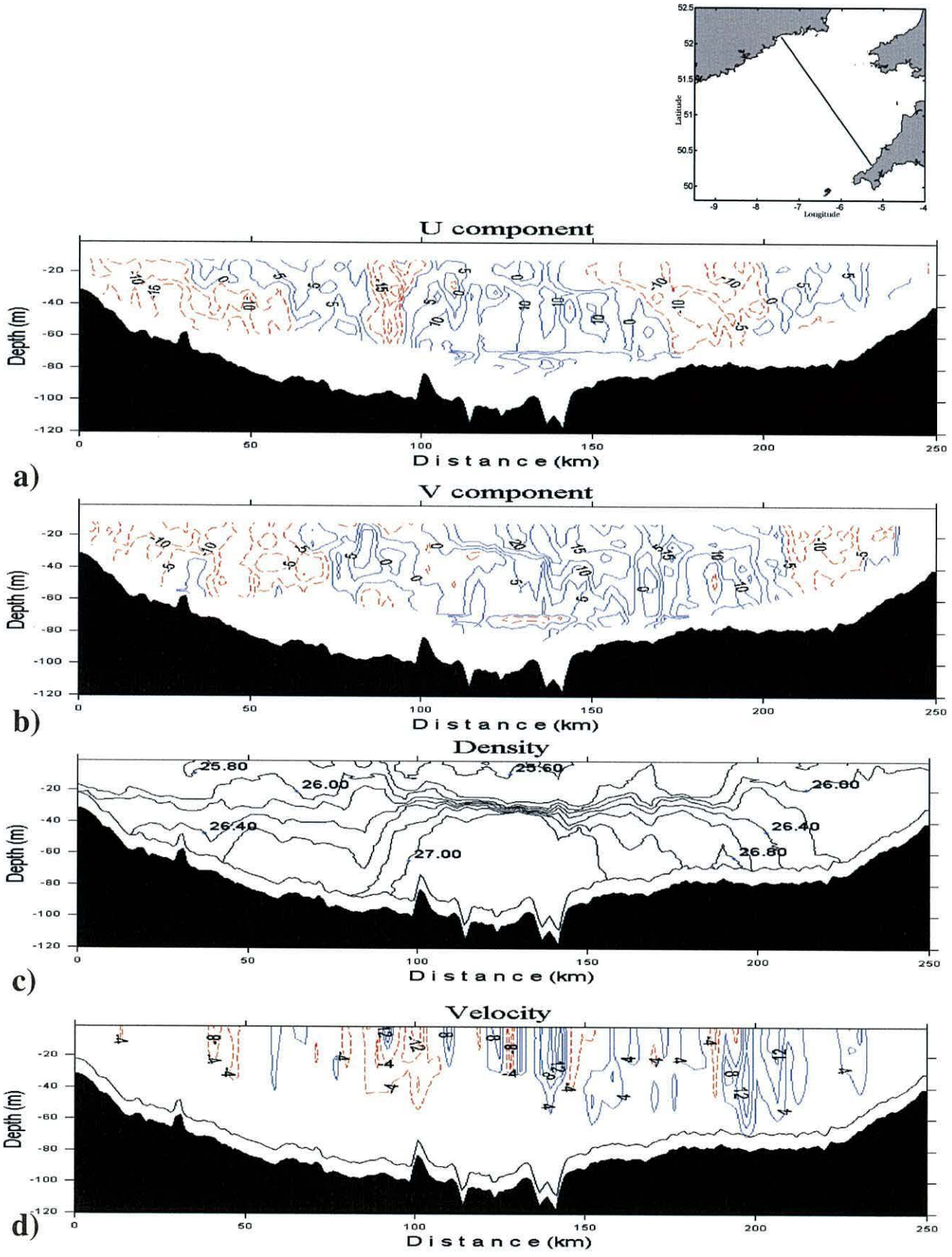

Figure 6.22 Vertical structure of the velocity residual field for Leg 182 (top-right corner panel shows location). a) U-component (west-east), b) V-component (north-south), c) density (σ_t) in kg m^{-3} and d) geostrophic velocities. Velocities in cm s^{-1}.

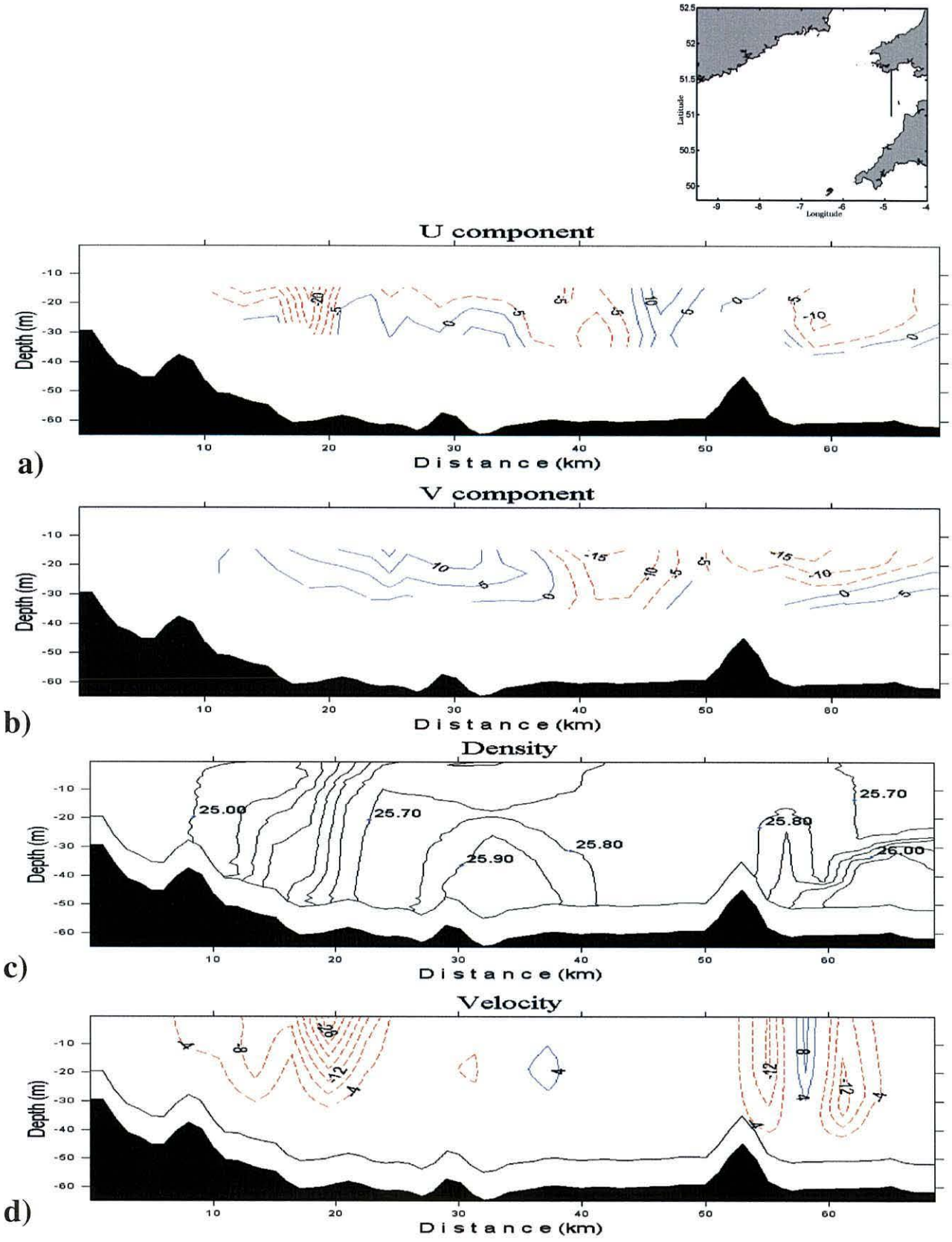

Figure 6.23 Vertical structure of the velocity residual field for Leg 223 (top-right corner panel shows location). a) U-component (west-east), b) V-component (north-south), c) density (σ_t) in kg m^{-3} and d) geostrophic velocities. Velocities in cm s^{-1}.

6.5 ADCP Bottom-mounted: Variability of the subtidal currents

In order to have more insight about the temporal variability of the velocity field of the study area, two bottom-mounted ADCP were used (Fig 6.24). Technical details of these instruments were described in section 3.5.4. One of these bottom-mounted ADCPs was located at the centre of the St. George's Channel (location J in Fig 6.24) at 104 m depth and operated for 45 days, the other was located in the Nymphe Bank area (location I in Fig 6.24) at 73 m depth and lasted for 41 days. The tidal currents were obtained by applying harmonic analysis to the ADCP moored data for the six main components (M_2, S_2, N_2, O_1, K_1 and M_4,) as proposed by Godin (1972). Non-tidal residuals were obtained by subtracting the tidal currents from the ADCP observations.

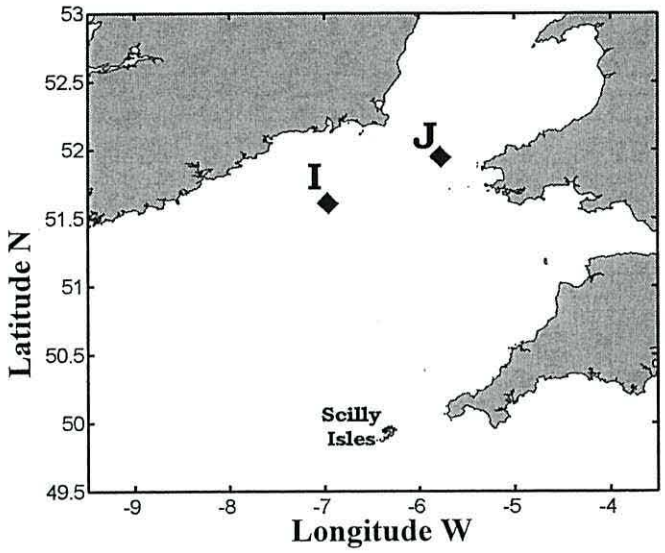

Figure 6.24 Map showing the locations of the two bottom-mounted ADCP moorings.

Figure 6.25 shows the time series of residual velocities from the mooring J located at the centre of the St. George's Channel. Residual velocities for the west-east component (u-component) (Fig 6.25a) were one order of magnitude stronger than for the north-south (v-component) (Fig 6.25b). The u-component velocities (Fig 6.25a) were near bed weak (< 0.05 m s^{-1}). However, they were stronger above 60 m depth, with cores of high velocities (0.20 m s^{-1}) centred between 30 and 40 m depth. In general, mooring J showed a near-surface westward flow centred at ~ 30-40 m with velocities up to 0.20 m s^{-1}, but in short periods (~ 10 days), velocities < 0.05 m s^{-1} were observed, perhaps associated with neap-spring tides. The north-south component (Fig 6.25b) was weak, velocities < 0.05 m s^{-1} mainly in a northward direction. These results agreed with the calculated geostrophic velocities and with ship-mounted ADCP observations for the central area of the St.

George's Channel where a westward flow was observed. Also, these results showed direct evidence of the westward flow that turn some drifters that passed over this area.

The second mooring (I) located at the Nymphe Bank area (Fig 6.24) showed relatively weak non-tidal residuals for most of the operating time (Fig 6.26). Velocities in the u-component (Fig 6.26a) were < 0.05 m s^{-1} in either west or east direction. However, by approximately Julian day 232, a strong westward flow reaching speeds up to 0.22 m s^{-1} was observed, with a core of maximum speed centred at ~ 30 m depth. V-component (Fig 6.26a) showed mostly northward velocities fluctuating between 0.02 and 0.06 m s^{-1} with an unclear periodicity. In addition, non-constant near surface (above 20 m depth) southward currents with speed up to 0.08 m s^{-1} were observed. As was noticed at mooring J (Fig 6.25), at mooring I (Fig 6.26) the highest speeds occurred above 40 m depth, *i.e.* above the thermocline. This is an important result, because it supports the prediction of surface flows driven by density bottom fronts. These results also confirm that a natural variability in the surface flows exists.

In order to estimate the wind influence upon the measured current from the bottom mounted ADCP, a complex least-squares regression was performed, as explained in section 5.5.1 for the drifter and wind data. Filtered wind data from a station located on the Scilly Isles (Fig 6.24) from British Atmospheric Data Centre was used. Results from this analysis are shown in Figure 6.27. The values of the goodness of the fit is given in percentage for each bin depth, the values represent the explained variance. Both moorings showed low values of correlation (Figs 6.27a and 6.27b), the values of the goodness of the fit were never > 15 %. However, the maximum was located at ~ 30 m, around the thermocline. These values showed that the wind was not the direct forcing mechanism of the observed flows.

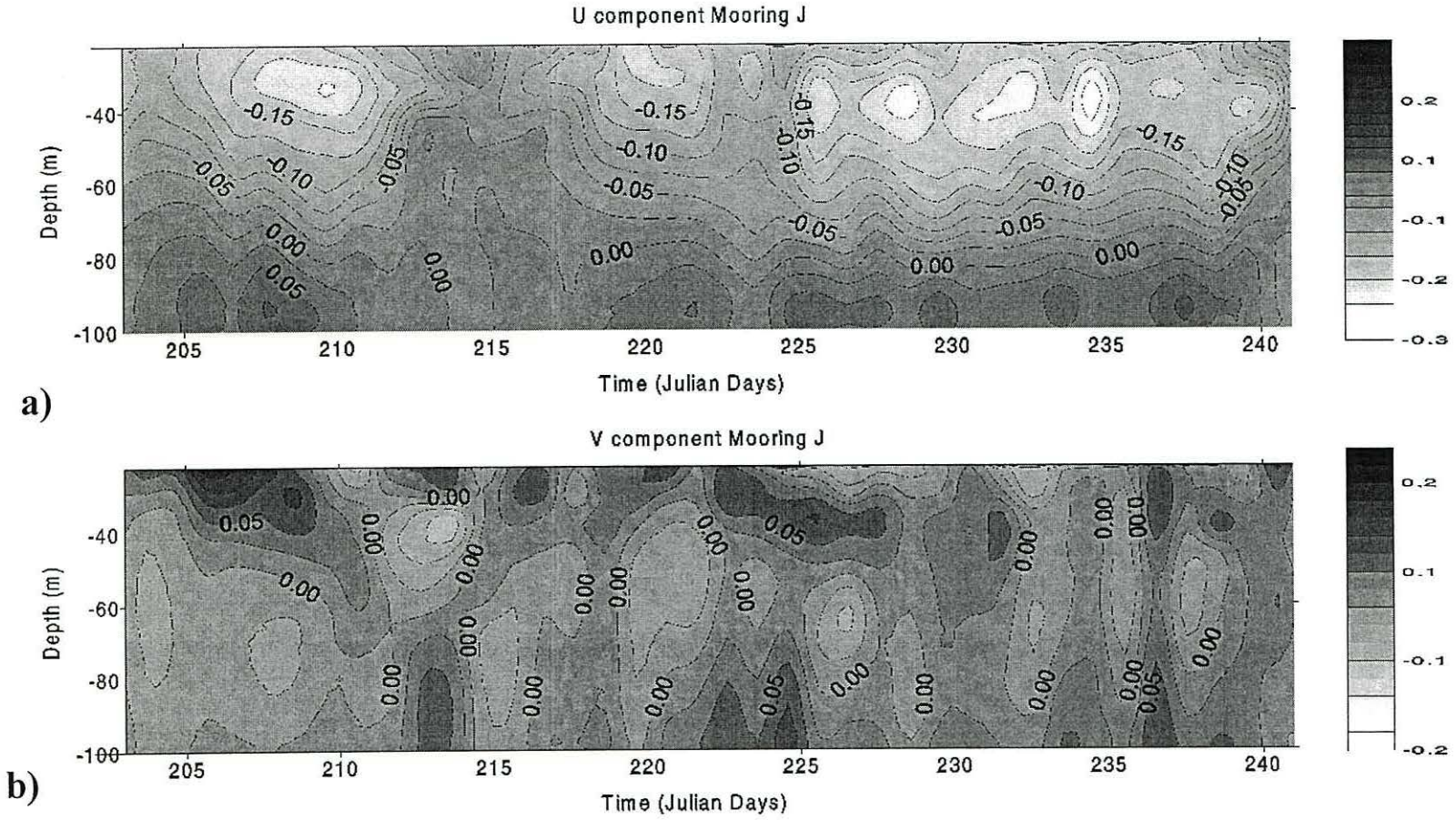

Figure 6.25 Time series of the residual velocity profile from the mooring J located at the centre of the Saint George's Channel. a) u-component (west-east) and b) v-component (north-south). Time is in Julian days and velocity in m s^{-1}.

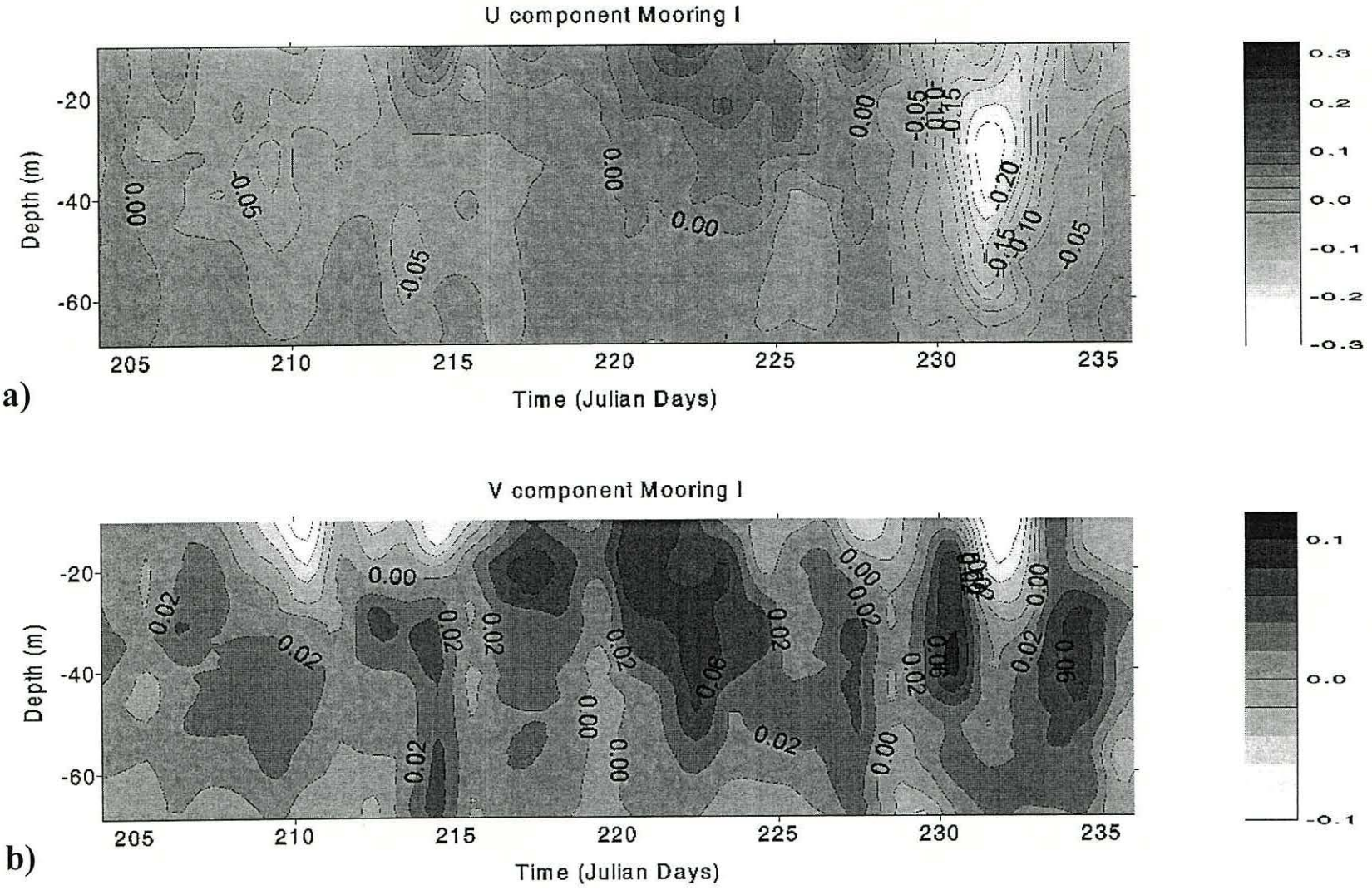

Figure 6.26 Time series of the residual velocity profile from the mooring I located at the Nymphe Bank. a) u-component (west-east) and b) v-component (north-south). Time is in Julian days and velocity in m s^{-1}.

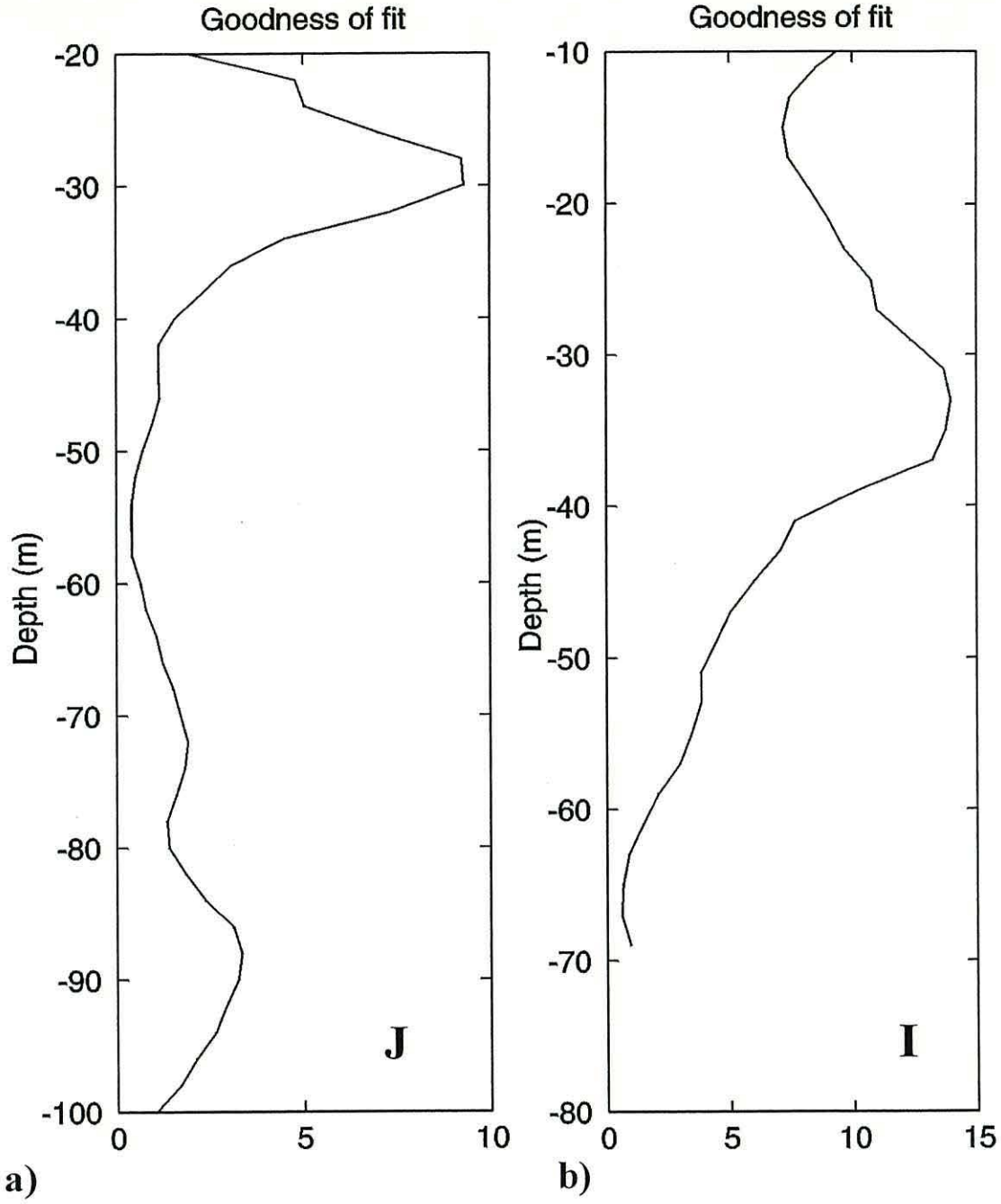

Figure 6.27 Vertical distribution of the explained variance expressed as the percentage of goodness of the fit for a) Mooring J and b) Mooring I.

6.6 Summary of main findings

In this chapter, the removal of the tidal signal from ship-mounted ADCP data and the analysis of their residuals was performed. Two conventional techniques to detide ship-mounted ADCP data were applied in the study area; a numerical model by Davies and Jones (1992b) and a numerical approximation to the data using polynomial spatial interpolation and least square as proposed by Candela *et al.* (1992). Although, the overall tidal current predictions from both methods were relatively similar, it is important to consider that some limitations of the methods were observed. Large values near the boundaries of the data distribution and underestimation and overestimation probably due to the simplicity of the functions used in the case of the polynomial and least square interpolation and due to the poor resolution of the dynamical model approximation. The limitations of both methods in solving the spatial tidal variations satisfactorily stimulated a search for a more reliable detiding technique. With the aim of obtaining the subtidal signal, an alternative detiding procedure was proposed, called here the *blending* technique. This is a linear combination of measured and modelled data and resembles the blending scheme used in data assimilation. This procedure consisted of a weighted averaged (linear combination) of the tidal results from the both techniques already mentioned and showed better results than the individual performance of each method alone.

Ship-mounted Acoustic Doppler Current Profiler (ADCP) measurements are routinely obtained in most of the oceanographic surveys and they often finish stored in a databank because of the unreliability of the detiding techniques. Neither detiding technique extracts the *real* tidal current field. However, in this thesis it has been shown that a combination of tidal currents from both the numerical dynamical model and the ADCP data will prove valuable in detiding tidal currents from ship-mounted ADCP measurements. On the other hand, while imperfect, the least squares method seems to resolve relatively well the tidal currents. It would be an interesting future avenue for research to explore more dynamical spatial functions and the normal modes of the tidal wave in the European shelf sea areas.

By considering the residuals obtained from the blending technique, a consistent overall horizontal residual circulation showing a similar cyclonic flow field portrayed by the drifters and geostrophic calculations was obtained. Estimated residuals showed relatively strong jet-like flows in regions with strong horizontal density gradients, as

expected from geostrophy, *i.e.* in Saint George's Channel. Although, the overall horizontal residual circulation agreed well with calculated geostrophic velocities, other flows, which were not directly related to frontal areas, were measured. These flows seemed essentially not as organized as the jet-like flows observed in the frontal areas. This variety of the flows in the horizontal velocity field of the Celtic Sea was observed, which also was identified by the measured Lagrangian field from drifters (chapter 5).

The vertical structure of the residuals from both bottom-mounted and ship-mounted ADCP measurements added evidence to the hypothesis of bottom density fronts as forcing mechanisms to drive the near-surface jet-like flows in the frontal areas of the Celtic Sea and St. George's Channel. The measured residual flow in the vicinity of each strong density bottom front has certainly points of similarity with calculated geostrophic flows, since each of the sharp horizontal bottom density gradients showed near surface (above 40 m depth) jet-like flows on the flanks of the bottom fronts. On the other hand, the observed residuals were sometimes weaker than the calculated geostrophic velocities. Other flows not associated with bottom frontal areas were observed. However, all the strongest flows were observed near the surface (*i.e.* above 40 m depth) above the location of the pycnocline, which suggests the susceptibility of the surface layers to other forcing. Moreover, ADCP-residuals represent instantaneous velocities and other subtidal signals such as wind, eddies and internal waves. Additional research is needed to elucidate this variability in the flow field. Nevertheless, the long-term circulation during the summer in the Celtic Sea seems to be consistent with density driven currents (baroclinic forcing).

To reproduce these observed features is a challenge for numerical models. A comparison of the hydrographic field and the velocities measured with results from a baroclinic three-dimensional regional-scale numerical model developed by the Proudman Oceanographic Laboratory for the shelf areas around the British Isles is explored in the next chapter.

Chapter 7

Comparison of observations with the POL 3D-Baroclinic European shelf model

7.1 Introduction

Coastal and shelf numerical models have been used to bring more insight into the dynamics of regions under study and to simulate a wide range of conditions and phenomena such as: plankton blooms, pollutant movement, sea level, temperature, salinity, sediment transport, etc. Whatever the use of the numerical models, their credibility depends on their capability to reproduce direct observations. In the particular case of baroclinic numerical models, this entails their ability to reproduce hydrographic features and to forecast reliable density-driven flow field. Thus, one of the most important tasks is the comparison of the model simulations with reliable field observations.

A three-dimensional shelf-wide baroclinic model was developed by the Proudman Oceanographic Laboratory (POL 3D-B) for application in the North-Western European shelf sea area around the British Isles (Proctor and James, 1996; Holt and James, 1999). POL 3D-B model (described in the next section) was run to simulate the temperature and transports of sediments in the NW European shelf sea area during November 1988 to October 1989. Its results have been compared with the large data set provided by the North Sea project 1988-1989 with a qualitatively good agreement (Holt and James, 1999). However, direct comparisons have not so far be made in other areas, because there was a lack of reliable data outside the North Sea area, and in particular, in the Celtic Sea.

The results obtained from our observational campaigns during the summer of 1998 represent a challenge for POL 3D-B, or for any baroclinic numerical model, in the Celtic Sea. This chapter deals with a comparison of the POL 3D-B simulation, corresponding to August 1989, with the observations obtained in the CORY998 campaign. The aim of the comparison is to investigate if the model can reproduce the summertime density structure and velocity field. Thus, this comparison points out similarities, differences and limitations of the model results with respect to the observations. It is important to consider

that the model results correspond to a different year (1989) from the observations (1998). However, it is expected that the density structure and velocity field are robust enough features during the summertime, in particular bottom fronts and their associated near-surface velocities, hence only small interannual variability might be expected. Although, a POL 3D-B model simulation for 1998 is desirable, it was not practical because it requires a considerable preparation time for the atmospheric forcing data and the boundary conditions for such a specific year, which is not a trivial task. The prime purpose in this thesis is not modelling. The intention here is the comparison of the obtained observations with an existing baroclinic model run in order to gain more insight in to the summer circulation in the Celtic Sea.

7.2 POL 3D-Baroclinic model brief description

Before the results from the comparison are shown, some characteristics of the model are described here, although a detailed description of the model can be found in Holt and James (1999) and Proctor and James (1996).

The three-dimensional shelf-wide baroclinic model from the Proudman Oceanographic Laboratory, or simply POL 3D-B, is a finite difference model based on an Arakawa B-grid in the horizontal and sigma-coordinates in the vertical. Sigma-coordinates transform the varying depth to a constant interval depth (Fig 7.1) with the same number of grid points in the vertical (levels) at each geographical position (James, 1986). The model has 18 depth levels, which give a vertical resolution of 0.5 m in shallow areas and up to 8 m in deep areas. The model domain was the shelf around the British Isles (48° N to 63° N and 12° W to 13° E), however here only a subset was used (Fig 7.2). In the horizontal, the mesh-size is 1/9° latitude by 1/6° longitude *i.e.* ~12 km of horizontal resolution (Fig 7.2b). The bathymetry used was also a 12 km resolution. In shallow seas, it is important to consider the numerical solution of the advection scheme, because strong tidal advection causes numerical diffusion which can erode the density structure (Proctor and James, 1996). Therefore, to maintain horizontal gradients over a few grid points and minimize numerical diffusion a "Piecewise Parabolic Method" was used (James, 1996, Holt and James, 1999).

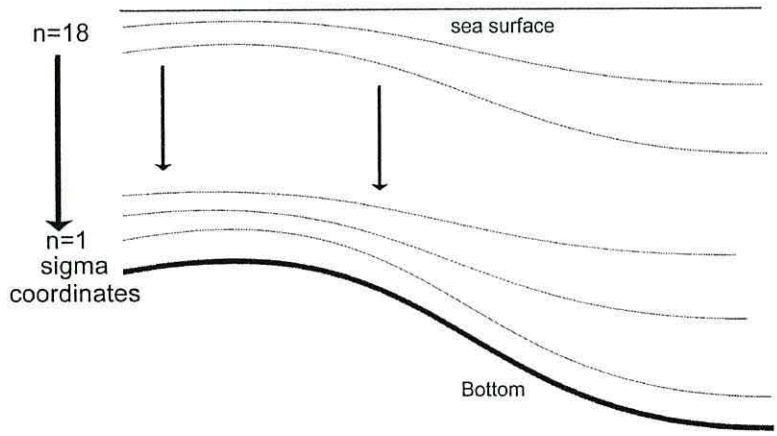

Figure 7.1 Schematic representation of the vertical gridding of the model as sigma coordinates. Sigma coordinates are referenced to the water depth transforming the vertical coordinates into n levels in every geographical position.

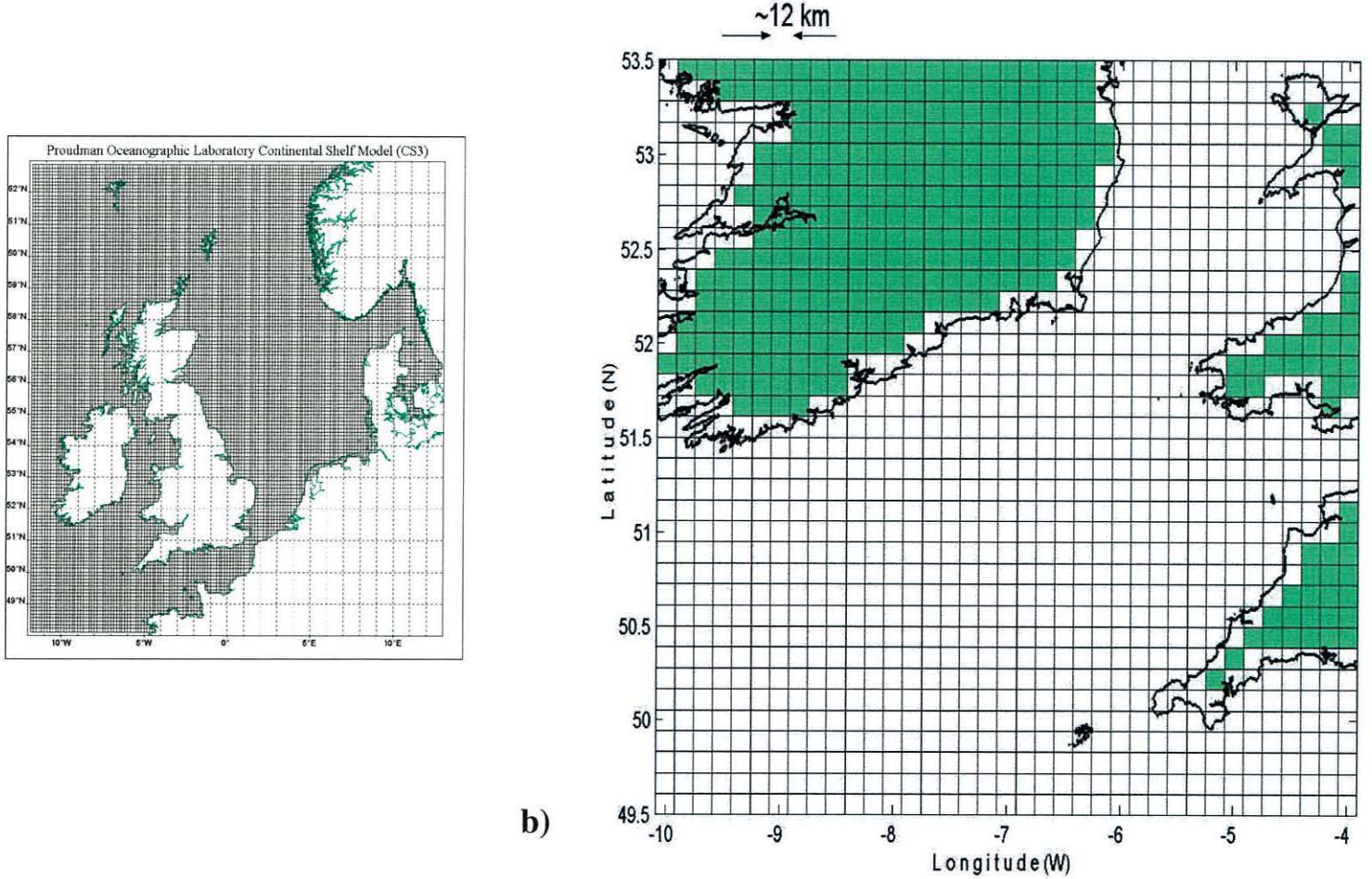

Figure 7.2 a) Domain of the POL-3D baroclinic model and area subsampled for the Celtic Sea area square. b) shows a close-up of the model in the Celtic Sea, grid size is shown at the top of the panel, green cells represent land in the model.

The surface forcing of momentum and heat used data from a UK Meteorological office model interpolated onto the POL 3D-B grid at 3 hourly intervals (Holt and James, 1999). The density field was controlled using a prognostically evolving temperature field forced by surface heat fluxes calculated using bulk equations using the algorithms of Goldsmith and Bunker (1979). These take account of the diurnal and seasonal variation of solar heating (Proctor and James, 1996). The meteorological variables were air temperature, pressure, relative humidity and percent cloud cover (Holt and James, 1999). The model temperature was updated using a down-welling irradiation scheme and at the sea bed a non-reflective condition was imposed, so any fraction of heat reaching the bed is lost (Holt and James, 1999). However, salinity was not considered to evolve in the simulation. The salinity field was the result of the distribution of the initial salinity field by the velocity field only. The narrow coastal zone, where freshwater influence can be expected, is not resolved by this grid size and fresh water sources were not included (Holt and James, 1999).

Vertical mixing was represented in the model using a Mellor-Yamada-Galperin level 2.5 turbulence closure scheme (Holt and James, 1999), and the open boundaries were handled by a flux/radiation scheme for momentum; temperature was not advected at the boundary (*i.e.* zero net advective heat flux) (Holt and James, 1999). Initial conditions were obtained after four years of simulation using wind forcing and meteorological conditions from the UK Meteorological office (Holt, personal communication). The model was initialized on 1 November 1988 with the mean temperature for that month from North Sea Project observations and finished on 31 October 1989. Table 7.1 summarizes the model characteristics and the forcing used in this simulation.

Table 7.1 Characteristics of the POL 3D-B model used for the simulation of the POL 3D-B simulation, corresponding to August 1989.

Application	Shelf Sea circulation
Spatial dimensions	Three-dimensional
Type of numerical model	• finite difference • Arakawa B-grid on the horizontal • sigma-coordinates on the vertical (18 levels)
Horizontal resolution	1/9° latitude by 1/6° longitude *i.e.* ~12 km
Vertical resolution	0.5 m - 8 m
Main Forcing Mechanisms	• Surface Heat • Tides • Wind
Vertical mixing scheme	Mellor-Yamada-Galperin level 2.5 turbulence closure scheme
Numerical solution for Advection scheme	Piecewise Parabolic Method
Open boundary conditions	• Flux/radiation for momentum • Zero net advective heat flux
Bathymetry	12 km resolution

7.3 Comparison with observations

We will concentrate the comparison of the hydrographic field in both the horizontal and the vertical, and also in the velocity field, in particular, around the frontal areas. The model results used in the comparison correspond to the nearest grid point to the observation position. It was found that selecting the model results in this way introduces less error than interpolation, which tends to over-smooth the values because the coarseness of the model grid.

7.3.1 Hydrographic comparisons

Horizontal field

Although of coarse grid-resolution, the model was able to reproduce the main temperature features (Fig 7.3a) shown in the observations (Fig 7.3b) and only some of the density field (Figs 7.3e and 7.3f), which are summarized next. The surface distribution of temperature and density in simulations (Figs 7.3a and 7.3e) showed the intrusion of cold water from the Irish Sea as in observations (Figs 7.3b and 7.3e), but differed in position and extension. The model results showed the intrusion constrained close to the Irish coast and it did not reach the central Celtic Sea (Figs 7.3a and 7.3e). On the other hand, the model showed the tongue of relatively warmer Celtic Sea water towards the Irish Sea at the eastern side of the St. George's Channel as in observations. In general, the model showed higher surface temperature than observations.

Comparisons with salinity are not appropriate because model salinity distribution depended on the advection of the salinity field prescribed by the initial conditions. Even when the density field is largely controlled by temperature (section 4.3), salinity affects it too, resulting in a poor agreement of the modelled density field (Fig 7.3e) with observations (Fig 7.3f) in areas with fresher water influence such as the Bristol Channel and the Irish Sea (Fig 7.3d).

Near the sea bed, the modelled temperature (Fig 7.4a) and density (Fig 7.4e) distributions showed roughly the same features as seen in the observations (Figs 7.4b and 7.4f). However the model did not show details such as the cold bottom water at the Celtic Deep observed in our measurement campaigns (Figs 7.4b and 7.4f). The simulation of the bottom temperature and bottom density (Figs 7.4a and 7.4e) displayed stronger horizontal gradients than observations (Figs 7.4b and 7.4f), in particular, near the Irish coast. In

addition, it is interesting to see that the isotherms from the model (Fig 7.4a) followed the shape of the Bristol Channel entrance and they were less curved in the observations (Fig 7.4d). Again, the simulated bottom salinity distribution (Fig 7.4c) differed from observations (Fig 7.4d). However, the tongue of salty water showed in observations (Fig 7.4d), approximately in the southeast of the Celtic Sea, was observed in the simulation too (Fig 7.4c), which implies that the tongue was the result of the advection of bottom water from the Atlantic.

In order to assess the capability of the model to reproduce the distribution of the stratification in the Celtic Sea, a comparison was made of the potential energy anomaly Φ (see section 4.3) calculated from model results and observations. In general, the spatial distribution of the stratification was reproduced by the model to first order for most part of the Celtic Sea and near-coast areas were well-mixed (Figs 7.5a and 7.5b). Although the Φ values were higher in the model (Figs 7.5a) than in observations (Figs 7.5b), the horizontal gradients of Φ were sharper in the observations than in the simulation (Fig 7.5a), in particular, around the St. George's Channel (Fig 7.5b). In addition, the observed closed contour (the value of $\Phi = 140$ J m^{-3}) around the Celtic Deep was not apparent in the model results, suggesting that the model Φ contours followed the coastal contours rather than the bathymetry. The relative importance of the bathymetry used in the model over the results is discussed in last section.

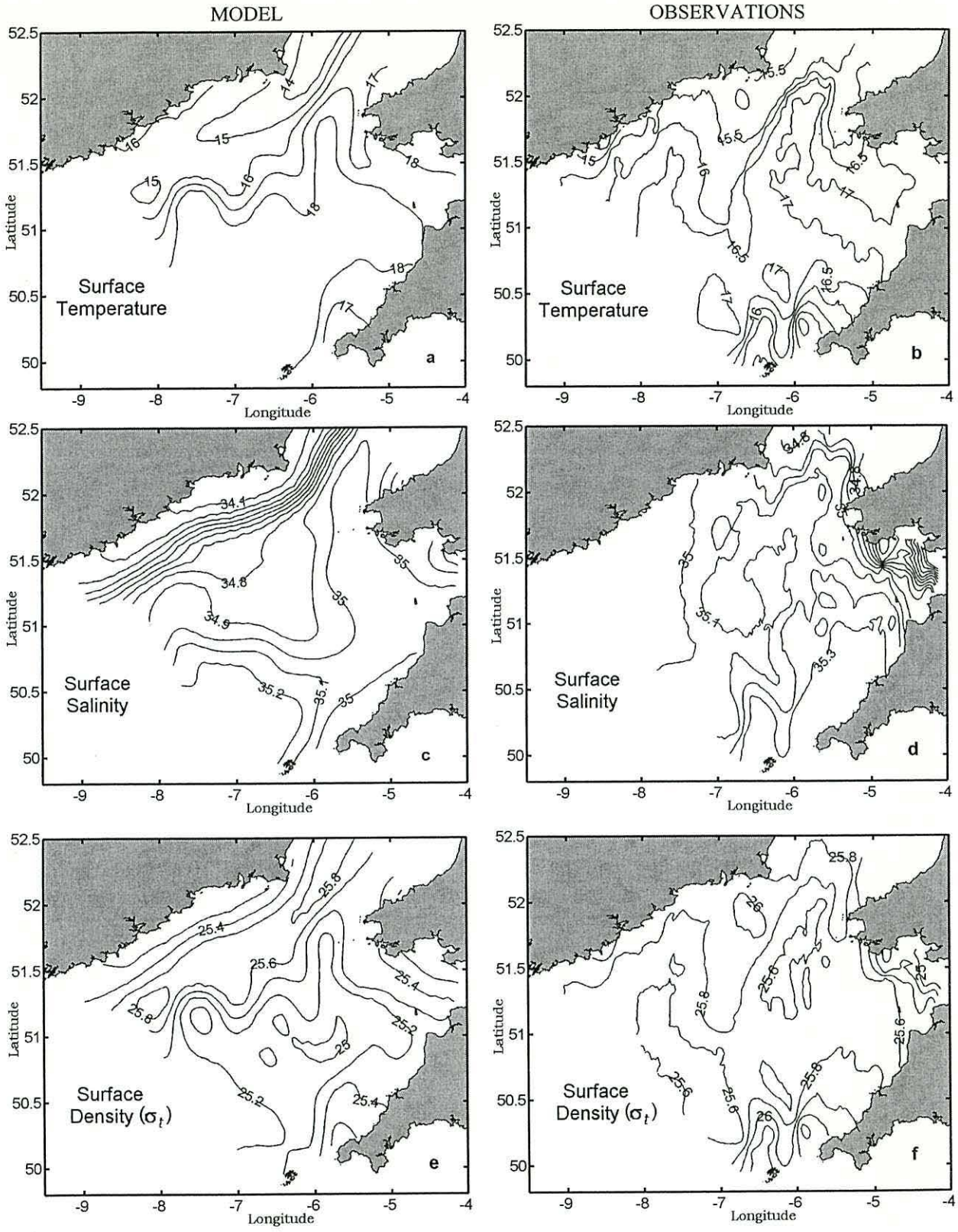

Figure 7.3 Spatial distribution of hydrographic properties at the surface: Temperature (°C), salinity and density (σ_t) in kg/m^3 from model results (August 1989) and observations (CORY998, August 1998).

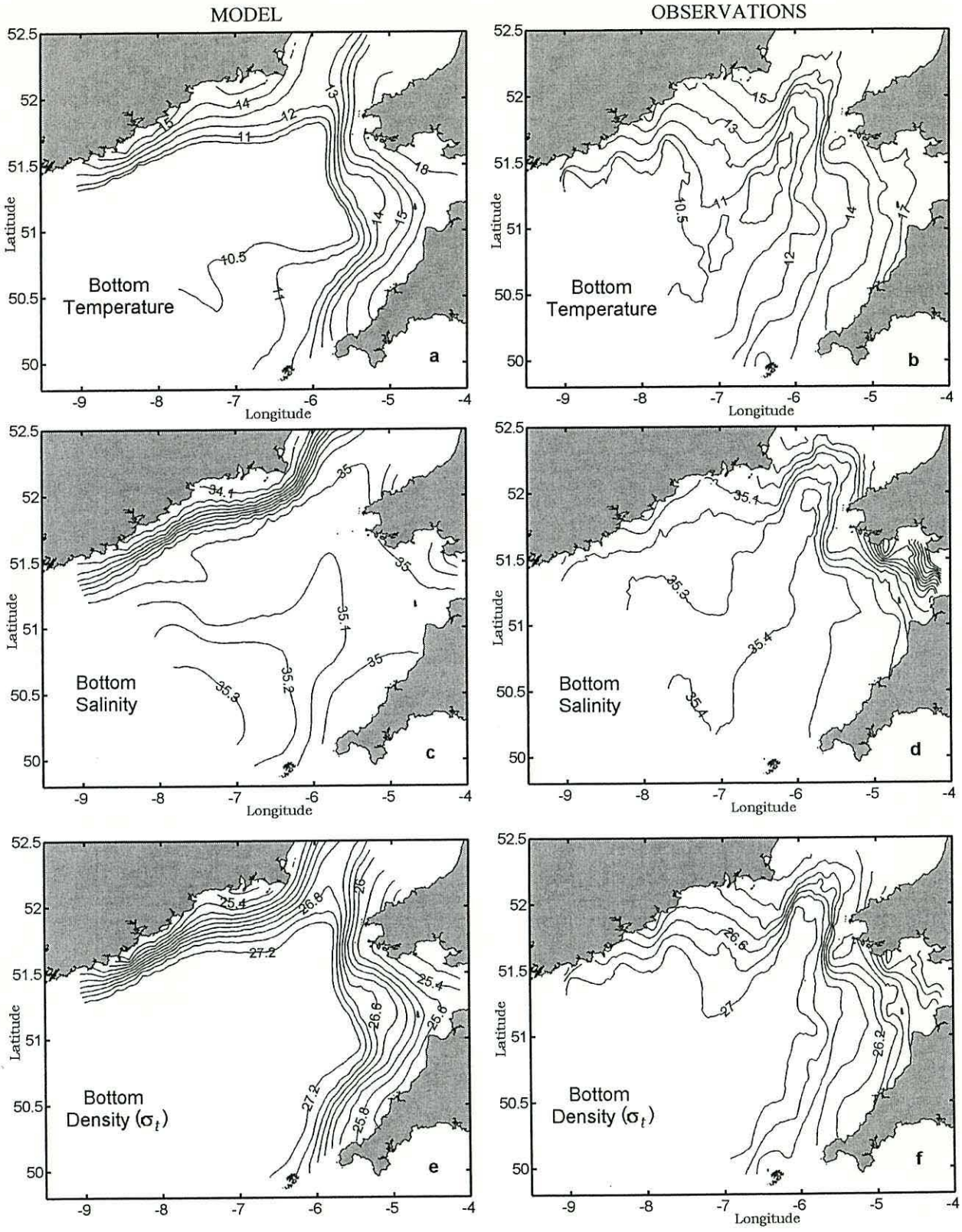

Figure 7.4 Spatial distribution of hydrographic properties at the bottom: Temperature (°C), salinity and density (σ_t) in kg/m^3 from model results (August 1989) and observations (CORY998, August 1998).

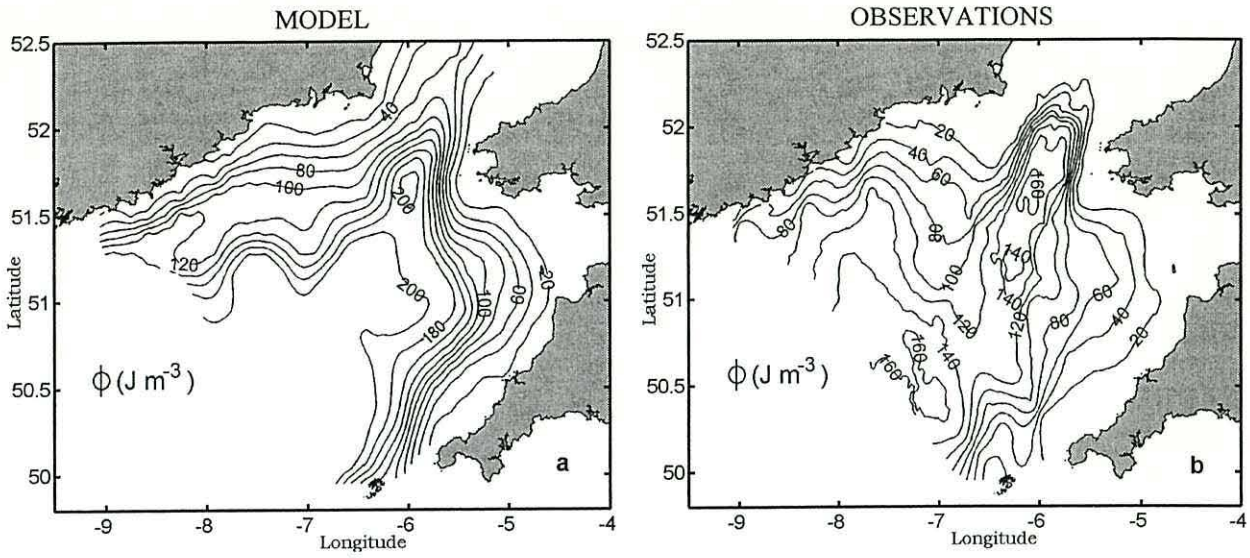

Figure 7.5 Spatial distribution of potential energy anomaly Φ (J m^{-3}) for (a) Model (August 1989) and (b) observations (CORY998, August 1989).

Vertical structure

In order to compare the vertical structure produced by the model with observations, two sections were selected. One from north to south (Leg 202 and 190) (Fig 7.6) and the other from west to east (Leg 182) (Fig 7.10), both passing through the centre of the Celtic Sea and its frontal areas. For convenience the density field will be shown together with the velocity field, although, the velocity field comparison is described in the next section.

In the north-south cross-section, the model (Figs 7.6a, 7.6b and 7.7a) reproduced to first order the main features shown in the observations (Figs 7.8a, 7.8b and 7.9a), but with less detail in the structure. The tidal frontal area was visible in the simulation at approximately 180-240 km distance along the x-axis (Figs 7.6a and 7.7a) isolating the core of cold bottom water (cold pool) in relatively good correspondence with observations (Figs 7.8a and 7.9a). It can be seen that model results (Fig 7.7a) showed weaker horizontal density gradients than observations (Fig 7.9a). In addition, the modelled distribution of density (Fig 7.9a) lacked details in the structure, and the eddy feature (see Fig 7.9a) did not appear in the simulation. The model simulation displayed a well-defined thermocline at ~ 30 m depth (Fig 7.6a) which is shallower than observations (~ 40 m depth) (Fig 7.8a). Temperature values from the model (Fig 7.6a) were comparable with observations (Fig 7.8a), but were slightly warmer at the surface and colder at the bottom. Regardless of the fact that salinity did not evolve, as did temperature in the model, the simulated vertical salinity distribution (Fig 7.6b) agreed qualitatively with observations (Fig 7.8b). However

they differed in their values (by up to 0.4), with the model underestimating the observed salinity values.

In the case of west-east sections (Fig 7.10), the model results were also to first order close to the observations. The cold pool in the simulation (Fig 7.10a), which was located approximately at the same position as in the observations (Fig 7.10c), was shown. The frontal areas were reproduced by the model (Figs 7.10, 7.11 and 7.12). However, they differed in position. While the frontal area at the right side of the cold pool (*i.e.* towards the Cornish coast) was modelled at approximately the same position (around 150-220 km distance along the x-axis, Figs 7.10a and 7.11a) as the observations (Figs 7.10c and 7.12a), the frontal area on the left flank of the cold pool was 40 km westward compared to that from observations. Also, the model results showed stronger horizontal density gradients (Fig 7.11a) than the observations (Fig 7.12a), due to the fact that the model probably over-mixed near the coastal areas. Salinity was underestimated by the model. However the model results (Fig 7.10b) showed the saltiest water of Atlantic origin at the bottom near the right flank of the cold pool at approximately the same location as in the observations (Fig 7.10d).

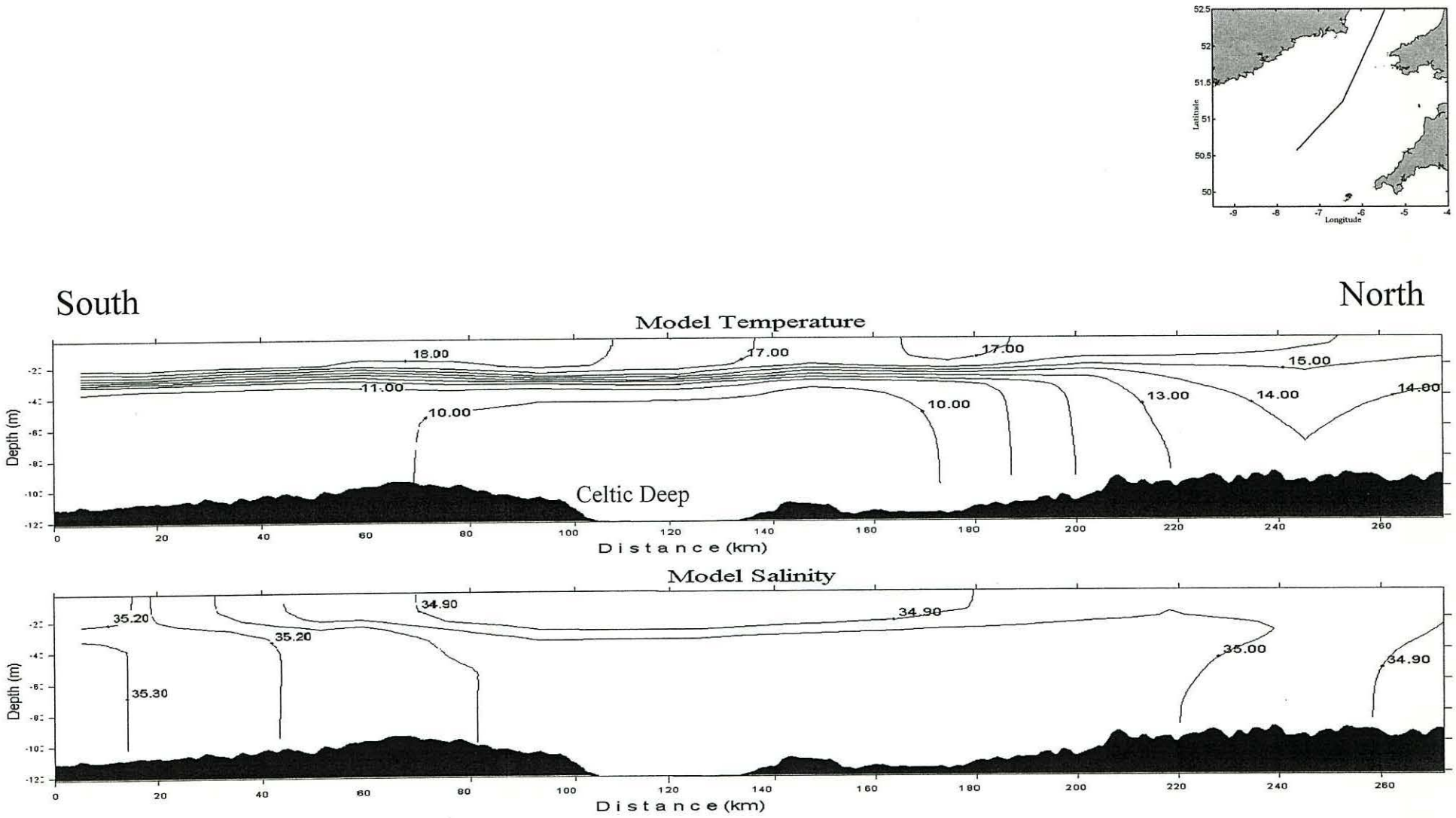

Figure 7.6 Along north-south cross-section, similar to the constructed with legs 190 and 202 cruise CORY998, showing the vertical structure of: (a) Temperature (°C) and (b) Salinity. The location of the cross-section is observed in the top right corner of the page.

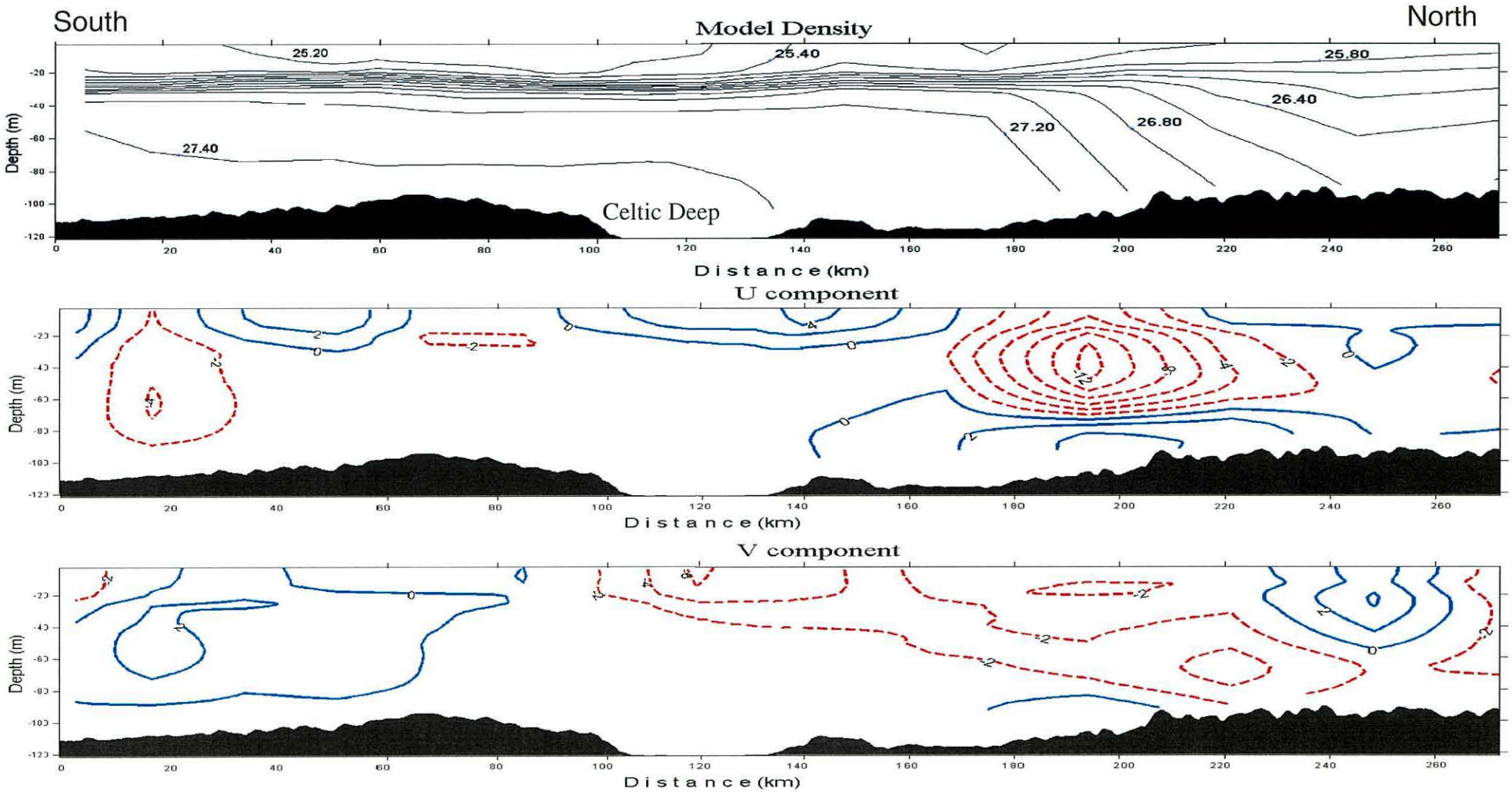

Figure 7.7 Model results: Vertical structure of the density (σ_t) in kg/m^3, west-east U component in cm/s and north-south V component in cm/s for a cross-section from north to south to corresponding to Leg 202 and 190.

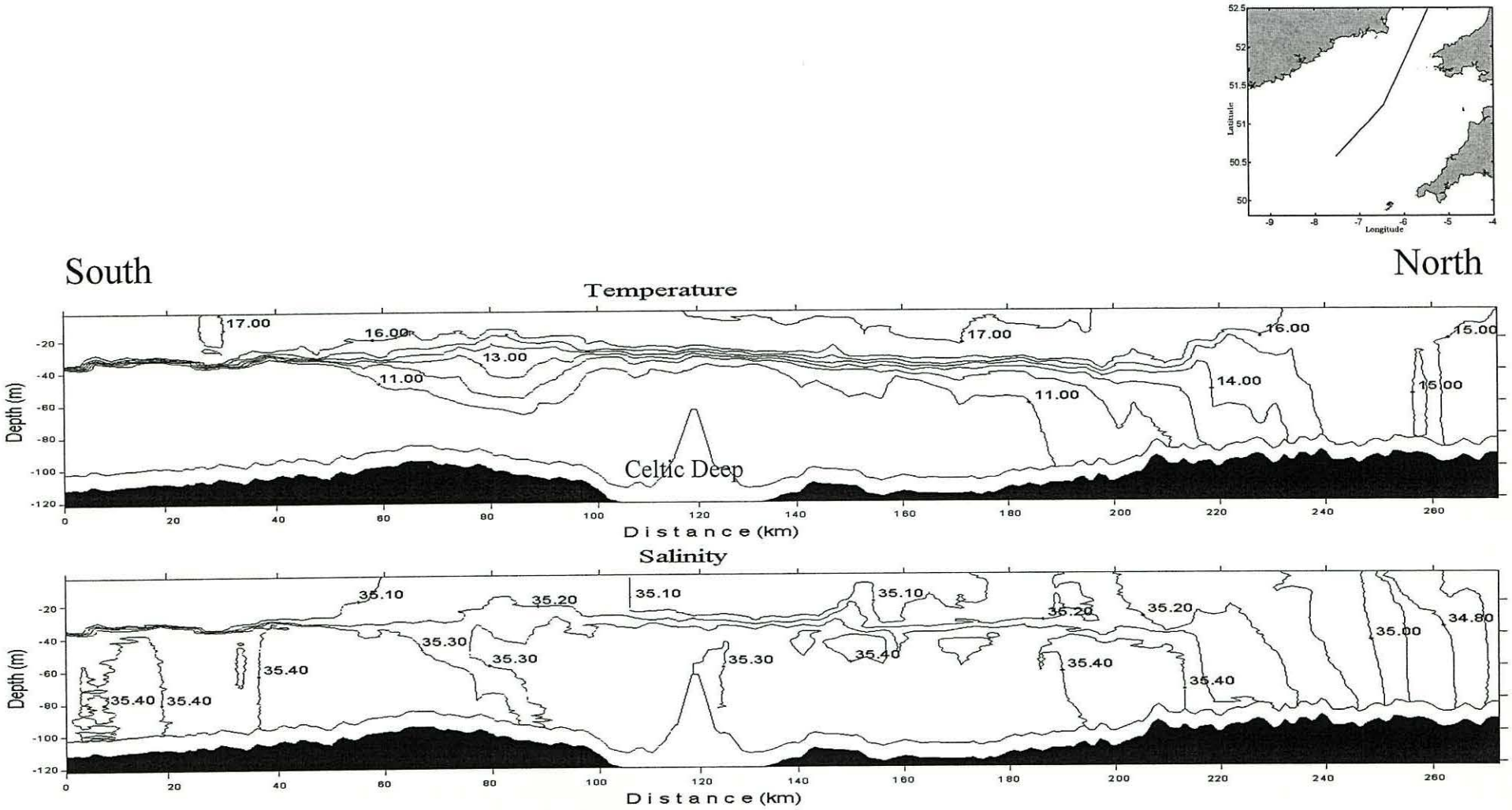

Figure 7.8 Along north-south cross-section constructed with legs 190 and 202 cruise CORY998, showing the vertical structure of: (a) Temperature (°C) and (b) Salinity. The location of the cross-section is observed in the top right corner of the page.

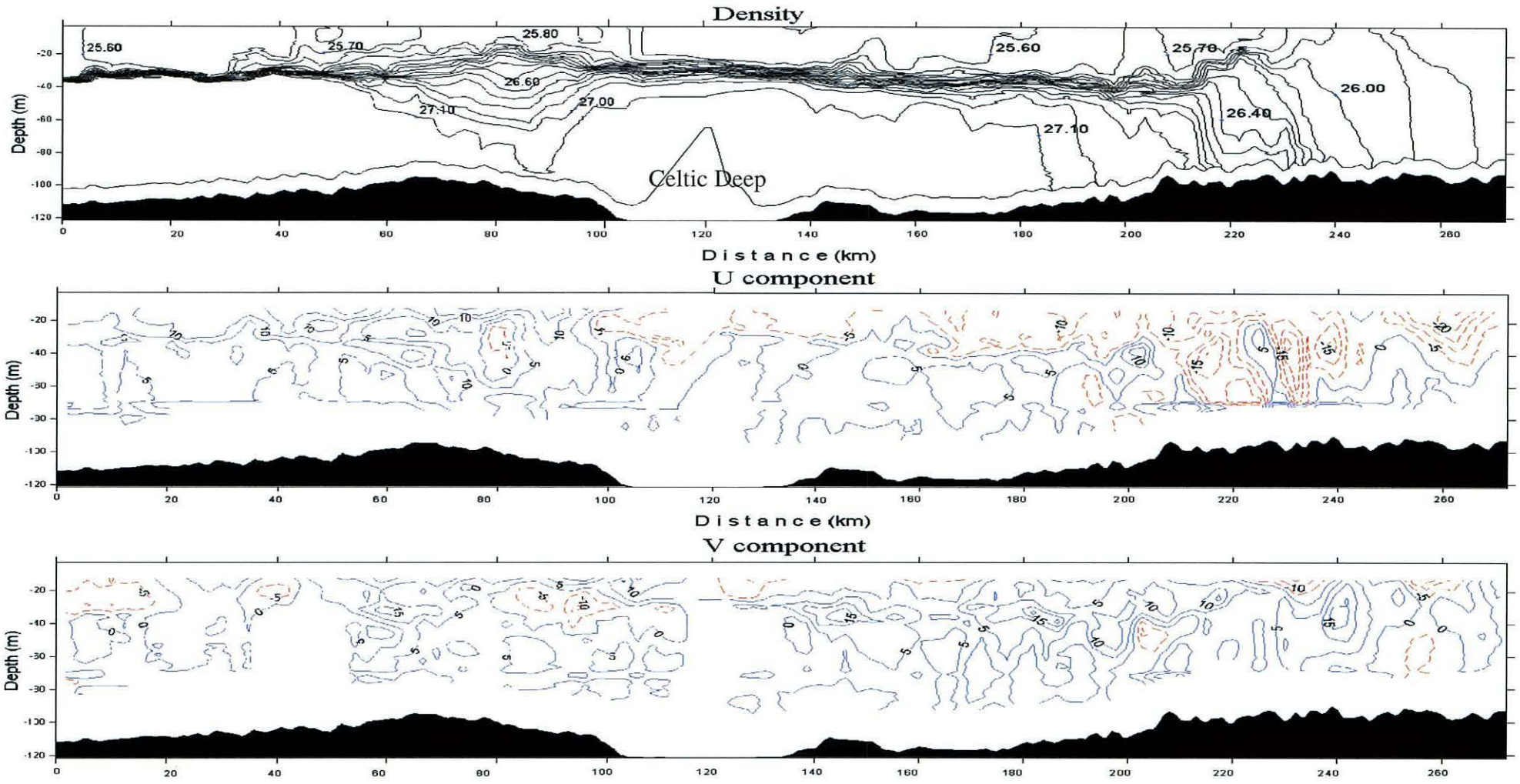

Figure 7.9 Vertical density field observed (σ_t) in kg/m^3 and residual velocities from ADCP: west-east U component in cm/s and north-south V component in cm/s for a cross-section from north to south to corresponding to Leg 202 and 190 .

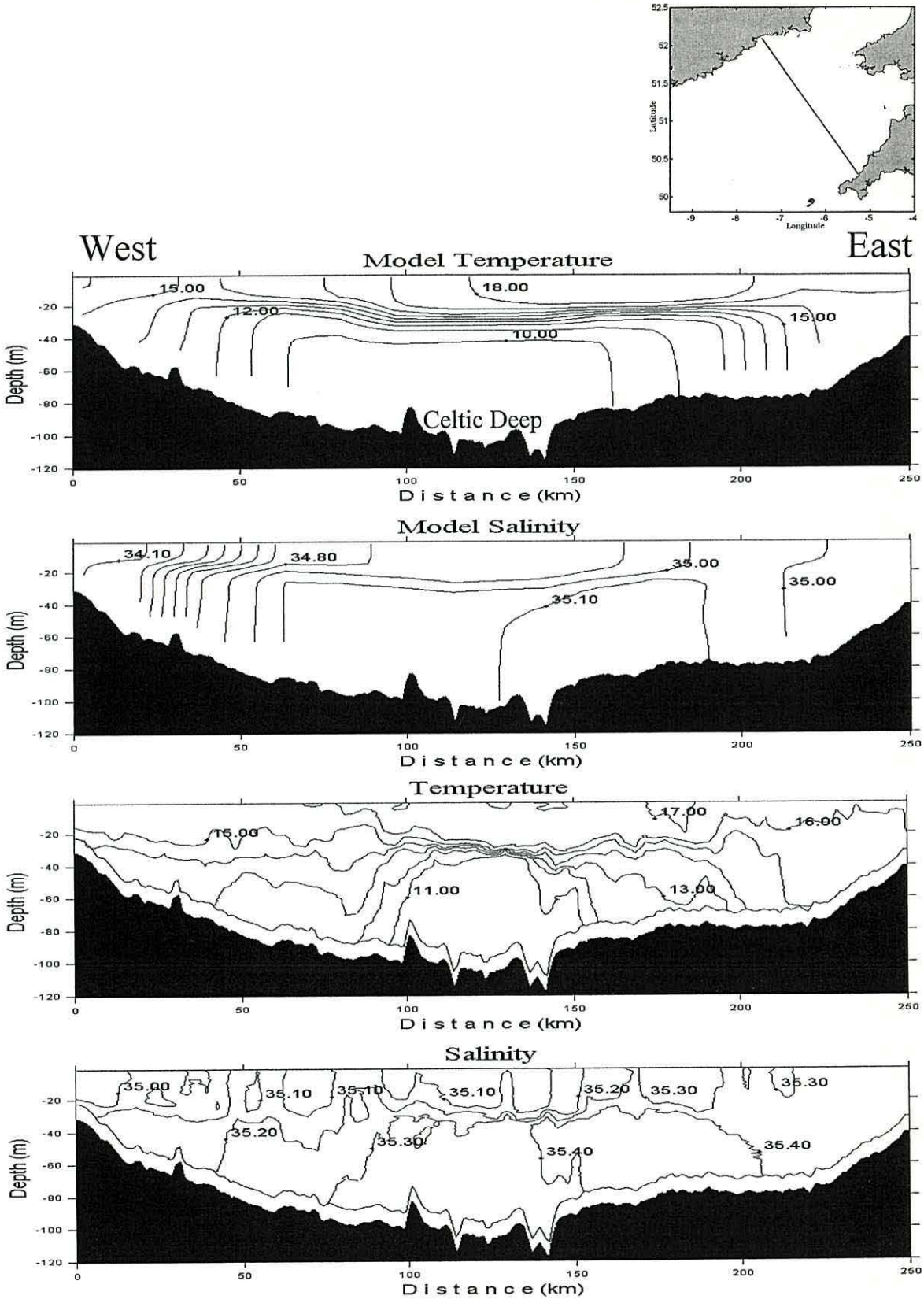

Figure 7.10 Transverse section in the Celtic Sea corresponding to leg 182 showing the vertical structure of: Temperature (°C) and Salinity from model and observations. The location of the cross-section is observed in the top right corner of the page.

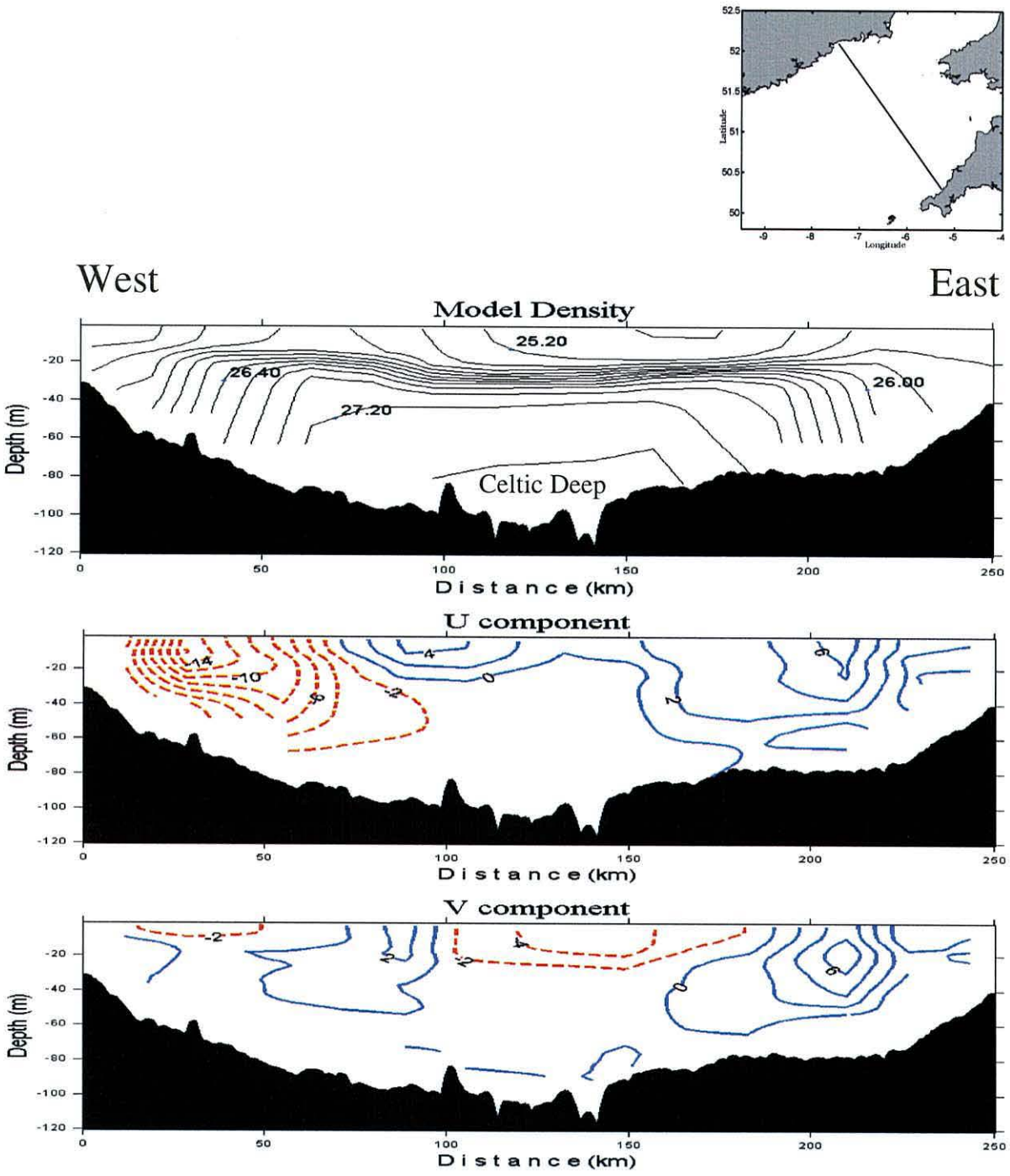

Figure 7.11 Model results: Vertical structure of the density (σ_t) in kg/m^3, west-east U component in cm/s and north-south V component in cm/s for a cross-section from west to east Celtic Sea corresponding to Leg 182 (top-right corner panel shows location).

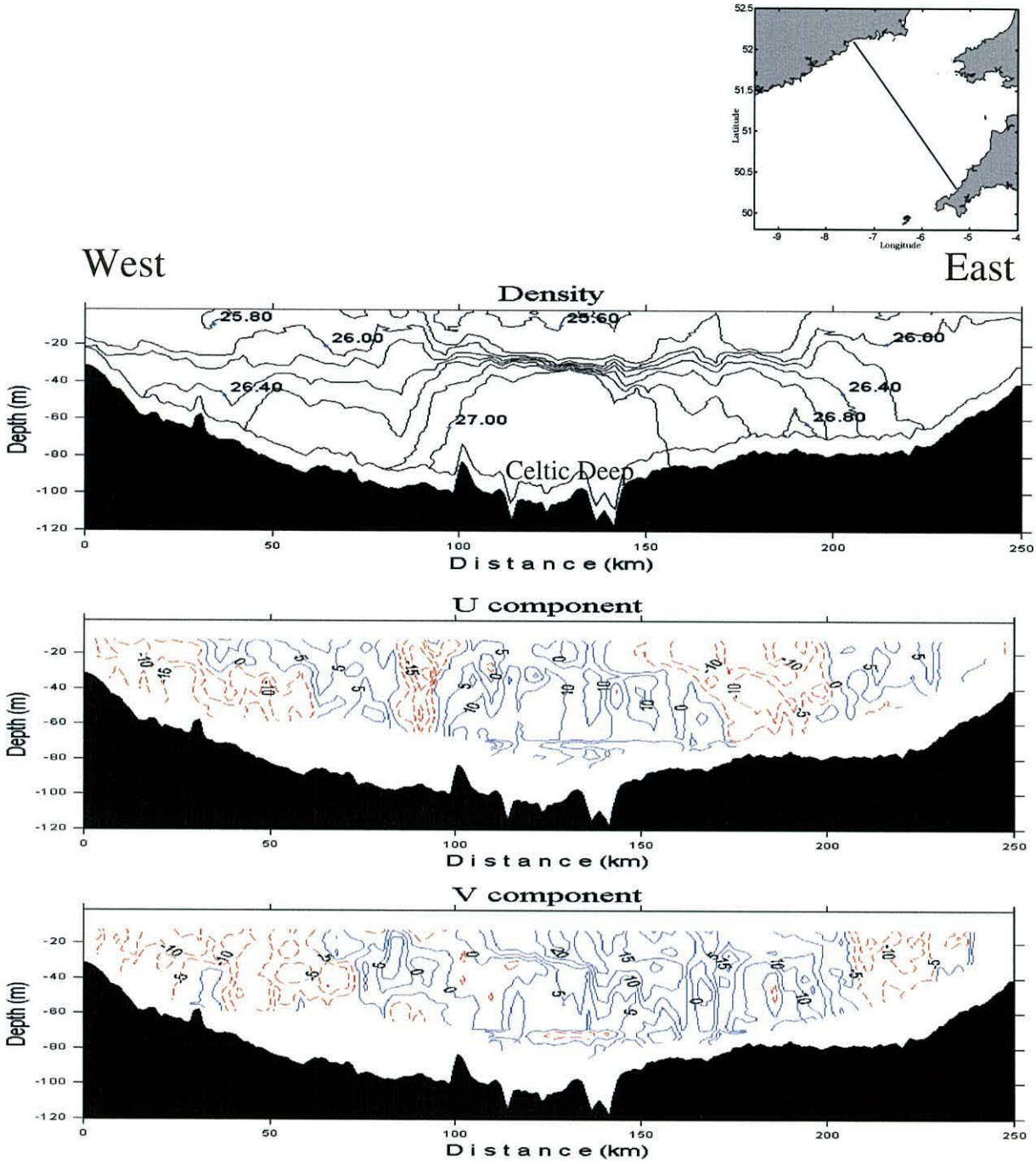

Figure 7.12 Vertical density field observed (σ_t) in kg/m^3 and residual velocities from ADCP: west-east U component in cm/s and north-south V component in cm/s for a cross-section from west to east Celtic Sea corresponding to Leg 182 (top-right corner panel shows location).

7.3.2 Velocity field: model and observations

Before the comparison is presented, it is important to consider that the modelled velocity field corresponds to the non-tidal residual velocities, which contain a wind-driven component and a density-driven component. In addition, this represents the mean field for August, so a smooth field is expected.

Horizontal field

Although the horizontal model resolution was limited, the horizontal velocity field shown by the model at 30m depth (Fig 7.13a) agreed with a cyclonic circulation portrayed by the geostrophic calculations (Fig 7.13c) and direct observations from ADCP (Fig 7.13b) and drifters (Fig 7.13d). However, the model circulation (Fig 7.13a) did not show the jet-like structure towards the centre of the Celtic Sea from the St. George's Channel. Instead, a coastal southward current was observed. The pattern of flow from the model (Fig 7.13a) agreed with geostrophic estimates (Fig 7.13c) and observations (Figs 7.13b and 7.13d) at the St. George's Channel frontal area, showing the cyclonic flow around the St. George's Channel. However, little exchange between the Celtic Sea and the Irish Sea was shown by the modelled velocity field (Fig 7.13a), which was not clear in the observations (Figs 7.13b and 7.13d), in particular, from the drifter trajectories (see Fig 5). In addition, the cyclonic circulation around the St. George's Channel was located further north in the observations than in the model results. The model showed weak velocities at the centre of the Celtic Sea, where some considerable velocities were observed in the ADCP data (Fig 7.13b) and in the quasi-Eulerian field portrayed by the ARGOS drifters (Fig 7.13d). However, the model agreed with the observed southward flow along the Irish coast. The modelled velocities (Fig 7.13a) followed approximately the modelled bottom density and stratification contours (see Figs 7.4e and 7.5a), indicating that most of the circulation was due to density gradients. However, around the southern open communication of the Celtic Sea with the Atlantic Ocean other velocities (< 0.10 m s^{-1}) mainly in a northwestward direction were observed, probably wind-driven. The magnitude of the velocities from the model (Fig 7.13a) agreed relatively well with observations (Figs 7.13b and 7.13d) at the frontal areas, though they were weaker than observations. It is important to consider that outside the frontal areas, they were up to one order of magnitude smaller than observations.

Vertical structure

In the vertical, the model velocity structure showed a circulation that can be related to the dome shape in the isopycnals forming the bottom front, which isolates a cold and dense pool at the centre of the Celtic Sea (Figs 7.7 and 7.11). This agreed qualitatively well with our observations in the north-south cross-section (Figs 7.9) around the frontal areas, in particular the u-component (Fig 7.9b), giving support to the theory of bottom fronts as drivers of surface organized jet-like flows. However, modelled velocities (Figs 7.7b and 7.7c) were up to 0.05 m s^{-1} weaker than observations (Figs 7.9b and 7.9c) at the frontal areas and the ADCP observations displayed more velocity structure than the model velocity fields and over much of the water column. In the west-east cross section (Fig 7.11), the modelled u-component (Fig 7.11b) showed a cyclonic circulation, however this was not evident in the v-component (Fig 7.11c). Observations in this cross-section displayed more velocity structure in both the u- (Fig 7.12b) and v-component (Fig 7.12c). Modelled velocities and ADCP observations closely agreed in the nearly southward flow close the Irish coast, clearly evident in the u-component.

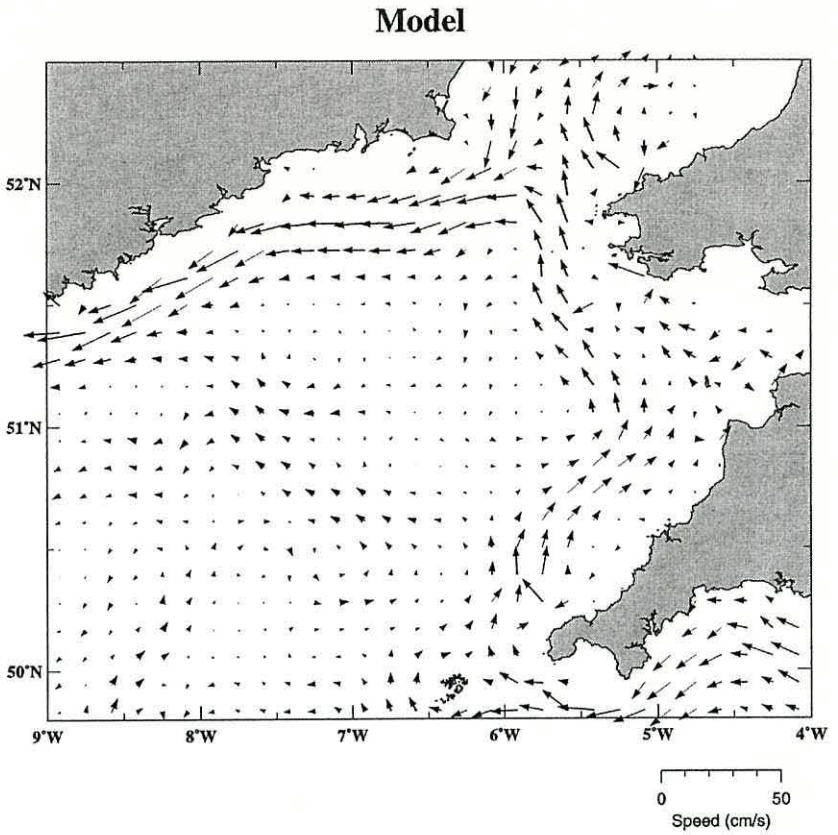

a)

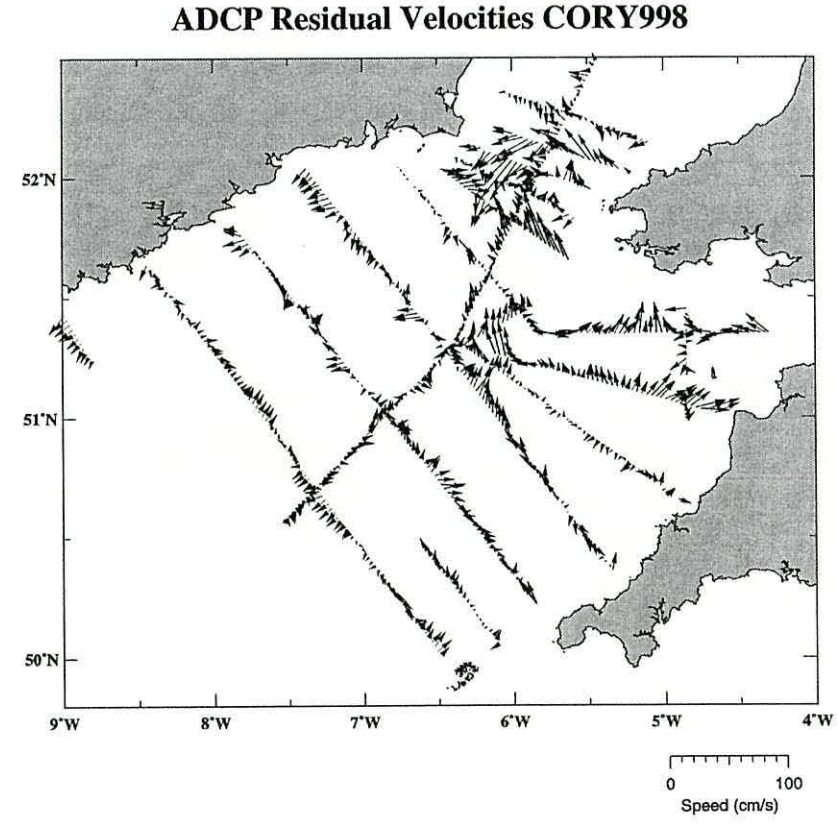

b)

Figure 7.13 Velocity field obtained from: a) the model at 30m, (b) ADCP at 30m depth, c) geostrophy at 10m relative to the bottom and d) Quasi-Eulerian field obtained from ARGOS drifters. Scale is show at the bottom right of each panel. Notice the different scales used.

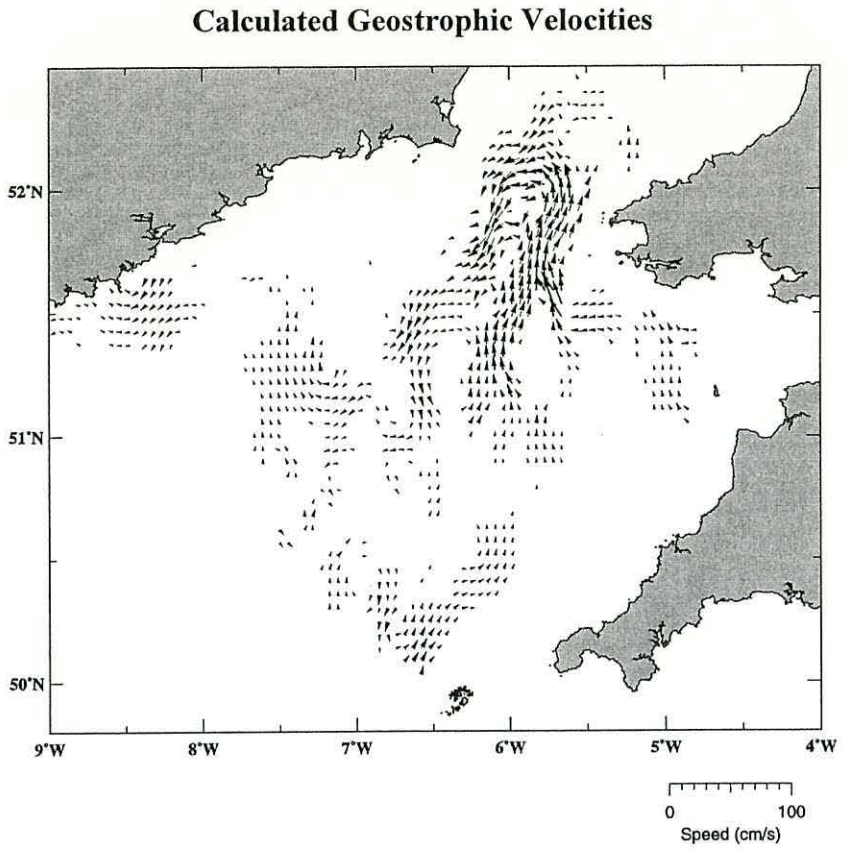

c)

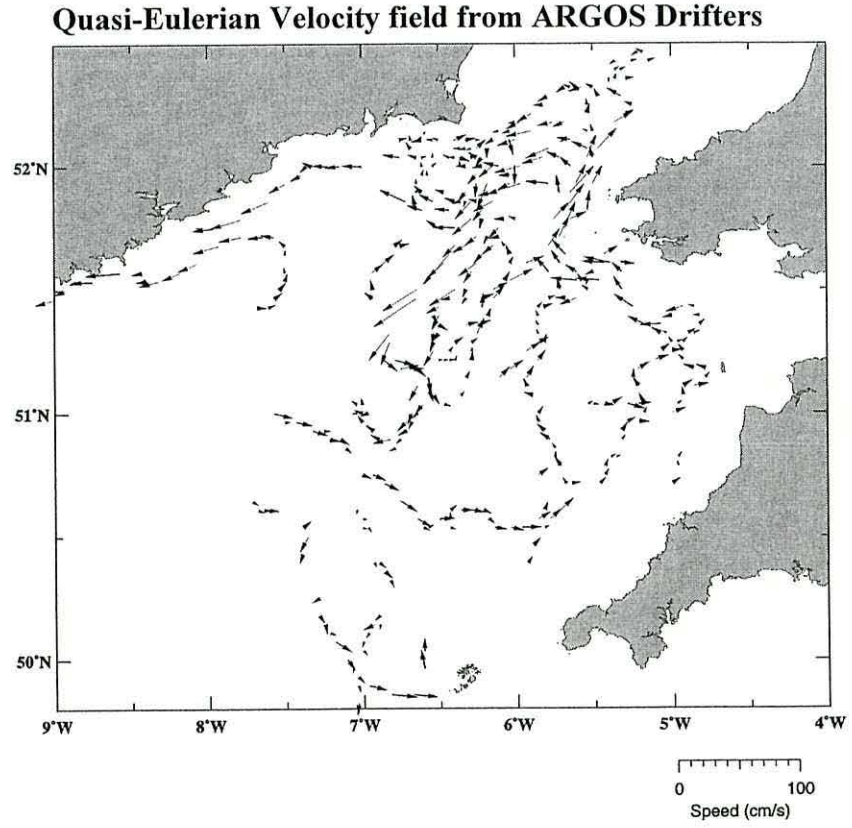

d)

Figure 7.13 Continued.

7.4 Summary, discussions and recommendations

In general, the POL 3-D-Baroclinic model was only capable of reproducing some of the main features of the temperature and velocity fields. However with such a limited resolution (12 km), the model was not expected to reproduce the details of the horizontal distribution shown in the observations, as the 12 km grid size is still too coarse to resolve frontal areas. The minimum length scale to resolve frontal areas in shelf seas is given by the Rossby radius of deformation R_D (* see next page for definition), which for typical values in frontal shelf sea areas are ~ 5 km. Thus, model horizontal resolution plays an important role in the position of the tidal mixing fronts and description of features such as eddies. The fact that the horizontal velocity field did not show the intrusion along the Celtic Deep towards the centre of the Celtic Sea (instead a southward flow along the Irish coast was observed) implies that bathymetry plays a decisive role in the distribution of the density field, in particular, the position of the tidal mixing fronts. Figure 7.14 shows the bathymetry used by the model and the one extracted from our observations. Although the latter requires more data to improve the resolution. Differences between both bathymetries can be seen mostly around the centre of the Celtic Sea where the Celtic Deep was not represented in the bathymetry used by the model. It was stressed by Brown *et al.* (1999b) that a fine resolution bathymetry is important for modelling of the shelf sea areas.

Salinity was a limiting parameter in the POL 3-D-Baroclinic model, mainly in the fresh water influence areas, such as the Irish coast and Bristol Channel, where density is likely to be locally affected by it, and so the velocity field. Therefore, fresh water sources and the evolution of the salinity field are important to be considered in any future modelling of this shelf sea area.

In summary, whilst there is agreement between model and observations concerning large-scale features there are some important differences. Additionally, we have to take into consideration that the model ran for a different year with emphasis on the North Sea, including data from the North sea project. This, however, is not a primary justification for the differences between model and observations shown here, since the main density structure during the summertime is expected to be robust. Despite these limitations, to first order the main features were reproduced, such as the frontal areas. On the other hand, poor resolution of the model could not alone be responsible for the lack of correspondence in the velocity field. Direct observations from drifters and in particular, from ship-mounted

ADCP are snapshots of the circulation, while the model results represent long-term circulation or at least mean monthly circulation and so some discrepancies can be expected. Outside the frontal areas, it is also possible to find velocities < 0.10 m s^{-1} in the modelled velocity field, probably wind driven. Nevertheless, to a first approximation the summertime modelled circulation in the Celtic Sea was mainly cyclonic and the model results are consistent with this being predominantly density driven.

---

* *Rossby radius of deformation* R_D defined as

$$R_D = \sqrt{(g'H)}/f$$

where g' is the reduced gravity ($g'=g\Delta\rho/\rho$, and $\Delta\rho$ is the density difference between layers), f the coriolis parameter, and H is the depth scale chosen of the system (*i.e.* depth of the upper layer, or depth of the water column) (Pedlosky, 1979).

a)

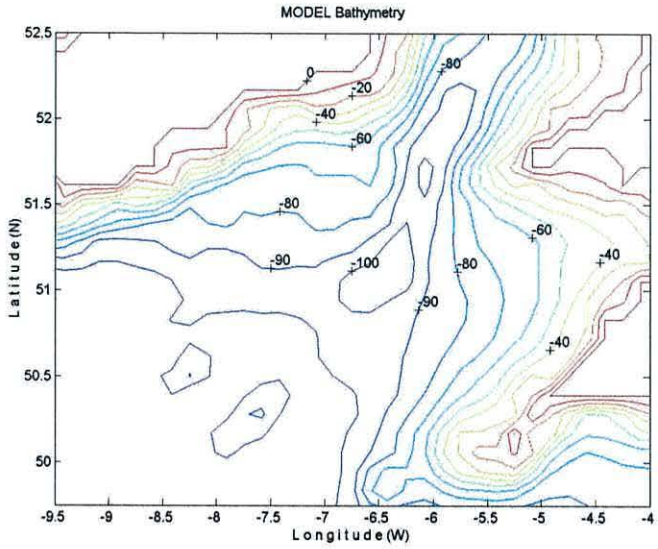

b)

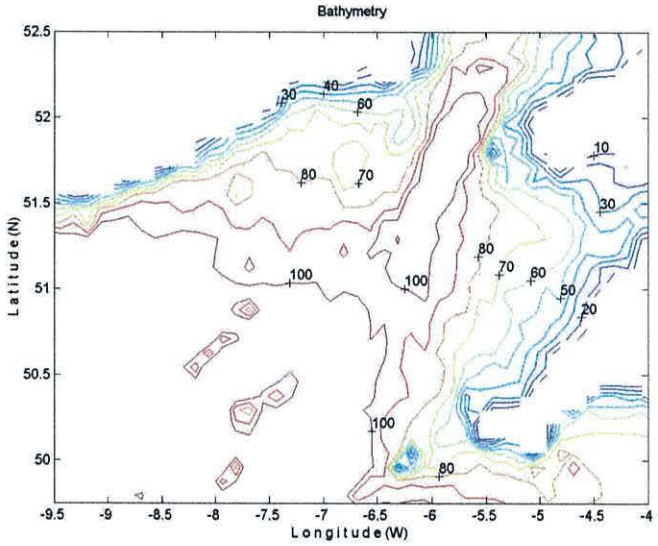

Figure 7.14 Bathymetry used by the model (a) and bathymetry from our observations (b). Depth is denoted in metres.

Chapter 8

Discussion

8.1 Introduction

The principal aims of the present observational work have been to define the summer circulation in the shelf area of the Celtic Sea and to establish whether or not the observed summer surface circulation was driven by bottom density fronts. In order to do that, a combination of observational techniques (see Chapter 3) has been applied obtaining the first direct current measurements and extensive hydrographic data collected during the summertime in the Celtic Sea to date. This combination of instrumentation technology (ADCP, satellite-tracked drifters and high-resolution hydrographic observations) allowed us to gain insight into the summer circulation in the shelf area of the Celtic Sea for the first time. Through Chapters 4, 5 and 6, evidence was added supporting the perspective of a baroclinic circulation in this region. In this chapter, the main findings of this thesis are discussed, analyzing the results in the context of density-driven surface circulation, particularly jet-like flows associated with bottom fronts. Also, some implications of these results and some lines of future work are suggested.

8.2 Discussion regarding the existing bottom fronts and surface circulation in the Celtic Sea

The present results highlighted the importance of baroclinic jets in the Celtic Sea. These baroclinic jet-like flows were already reported by Simpson (1976) and Horsburgh *et al.* (1998), in discrete localised areas of the Celtic Sea (*i.e.* the total circulation was not evident on account of limited spatial coverage). Other baroclinic studies in the area (James, 1977, 1978 and 1984) only concentrated on the dynamics of frontal areas, but these density-driven flows were not extrapolated in the context of organised flows in the relatively extended shelf area of the Celtic Sea. The present study goes further, however, portraying an overall circulation based on direct current measurements and using the hydrographic measurements as a background and the basis of bottom frontal dynamics. In this context, the results of this thesis add grounds to the growing body of evidence for density-driven summer currents caused by bottom fronts.

With the obtained hydrographic observations (Chapter 4) it was possible to define during the summer, a dense cold pool bottom structure as the shelf of the Celtic Sea. This cold pool was isolated from the surface layers by a strong thermocline located at ~30-40 m depth and bounded by sharp bottom fronts. The cold pool structure and, in particular, the associated bottom fronts were persistent structures during the summer as they were observed in both July and August cruises. Moreover, the horizontal bottom density gradients became progressively stronger later into the summer. The fact that the main observed density structure (*e.g.* tidal mixing fronts) during summer 1998 (Chapter 4) was simulated by the numerical model (Chapter 7) for the summer of a different year (August 1989) corroborated the notion of a robust bottom density field for the summertime.

According to the theory of bottom fronts (Garrett and Loder, 1981, see section 1.2), the horizontal density gradients associated with the bottom front are expected to generate significant surface, along-front jet-like flows. Evidence presented throughout the chapters 4, 5, 6 and 7 suggest the presence of density driven currents in the study area. Lagrangian observations (Chapter 5) and ADCP measurements (Chapter 6) showed clear direct evidence of near-surface (at ~30-40 m depth) jet-like flows (up to 0.30 m s^{-1} and 10-20 km wide) associated with the margins of bottom density fronts. It was notable that the order of magnitude of the geostrophic velocities calculated was approximately the same as the observed values from the ADCP residuals (section 6.4) and with those of the drifter

velocities when crossing the sections (Table 5.3, section 5.6). These findings imply that, to first approximation, the circulation can be predicted by geostrophy, because the strongest observed velocities with the ADCP were confined to the position of the strongest bottom density gradients. On the other hand, some error is assumed or is implicit in our geostrophic calculations. There are some limitations to this simplified approach (*i.e.* geostrophic calculations), since several forcing mechanisms have been ignored such as friction, and the no-motion level was selected at the seabed. However, the direct measurements certainly provide support to the geostrophic calculations. In contrast, outside the bottom frontal areas, flows with not well organised patterns of circulation were observed, with considerable velocities (up to 0.15 m s^{-1}). The considerable ADCP residual flows in the non-frontal areas are almost certainly accounted for by other driving mechanisms (non-density driven); as they were not revealed by geostrophy. Additionally, drifter trajectories showed a variety of spatial structures confirming that there were other flows not directly related to bottom fronts. Nevertheless, the cold pool and its associated bottom density fronts in the Celtic Sea are potentially important structures for the maintenance of surface flows. Consequently, a picture of a baroclinic summer circulation in the Celtic Sea emerges.

An overall baroclinic, cyclonic circulation, with velocities reaching up to 0.30 m s^{-1} in narrow (10-20 km wide) jet-like flows centred at ~ 30-40 m depth, was found in the shelf of the Celtic Sea during the summer of 1998. The obtained cyclonic circulation qualitatively agrees with the indirect approaches to the circulation from the earlier works of Matthews (1913), Harvey (1929) and Cooper (1961a and 1961b) (see section 1.4). In contrast, these results are in disagreement with the portrait of a weak long-term circulation for the Celtic Sea (Thompson and Pugh, 1986; Pingree and Le Cann, 1989). Previous direct current measurements (Thompson and Pugh, 1986; Pingree and Le Cann, 1989) failed to identify baroclinic cyclonic circulation in this region because most of the previous observations were obtained during winter-spring seasons. Only few summer measurements prior to the present study were undertaken in the Celtic Sea. Moreover, none attempted to obtain a picture of the circulation in the Celtic Sea using sparse data and only discrete surface measurements. Additionally, as was stressed in other shelf sea circulation studies similar to the present one (Hill *et al.*, 1997b; Brown *et al.*, 1999a; Horsburgh *et al.*, 2000) using only moorings makes it not possible to obtain the circulation of an extended region and it is difficult to define narrow (10-20 km width) jet-like flows.

Prior to this study the circulation was largely portrayed as barotropic and mainly wind-driven (see section 1.4). A mainly wind-driven circulation might be occurring during the winter, when barotropic conditions are expected to dominate in the Celtic Sea. However, during the summer, baroclinic conditions prevail. The hypothesis that the wind is a possible mechanism to drive the observed circulation can be discarded, because no correlation between the surface Lagrangian circulation and wind was found (see section 5.5.1). Lack of correlation between the strong observed velocities (up to 0.30-0.40 m s^{-1}) and the wind field can be expected since barotropic numerical model results suggest only weak wind-driven residuals for the Celtic Sea shelf (Thompson and Pugh, 1986; Pingree and LeCann, 1989; Young *et al.,* 2001). Consequently, the strong near-surface observed velocities are likely to be baroclinic (density-driven).

In general terms, density-driven summer currents caused by bottom fronts in the Celtic Sea is a summer feature in common with other European shelf sea regions, such as the Irish Sea and North Sea (Hill, *et al.*, 1994; Brown, *et al.*, 1999a; Horsburgh *et al.*, 2000). However, some different aspects are clearly present in the Celtic Sea tidal mixing front. Undoubtedly, the existence of the St. George's Channel makes a difference compared with the tidal mixing fronts of the open shelf of the North Sea and the relatively closed shelf of the Irish Sea.

The most outstanding results were found in the frontal area of the Saint George's Channel, with the strongest horizontal density gradients and the highest velocities (up to 0.30-0.40 m s^{-1}). It is interesting to note that the measured jet-like flows were not always as strong and permanent as would be theoretically expected from a stable bottom front. Residuals from the mooring located in the Saint George's Channel (location J, section 6.5) confirm the persistence of the surface flows. However, a small degree of variability in the magnitude of the flow was noticed. This variability in the flows could be an explanation of why the jet-like flows were not always observed in the ship-mounted ADCP data in the St. George's Channel, where several cross-sections were undertaken. The degree of variability of the jet-like flows presumably is due to instabilities expected in such a strong baroclinic area. Griffiths and Linden (1981) experimentally demonstrated the development of instabilities in a sharp front in a two-layer rotating fluid. Baroclinic instabilities are expected in frontal areas in eddy-like forms (Pingree 1978; James, 1981). It has been observed numerically (James 1981; 1984; 1988) that initial perturbations of the front grow wave-like disturbances which eventually curl up, usually in the same sense as the Earth's

rotation, developing in eddy-like features with scales in the range 20-40 km (Simpson, 1981).

James (1984) numerically demonstrated that perturbations of the front can be produced by changes to the flow. Around the headlands in the St. George's Channel strong barotropic tidal residuals and eddy formation can be expected (see sections 5.2 and 5.5.2; one drifter was trapped by an eddy near the headland of the Irish Sea, Figure 5.3v). Consequently, it is likely that they can affect the frontal area in the St. George's Channel, changing the velocity field and generating baroclinic instabilities.

An eddy-like structure located at the centre of the Celtic Sea (~ 50 km wide, see Fig 4.9a and c) was captured in the detailed hydrographic observations, which seemed to co-exist with density bottom fronts. Although the position of this eddy-like feature was far (~140 km) from stronger fronts (*i.e.* the Saint George's Channel), eddies might move in the direction of the surface along-front flow (James, 1981; 1984). Since frontal eddies do influence the larger scale flow (shelf scale) (James, 1984), these eddy-like structures could add variability and complexity to the expected and predicted density driven currents.

In spite of the baroclinic instabilities, bottom fronts and their associated surface jet-like flows are, to a first approximation, robust and stable structures. While bottom density distribution was consistently stable, the surface distribution was not, which could be evidence of the susceptibility of the surface (*i.e.* above the thermocline located at ~30-40 m depth) in response to forcing. Although the distribution of the cold pool was directly related to the bathymetry and the spatial distribution of the tidal currents, the surface front in the Saint George's Channel did not strictly follow the contours of the stratification parameter h/u^3, which is generally used to predict tidal mixing frontal position (Simpson and Hunter, 1974; Pingree and Griffiths, 1978). The hydrographic observations (Chapter 4) and SST images (Fig 4.4) showed a convoluted surface front. The shape of this front appears as a northward tongue of warm water from the Celtic Sea in the central and eastern side of the St. George's Channel and a southward cold one from the southern Irish Sea in the western side of the channel. However, this tongue-like shape of the surface front can distort becoming intrusions of water (*i.e.* exchange) either from the tidally mixed southern Irish Sea or from the stratified Celtic Sea.

The southward and northward flows were approximately the same order of magnitude. However, the extent of the southward intrusion was more extensive than the northward one (~ 120 km versus ~ 50 km) in these observations. Horsburgh *et al.* (1998) reported both intrusions, but suggested that the northward intrusion was more extensive (up to 100 km). A re-examination of cloud-free SST satellite images shows that these surface water intrusions in the St. George's Channel are quite variable and not persistent features of the Celtic Sea frontal area as reported previously (Simpson *et al.*, 1978, Horsburgh *et al.*, 1998). In particular, the northward intrusion seems more constant that the southern one. The intrusions seem to be intermittent. Also, variability in these intrusions was indirectly observed by the different drifter trajectories when they passed over a common area and followed different trajectories (*i.e.* only two of the drifters that crossed the St. George's Channel followed the cold water southward intrusion and only one drifter left towards the southern Irish Sea, Chapter 5).

The causes of the variability of the intrusions or exchange of water between the Irish Sea and the Celtic Sea is still a question to be addressed. The effects of advection by the residual flows (observed in the satellite tracked drifters, Chapter 5, and in the ADCP current observations, Chapter 6) could be the main cause of the distortion of the surface front (Simpson, 1981). However, this does not explain the cause of the distortion of the surface front becoming intrusions. Baroclinic instabilities seem to play an important role in the variability of the flows in the frontal areas, and could be another forcing that causes the intrusion.

A probable explanation of the extent of these intrusions is provided by the numerical results from Wang *et al.* (1990) (see section 2.4). In their results, it is suggested that the tidal mixing front responds differently to wind direction (rather than to magnitude of the wind). A northerly wind causes a surface southward intrusion, which brings colder water from the location of the frontal position towards the central Celtic Sea. This reduces vertical stability and enhances vertical mixing leading to a rapid reduction of surface temperature and an apparent southward intrusion of cool water. In the case of a southerly wind episode, warm water moves over cool well-mixed water being counteracted by vertical mixing, consequently only a small change of surface temperature is observed and the surface front remains stationary (Wang *et al.*, 1990). Thus, a rapid advance occurs preferentially to northerly wind than to southerly winds (Wang *et al.*, 1990). This could explain why the northward intrusion of warmer water was not as extensive as the

southward in our observations and why the southern intrusion is more likely to be observed in SST images. In this context, it is probably that a northerly wind event (even with a modest wind stirring) could quickly erode the cool water and thermocline (as explained by Wang *et al.*, 1990) and contributes to the observed southward intrusion. However, a more detailed examination of the wind forcing to the frontal area of the Celtic Sea requires further studies.

Overall we can expect little exchange between the Irish Sea and Celtic Sea, because these intrusions apparently occur only infrequently. Evidence from SST images, from drifter trajectories and from ADCP residuals showed spatially confined flows to the bottom frontal area in the St. George's Channel. Thus, the flow was northward on the eastern side of the channel, then it turned westward and finally southward (*i.e.* in a cyclonic sense). Furthermore, two drifters followed an intrusion of cold water from the Irish Sea towards the stratified and relatively warmer Celtic Sea and just one drifter of 8 left the Saint George's Channel towards the Irish Sea and it did not go farther north. In this way, the exchange of water in this region seems to be restricted, and mainly a re-circulation of the Celtic Sea water might be expected. However, once an intrusion occurs, due to the high associated velocities (>0.30 m s^{-1}), they might have the capacity for significant temporal and spatial variability of the flux (Horsburgh *et al.*, 1998). Assuming a width of the southward intrusion of 10 km for the maximum observed velocity of 0.30 m s^{-1} located above 30 m depth, a broad estimation of the capability of a southward intrusion gives a volume flux of 9 x 10^4 m^3 s^{-1}. This transport value is considerable (compare for example with the annual volume flux (residual) through the North Channel of the Irish Sea of 7.7x10^4 m^3 s^{-1}, Knight and Howarth, 1999). Consequently, these intrusions might be potentially an effective exporting mechanism of biomass, nutrients and contaminants between the Irish Sea and Celtic Sea. Moreover, the modelling work in the Irish Sea uses the Celtic Sea and the St. George's Channel as a boundary condition. On account of the results obtained here (*e.g.* the relatively small exchange), care must be taken in the numerical modelling of the exchange of properties between these two shelf seas.

8.3 Implications of the results and future work

8.3.1 Implications

The results of this study clearly have implications for the management of the fishery industry and the evaluation of risk in event of oil or chemical spills. Shelf sea areas are spawning grounds for fish and shellfish species. In addition, most of the macrobenthic species in temperate waters reproduce with a relatively prolonged planktonic larval phase (Thorson, 1950). Consequently, advection by residual flows has important influences on the dispersal of species and on their recruitment success. The nearly-cyclonic circulation in the Celtic Sea, with relatively little exchange with the Irish Sea but with rapid transport pathways associated with cold pool jets, plays an important role in controlling the advection and dispersion of several commercially valuable species of fish and shellfish larvae in the area such as herring, plaice, sole, and crustacea larvae, particularly the decapod *Nephrops norvegicus*. It has been suggested that local retention may be the more pervasive and adaptive larval dispersal strategy for many coastal organisms with planktonic larvae, given the more favourable environmental conditions for larval growth and survival and the higher probability of encountering suitable adult habitat at the end of the larval development (Swearer *et al.*, 1999). The small exchange between the Celtic Sea and Irish Sea may strongly determine the local retention of some species near their suitable environment and increase the opportunity for recruitment. Stocks of *Nephrops norvegicus* have been observed in muddy patches in the seabed of the Celtic Deep (Mackie *et al.*, 1995). They are temperature dependent and require a muddy seabed to construct their semi-permanent burrows (Phillips *et al.*, 1980). The Celtic Deep is an area with low tidal energy which allows the water to stratify isolating the bottom from surface and maintaining temperature within a range of approximately 9-11 °C (only changes by about 1-2 °C from winter to summer, Elliott *et al.*, 1991). On the other hand, the low turbulence conditions permit deposition of finer deposits such as muddy sands and mud, that otherwise would not be possible in vertically well-mixed water. The Celtic Deep therefore presents suitable conditions for *Nephrops norvegicus*. Similar habitat conditions of this species were observed in the geographically isolated mud patch in the stratified western Irish Sea (Hill *et al.* 1994; Hill *et al.* 1997a; Horsburgh *et al.*, 2000). In that region, the baroclinic gyre-like circulation was suggested as a local retention mechanism of this species (Hill *et al.* 1994; Hill *et al.* 1997a; Horsburgh *et al.*, 2000).

The implications of these results are not confined to larval transport but also have implications for the dispersal of pollutants. In particular, an appropriate response to a major spill event (such as the Sea Empress incident off west Wales occurred during 1996, see Appendix 8) depends on a reliable forecasting of the residual currents. Most of the models for forecasting oil spill movement basically consider the net transport generated by the influence of the wind ignoring the effects of density-driven currents (Elliott and Jones, 2000). The Sea Empress incident off west Wales occurred during winter conditions (*i.e.* barotropic conditions). Thus, an accurate wind forecast (from meteorological information) could be the most important requirement for oil spill forecasting. However, this study has been shown that, during summer, density-driven currents are more significant than wind-driven residual currents. A comparable incident occurring during summertime in this area, when the baroclinic conditions persist, means that the eventual fate and dispersion of an oil spill would be completely different and probably unlikely to be forecast by spill models which presently neglect baroclinic conditions (Elliott and Jones, 2000).

Another important implication of the results of this thesis is that they change the perspective of the shelf circulation in the Celtic Sea (from barotropic weak wind-driven to baroclinic density-driven with near-surface seasonal cold pool jets). Consequently, the inclusion of horizontal density gradients, particularly bottom fronts, as a summertime forcing, must be seriously considered in baroclinic numerical models in order to determine a more realistic circulation in this region.

8.3.2 Future Work

A significant improvement in the understanding of the summer circulation in the Celtic Sea has been obtained with the results of this study. In particular, these results highlight the importance of the baroclinic conditions in the overall circulation of this shelf sea during the summer. We can then expect the pattern of circulation to last while strong bottom fronts continue to exist in the Celtic Sea. If the stratified conditions last from May to October (section 2.3), we can think that once this bottom structure is formed, it could provide the necessary conditions for the formation and maintenance of seasonal cold pool jets. During the winter, barotropic conditions might be expected. However, further observational and also numerical modelling studies are needed in order to obtain a complete picture of the seasonal (long-term) circulation in the shelf area of the Celtic Sea. In particular, further research to assess the most relevant forcing mechanisms during

winter (mostly barotropic conditions) and the transitions (*i.e.* spring and autumn) will be the next step in the circulation studies in this shelf sea area.

Future research has not to be limited to seasonal temporal scales in order to understand the long-term circulation. It was suggested here that eddy-like features and baroclinic instabilities could affect the expected (long-term) density-driven circulation in this region. Consequently, there is a need to explore the effects of eddies and baroclinic instabilities on the summer circulation in the Celtic Sea, in particular, near the Saint George's Channel. Numerical work combined with detailed observations orientated to study the temporal variability of the flows in terms of the baroclinic instabilities is desirable. In particular, the response of the frontal areas to wind forcing (with similar approach to that of Wang *et al.*, 1990) or to other forcing would help to clarify the intermittent exchange of water (intrusions) between the Irish Sea and the Celtic Sea. Quantitative studies of the residual (monthly or yearly) volume flux across the St. George's Channel would be valuable to determine the exchange of tracers (*e.g.* larvae, contaminants and nutrients) between the Irish Sea and the Celtic Sea.

In recent years, there has been a considerable interest in the impacts of the global warming in the increasing of the sea level and deep-sea circulation (re-distribution of heat). However, global warming and sea level changes must also have important implications in the evolution of the seasonal circulation in shelf areas. A contribution of the changing air temperature and increasing of wind mixing attributed to global warming would imply a change in the timing of onset and intensification of the seasonal stratification. Thus it can be expected stronger density gradients in the frontal areas and hence stronger density-driven currents.

Over longer past geological time-scales the effect of climate change is becoming better understood. According to heating-stirring system (see Chapter 1), water depth and tidal mixing determines the position of the bottom front structures. Consequently, the change of sea-level implies a different position of the frontal areas. This "migration" of the frontal areas and the evolution of the stratification during sea-level changes in the Celtic Sea have been reconstructed with paleotidal models and from continuous sedimentary records (Austin and Scourse, 1997). In particular, planktonic and benthic foraminifera has been used as indices of the impact of decadal-scale climate variations in the marine environment because frontal structures are zones of high organic productivity and

evidence in the biogenic component of shelf sediments accumulated in the bed, (Austin and Scourse, 1997). From these observations and model results, it has been shown that seasonal stratification water extended across the shelf during the early Holocene, first influencing the Central Celtic Sea aorund 9,000 years BP (Austin, and Scourse, 1994; Austin and Scourse, 1997). From the results of this thesis, the movement in the position of frontal areas, due to both long-term climate change (warm and cold phases) and sea-level changes, results in a different density-driven pattern of circulation. Thus, the potential effect of the climate change on the long-term (decadal-scale) baroclinic (density-driven) circulation in the Celtic Sea must be considered in future research.

The Celtic Sea sustains an important biodiversity. In particular, it is the suitable environment for several important commercial species such as *Nephrops norvegicus*. It is desirable to co-ordinate further observational studies of the circulation with marine environmental research (*i.e.* a biological approach) in order to determine regional fishery management strategies. In addition, future research could be oriented to understanding the interaction between the physical conditions of the marine environment and the community limitations, succession and reproductive strategies for spatially and temporally constrained resources.

References

Austin, R.M. and J.D. Scourse (1995) Paleotidal modelling of continental shelves: marine implications of land-bridge in the strait of Dover during the Holocene and Middle Pleistocene, in Preece, R.C. (Ed.). *Island Britain: A Quaternary perspective*. Special Publication of the Geological Society, **96**, 75-88.

Austin, W.E.N. and J.D. Scourse (1997) Evolution of seasonal stratification in the Celtic Sea during the Holocene. *Journal of the Geological Society, London*, **154**, 249-256.

Badan-Dangon, A., C.E. Dorman, M.A. Merrifield and C.D. Winant (1991) The lower atmosphere over the Gulf of California. *J. Geophys. Res.*, **96**, 16877-16896.

Bogden, P.S. and J. O'Donnell (1998) Generalized inverse with shipboard current measurements: tidal and nontidal flows in Long Island Sound. *Journal of Marine Research*, **56**, 995-1027.

Bowden, K.F. (1950) Processes affecting the salinity of the Irish Sea. *Monthly Notices of the Royal astronomical Society*, Geophysical Supplement, **6**, 63-90.

Bowers, D.G. and J.H. Simpson (1987) Mean position of tidal fronts in European-shelf seas. *Continental Shelf Research*, **7**, 35-44.

Brink, K.H. (1998) Hydrographic observations in the coastal ocean. In: *The Sea, Volume 10*, (K.H. Brink and A.R. Robinson, eds). John Wiley & Sons Inc., New York, pp. 359-366.

Brown, J. (1991) The final voyage of *Rapaiti*: a measure of sea-surface drift velocity in relation to the surface wind. *Marine Pollution Bulletin*, **22**, 37-40.

Brown, J., K. Brander, L. Fernand, L. and A.E. Hill (1996) Scanfish: High performance towed undulator. *Sea Technology*, **37**(9), 23-27.

Brown, J., A.E. Hill, L. Fernand and K.J. Horsburgh (1999a) Observations of a seasonal jet-like circulation at the Central North Sea cold pool margin. *Estuarine Coastal and Shelf Science*, **49**, 343-355.

Brown, J., A.E. Joyce, J.N. Aldridge, E.F. Young, L. Fernand and P.A. Gurbutt (1999b) Further identification and acquisition of bathymetric data for Irish Sea modelling. DETR research contract CW0753.

Candela, J., R.C. Beardsley and R. Limeburner (1992) Separation of tidal and subtidal currents in ship-mounted acoustic doppler current profiler observations. *Journal of Geophysical Research*. **97**(C1), 769-788.

Chereskin, T.K. (2001) ADCP measurement techniques (online). University of California San Diego. Available from: http://tryfan.ucsd.edu/~teri/ (Accessed 10 November 2001).

Clark, R.B. (1977) Oceanic management: Conflicting Uses of the Celtic Sea and other Western U.K. waters (Edited by M.M. Sibthorp assisted by M. Unwin). Report of a conference held at University College of Swansea, 19-22 September 1975. Europa publications. London. xiii-xv pp.

Cooper, L.H.N. (1961a). The oceanography of the Celtic Sea: I Wind Drift. *Journal of the Marine Biological Association of the United Kingdom*, **41**, 223-233.

Cooper, L.H.N. (1961b) The oceanography of the Celtic Sea: II Conditions in the spring of 1950. *Journal of the Marine Biological Association of the United Kingdom*, **41**, 235-270.

Cooper, L.H.N. (1967) The physical oceanography of the Celtic Sea. *Oceanogr. Mar. Biol. Ann. Rev.*, **5**, 99-110.

Davies, A.M. and G.K. Furnes (1980) Observed and computed M2 tidal currents in the North Sea. *Journal of Physical Oceanography*, **10**, 237-257.

Davies, A.M. and J.E. Jones (1992a) A three-dimensional wind driven circulation model of the Celtic Sea and Irish Seas. *Continental Shelf Research*, **12**, 159-188.

Davies, A.M. and J.E. Jones (1992b) A three dimensional model of the M2, S2, N2, K1 and O1 tides in the Celtic Sea and Irish Seas, *Prog. Oceano*. **29**, 197-234.

Davis, R.E. (1985) Drifter observations of coastal surface currents during CODE: The method and descriptive view. *Journal of Geophysical Research*, **90**(C3), 4741-4755.

Dowd, M. and K.R. Thompson (1996) extraction of tidal streams from a ship-borne acoustic Doppler current profiler using a statistical-dynamical model. *Journal of Geophysical Research*, **101**(C4), 8943-8956.

Durazo-Arvizu, R. (1993) Horizontal circulation and diffusion at tidal fronts. PhD thesis, University of Wales, Bangor, U.K.

Dyrynda, P. and R. Symberlist (2000) Sea Empress oil spill (online). University of Wales Swansea. Available from: http://www.swan.ac.uk/biosci/empress/main.htm (Accessed 20 November 2001).

Elliott, A.J. and T. Clarke (1991) Seasonal stratification in the northwest European shelf seas. *Continental Shelf Research*, **11**, 467-492.

Elliott, A.J., T. Clarke and Z. Li (1991) Monthly distributions of surface and bottom temperatures in the northwest European shelf seas. *Continental Shelf Research*, **11**, 453-466.

Elliott, A.J. and Z. Li (1991) Thermocline depths and water temperatures at selected sites in the N.W.European shelf seas. *Marine Pollution Bulletin*, **22**, 282-286.

Elliott, A.J. and B. Jones. (2000) The Need for Operational Forecasting During Oil Spill Response. *Marine Pollution Bulletin*, **40**(2), 110-121.

Emery, W.J. and R.E. Thompson (2001) *Data analysis methods in physical oceanography.* Second edition. Elsevier Science B.V., Amsterdam. 619 pp.

Fernand, L. (1999) High resolution measurements of the velocity and thermohaline structure of the western Irish Sea gyre. *PhD thesis*, University of Wales, Bangor, U.K.

Firing, E., J. Ranada and P. Caldwell (1995) Processing ADCP data with the CODAS software system version 3.1, user's manual, *University of Hawaii*. Manual and software available electronically at ftp://noio.soest.hawaii.edu/pub/codas3.

Foreman, M.G.G. and Freeland H.J. (1991) A comparison of techniques for tide removal from ship-mounted acoustic Doppler measurements along the southwest coast of Vancouver Island. *Journal of Geophysical Research*, **96**(C9), 17007-17021.

Garcia-Gorriz, E., J. Font and J. Candela (1997) Data quality control for vessel mounted Acoustic Doppler current profiler. Application for the Western Mediterranean Sea. *Scientia Marina*, **61**(4), 417-430.

Garrett, C.J.R. and E. Horne (1978) Frontal circulation due to cabbeling and double diffusion. *Journal of Geophysical Research*, **83**, 4651-4656.

Garrett, C.J.R. and J.W. Loder (1981) Dynamical aspects of shallow sea fronts. *Philosophical Transactions of the Royal Society of London*, **A302**, 563-581.

Geyer, W.R. and R. Signell (1990) Measurements of tidal flow around a headland with a shipboard acoustic current profiler. *Journal of Geophysical Research*, **95**(C3), 3189-3197.

Goldsmith, R.A. and A.F. Bunker (1979) Woods Hole Oceanographic Institution collection of climatology and air-sea interaction (CASI) data. *Woods Hole Oceanographic Institute technical Report* WHOI-79-70, 75 pp.

Griffiths, R.W. and P.F. Linden (1981) The stability of vortices in a rotating stratified fluid. *Journal of Fluid Mechanics*, **105**, 283-316.

Harvey, H.W. (1929) Hydrodynamics of the waters southeast of Ireland. *J. Cons. Perm. Int. Explor. Mer*, **4**, 80-92.

Hill, A.E. (1993) Seasonal gyres in shelf seas. *Annales Geophysicae*, **11**, 1130-1137.

Hill, A.E. (1996) Spin-down and the dynamics of dense pool gyres in shallow seas. *Journal of Marine Research*, **54**, 471-486.

Hill, A.E. (1998a) Buoyancy effects in coastal and shelf seas. In: *The Sea, Volume 10*, (K.H. Brink and A.R. Robinson, eds). John Wiley & Sons Inc., New York, pp. 21-62.

Hill, A.E. (1998b) Diel vertical migration in stratified tidal flows: Implications for plankton dispersal. *Journal of Marine Research*, **56**, 1069-1096.

Hill, A.E., I.D. James, P.F. Linden, J.P. Matthews, D. Prandle, J.H. Simpson, E.M. Gmitrowicz, D.A. Smeed, K.M.M. Lwiza, R. Durazo, A.D. Fox and D.G. Bowers (1993) Dynamics of tidal mixing fronts in the North Sea. *Phil. Trans. R. Soc. Lond.*, **A343**, 431-446.

Hill, A.E., R. Durazo and D.A. Smeed (1994) Observations of a cyclonic gyre in the western Irish Sea. *Continental Shelf Research*, **14**, 479-490.

Hill, A.E., J. Brown and L. Fernand (1997a) The summer gyre in the western Irish Sea: shelf sea paradigms and management implications. *Estuarine, Coastal and Shelf Science,* **44** (Supplement A), 83-95.

Hill, A.E., K.J. Horsburgh, R.W. Garvine, P.A. Gillibrand, G. Slesser, W.R. Turrell and R.D. Adams (1997b) Observations of a density-driven recirculation of the Scottish coastal current in the Minch. *Estuarine Coastal and Shelf Science*, **45**, 473-484.

Holt, J. T. and I.D. James (1999) A simulation of the Southern North Sea in comparison with measurements from the North Sea project. Part 1: Temperature. *Continental Shelf Research*, **19**, 1087-1112.

Horsburgh, K. (1999) Observations and modelling of the Western Irish Sea Gyre. *PhD thesis*, University of Wales, Bangor, U.K.

Horsburgh, K.J., A.E. Hill and J. Brown (1998) A summer jet in the St. George's Channel of the Irish Sea. *Estuarine Coastal and Shelf Science*, **47**, 285-294.

Horsburgh, K.J., A.E. Hill, J. Brown, L. Fernand, R.W. Garvine and M.M.P. Angelico (2000) Seasonal evolution of the cold pool gyre in the western Irish Sea. *Progress in Oceanography*, **46**, 1-58.

Howarth, M.J. (1975) Current surges in St. George's Channel. *Estuarine Coastal and Shelf Science*, **3**, 57-70.

Howarth, M.J. and R. Proctor (1992) Ship ADCP measurements and tidal models of the North Sea. *Continental Shelf Research*, **12**, 601-623.

Huthnance, J.M. (1973) Tidal current asymmetries over the Norfolk Sandbanks. *Estuarine Coastal and Shelf Science*, **1**, 89-99.

Hydrographic Department (Admiralty) (1970) Underwater Handbook: Western Approaches to the British Isles. Hydrogr. Dep., MOD(N), Taunton.

James, I.D. (1977) A model of annual cycle of temperature in a frontal region of the Celtic Sea. *Est. Coast Mar. Sci.*, **5**, 339-353.

James, I.D. (1978) A note on the circulation induced by a shallow-sea front. *Est. Coast Mar. Sci.*, **7**, 197-202.

James, I.D. (1980) Thermocline Formation in the Celtic Sea. *Est. Coast Mar. Sci.*, **10**, 597-607.

James, I.D. (1981) Fronts and shelf-circulation models. *Phil. Trans. R. Soc. Lond.*, **A302**, 597-604.

James, I.D. (1984) A three-dimensional numerical shelf-sea front model with variable eddy viscosity and diffusivity. *Continental Shelf Research,* **3**, 69-98.

James, I.D. (1986) A front-resolving sigma co-ordinate sea model with a simple hybrid advection scheme. *Appl. Math. Modelling*, **10**, 87-92.

James, I.D. (1988) Experiments with numerical model of coastal currents and tidal mixing fronts. *Continental Shelf Research,* **8**(12), 1275-1297.

James, I.D. (1989) A three-dimensional model of circulation in a frontal region in the North Sea. *Deutsche Hydrographishe Zeitschrift*, **14**, 479-490.

James, I.D. (1990) *Numerical modeling of density driven circulation in shelf seas*. In: Modelling Marine Systems Vol II, (A.M. Davies, ed.), CRC Press, Florida, pp. 345-372.

Jones, S.R. and J.W. Read (1993) Ministry of Agriculture, Fisheries and Food current meter system and data inventory, 1987-89. *Fisheries research technical report, MAFF Direct. Fish. Res.*, Lowestoft, **94**, 1-28.

Joyce, T.M. (1989). On situ "calibration" of shipboard ADCP's. *J. Atmos. Oceanic Technol.*, **6**, 169-172.

Knight, P.J. and M.J. Howarth (1999) The flow through the north channel of the Irish Sea. *Continental Shelf Research*, **19**, 693-716.

Kosro, P.M. (1985) Shipboard Acoustic Current Profiling during the Coastal Ocean Dynamic Experiment. *PhD thesis*, University of California, San Diego (Scripps Inst. Of Oceanogr., La Jolla., Calif.). Ref. 85-8.

Lavín, M.F., R. Durazo, E. Palacios, M.L. Argote and L. Carrillo (1997) Lagrangian observations of the circulation in the northern Gulf of California. *J. Phys. Ocean.*, **27**(10), 2298-2305.

Lermusiaux, P.F.J. (1997) Error subspace data assimilation methods for ocean field estimation: theory, validation and application. *PhD thesis*, Harvard University, Cambridge, Mass.

Limeburner R. and R.C. Beardsley (1996) Near-surface recirculation over Georges Bank. *Deep-Sea Research II*, **43**(7-8), 1547-1574.

Linden, P.F. and G.J.F. van Heisjt (1984) Two-layer spin-up and frontogenesis. *Journal of Fluid Mechanics*, **143**, 69-94.

Loder, J.W. (1980) Topographic rextification of tidal currents on the sides of Georges Bank. *Journal of Physical Oceanography*, **10**, 1399-1416.

Longuet-Higgins, M.S. (1969) On the transport of mass by time-varying ocean currents. *Deep-Sea Research*, **16**, 431-447.

Lwiza, K.M.M.. (1990) A study of tidal front dynamics using ADCP. *PhD thesis*, University of Wales, Bangor, U.K.

Lwiza, K.M.M., D.G. Bowers and J.H. Simpson (1991) Residual and tidal flow at a tidal mixing front in the North Sea. *Continental Shelf Research*, **11**, 1379-1395.

Mackie, A.S.Y., P.G. Oliver and E.I.S Rees (1995) Benthic biodiversity in the southern Irish Sea. *Studies in marine Biodiversity and Systematics from the National Museum of Wales. BIOMÔR Reports*, 1:263 pp.

Mann, K.H. and J.R.N. Lazier (1991) *Dynamics of Marine Ecosystems*. Blackwell Scientific Publications, Boston. USA. 466pp.

Mass, L.R.M. and J.J.M. van Haren (1987) Observations on the vertical structure of tidal and inertial currents in the central North Sea. *J. Mar. Res.*, **45**, 293-318.

Matthews, D.J. (1913) The salinity and temperature of the Irish Channel and waters of Ireland. *Fisheries Ireland, Scientific Investigations*, 1913, **IV**, 26pp.

Münchow, A. (2000) Detiding three-dimensional velocity survey data in coastal waters, *J. Atmos. Ocean. Technol.*, **17**, 736-749.

Münchow A., R.W.Garvine, and T.F. Pfeiffer (1992) Sudtidal currents from a shipboard acoustic Doppler current profiler in tidally dominated waters. *Continental Shelf Research,* **12**(4), 499-515.

Niiler, P.P., A.S. Sybrandy, K. Bi, P.M. Poulain and D. Bitterman (1995) Measurement of the water-following capability of holey sock and tristar drifters. *Deep Sea Research*, **42**, 1951-1964.

Open University (1989) *Ocean Circulation* (prepared by an open university course team). First edition. Pergamon press, England. 238 pp.

Pedlosky, J. (1979) *Geophysical Fluid Dynamics*. Springer-Verlag, New York, 710pp.

Phillips, B.F., J.S. Cobb and R.W. George (1980) *The biology and management of lobsters. Volumen I Physiology and Behaviour*. Academic Press. New York, 463 pp.

Pingree, R.D. (1978) Cyclonic eddies and cross-frontal mixing. *Journal of the Marine Biological Association of the United Kingdom*, **58**, 955-963.

Pingree, R.D. (1979) Baroclinic eddies bordering the Celtic Sea in late summer. *Journal of the Marine Biological Association of the United Kingdom*, **59**, 689-698.

Pingree, R.D. (1980) Physical Oceanography of the Celtic Sea and English Channel. In: *The northwest European shelf seas: The sea bed and the sea in motion. II Physical and chemical oceanography and physical resources*. Ed: F.T. Banner, M.B. Collins, and K.S. Massie. Elsevier Oceanography Series. Amsterdam/Oxford/New York. p 415-465.

Pingree, R.D. (1994) Winter warming in the southern Bay of Biscay and lagrangian eddy kinematics from a deep-drogued ARGOS buoy. *Journal of the Marine Biological Association of the United Kingdom*, **74**, 107-128.

Pingree, R.D., P.R. Pugh, P.M. Holligan and G.R. Forster (1975) Summer phytoplankton blooms and red tides along tidal fronts in the approaches to the English Channel. *Nature*, **258**, 672-677.

Pingree, R.D., P.M.. Holligan, G.T. Mardell and R.N. Head (1976) The influence of physical stability on spring, summer and autumn phytoplankton blooms in the Celtic Sea. *Journal of the Marine Biological Association of the United Kingdom*, **56**, 845-873.

Pingree, R.D. and D.K. Griffiths (1978) Tidal fronts on the shelf seas around the British Isles. *Journal of Geophysical Research*, **83**, 4615-4622.

Pingree, R.D. and B. Le Cann (1989) Celtic and Armorican slope and shelf residual currents. *Progress in Oceanography*, **23**, 303-338.

Pollard, R.T.and J. Read (1989) A method for calibrating shipmounted acoustic Doppler profilers and the limitations of gyro compasses. *Journal of Atmospheric and Oceanic Technology*, **6**, 859-865.

Prandle, D. (1982) the vertical structure of tidal currents and other oscillatory flows. *Continental Shelf Research*, **1**, 191-207.

Prandle, D. (1984) A modelling study of the mixing of ^{137}Cs in the seas of the European continental shelf. *Philosophical Transactions of the Royal Society of London*, **A310**, 407-436.

Prandle, D. and J. Matthews (1990) The dynamics of nearshore surface currents generated by tides, wind and horizontal density gradients. *Continental Shelf Research*, **10**, 665-681.

Proakis, J.G. and D.G. Manolakis (1992) *Digital signal processing: Principles, algorithms and applications*, Second edition. Macmillan Publishing Company, New York, 969 pp.

Proctor, R. and I.D. James (1996) A fine-resolution 3D model of the Southern North Sea. *Journal of Marine Systems*, **8**, 285-295.

Pugh, D.T. (1987) *Tides, surges and mean sea-level.* John Wiley and Sons Ltd., Chichester, U.K. 472pp.

RDI (1989) Acoustic Doppler current profilers principles of operation: a practical primer. *RD Instruments*, San Diego, Ca. 36 pp.

RDI (2001) RD Instruments: Acoustic Doppler solutions (online). *RD Instruments* San Diego, Ca. Available from: http://www.rdinstruments.com (Accessed 15 May 2001).

Robinson, I.S. (1979) The tidal dynamics of the Irish Sea and Celtic Sea. *Geophysical Journal of the Royal Astronomical Society*, **56**, 159-197.

Robinson, A.R., P.F.J. Lermusiaux and N. Q. Sloan III (1998) *Data Assimilation. In: The Sea, Volume 10*, (K.H. Brink and A.R. Robinson, eds). John Wiley & Sons Inc., New York, pp. 541-594.

Signell, R.P. and R. Geyer (1991) Transient eddy formation around headlands. *Journal of Geophysical Research*, **96**(C2), 2561-2575.

Simpson, J.H. (1976) A boundary front in the summer regime of the Celtic Sea. *Estuarine and Coastal MarineScience*, **4**, 71-81.

Simpson, J.H. (1981) The shelf-sea fronts: implications of their existence and behaviour. *Phil. Trans. R. Soc. Lond.*, **A302**, 531-546.

Simpson, J.H. (1998) The Celtic Seas coastal segment (19,E). In: *The Sea, Volume 11*, (K.H. Brink and A.R. Robinson, eds). John Wiley & Sons Inc., New York, pp. 659-698.

Simpson, J.H. and J.R. Hunter (1974) Fronts in the Irish Sea. *Nature* (London), **250**, 404-406.

Simpson, J.H., C.M. Allen and N.C.G. Morris (1978) Fronts on the Continental shelf. *Jour. Geophys. Res.*, **83**, 4607-4614.

Simpson, J.H. and R.D. Pingree (1978) Oceanic fronts in coastal processes. In: *Proceedings of a workshop help at the Marine Sciences research Center*. M.J. Bowman and E. Esaias, Editors. Stony Brook, New York, 1977.

Simpson, J.H. and D. Bowers (1981) Models of stratification and frontal movement in shelf seas. *Deep-Sea Research*, **28A**, 727-738.

Simpson, J.H. and D. Bowers (1984) The role of tidal stirring in controlling the seasonal heat cycle in shelf seas. *Annales Geophysicae*, **2**, 411-416.

Simpson, J.H., Mitchelson-Jacob, E.G., Hill, A.E. (1990) Flow structure in a channel from an acoustic Doppler current profiler. *Continental Shelf Research*, **10**, 589-603.

Sombardier, L. and P.P. Niiler (1994) Global surface circulation measured by Lagrangian drifters. *Sea Technology*, **35**, 21-24.

Souza, A.J., J.H. Simpson and F. Schirmer (1997) Current structure in the Rhine region of freshwater influence. *Journal of Marine Research*, **55**, 277-292.

Steger, J.M., C.A. Collins, F.B. Schwing, M. Noble, N. Garfield and M.T. Steiner (1998) An empirical model of the tidal currents in the Gulf of Farallones. *Deep-Sea Res. II*, **45**, 1471-1505.

Swearer, S.E., J.E. Caselle, D.W. Lea and R.R. Warner (1999) Larval retention and recruitment in an island population of coral-reef fish. Nature (London), 402, 799-802.

Thompson, K.R. and D.T. Pugh (1986) The subtidal behaviour of the Celtic Sea - II. *Currents. Continental Shelf Research*, **5**, 321-346.

Thorson, G. (1950) Reproductive and larval ecology of marine bottom invertebrates. *Biol. Rev.*, **25**, 1-45.

UNESCO (1978) Eight report of the join panel on oceanographic tables and standars. UNESCO Technical papers in Marine Science. No. 28, 35pp.

van Aken, H.M., G.J.F. van Heijst and L.R.M. Maas (1987). Observations of fronts in the North Sea. *Journal of Marine Research*, **45**, 579-600.

van Heijst, G.J.F. (1986) On the dynamics of a tidal mixing front. In: *Marine Interfaces Ecohydrodynamics*, J.C.J. Nihoul, editor, Elsevier Oceanography Series No. 42, Amsterdam, pp. 165-194.

Wang, D., D. Chen and T.J. Sherwin (1990) Coupling between mixing and advection in a shallow sea front. *Continental Shelf Research*, **10**(2), 123-136.

Williams, R. (1985) Vertical distribution of *Calanus finmarchicus* and *C. helgolandicus* in relation to the development of the seasonal thermocline in the Celtic Sea. *Marine Biology*, **86**, 145-149.

Williams, R. and D.V.P. Conway (1984) Vertical distribution, and diurnal migration of Calanus helgolandicus in the Celtic Sea. *Marine Biology*, **79**, 63-73.

Young, E.F., J. Brown and J.N. Aldridge (2001) Application of a large area curvilinear model to the study of the wind-forced dynamics of flows through the North Channel of the Irish Sea. *Continental Shelf Research*, **21**, 1403-1434.

Zimmerman, J.T.F. (1978) Topographic generation of residual circulation by oscillatory (tidal) currents. *Geophys. Astrophys. Fluid Dynamics*, **11**, 35-47.

Zimmerman, J.T.F. (1979) On the Euler-Lagrange transformation and Stoke's drift in the presence of oscillatory and residual currents. *Deep-Sea Research*, **26A**, 505-520.

APPENDICES

Appendix 1: The stratification parameter

A criterion was proposed by Simpson and Hunter (1974) to predict if stratification develops or not in the shelf sea area during the heating period. This criterion consists of balancing the potential energy increase that occurs when stratified water is mixed vertically, with the available turbulent kinetic energy from tidal currents. This results in a criteria that indicates that a water column will stratified if,

$$\frac{Qh}{U^3} \geq \frac{8C_p k\varepsilon\rho}{3\Pi\alpha g} \qquad \text{A1.1}$$

Where Q is the rate of solar heat input (W m^{-2}), U is the amplitude of the depth-mean tidal stream (m s^{-1}), h is the water depth (m), α is the linear expansion coefficient, C_p the specific heat capacity, g is gravitational acceleration (m s^{-2}), k is a quadratic drag coefficient, ρ the density and ε is the efficiency of the mixing by the tide (assumed constant in this model). The model assumes no contribution from horizontal advection (*i.e.* a local heating-stirring balance). When an exact balance between heating and stirring exists (equal sign in equation A1.1), it defines the location of tidal mixing fronts. Q can be considered as spatially invariant over a region the size of the Celtic Sea, therefore the relationship simplifies in the variable h/U^3. This variable is known as the *stratification parameter*. Maps of the stratification parameter using numerical modeled tidal currents show a good agreement with frontal observations from I-R imagery (Pingree and Griffiths, 1978).

Appendix 2: Scanfish Leg positions

Initial and final positions of Scanfish Legs for CORY798

LEG Number	Initial Latitude (North)	Initial Longitude (West)	Final Latitude (North)	Final Longitude (West)
107	51.8698	7.7248	51.3487	7.0197
108	51.3493	7.0058	51.3497	5.3499
113	51.3504	5.3922	51.3498	4.4052
118	51.304	6.3397	50.627	4.8313
121	51.29	6.3964	52.3833	5.5303
124	52.385	6.156	52.1	4.8861
129	52.1089	6.4509	51.7832	5.4356
131	51.2984	6.3385	51.674	5.2646
136	52.0812	7.4418	51.3007	6.3385
137	52.0941	6.8225	51.4017	6.1608

Initial and final positions of Scanfish Legs for CORY998

LEG Number	Initial Latitude (North)	Initial Longitude (West)	Final Latitude (North)	Final Longitude (West)
178	51.6605	8.4708	49.9549	6.4232
179	51.5092	9.0573	51.2461	8.812
180	51.8481	7.9276	50.2303	5.862
181	50.4514	6.5859	50.0547	6.0963
182	52.0843	7.4345	50.296	5.2712
186	52.1122	6.852	51.3568	5.8448
187	51.3548	5.8305	51.3503	4.3226
189	51.3009	6.3362	51.0017	4.5649
190	50.5774	7.526	51.3033	6.3538
201	51.3032	6.3404	50.6148	4.8049
202	51.2758	6.4176	52.5008	5.4324
209	52.1324	6.2507	51.9312	5.4285
210	52.3824	6.1555	52.0921	4.851
211	52.2346	6.2412	51.9976	5.1379
212	52.126	6.4935	51.7841	5.4323
213	52.0345	6.4723	51.6356	5.5881
214	51.2973	6.3349	51.6811	5.2482
223	51.6153	4.8515	50.9983	4.8504
224	51.5231	4.1223	51.1464	4.2957

Appendix 3: Hydrographic and calculated geostrophic velocities: Cross-sections

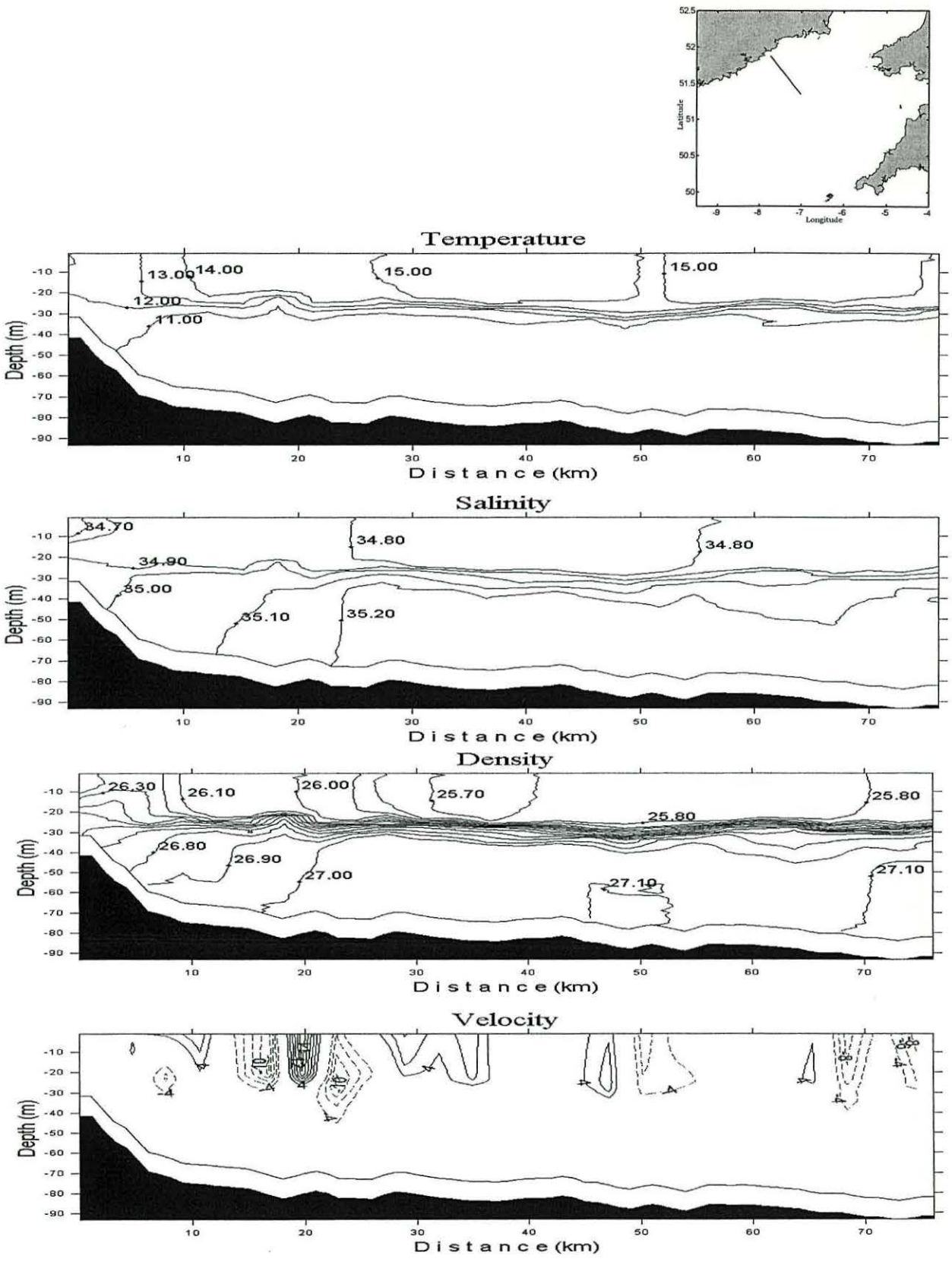

Figure A3.1 Transverse section crossing the Celtic Sea corresponding to the leg 107 (CORY798) showing the vertical structure of: (a) Temperature (°C), (b) Salinity, (c) density (σ_t in kg/m^3), and (d) geostrophic velocities in cm s^{-1} derived from the density field. In the latest, continuous lines represent water going into the page, contours with dashed lines water out the page. The location of the cross-section is observed in the top right corner of the page.

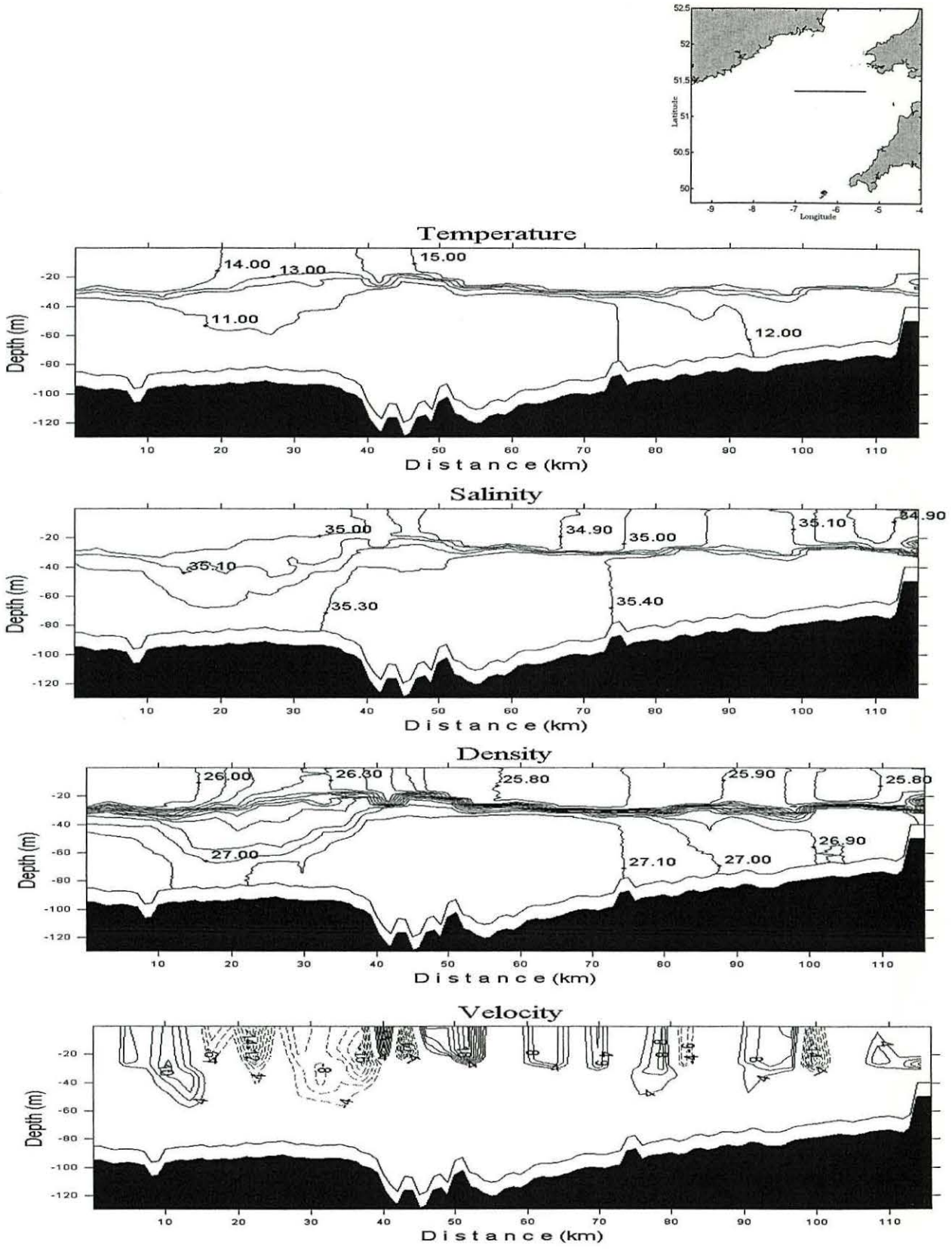

Figure A3.2 Transverse section crossing the Celtic Sea corresponding to the leg 108 (CORY798) showing the vertical structure of: (a) Temperature (°C), (b) Salinity, (c) density (σ_t in kg/m^3), and (d) geostrophic velocities in cm s^{-1} derived from the density field. In the latest, continuous lines represent water going into the page, contours with dashed lines water out the page. The location of the cross-section is observed in the top right corner of the page.

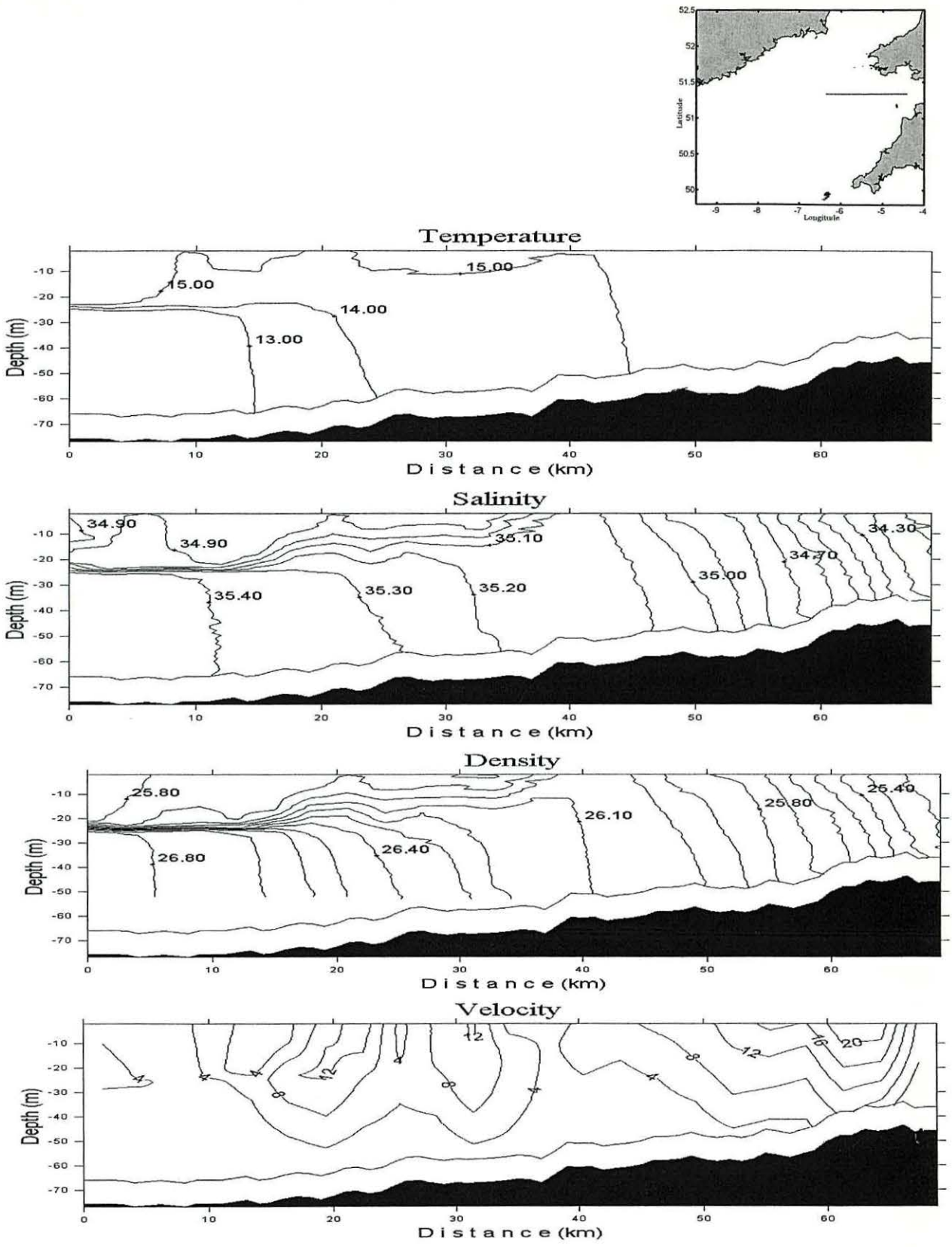

Figure A3.3 Transverse section crossing the Celtic Sea corresponding to the leg 113 (CORY798) showing the vertical structure of: (a) Temperature (°C), (b) Salinity, (c) density (σ_t in kg/m^3), and (d) geostrophic velocities in cm s^{-1} derived from the density field. In the latest, continuous lines represent water going into the page, contours with dashed lines water out the page. The location of the cross-section is observed in the top right corner of the page.

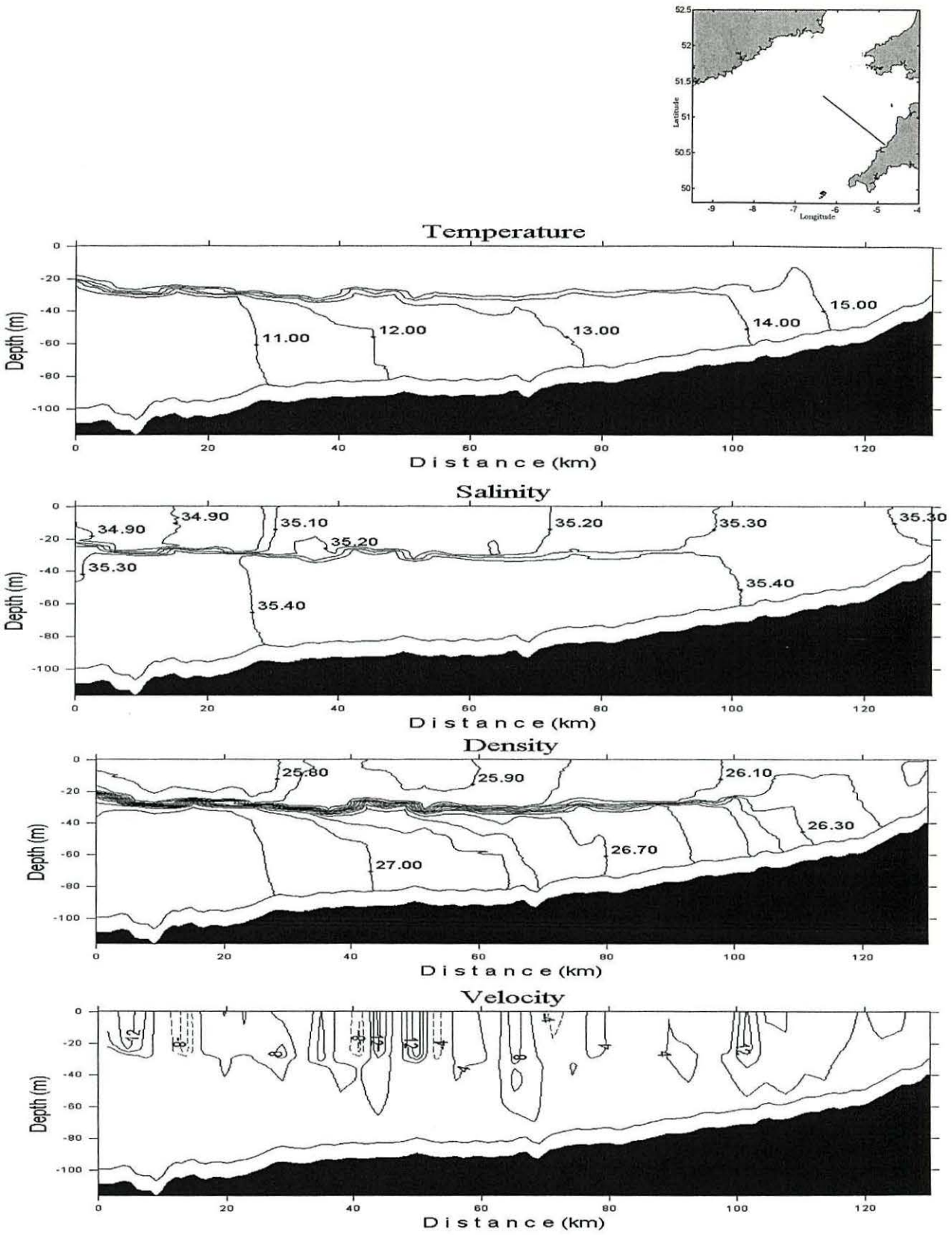

Figure A3.4 Transverse section crossing the Celtic Sea corresponding to the leg 118 (CORY798) showing the vertical structure of: (a) Temperature (°C), (b) Salinity, (c) density (σ_t in kg/m^3), and (d) geostrophic velocities in cm s^{-1} derived from the density field. In the latest, continuous lines represent water going into the page, contours with dashed lines water out the page. The location of the cross-section is observed in the top right corner of the page.

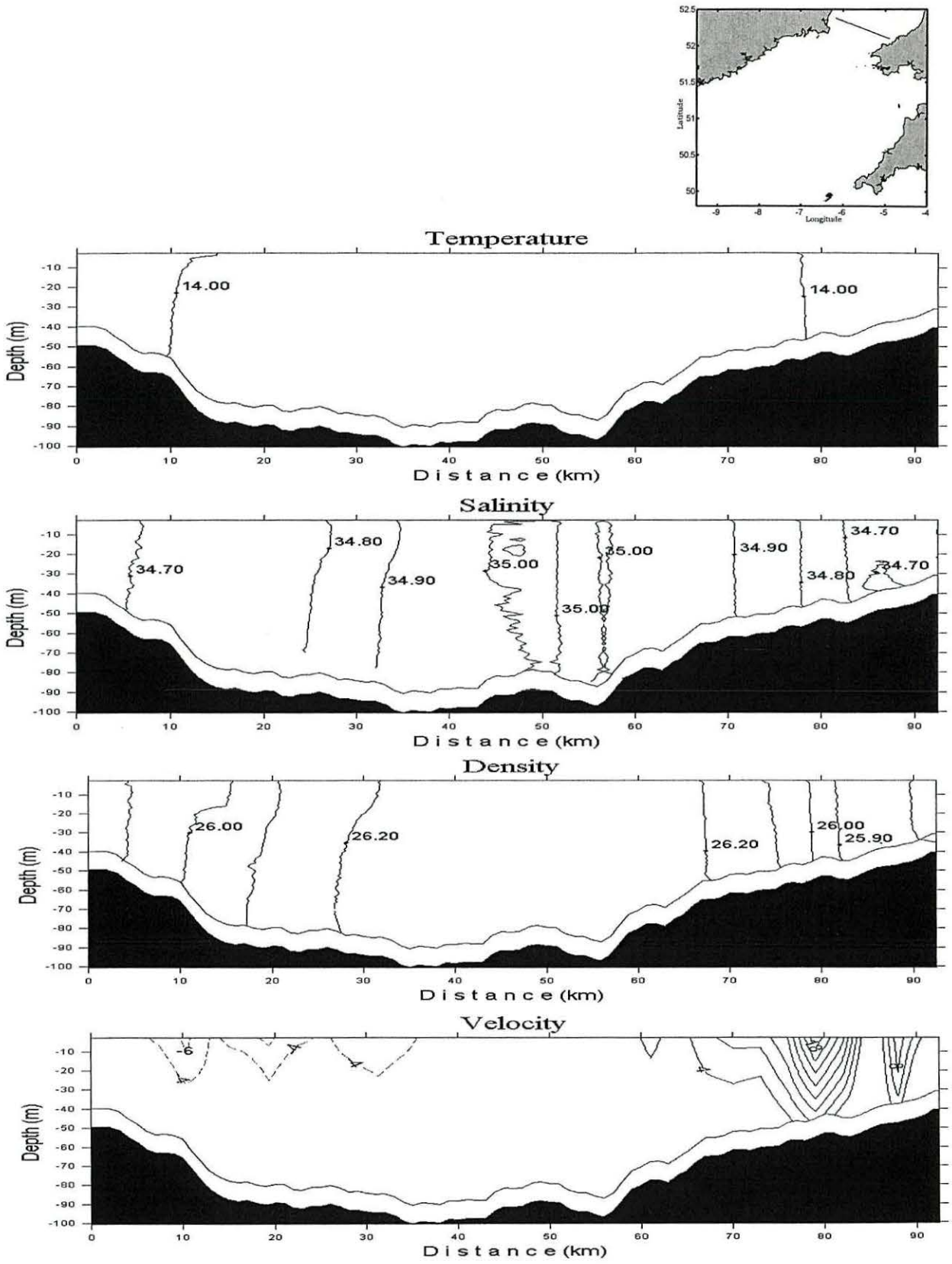

Figure A3.5 Transverse section crossing the Celtic Sea corresponding to the leg 124 (CORY798) showing the vertical structure of: (a) Temperature (°C), (b) Salinity, (c) density (σ_t in kg/m^3), and (d) geostrophic velocities in cm s^{-1} derived from the density field. In the latest, continuous lines represent water going into the page, contours with dashed lines water out the page. The location of the cross-section is observed in the top right corner of the page.

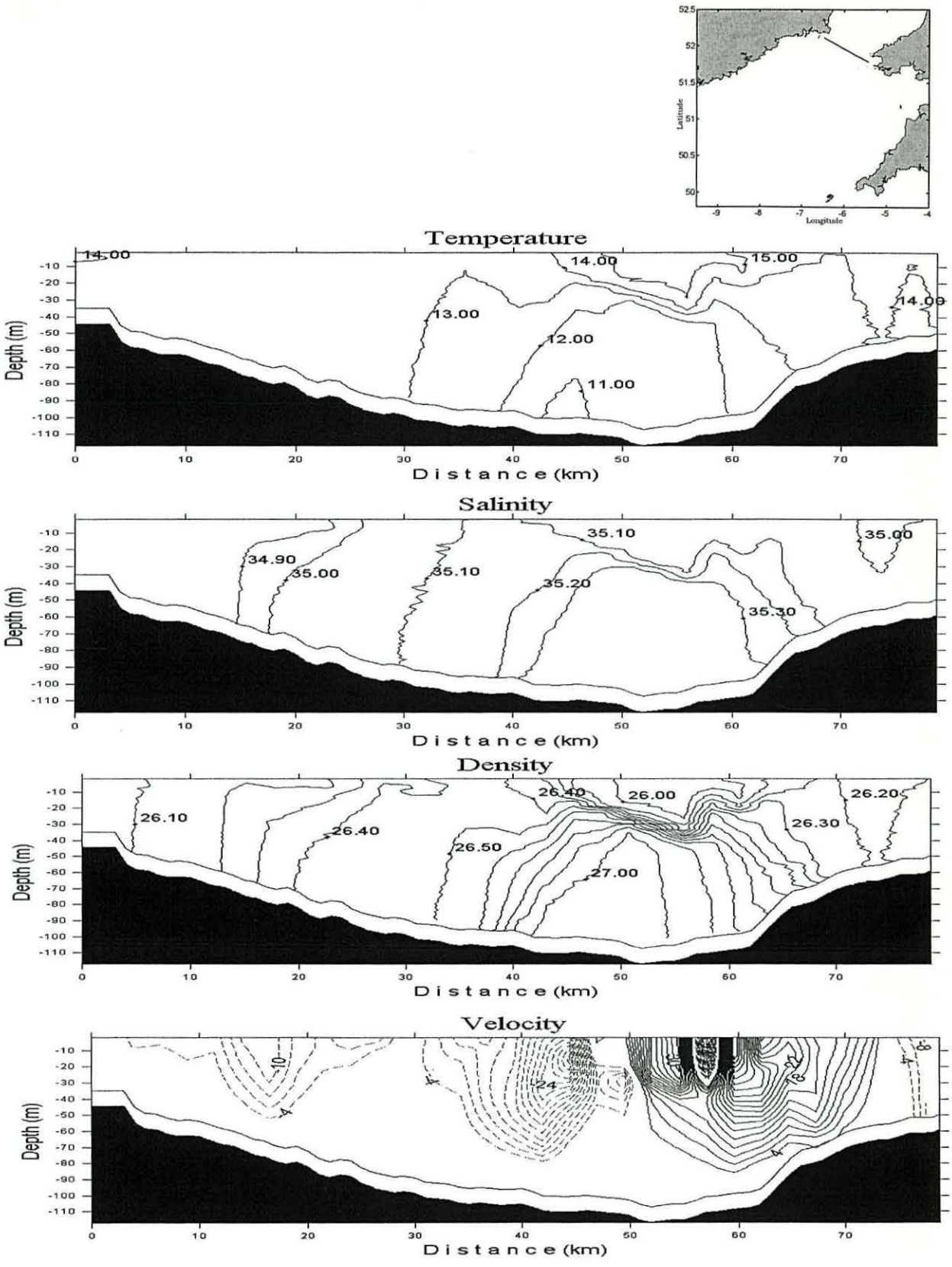

Figure A3.6 Transverse section crossing the Celtic Sea corresponding to the leg 129 (CORY798) showing the vertical structure of: (a) Temperature (°C), (b) Salinity, (c) density (σ_t in kg/m^3), and (d) geostrophic velocities in cm s^{-1} derived from the density field. In the latest, continuous lines represent water going into the page, contours with dashed lines water out the page. The location of the cross-section is observed in the top right corner of the page.

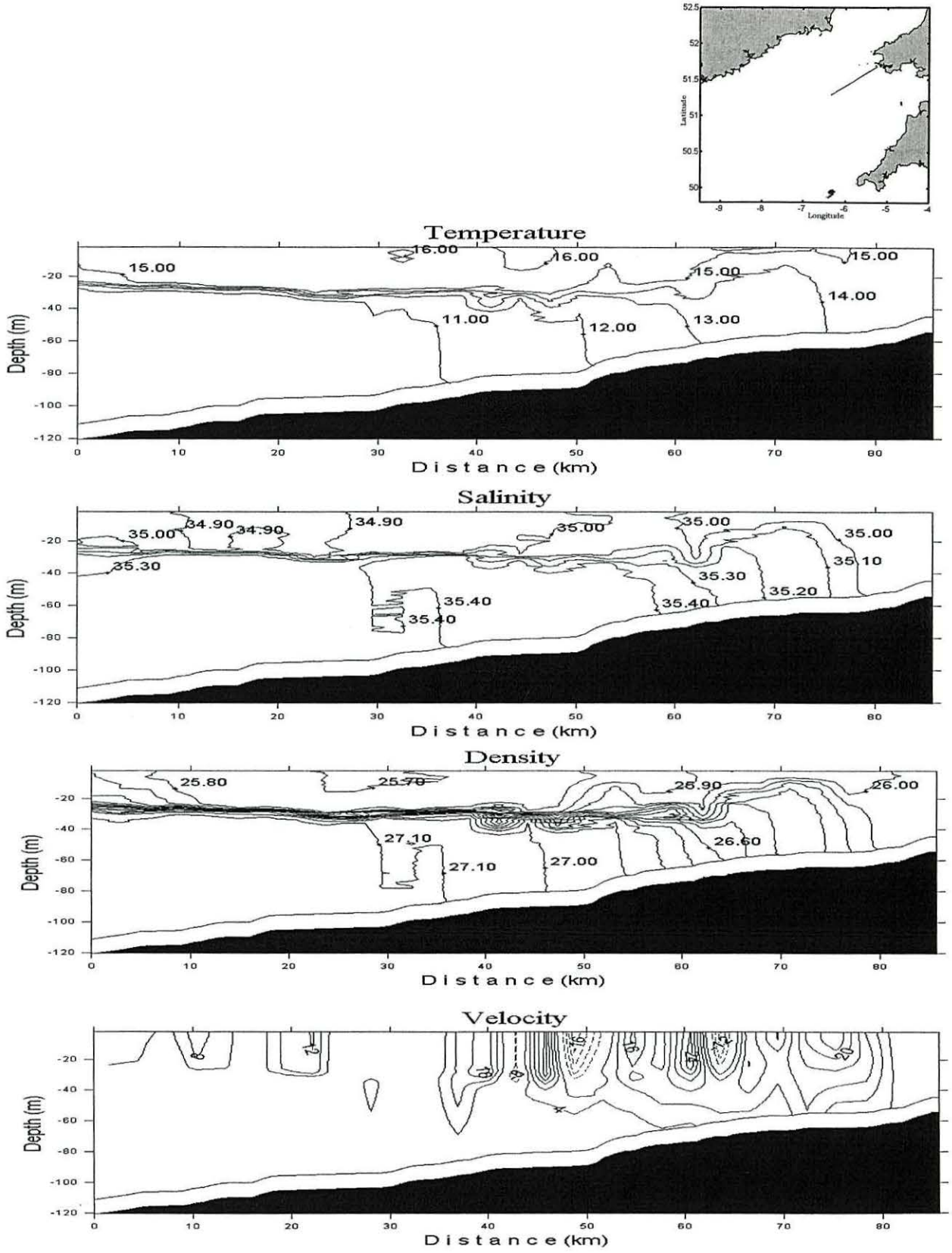

Figure A3.7 Transverse section crossing the Celtic Sea corresponding to the leg 131 (CORY798) showing the vertical structure of: (a) Temperature (°C), (b) Salinity, (c) density (σ_t in kg/m^3), and (d) geostrophic velocities in cm s^{-1} derived from the density field. In the latest, continuous lines represent water going into the page, contours with dashed lines water out the page. The location of the cross-section is observed in the top right corner of the page.

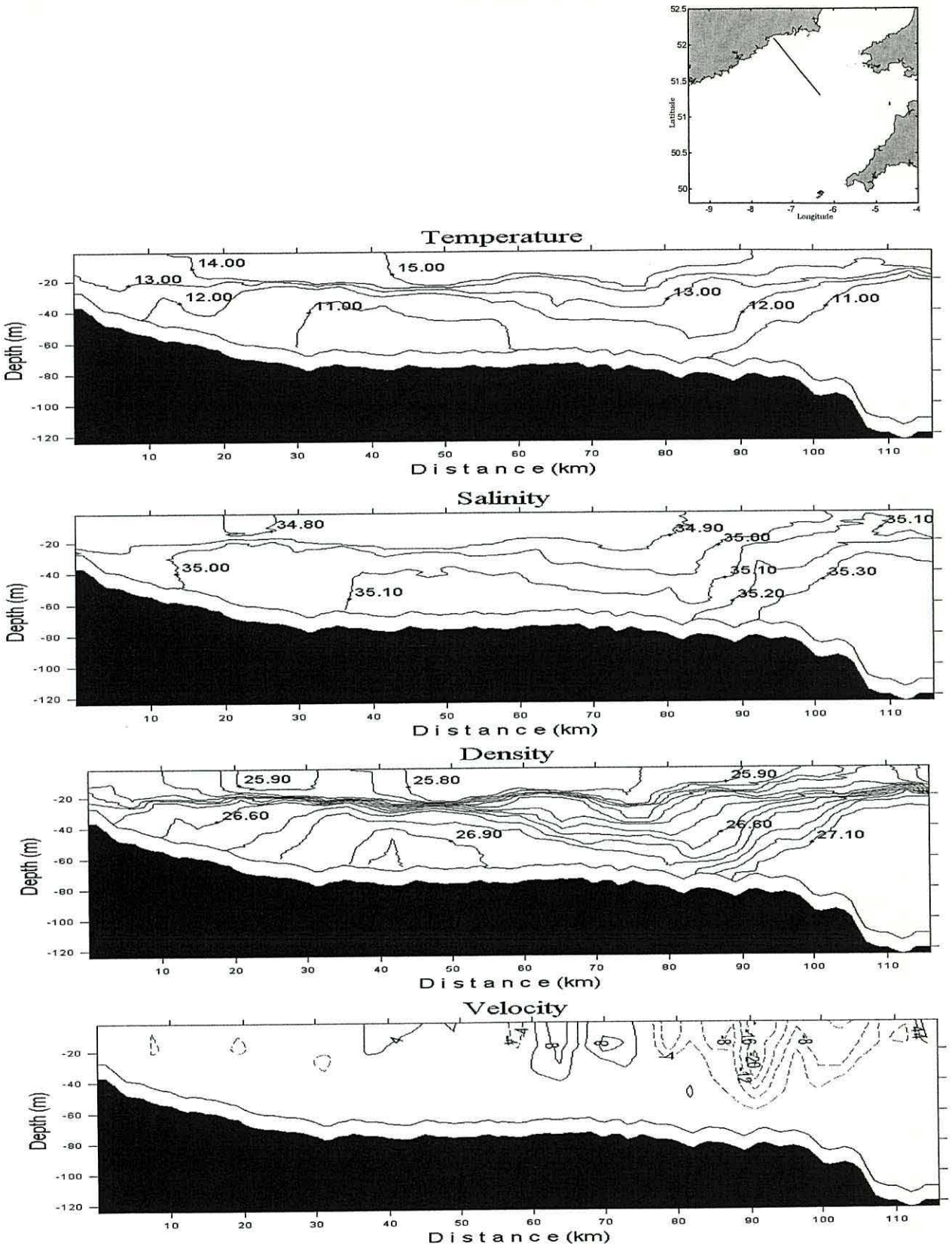

Figure A3.8 Transverse section crossing the Celtic Sea corresponding to the leg 136 (CORY798) showing the vertical structure of: (a) Temperature (°C), (b) Salinity, (c) density (σ_t in kg/m^3), and (d) geostrophic velocities in cm s^{-1} derived from the density field. In the latest, continuous lines represent water going into the page, contours with dashed lines water out the page. The location of the cross-section is observed in the top right corner of the page.

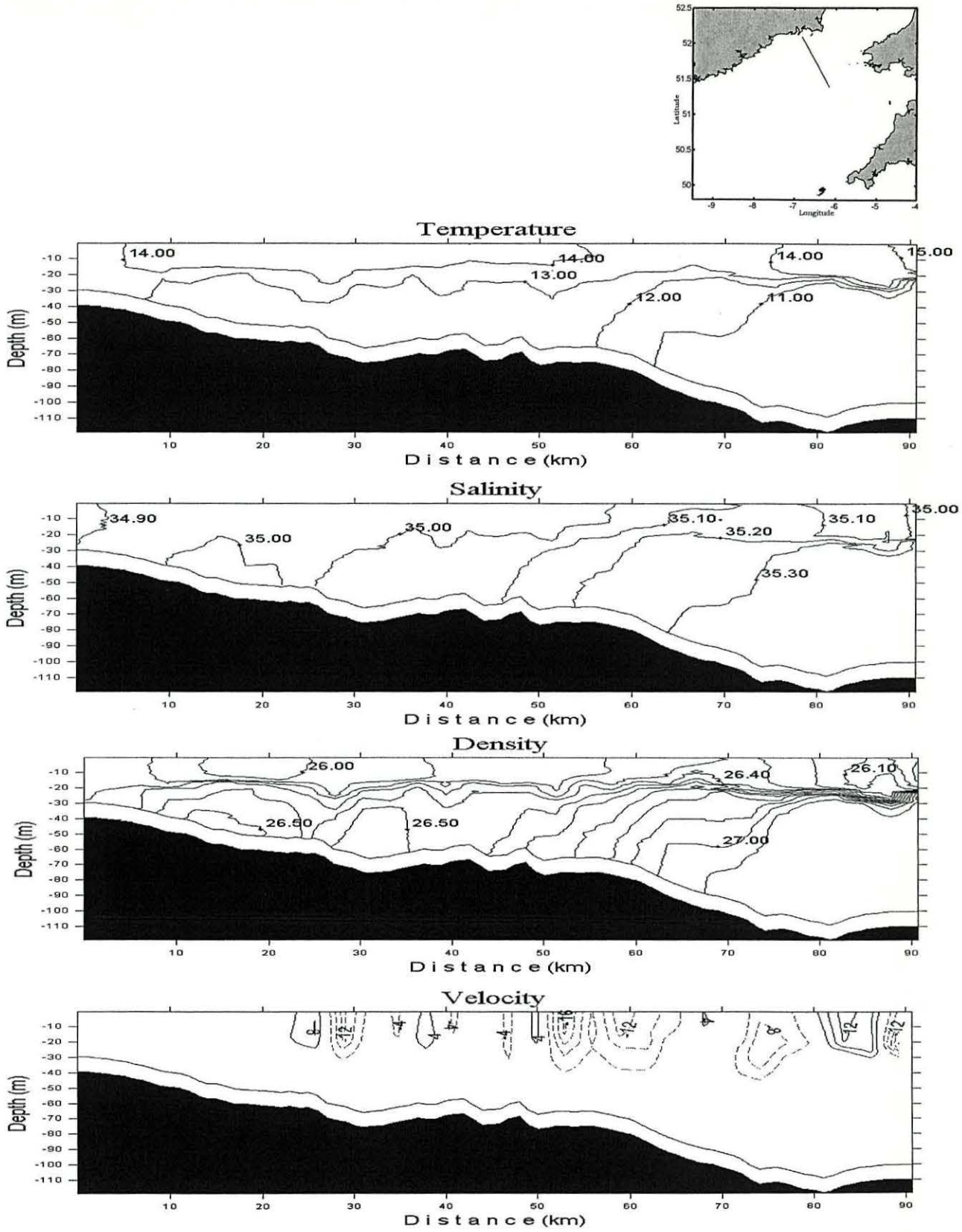

Figure A3.9 Transverse section crossing the Celtic Sea corresponding to the leg 137 (CORY798) showing the vertical structure of: (a) Temperature (°C), (b) Salinity, (c) density (σ_t in kg/m^3), and (d) geostrophic velocities in cm s^{-1} derived from the density field. In the latest, continuous lines represent water going into the page, contours with dashed lines water out the page. The location of the cross-section is observed in the top right corner of the page.

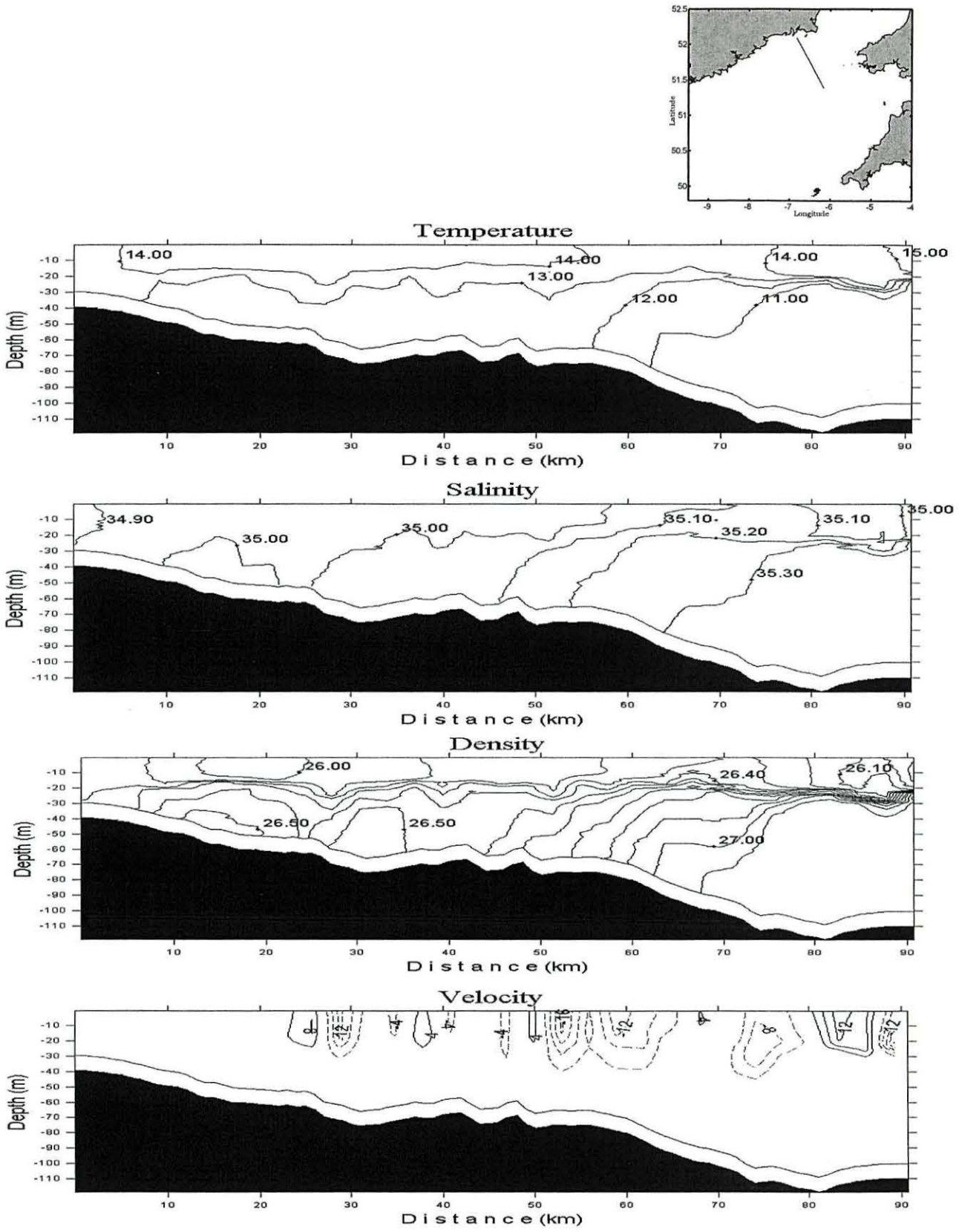

Figure A3.9 Transverse section crossing the Celtic Sea corresponding to the leg 137 (CORY798) showing the vertical structure of: (a) Temperature (°C), (b) Salinity, (c) density (σ_t in kg/m^3), and (d) geostrophic velocities in cm s^{-1} derived from the density field. In the latest, continuous lines represent water going into the page, contours with dashed lines water out the page. The location of the cross-section is observed in the top right corner of the page.

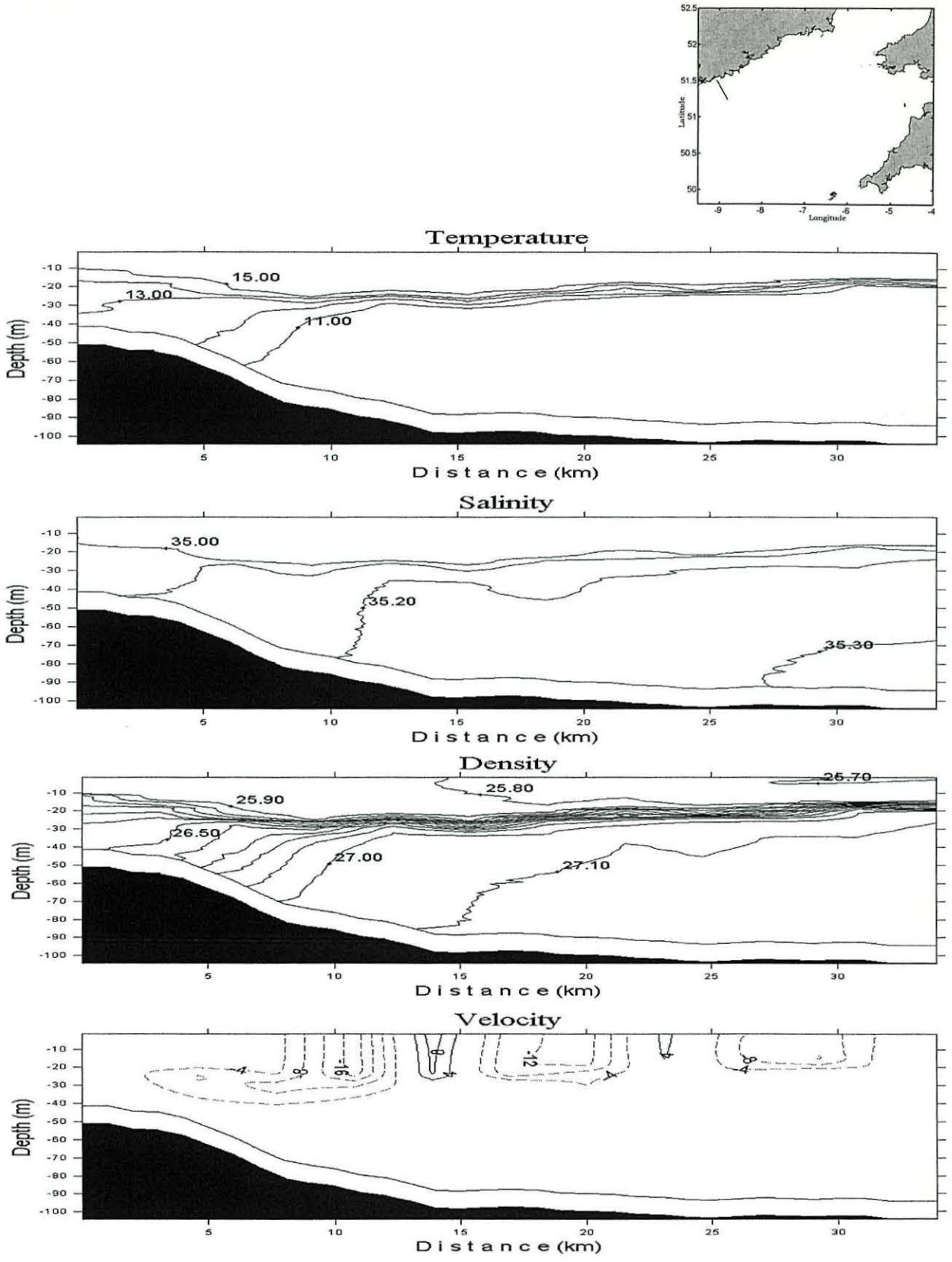

Figure A3.10 Transverse section crossing the Celtic Sea corresponding to the leg 179 (CORY998) showing the vertical structure of: (a) Temperature (°C), (b) Salinity, (c) density (σ_t in kg/m^3), and (d) geostrophic velocities in cm s^{-1} derived from the density field. In the latest, continuous lines represent water going into the page, contours with dashed lines water out the page. The location of the cross-section is observed in the top right corner of the page.

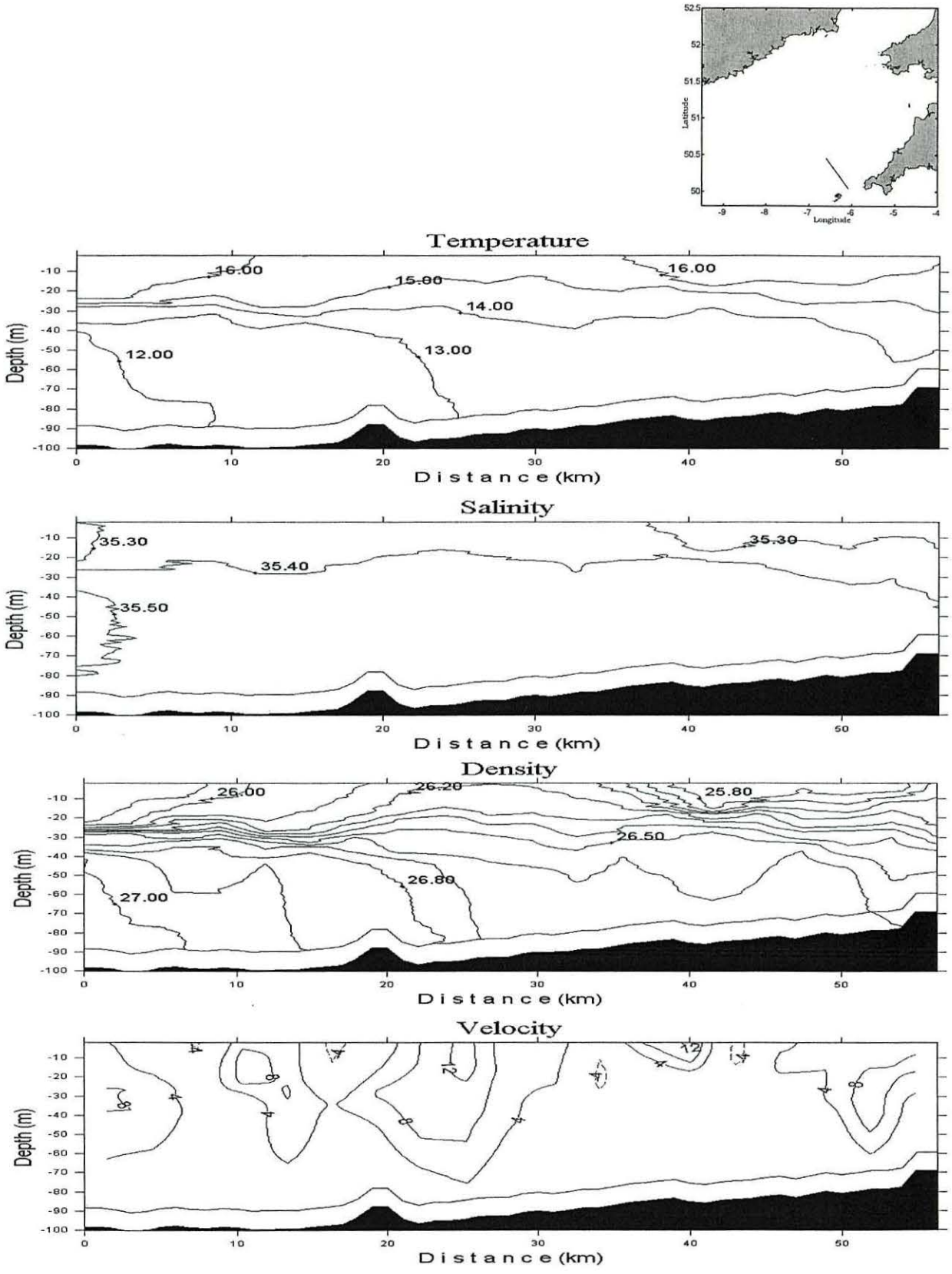

Figure A3.11 Transverse section crossing the Celtic Sea corresponding to the leg 181 (CORY998) showing the vertical structure of: (a) Temperature (°C), (b) Salinity, (c) density (σ_t in kg/m^3), and (d) geostrophic velocities in cm s^{-1} derived from the density field. In the latest, continuous lines represent water going into the page, contours with dashed lines water out the page. The location of the cross-section is observed in the top right corner of the page.

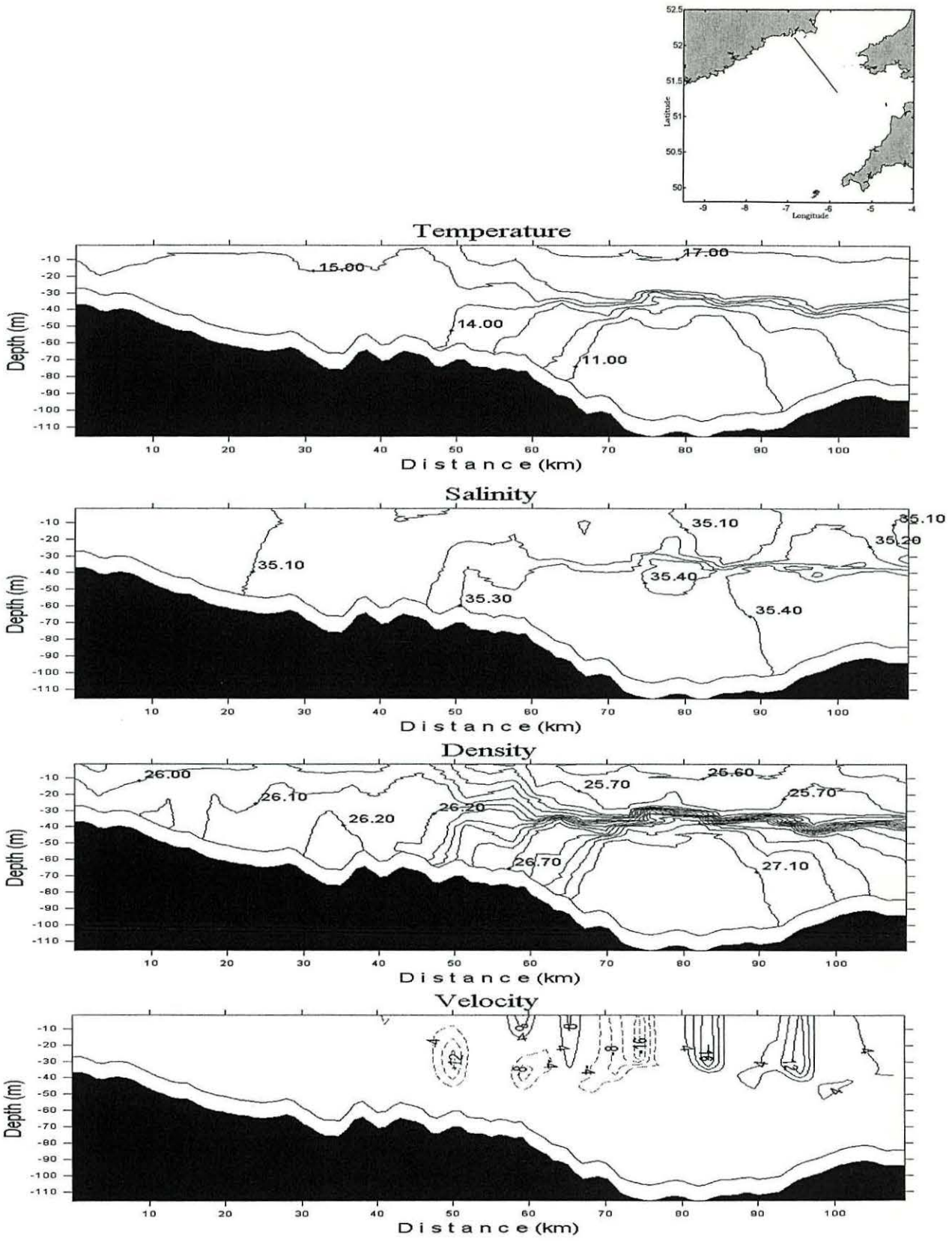

Figure A3.12 Transverse section crossing the Celtic Sea corresponding to the leg 186 (CORY998) showing the vertical structure of: (a) Temperature (°C), (b) Salinity, (c) density (σ_t in kg/m^3), and (d) geostrophic velocities in cm s^{-1} derived from the density field. In the latest, continuous lines represent water going into the page, contours with dashed lines water out the page. The location of the cross-section is observed in the top right corner of the page.

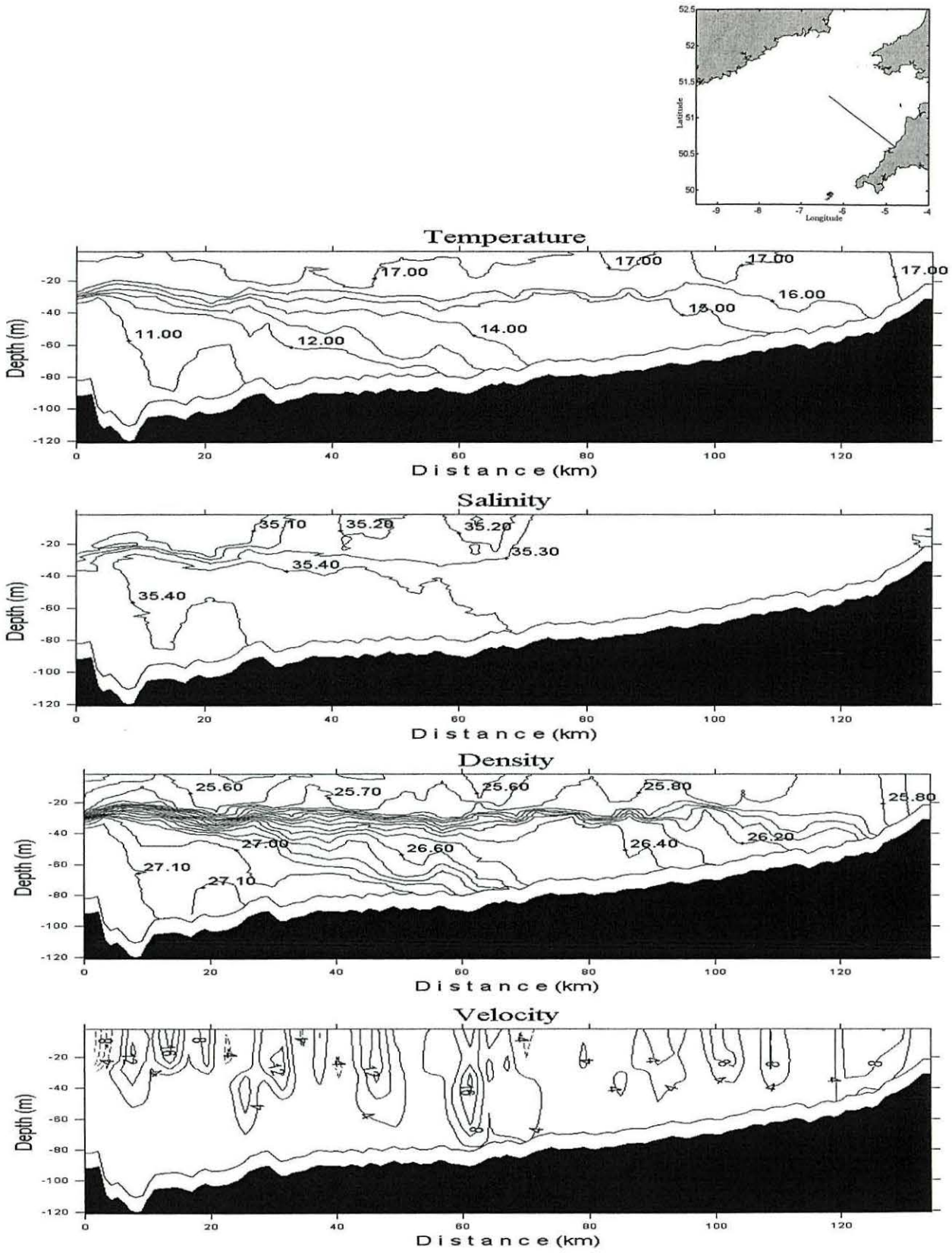

Figure A3.13 Transverse section crossing the Celtic Sea corresponding to the leg 201 (CORY998) showing the vertical structure of: (a) Temperature (°C), (b) Salinity, (c) density (σ_t in kg/m^3), and (d) geostrophic velocities in cm s^{-1} derived from the density field. In the latest, continuous lines represent water going into the page, contours with dashed lines water out the page. The location of the cross-section is observed in the top right corner of the page.

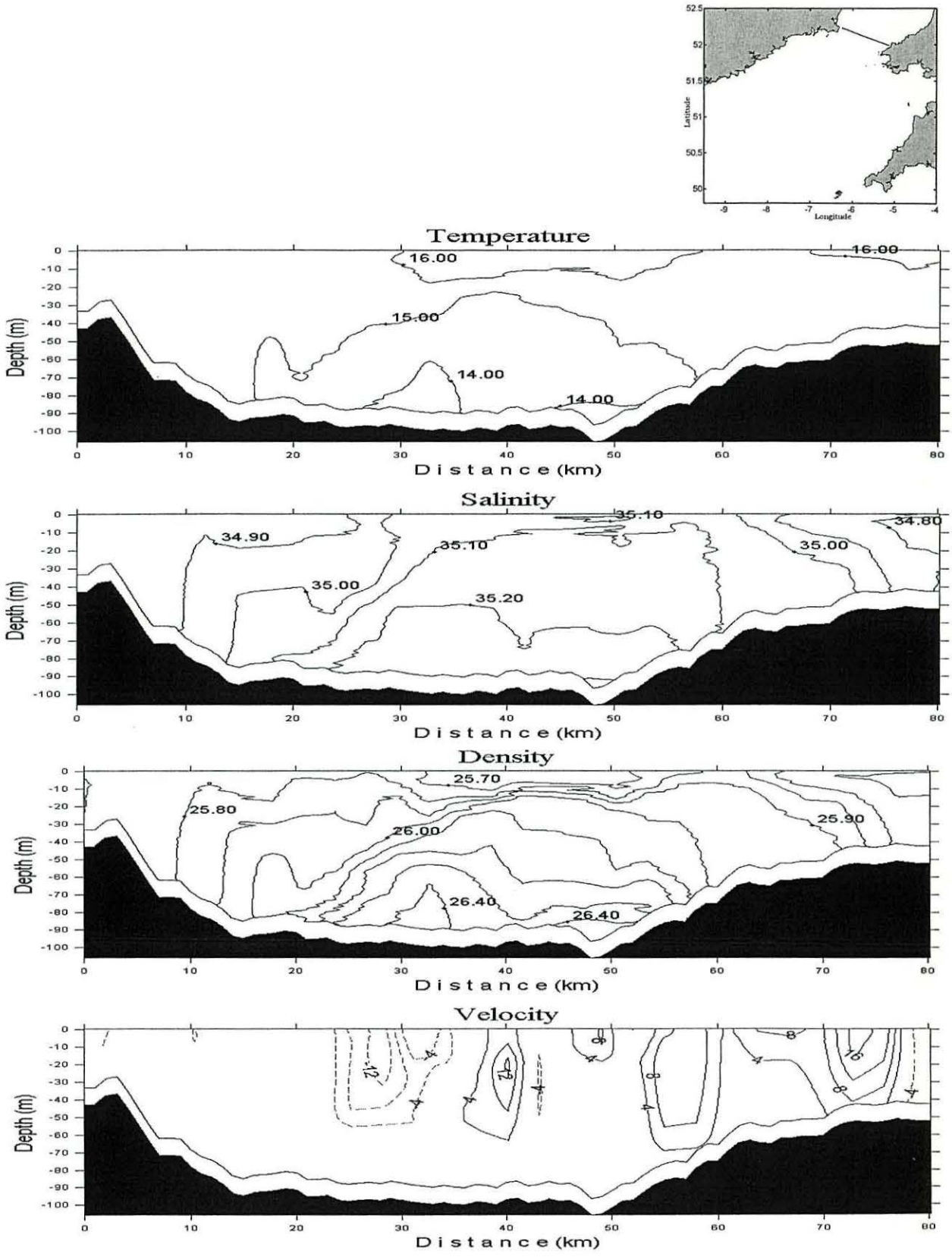

Figure A3.14 Transverse section crossing the Celtic Sea corresponding to the leg 211 (CORY998) showing the vertical structure of: (a) Temperature (°C), (b) Salinity, (c) density (σ_t in kg/m^3), and (d) geostrophic velocities in cm s^{-1} derived from the density field. In the latest, continuous lines represent water going into the page, contours with dashed lines water out the page. The location of the cross-section is observed in the top right corner of the page.

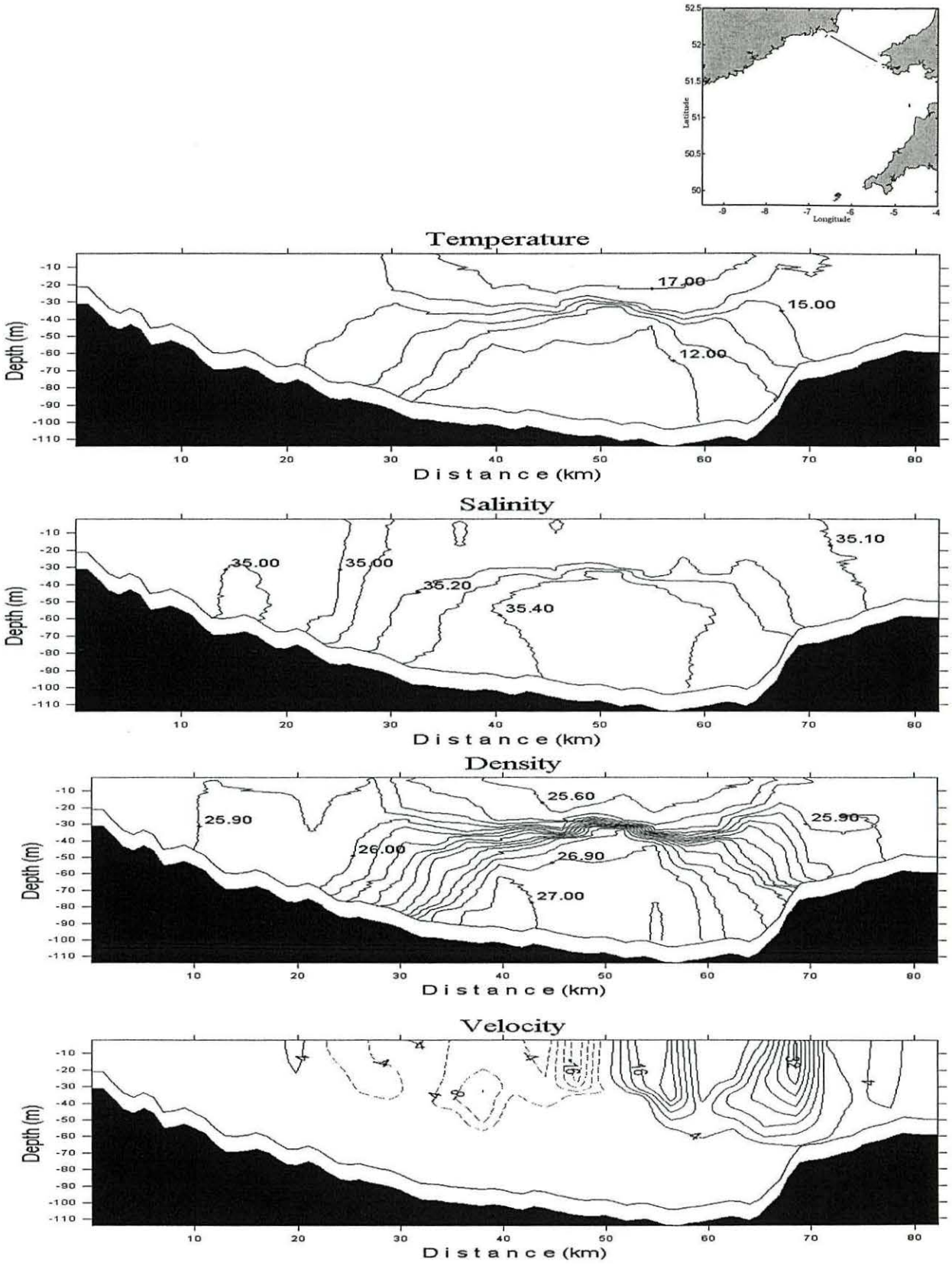

Figure A3.15 Transverse section crossing the Celtic Sea corresponding to the leg 212 (CORY998) showing the vertical structure of: (a) Temperature (°C), (b) Salinity, (c) density (σ_t in kg/m^3), and (d) geostrophic velocities in cm s^{-1} derived from the density field. In the latest, continuous lines represent water going into the page, contours with dashed lines water out the page. The location of the cross-section is observed in the top right corner of the page.

Appendix 4: ADCP-derived steady field from polynomial method

One advantage of the detiding technique of least squares and polynomial spatial interpolation is the capacity to extract additional information from the ADCP data, such as information about the steady current field, *i.e.* the velocity field time invariant over the length of the observations (Candela *et al.*, 1992). However, as pointed out by Candela *et al.* (1992), its interpretation must be addressed in combination with all available knowledge about the general circulation. Based on the results already observed from the density driven currents obtained from geostrophy (Chapter 4) and the Lagrangian flow field from drifters (Chapter 5), the steady field obtained might be defined as the *expected* velocity field from the horizontal density gradient.

The depth-averaged steady field obtained from the ADCP data as part of the polynomial detiding technique (estimation of the steady field (u_o, v_o) was obtained using a second degree polynomial, section 6.2.2) is presented in Figure A4.1. The flow pattern in both cruises was similar. Basically, the results show a cyclonic circulation with strong velocities in the western St. George's Channel, Bristol Channel and southwest of the Irish coast and weak velocities at the centre of the Celtic Sea. This flow pattern is in agreement with the circulation obtained from geostrophy and drifters confirming the expectations of a cyclonic density driven circulation (Fig A4.1). However, the magnitudes of the mean field velocities were slightly lower and smoother than that obtained from geostrophy and derived from drifters, probably due to the interpolation scheme in the obtained steady field.

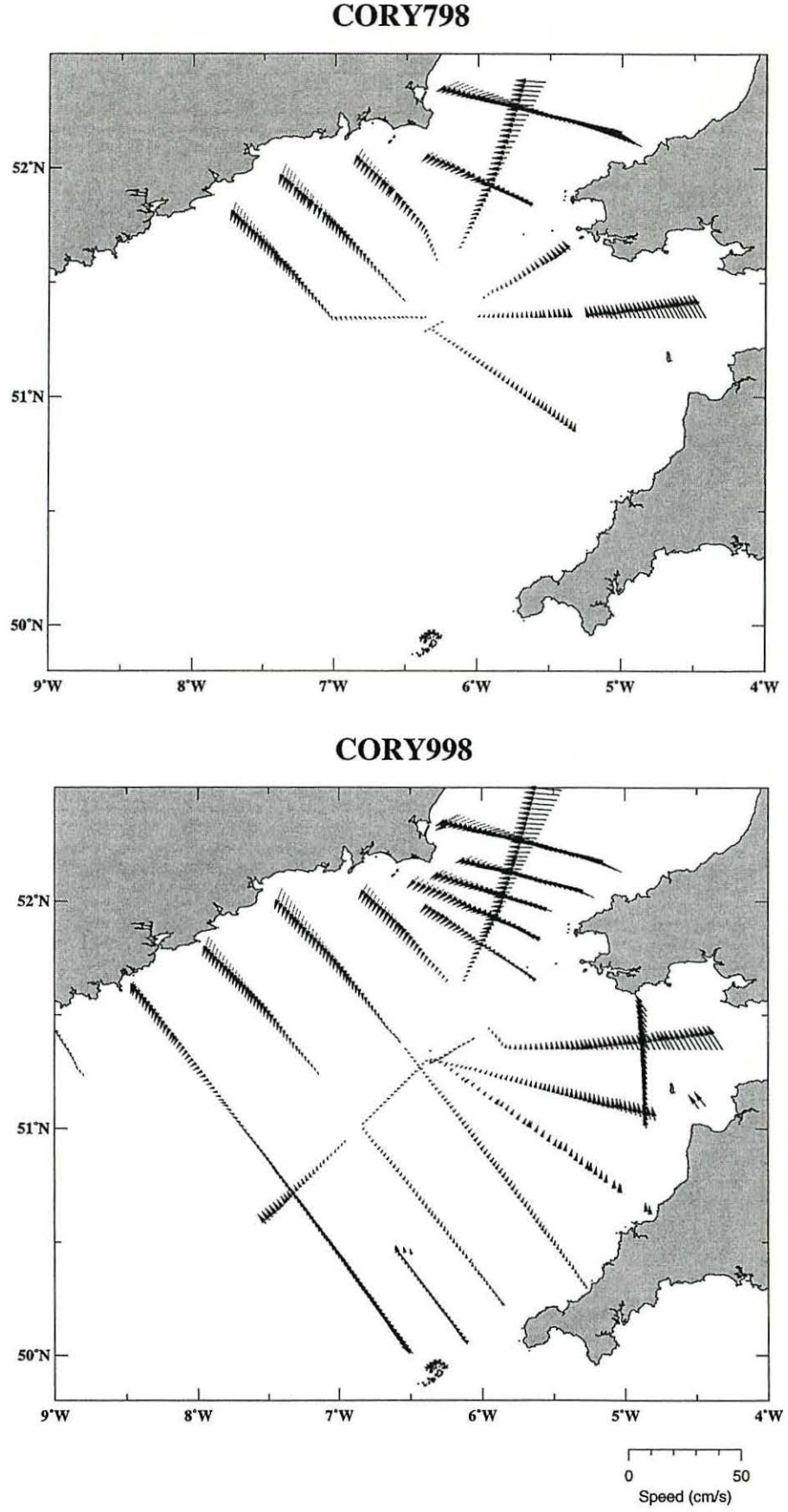

Figure A4.1 Steady field obtained from polynomial and least squares method applied to depth averaged velocities for CORY798 (top panel) and CORY998 (bottom panel). Scale is displayed at the bottom right of the bottom panel.

Appendix 5: Residual velocities from polynomial and least squares method and numerical model

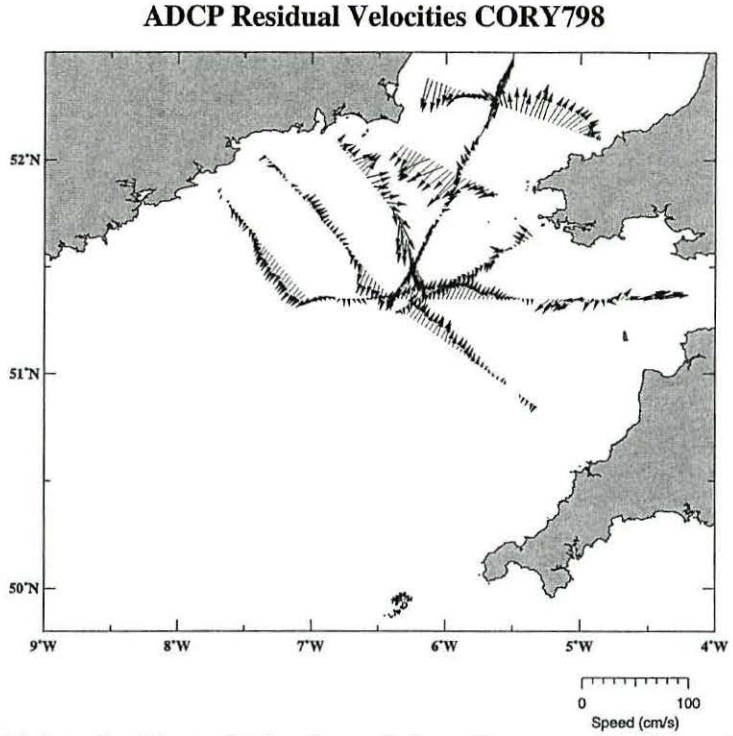

Figure A5.1 Subtidal velocities obtained applying the numerical model to depth averaged velocities for CORY798. Scale is displayed at the bottom right of the

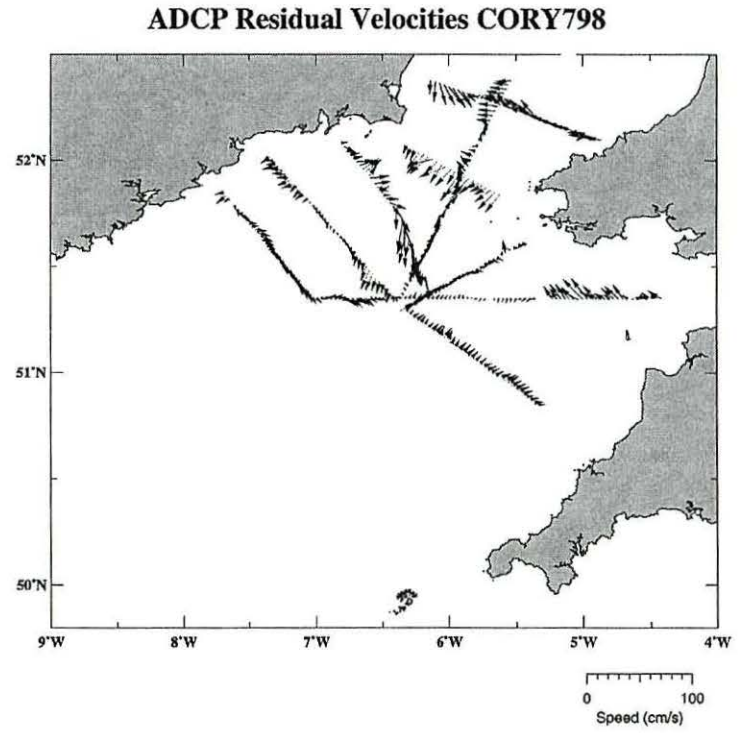

Figure A5.2 Subtidal velocities obtained applying the polynomial method to depth averaged velocities for CORY798. Scale is displayed at the bottom right of the panels.

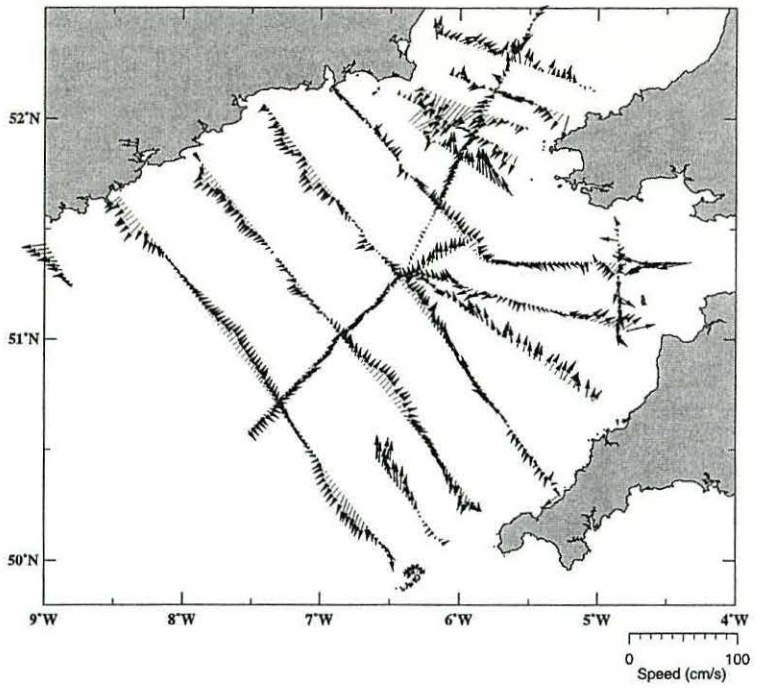

Figure A5.3 Subtidal velocities obtained applying the numerical model to depth averaged velocities for CORY998. Scale is displayed at the bottom right of the

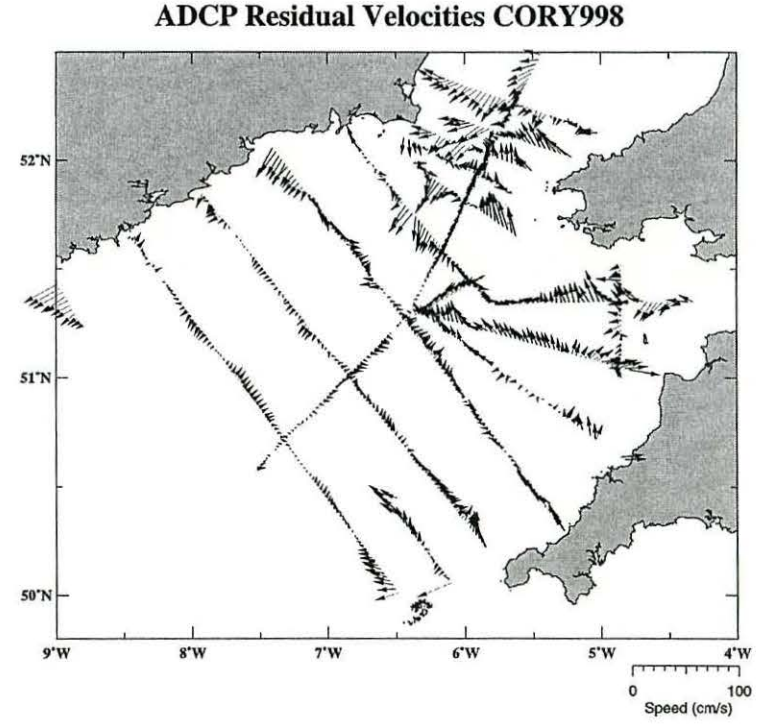

Figure A5.4 Subtidal velocities obtained applying the polynomial method to depth averaged velocities for CORY998. Scale is displayed at the bottom right of the panels.

Appendix 6: Tidal current profile derived from boundary layer theory

The vertical structure of the tidal currents in shallow seas is influenced by seabed friction which reduces the tidal current amplitude near the boundary layer. Thus a retardation of the flow towards the bottom of the profile is produced, i.e. a phase difference exits between the surface tidal current and the near bottom tidal current (Open University, 1989). Theoretical efforts to obtain the vertical structure of tidal currents in homogeneous water column have been realized by Prandle (1982). He proposed that in absence of stratification the vertical structure of tidal currents can be represented as

$$U(z)=\left\{\frac{e^{\frac{z}{\delta}}+e^{-\left(\frac{z}{\delta}-2y\right)}}{T}+Q\right\}\overline{U}$$

where

$$T=(1-e^{2y})\left\{j-\frac{1}{y}-1\right\}-2e^{2y}$$

$$Q=\frac{j\left(1-e^{2y}\right)-1-e^{2y}}{T}$$

$$j=\frac{3\pi N_z}{8\delta k|\overline{U}|}$$

$$y=\frac{D}{\delta}$$

and $\delta=\left(\frac{N_z}{i\omega}\right)^{\frac{1}{2}}$

$|\overline{U}|$ is the depth average velocity amplitude, N_Z is the eddy viscosity, ω is the tidal frequency, f is the Coriolis parameter, k is the bottom drag coefficient. Thus the velocity profile is a function of the variables j and y. The modulus of y can be interpreted as a depth parameter converted to dimensionless form by Ekman scaling (Prandle, 1982). The modulus of j reflects the effect of the bottom stress through the bed stress coefficient k and the velocity $\overline{U}$.

Appendix 7: Residual velocities from blending technique : Cross-sections

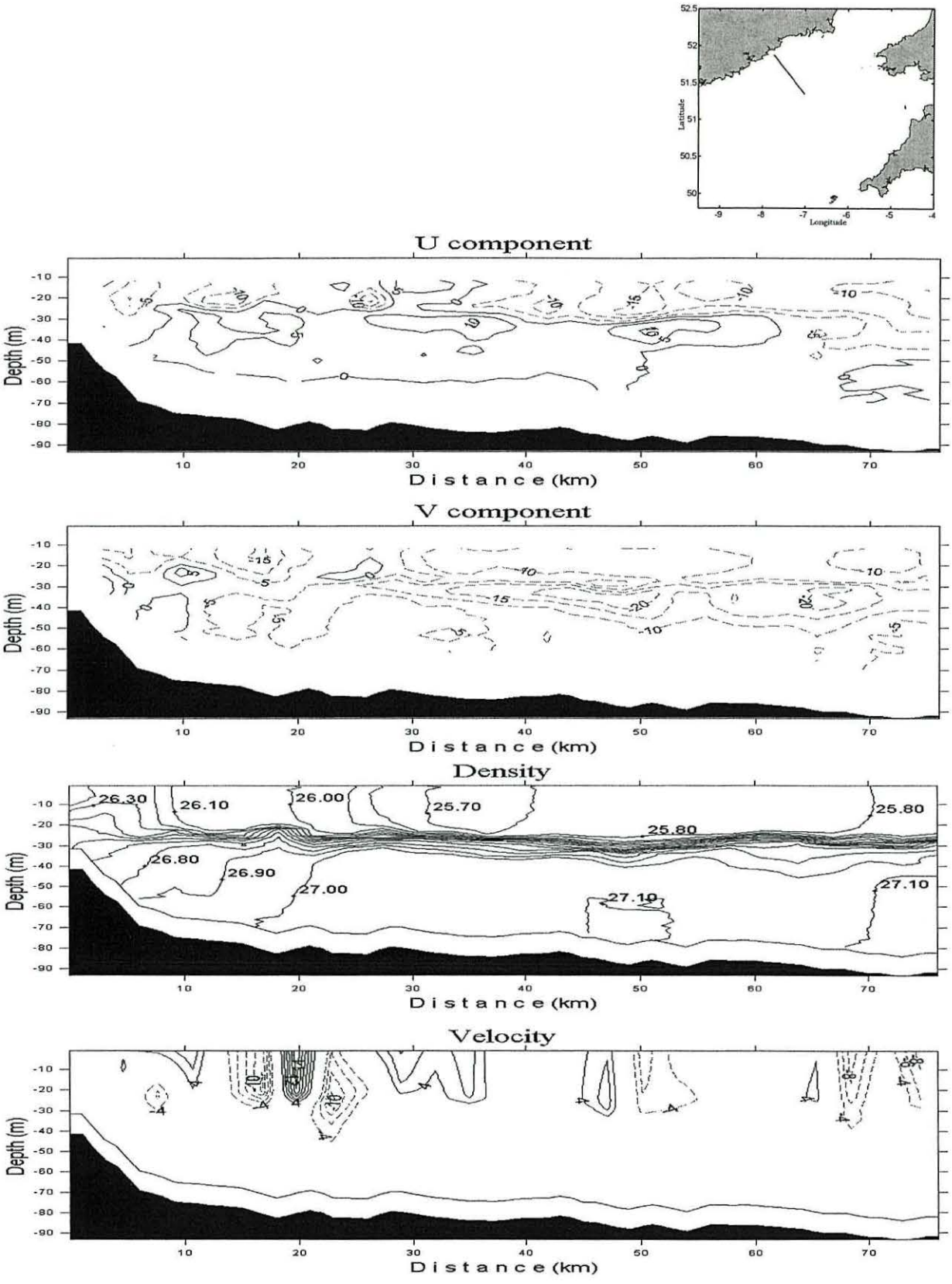

Figure A7.1 ADCP residuals for Leg 107 (top-right corner panel shows location). a) U-component (west-east), b) V-component (north-south), c) density (σ_t) in kg m^{-3} and d) geostrophic velocities. Velocities in cm s^{-1}.

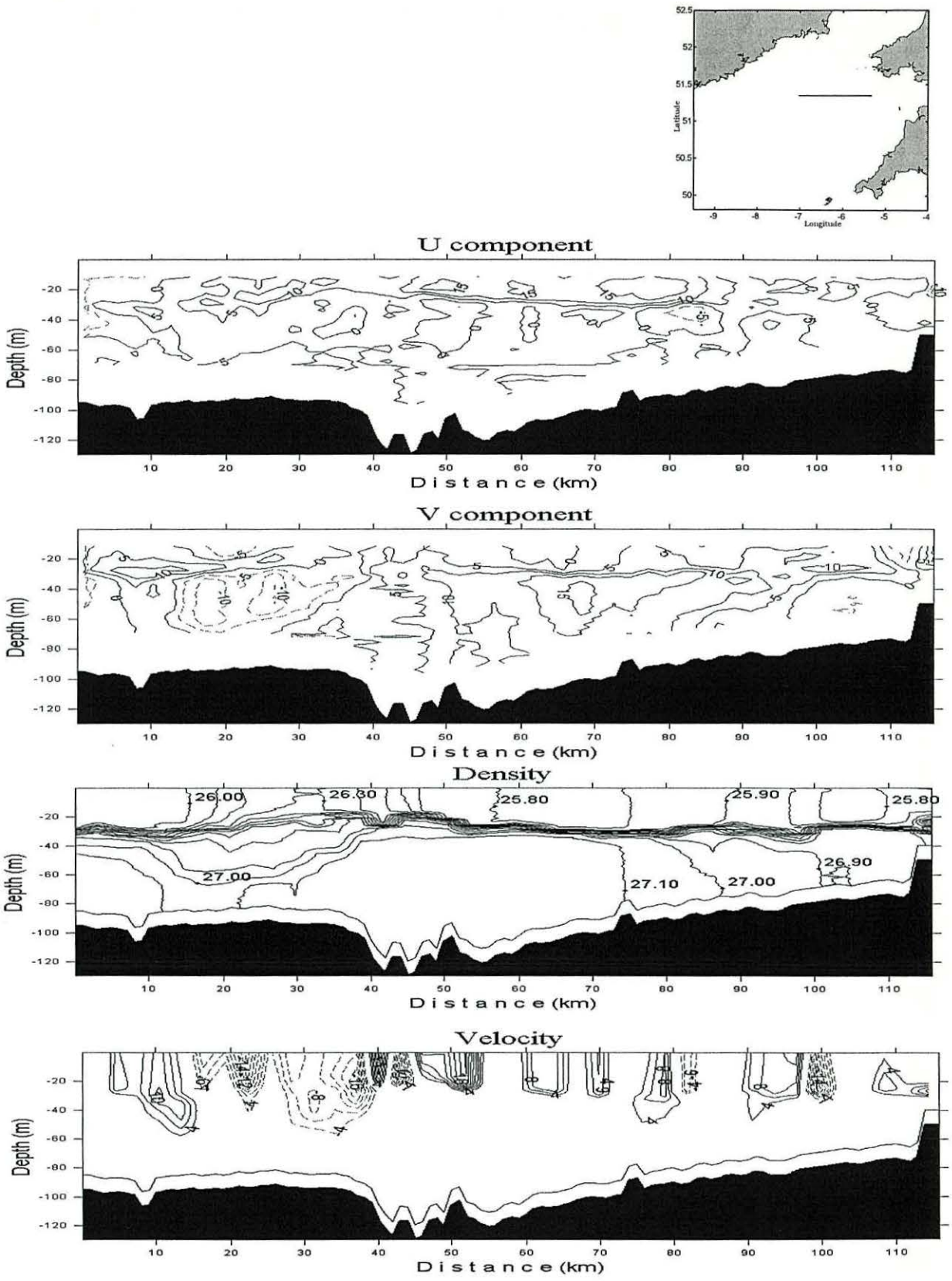

Figure A7.2 ADCP residuals for Leg 108 (top-right corner panel shows location). a) U-component (west-east), b) V-component (north-south), c) density (σ_t) in kg m^{-3} and d) geostrophic velocities. Velocities in cm s^{-1}.

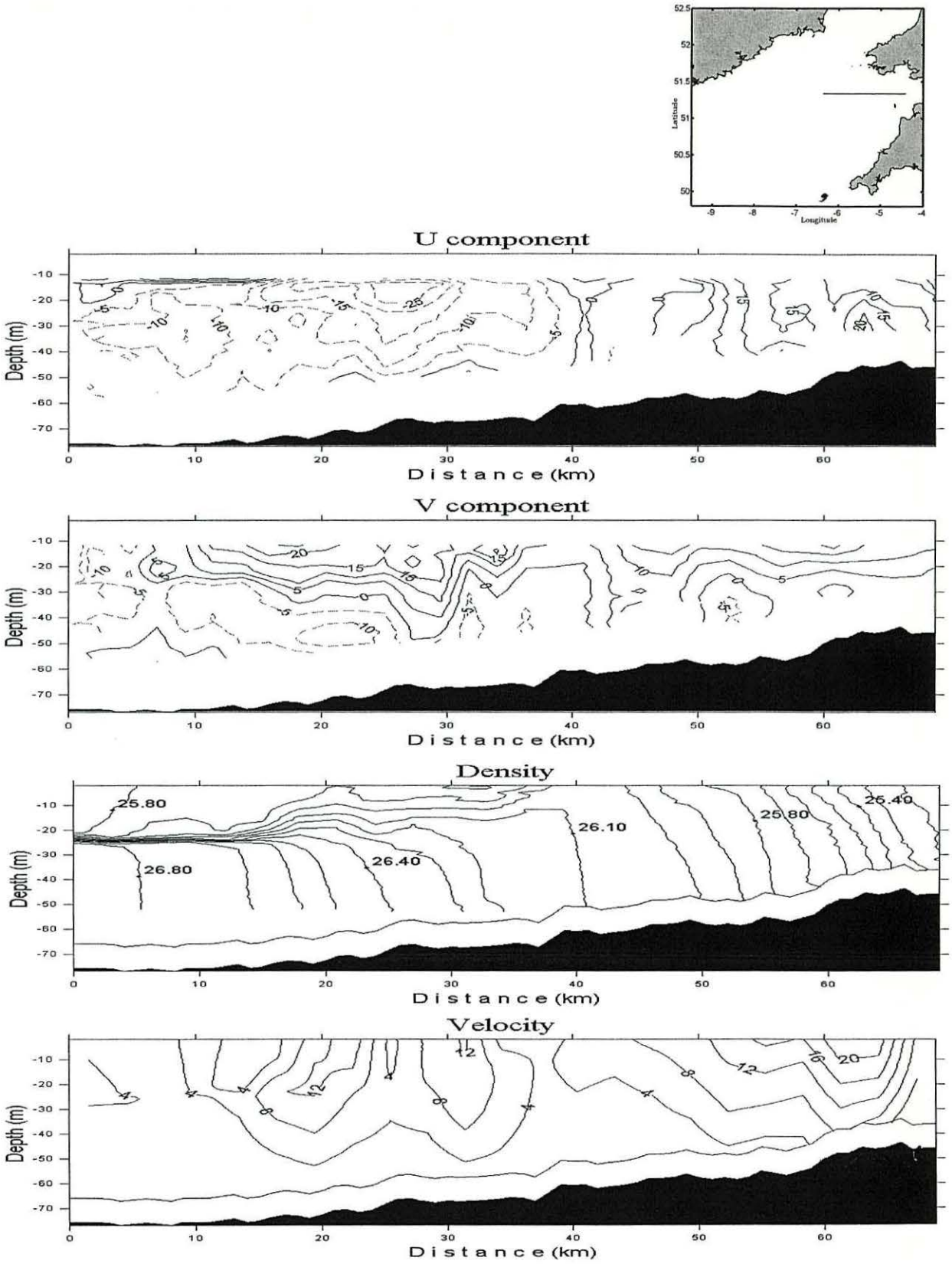

Figure A7.3 ADCP residuals for Leg 113 (top-right corner panel shows location). a) U-component (west-east), b) V-component (north-south), c) density (σ_t) in kg m^{-3} and d) geostrophic velocities. Velocities in cm s^{-1}.

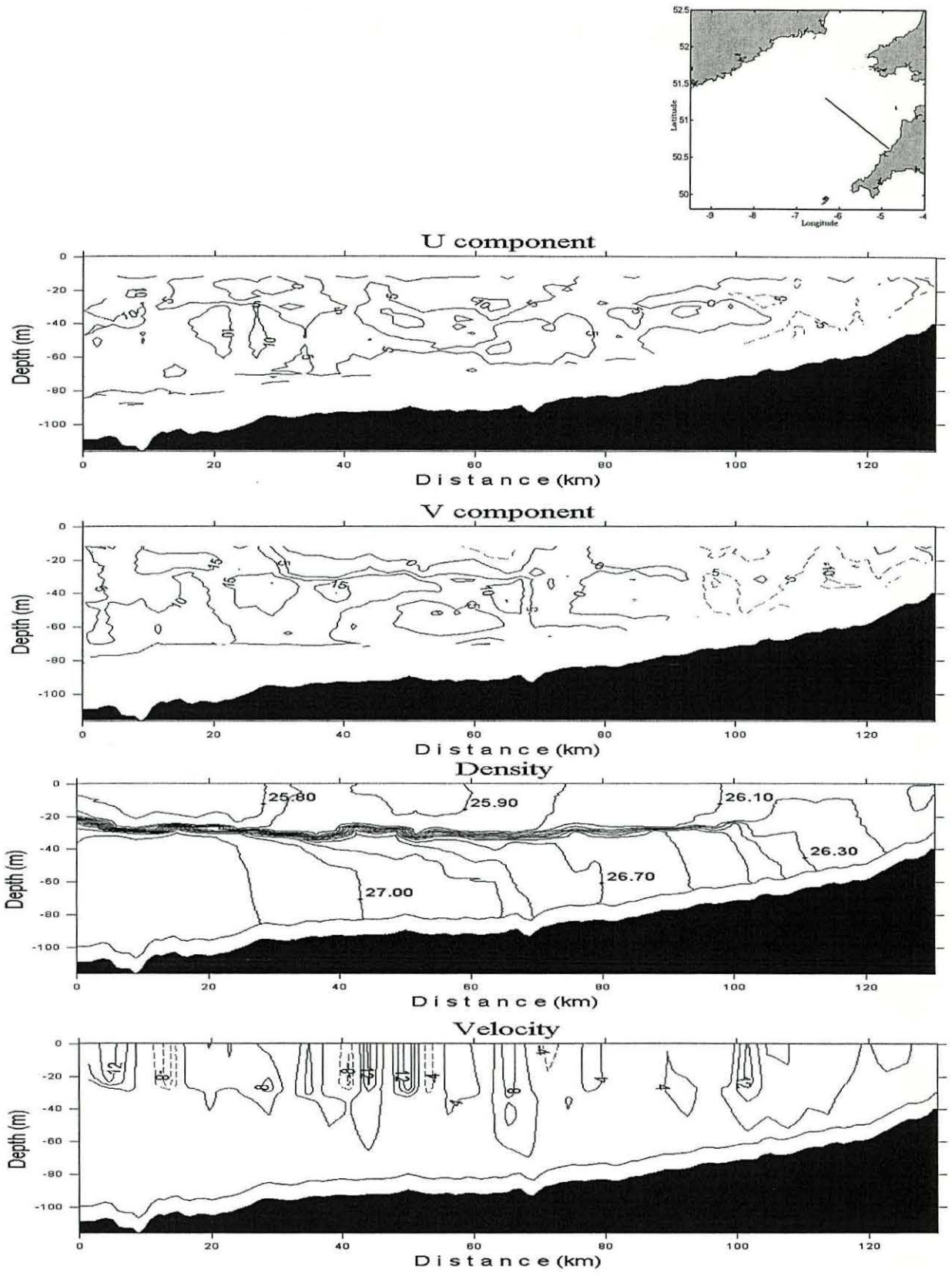

Figure A7.4 ADCP residuals for Leg 118 (top-right corner panel shows location). a) U-component (west-east), b) V-component (north-south), c) density (σ_t) in kg m^{-3} and d) geostrophic velocities. Velocities in cm s^{-1}.

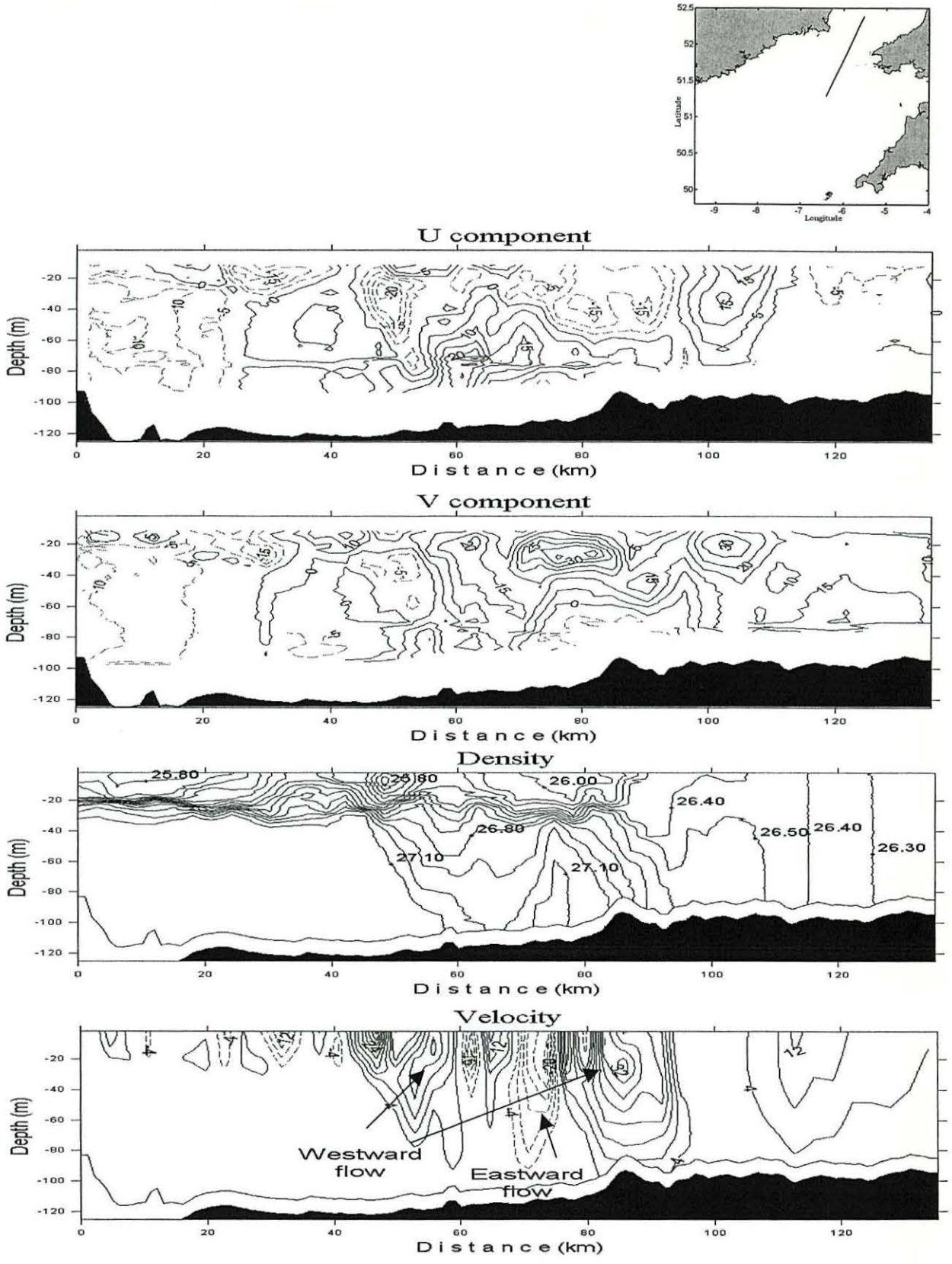

Figure A7.5 ADCP residuals for Leg 201 (top-right corner panel shows location). a) U-component (west-east), b) V-component (north-south), c) density (σ_t) in kg m^{-3} and d) geostrophic velocities. Velocities in cm s^{-1}.

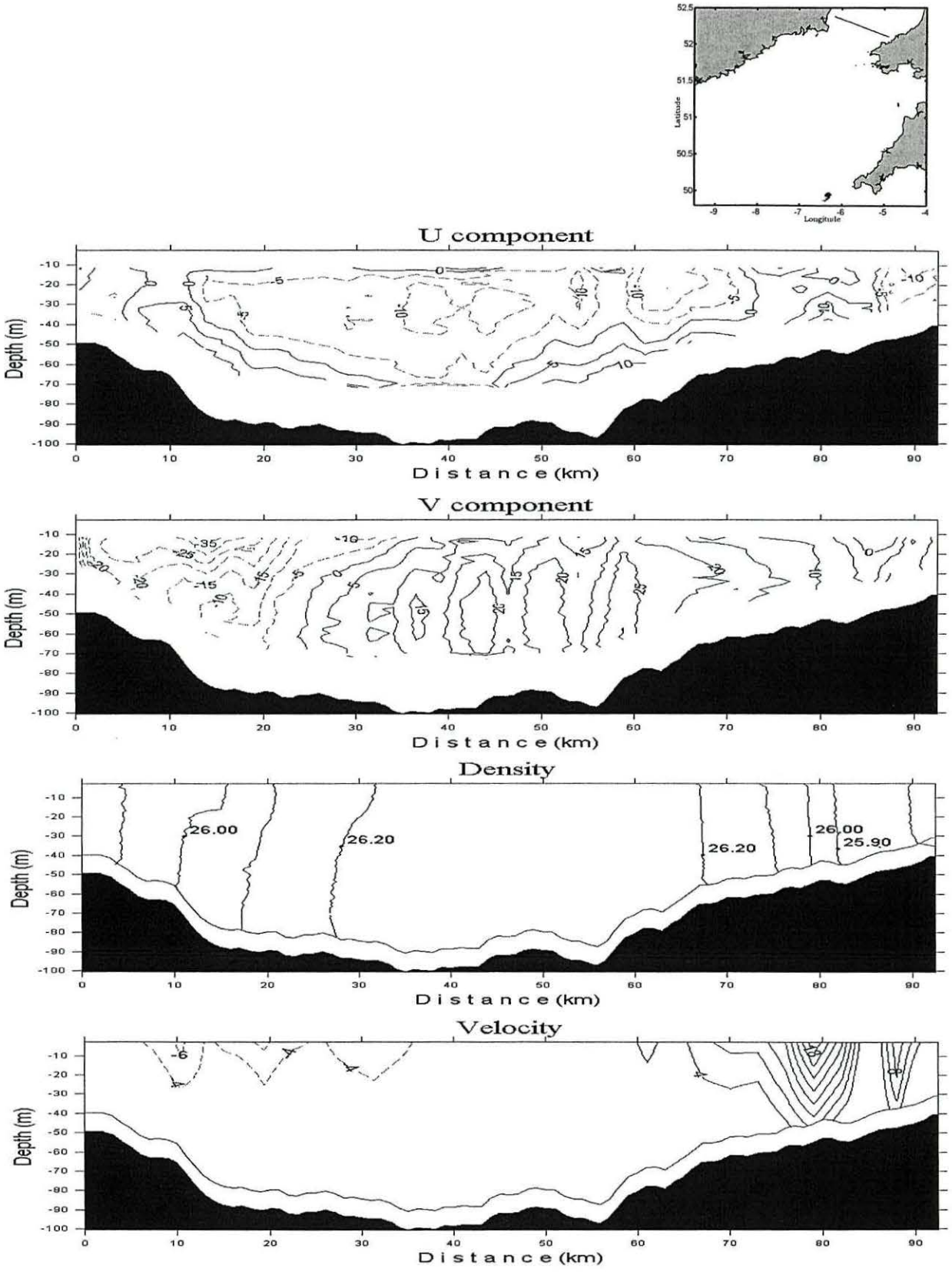

Figure A7.6 ADCP residuals for Leg 124 (top-right corner panel shows location). a) U-component (west-east), b) V-component (north-south), c) density (σ_t) in kg m^{-3} and d) geostrophic velocities. Velocities in cm s^{-1}.

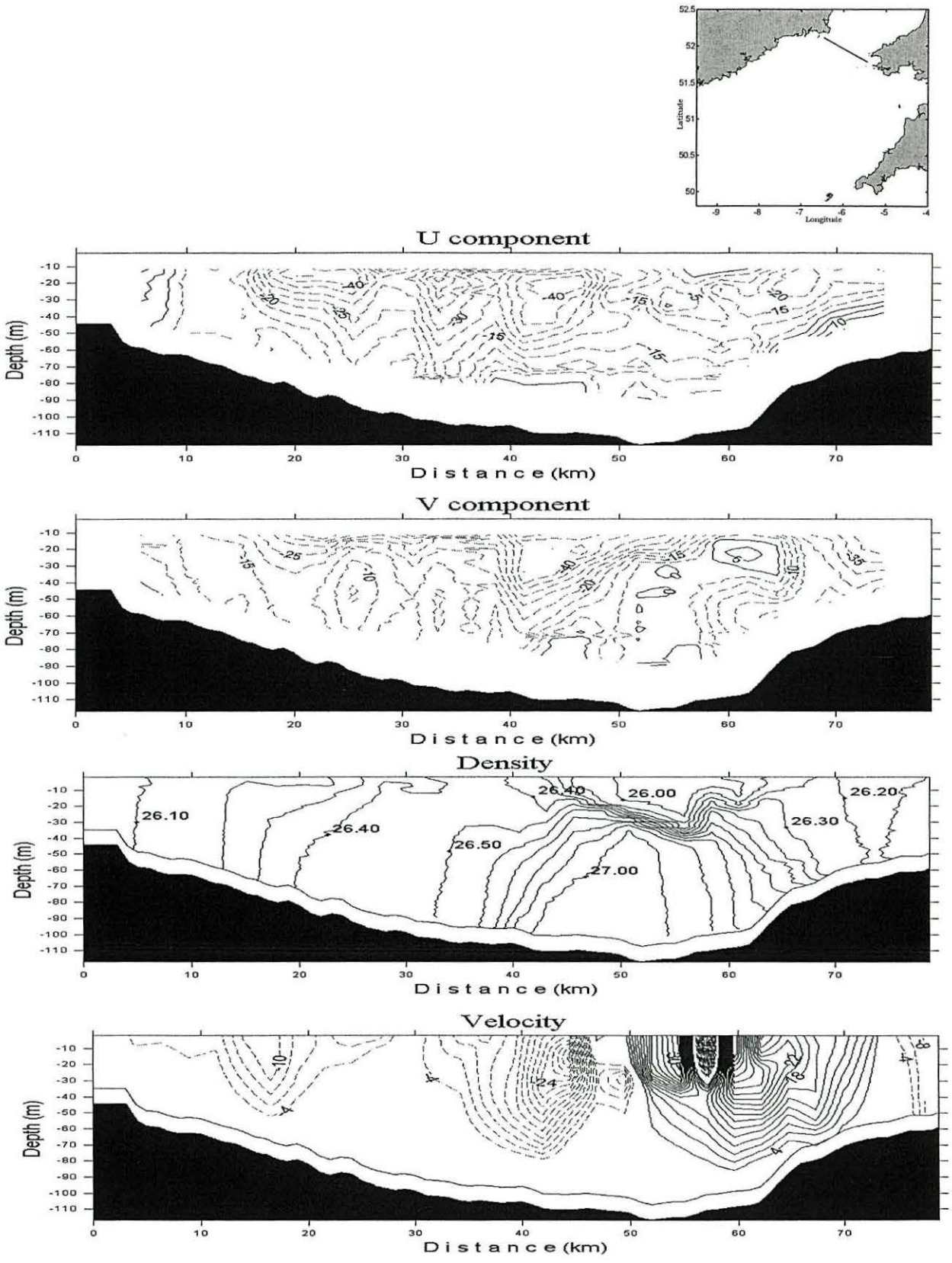

Figure A7.7 ADCP residuals for Leg 129 (top-right corner panel shows location). a) U-component (west-east), b) V-component (north-south), c) density (σ_t) in kg m^{-3} and d) geostrophic velocities. Velocities in cm s^{-1}.

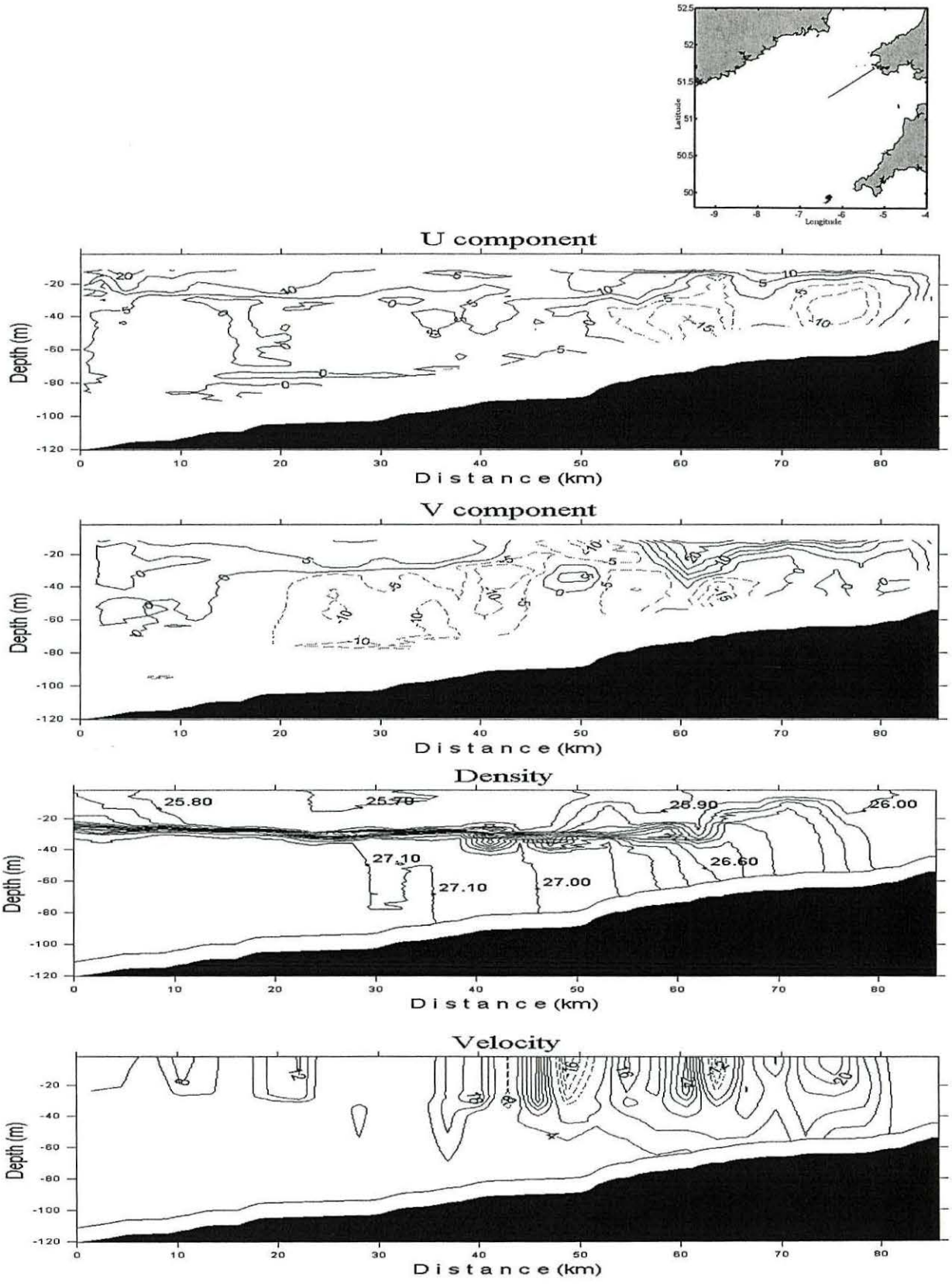

Figure A7.8 ADCP residuals for Leg 131 (top-right corner panel shows location). a) U-component (west-east), b) V-component (north-south), c) density (σ_t) in kg m^{-3} and d) geostrophic velocities. Velocities in cm s^{-1}.

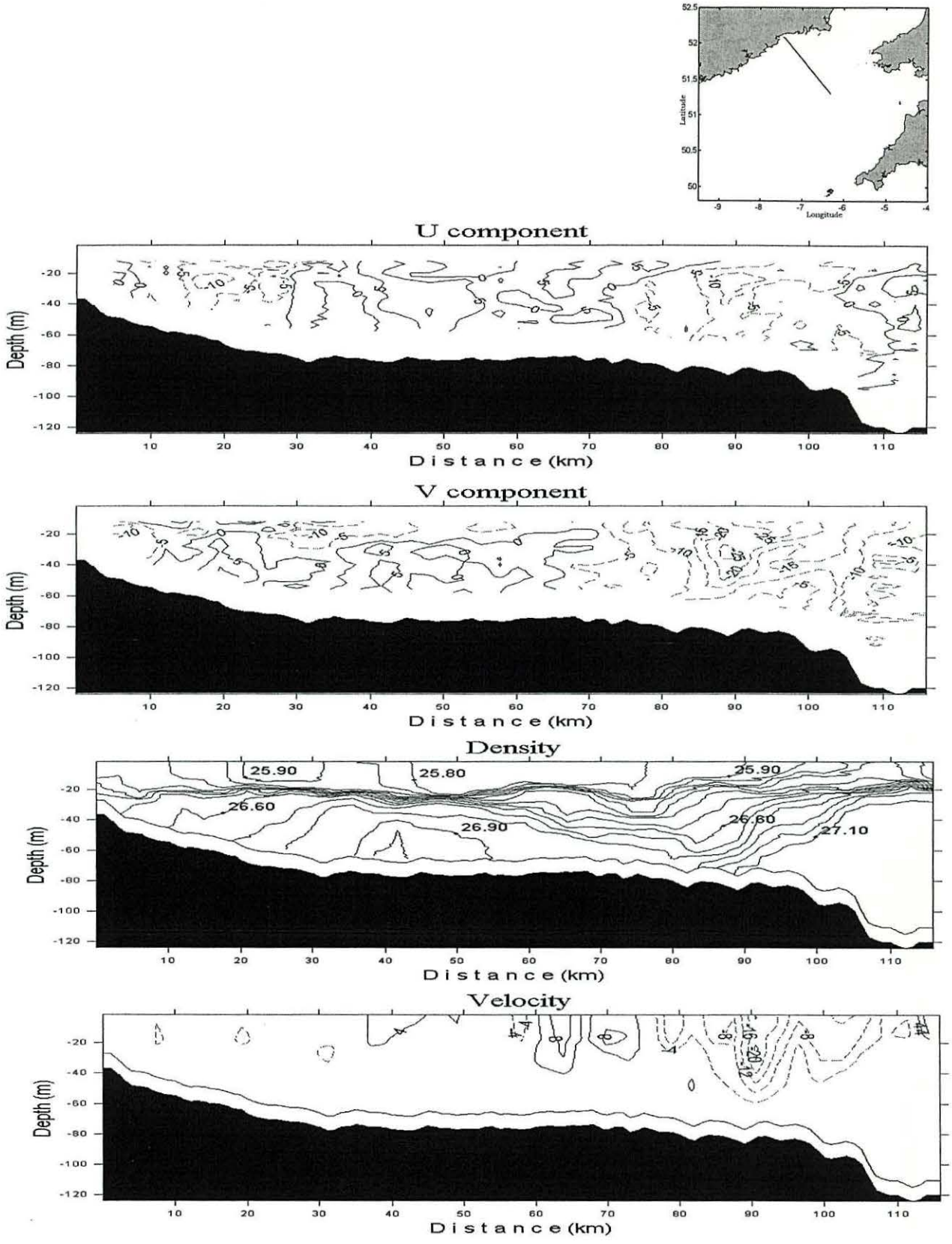

Figure A7.9 ADCP residuals for Leg 136 (top-right corner panel shows location). a) U-component (west-east), b) V-component (north-south), c) density (σ_t) in kg m^{-3} and d) geostrophic velocities. Velocities in cm s^{-1}.

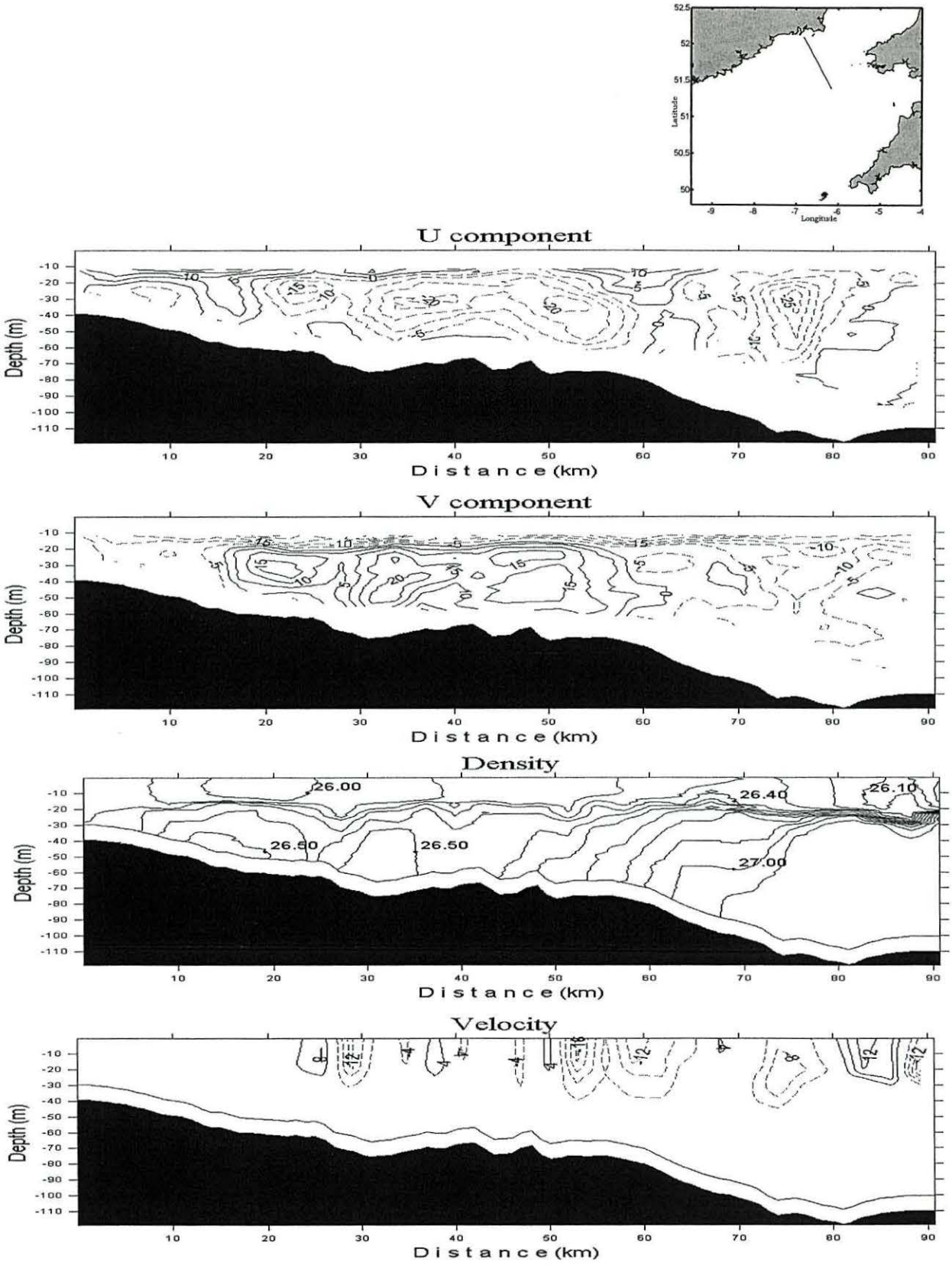

Figure A7.10 ADCP residuals for Leg 137 (top-right corner panel shows location). a) U-component (west-east), b) V-component (north-south), c) density (σ_t) in kg m^{-3} and d) geostrophic velocities. Velocities in cm s^{-1}.

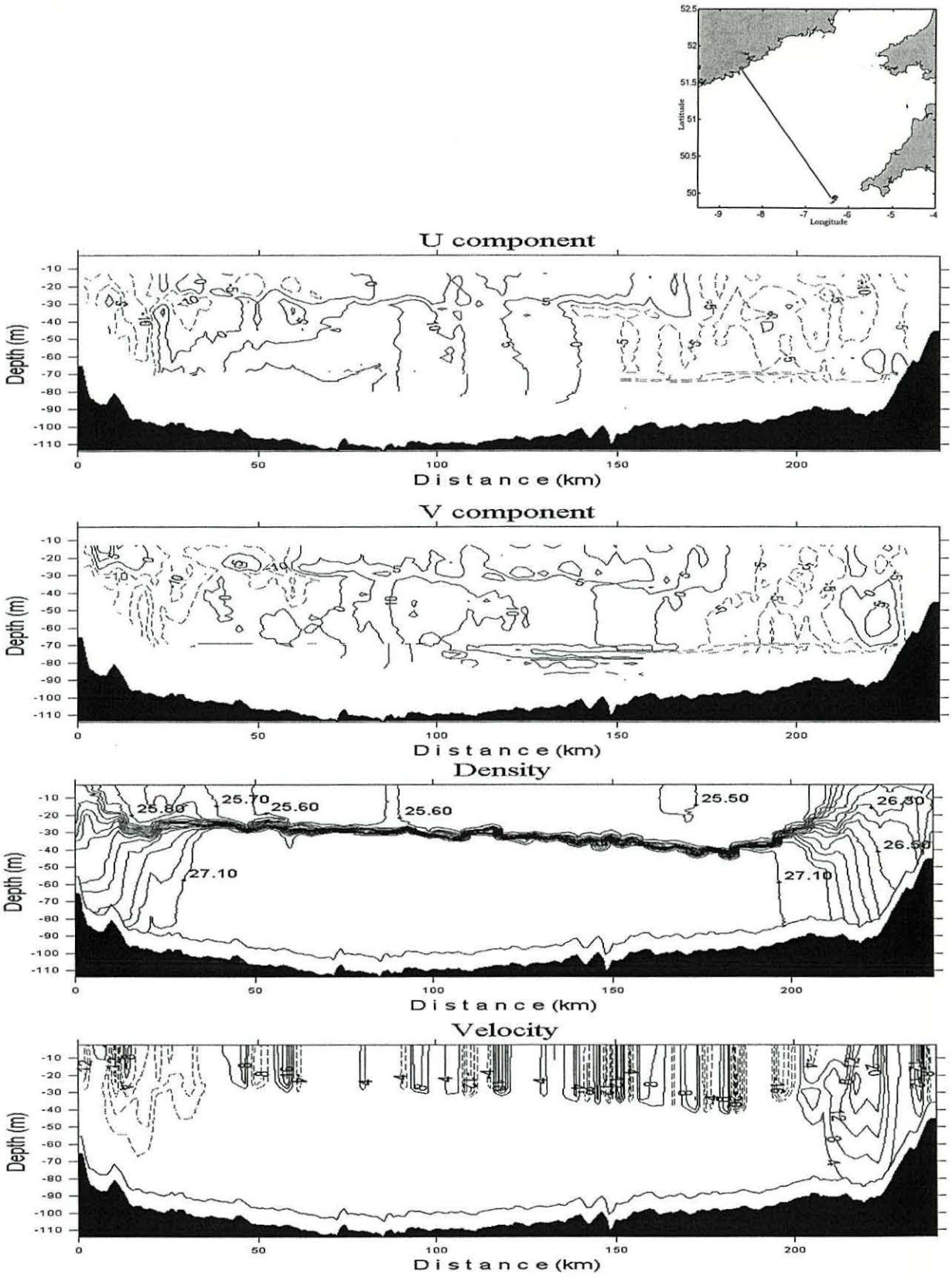

Figure A7.11 ADCP residuals for Leg 178 (top-right corner panel shows location). a) U-component (west-east), b) V-component (north-south), c) density (σ_t) in kg m^{-3} and d) geostrophic velocities. Velocities in cm s^{-1}.

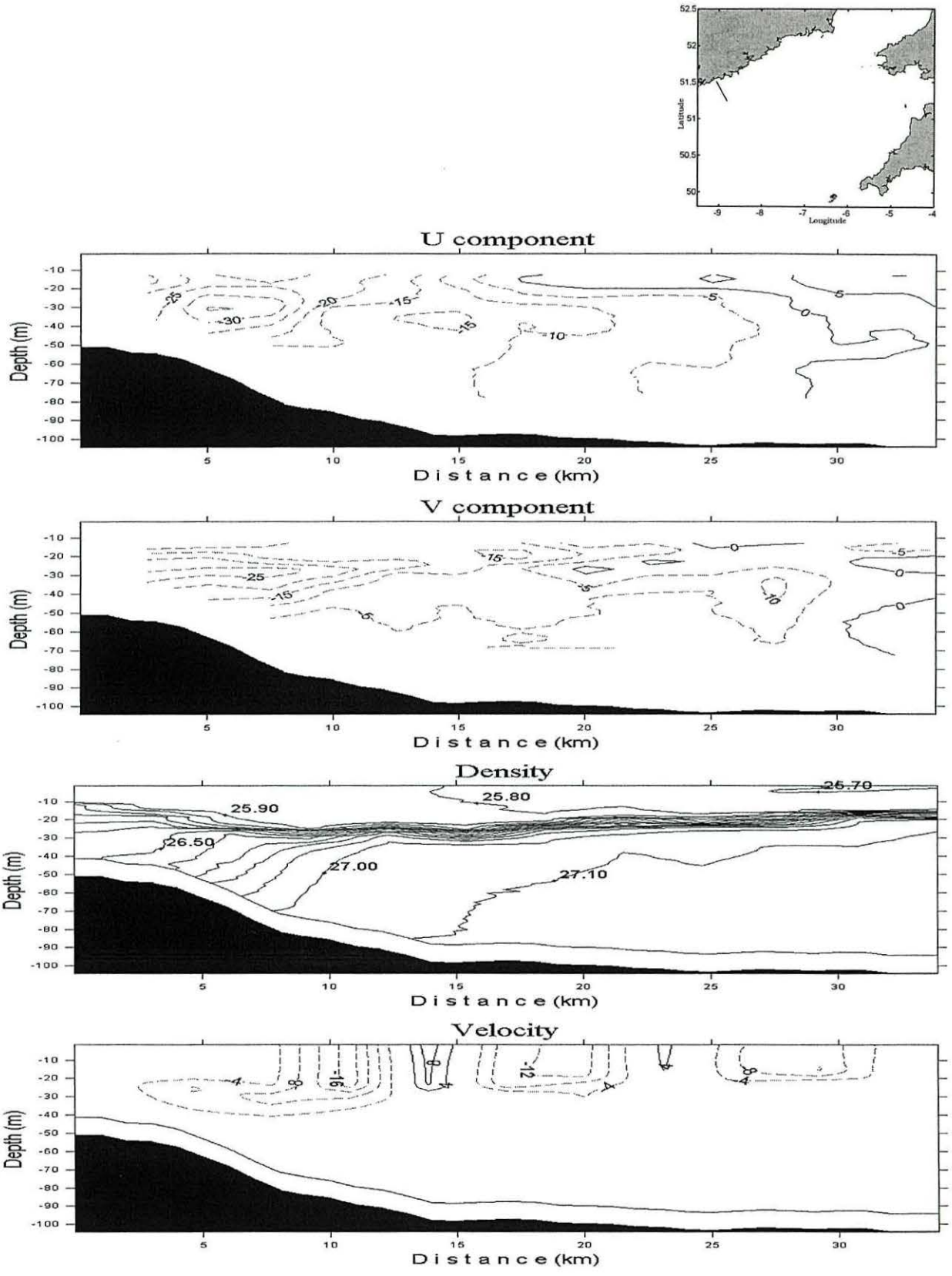

Figure A7.12 ADCP residuals for Leg 179 (top-right corner panel shows location). a) U-component (west-east), b) V-component (north-south), c) density (σ_t) in kg m^{-3} and d) geostrophic velocities. Velocities in cm s^{-1}.

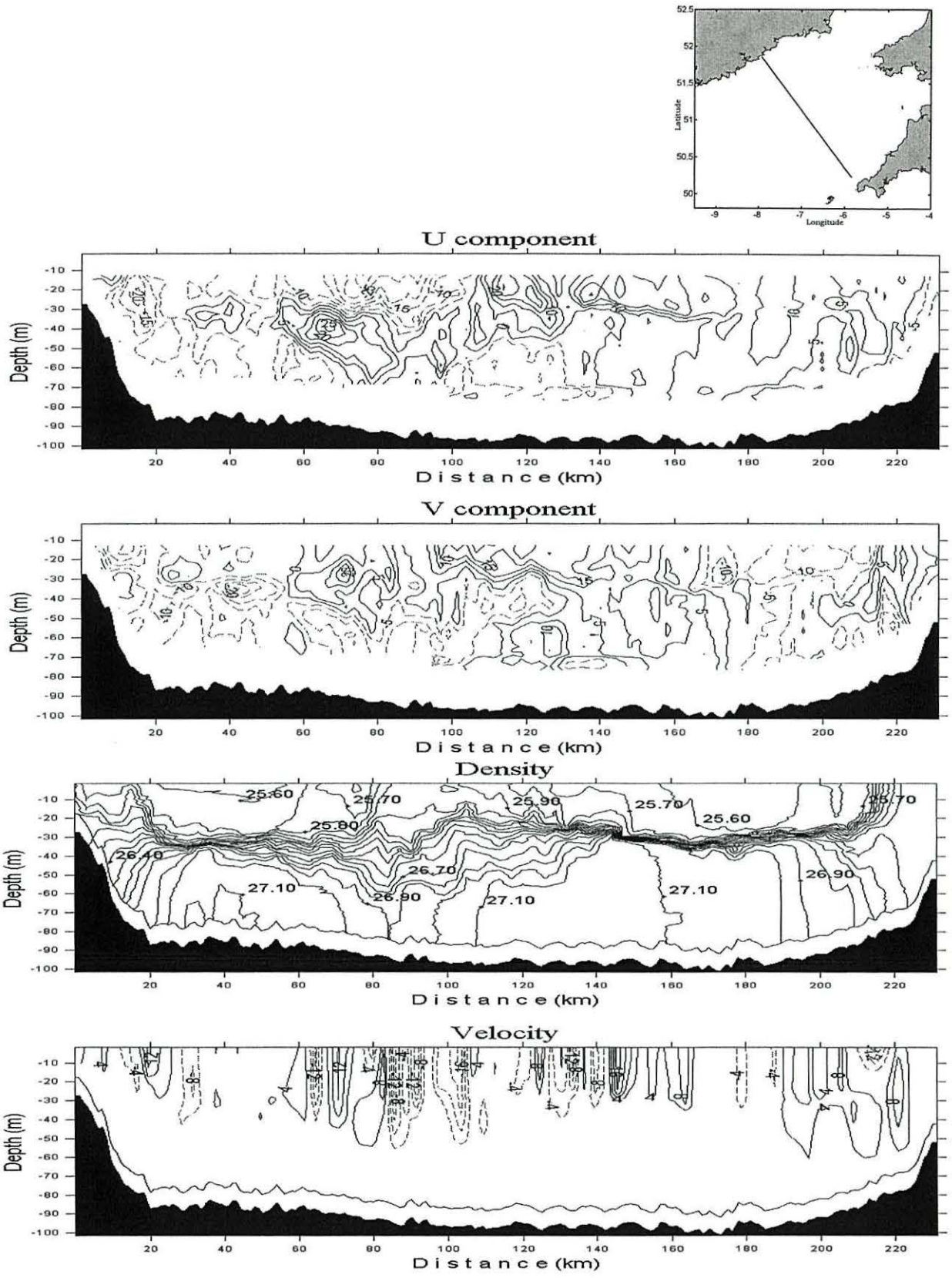

Figure A7.13 ADCP residuals for Leg 180 (top-right corner panel shows location). a) U-component (west-east), b) V-component (north-south), c) density (σ_t) in kg m^{-3} and d) geostrophic velocities. Velocities in cm s^{-1}.

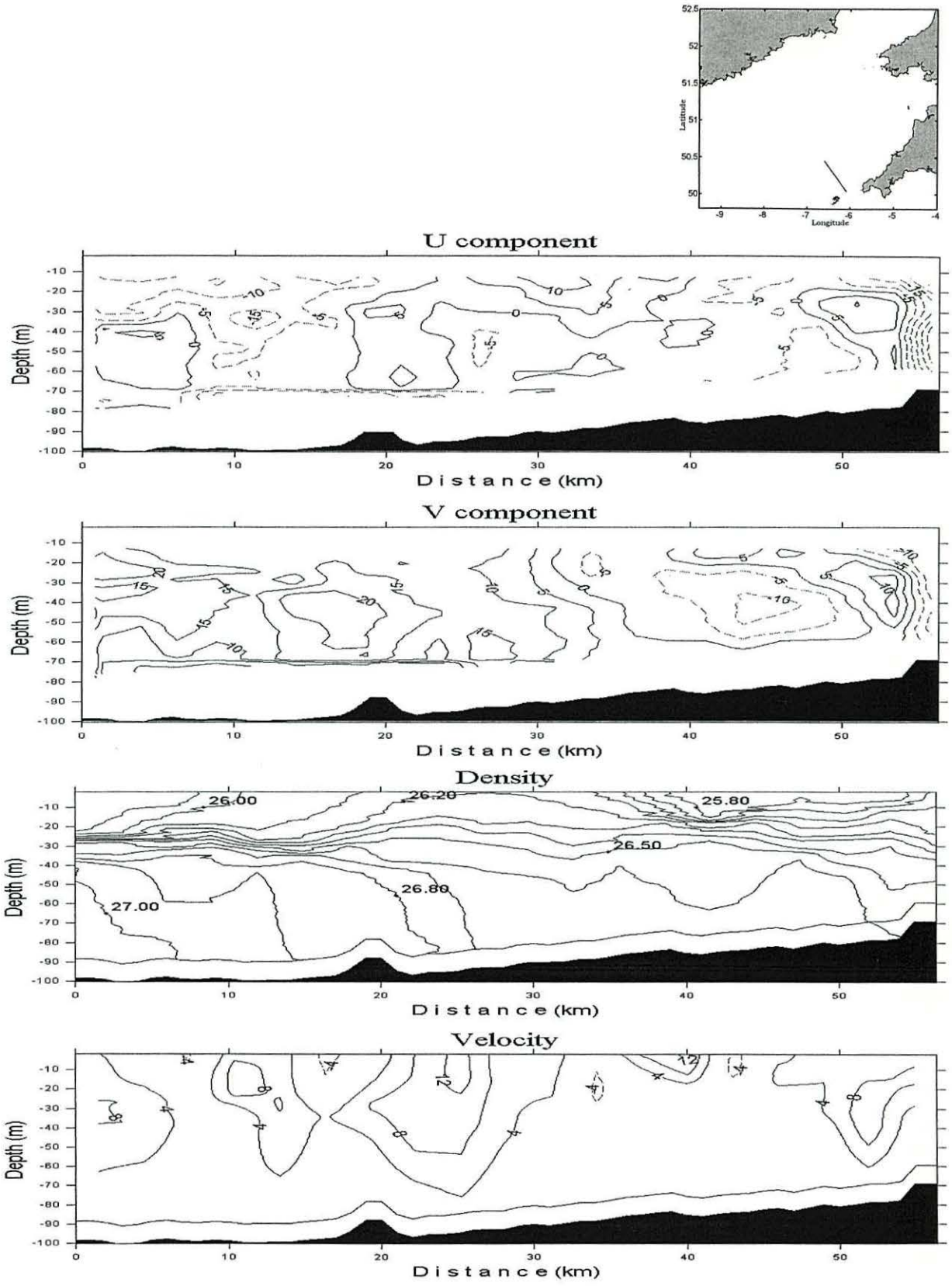

Figure A7.14 ADCP residuals for Leg 181 (top-right corner panel shows location). a) U-component (west-east), b) V-component (north-south), c) density (σ_t) in kg m^{-3} and d) geostrophic velocities. Velocities in cm s^{-1}.

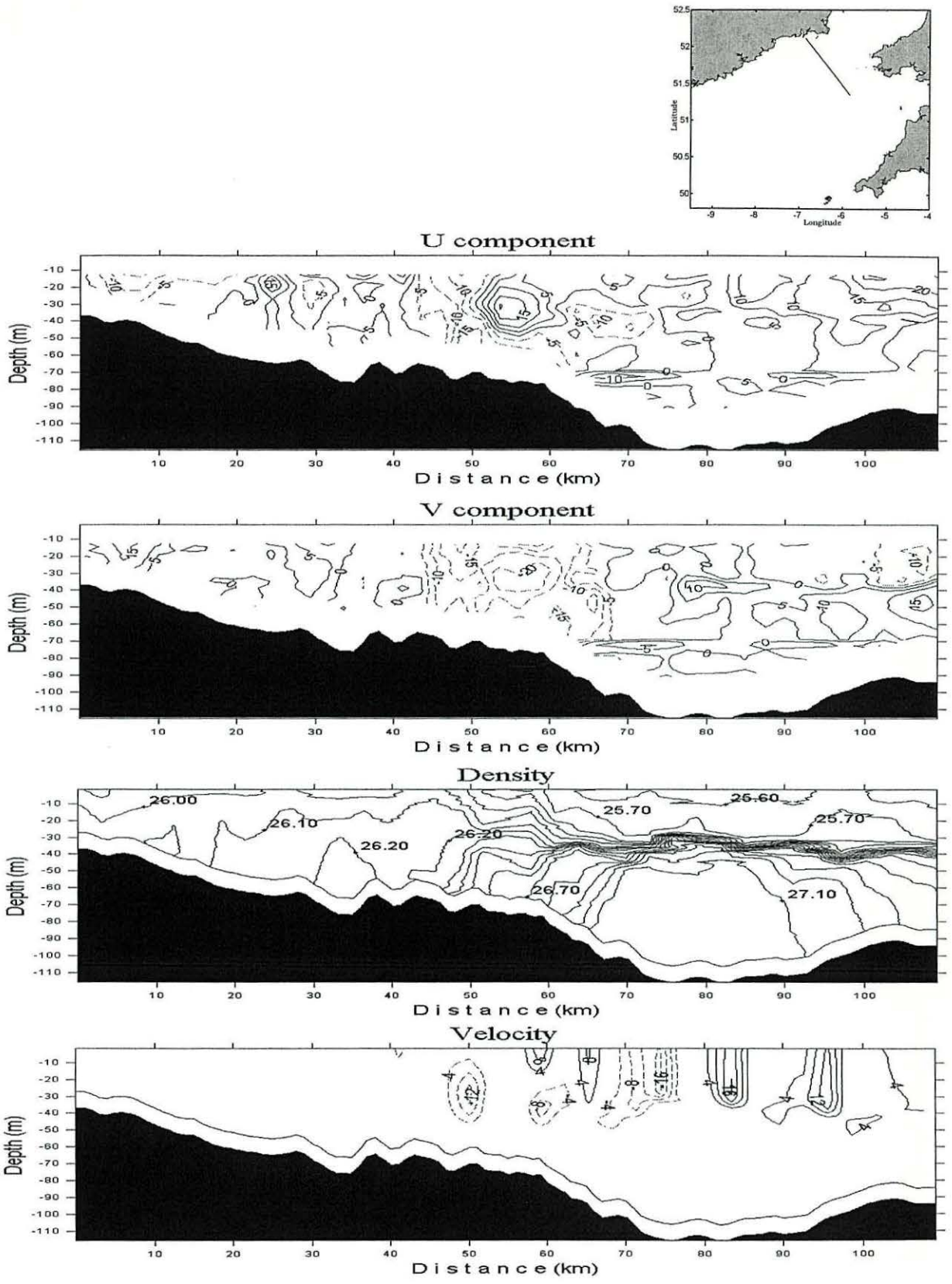

Figure A7.15 ADCP residuals for Leg 186 (top-right corner panel shows location). a) U-component (west-east), b) V-component (north-south), c) density (σ_t) in kg m^{-3} and d) geostrophic velocities. Velocities in cm s^{-1}.

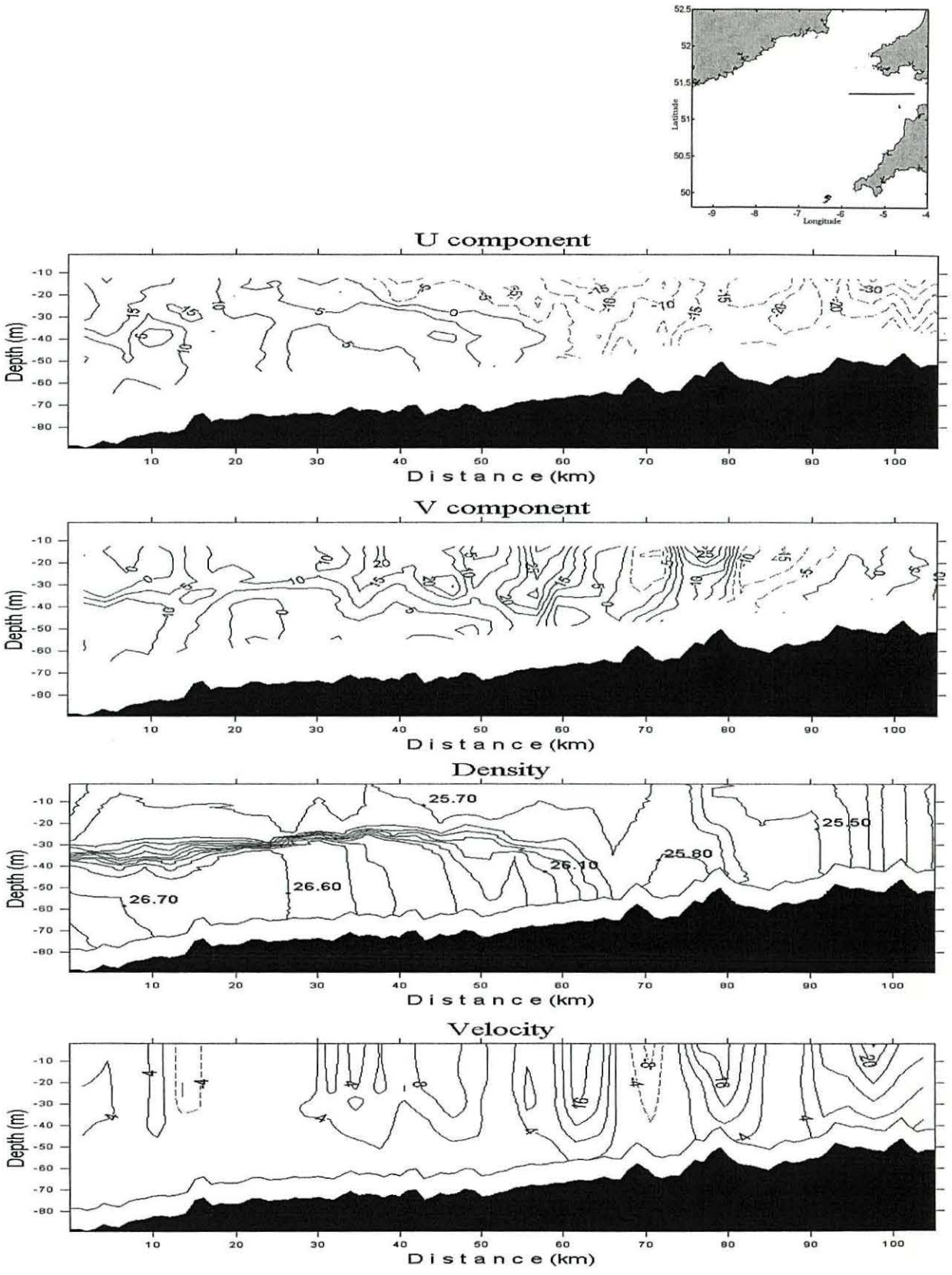

Figure A7.16 ADCP residuals for Leg 187 (top-right corner panel shows location). a) U-component (west-east), b) V-component (north-south), c) density (σ_t) in kg m^{-3} and d) geostrophic velocities. Velocities in cm s^{-1}.

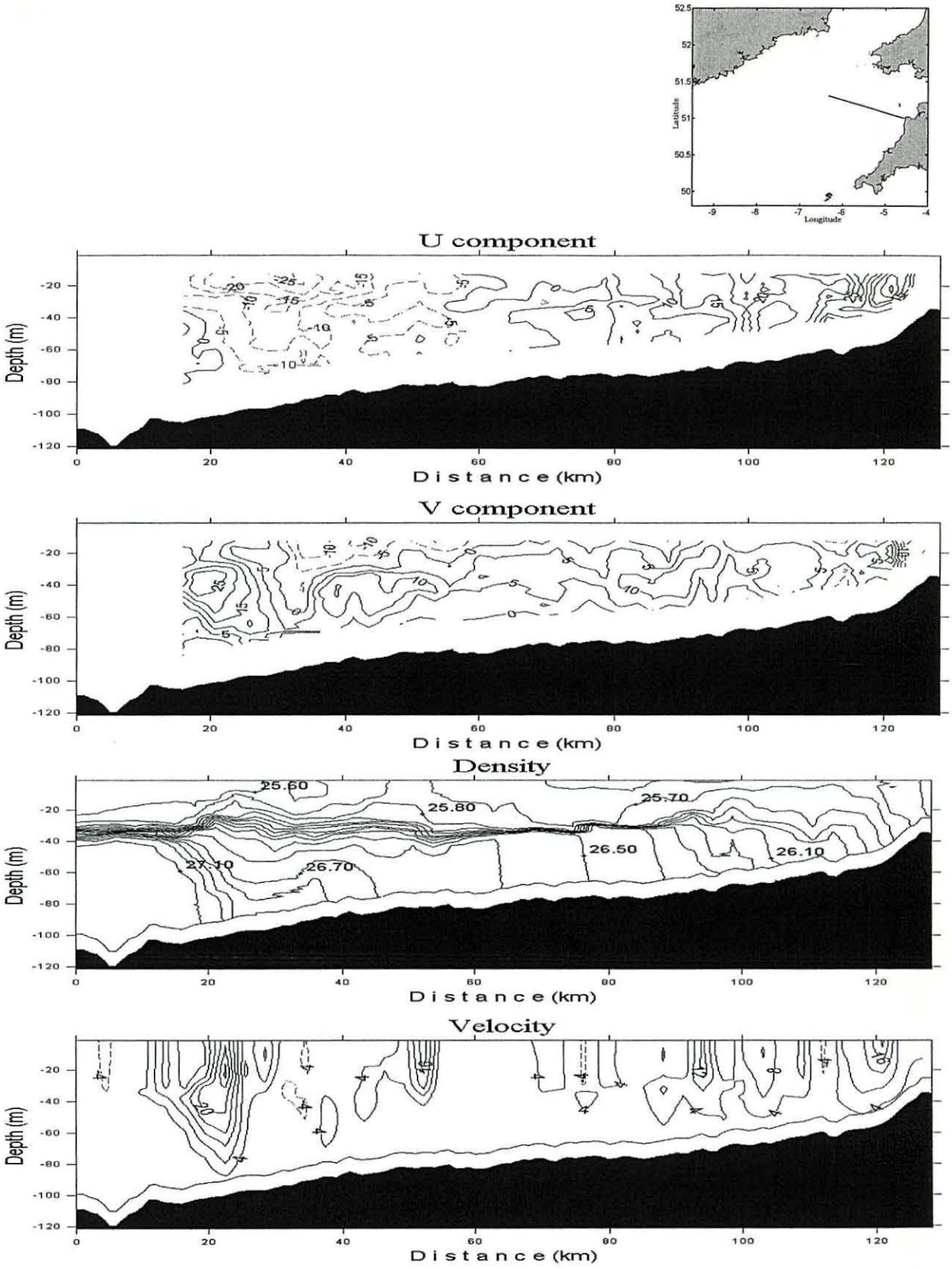

Figure A7.17 ADCP residuals for Leg 189 (top-right corner panel shows location). a) U-component (west-east), b) V-component (north-south), c) density (σ_t) in kg m^{-3} and d) geostrophic velocities. Velocities in cm s^{-1}.

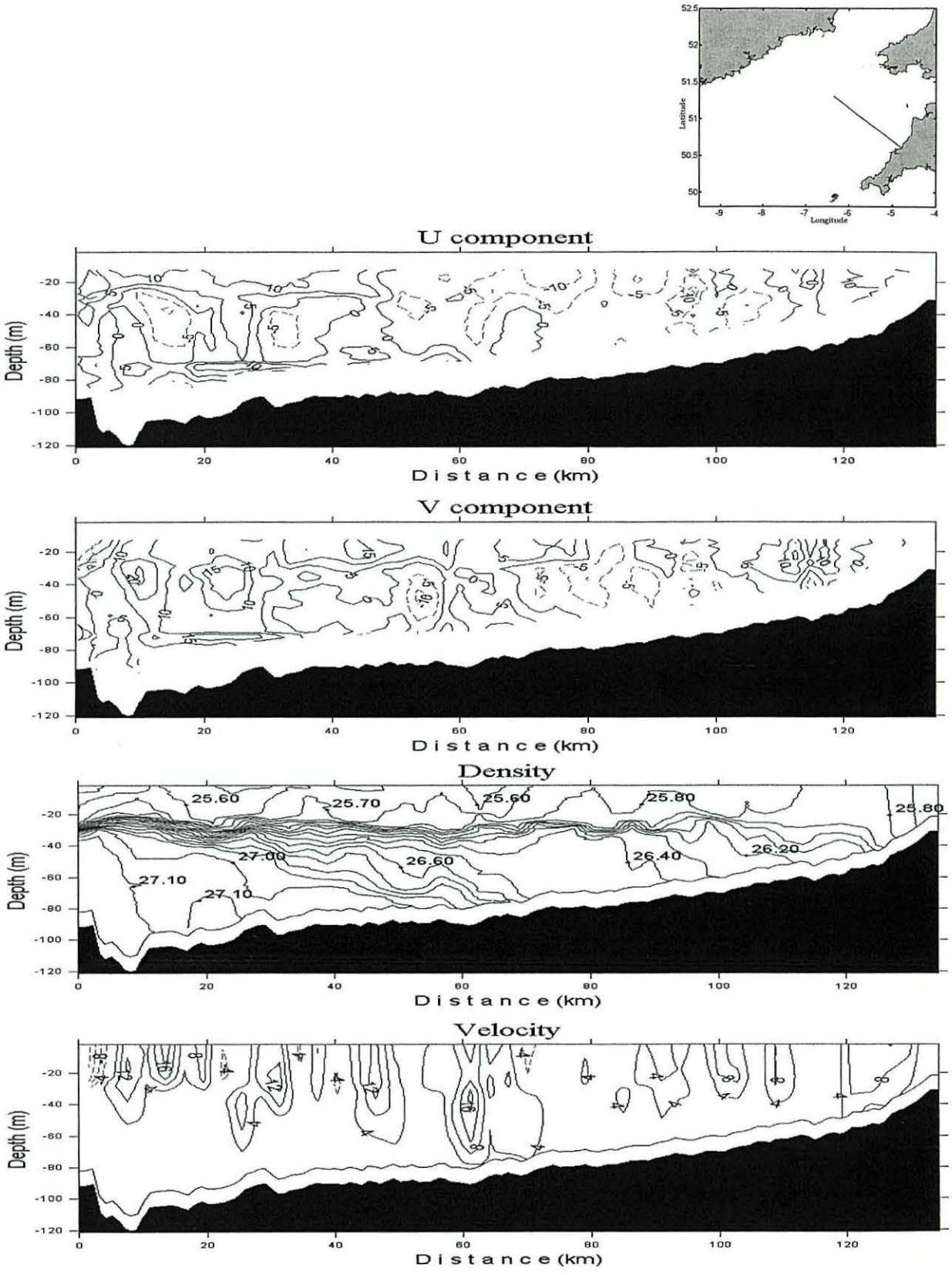

Figure A7.18 ADCP residuals for Leg 201 (top-right corner panel shows location). a) U-component (west-east), b) V-component (north-south), c) density (σ_t) in kg m^{-3} and d) geostrophic velocities. Velocities in cm s^{-1}.

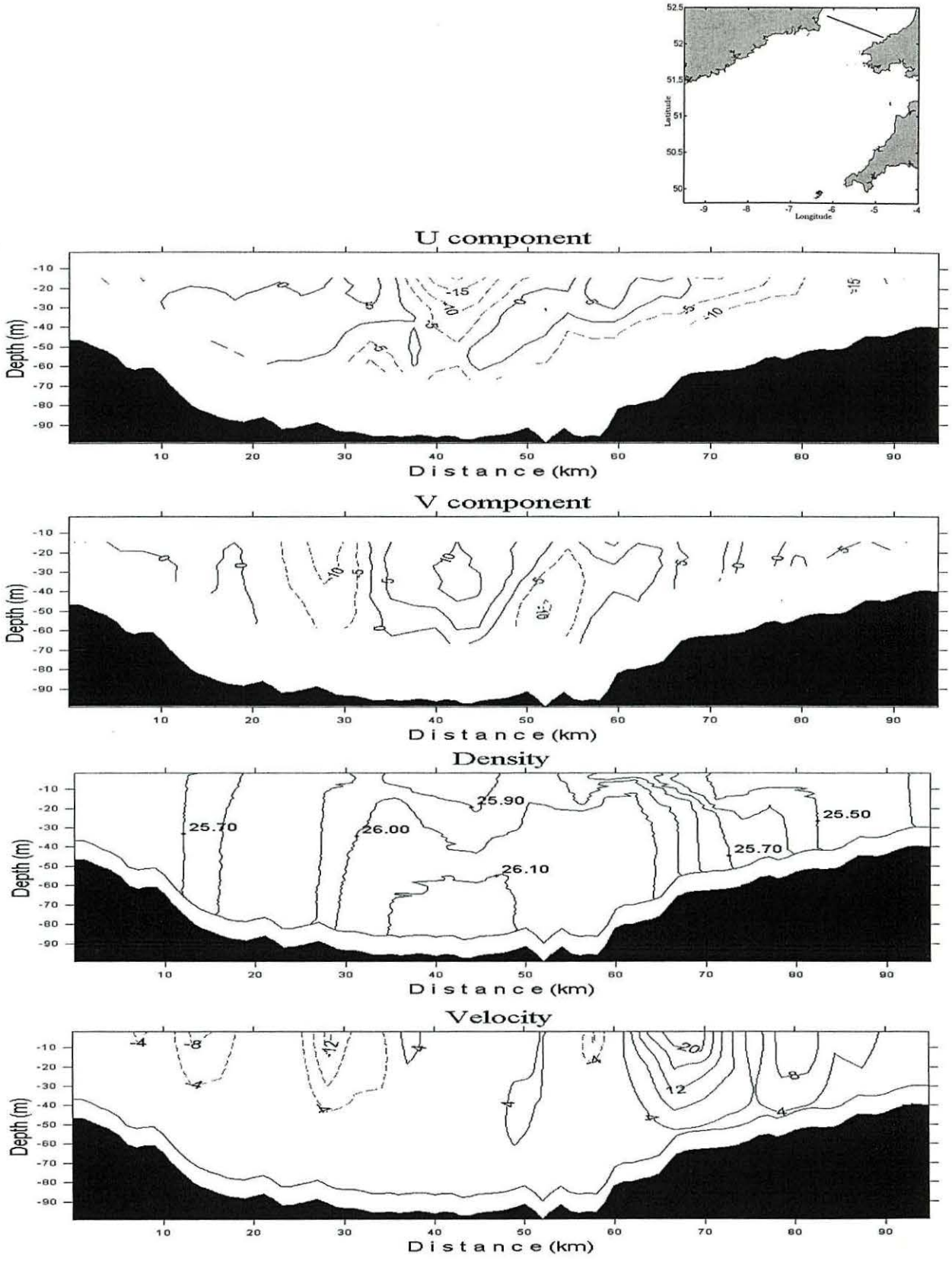

Figure A7.19 ADCP residuals for Leg 210 (top-right corner panel shows location). a) U-component (west-east), b) V-component (north-south), c) density (σ_t) in kg m^{-3} and d) geostrophic velocities. Velocities in cm s^{-1}.

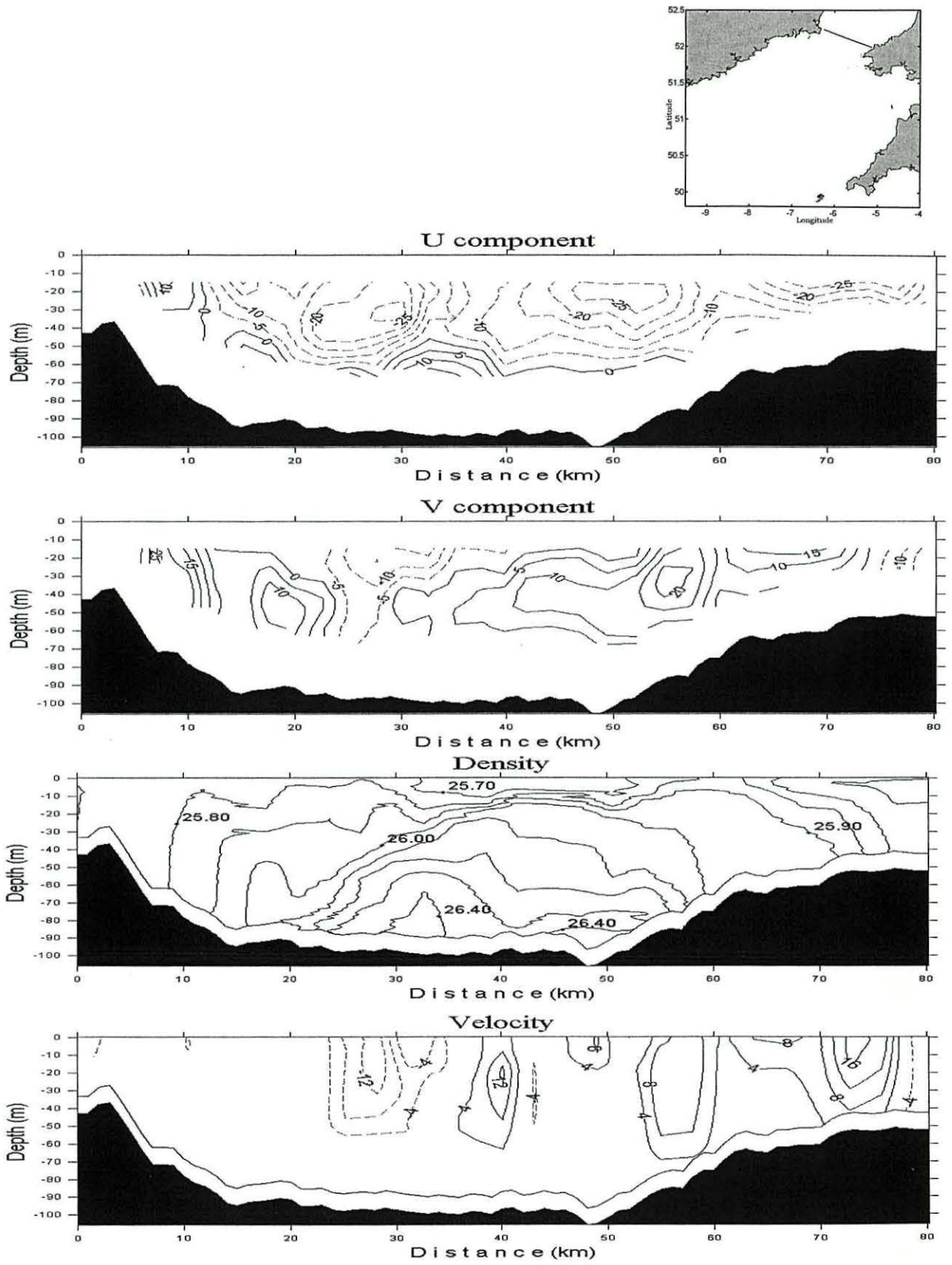

Figure A7.20 ADCP residuals for Leg 211 (top-right corner panel shows location). a) U-component (west-east), b) V-component (north-south), c) density (σ_t) in kg m^{-3} and d) geostrophic velocities. Velocities in cm s^{-1}.

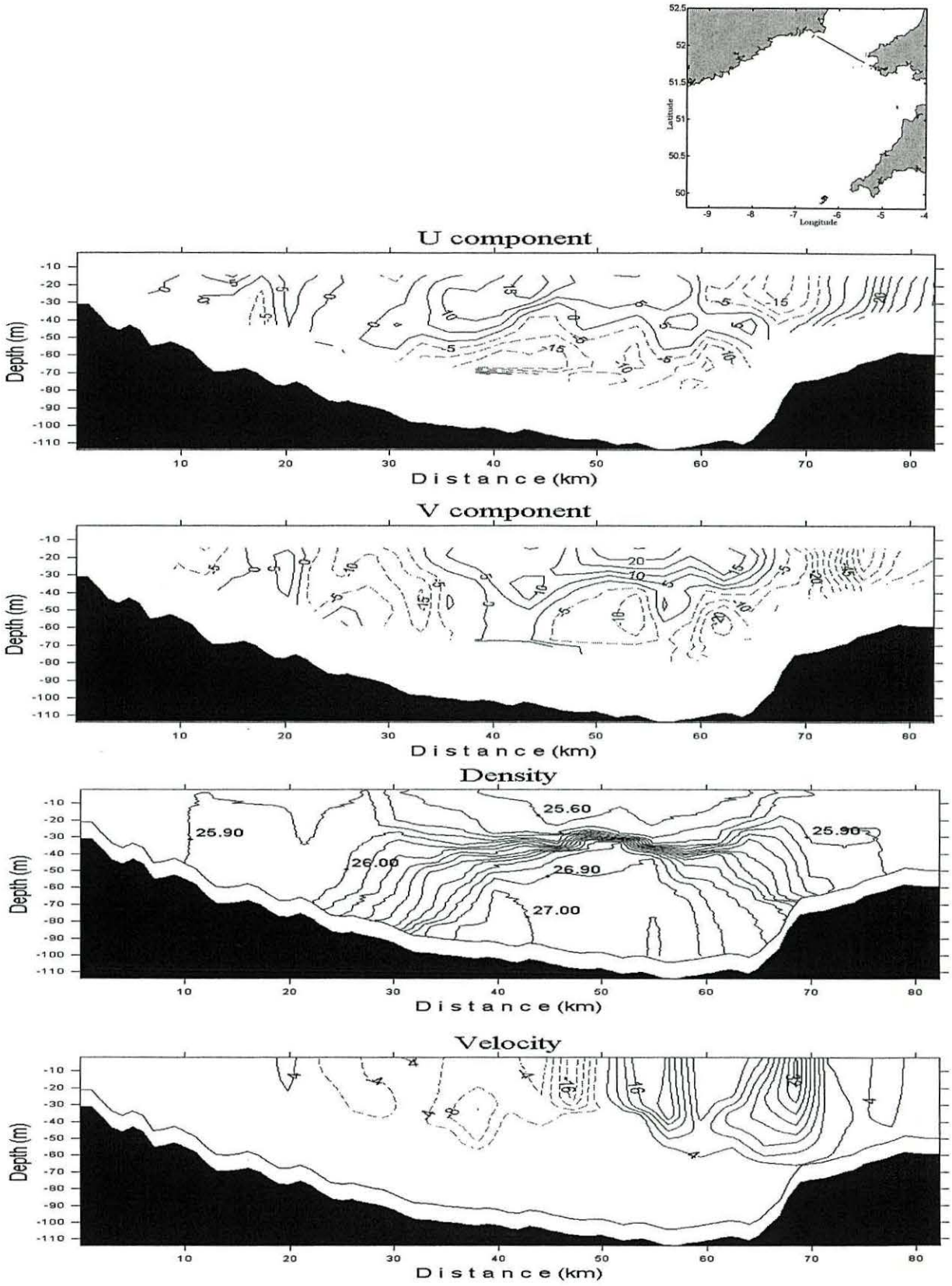

Figure A7.21 ADCP residuals for Leg 212 (top-right corner panel shows location). a) U-component (west-east), b) V-component (north-south), c) density (σ_t) in kg m^{-3} and d) geostrophic velocities. Velocities in cm s^{-1}.

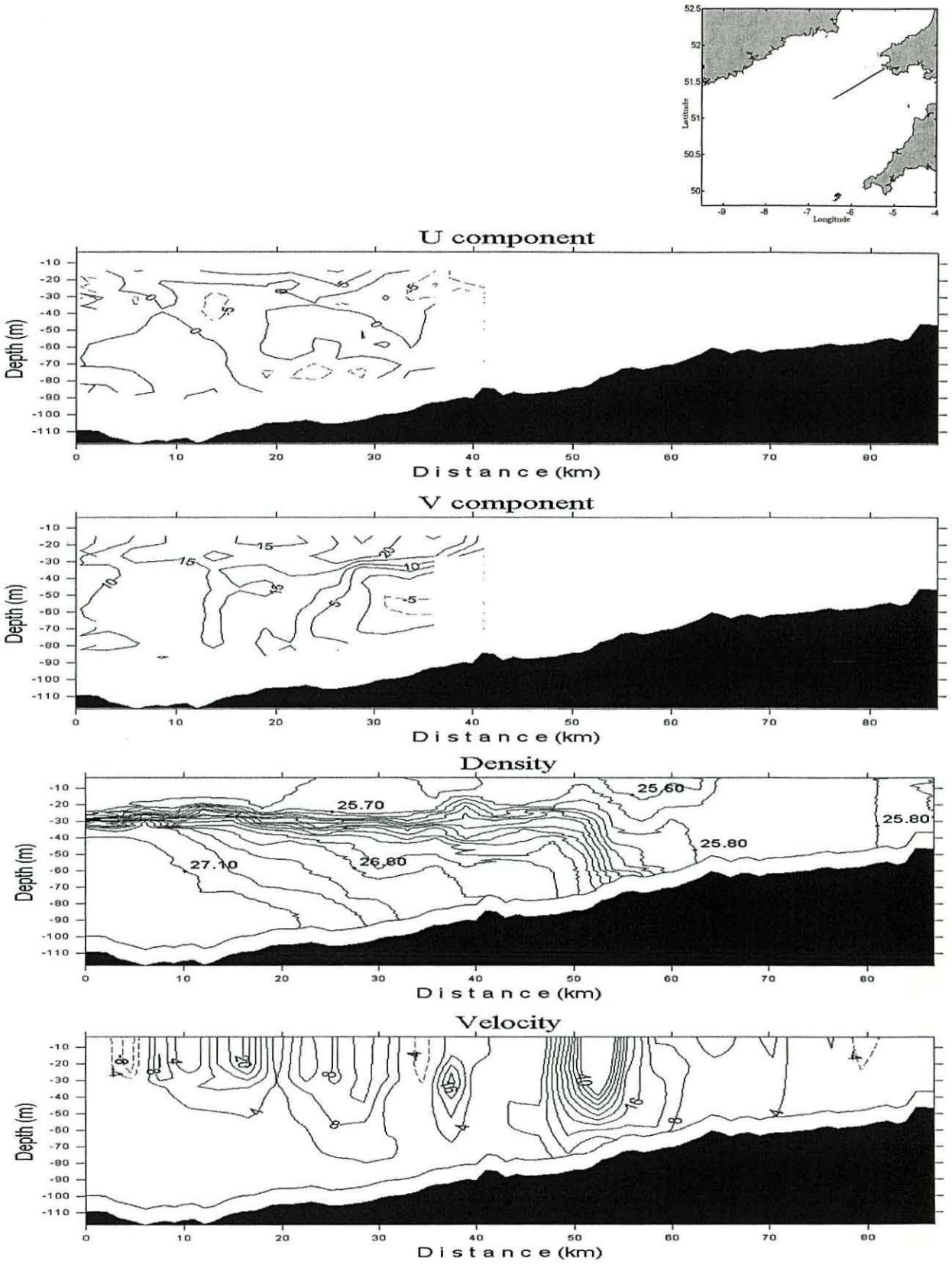

Figure A7.22 ADCP residuals for Leg 214 (top-right corner panel shows location). a) U-component (west-east), b) V-component (north-south), c) density (σ_t) in kg m^{-3} and d) geostrophic velocities. Velocities in cm s^{-1}.

Appendix 8: Sea Empress oil spill off west Wales

The Sea Empress incident occurred on 15th February 1996, off west Wales (Figure A8.1). A total of 72,000 tonnes of light crude and 480 tonnes of fuel oil are estimated to have been spilled (Elliott and Jones, 2000).

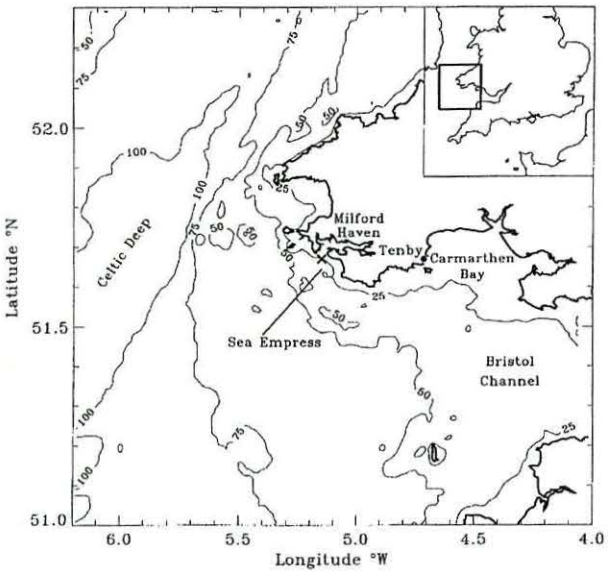

Figure A8.1.Location of the Sea Empress incident. (From Elliott and Jones, 2000).

The vessel ran aground outside the mouth of Milford Heaven, affecting the nearest shores to the south and east of the point of grounding. However, the oil spread further eastwards along the open Pembrokeshire coast (Fig A8.2) and, during the weeks of the incident, the oil was observed across a wide area of the Bristol Channel (Fig A8.1) (Dyrynda and Symberlist, 2000, http://www.swan.ac.uk/biosci/empress/main.htm). The most distant zones affected included those around Lundy Island (Fig A8.1) and south-east coast of Ireland (Dyrynda and Symberlist, 2000, http://www.swan.ac.uk/biosci/empress/main.htm).

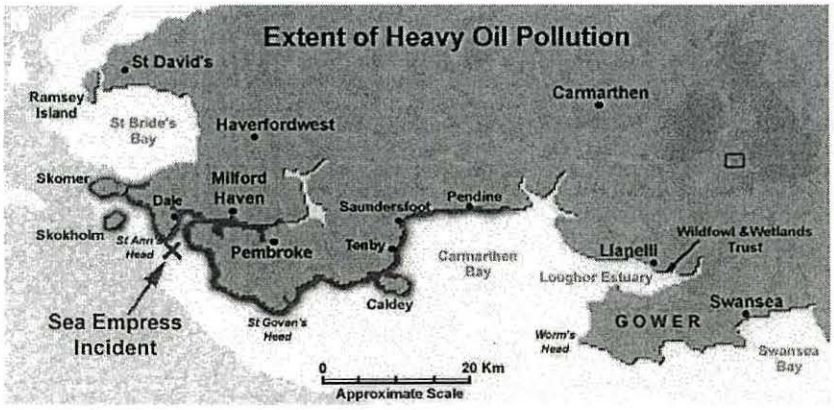

Figure A8.2. Map showing the area affected by the oil pollution during February and March 1996 by the Sea Empress incident. (From Dyrynda and Symberlist, 2000, http://www.swan.ac.uk/biosci/empress/main.htm).

Figure A8.3 shows a simulation of the oil movement by the spill model (barotropic and wind forced) used by Elliott and Jones (2000). The simulated slicks agreed well with observations of the oil movement which followed the changes in wind direction (Elliott and Jones, 2000). Initially, the oil spill responded to westerly winds (Fig A8.4) moving eastward along the coast (Fig A8.3a). About three days after the incident, wind changed its direction towards more northerly winds (Fig A8.4) moving the oil spill offshore (Fig A8.3b). After 21st February, a reversal in the wind direction was observed (Fig A8.4) influencing the returned onshore of the oil (Figs A8.3c and 3b) (Elliott and Jones, 2000).

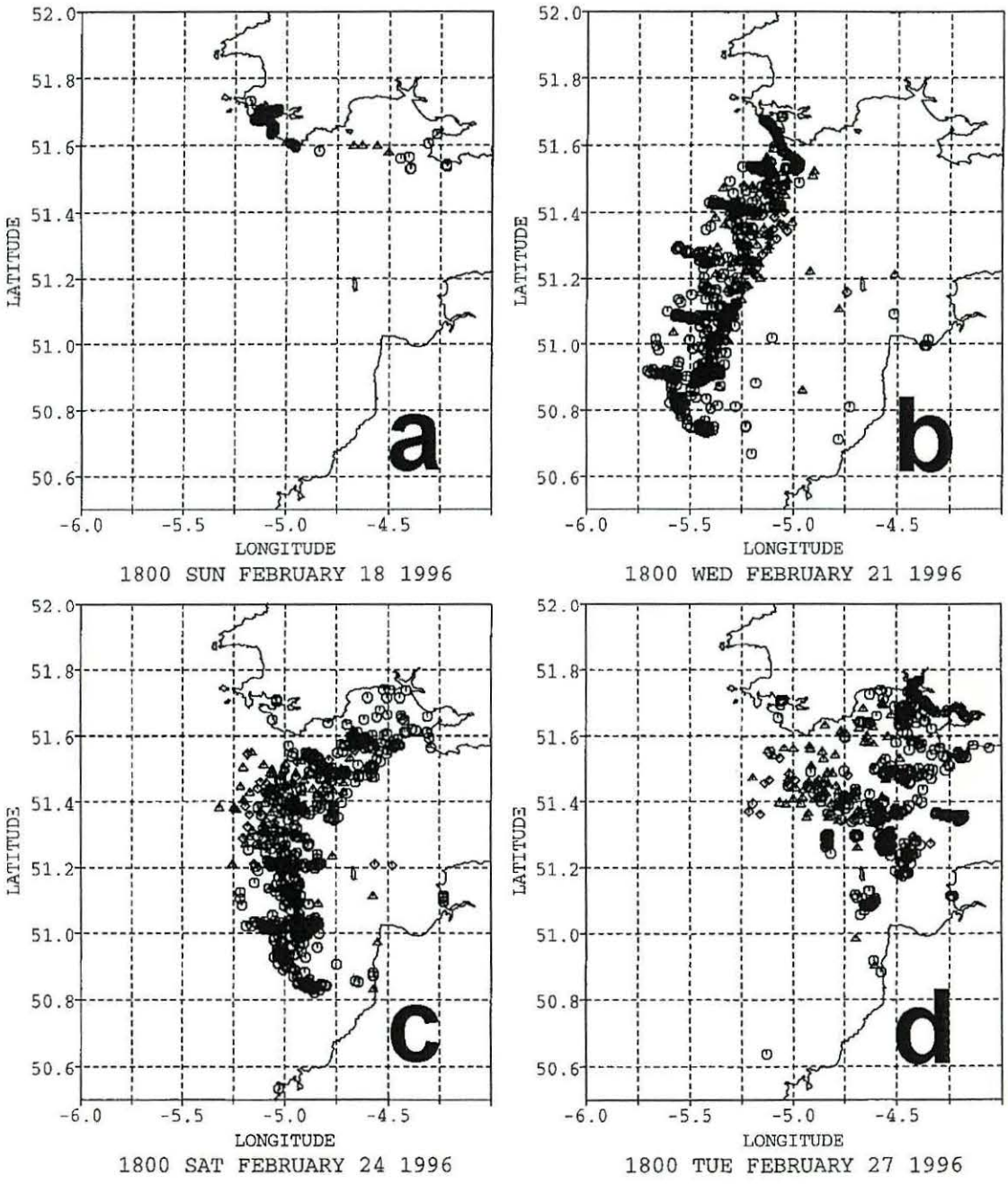

Figure A8.3. Hindcast simulations of oil movement, the slick position is shown at 3 day intervals. (From Elliott and Jones, 2000).

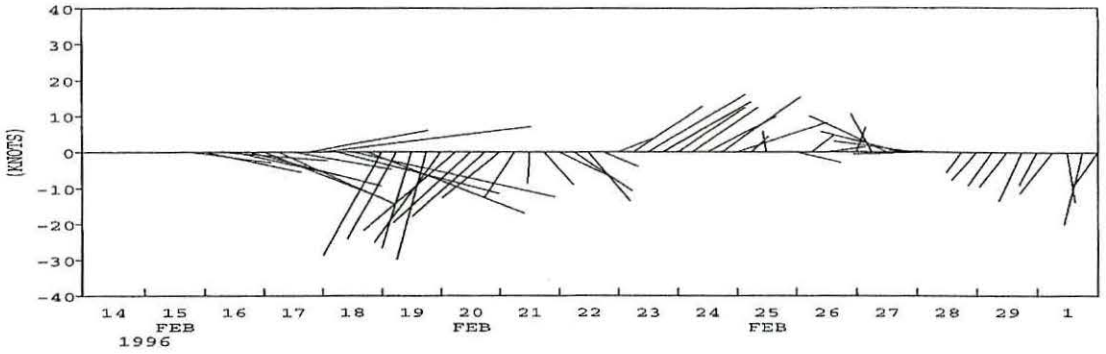

Figure A8.4. Time series of wind vector in the area derived from the UKMOD mesoscale model. (From Elliott and Jones, 2000).

The incident caused considerable difficulties for the fishing industry within the region, made unpleasant major bathing beaches and significantly damaged the wildlife. However, a natural recovery is expected in the long-term. The Sea Empress incident occurred during winter but measurements in this thesis (*e.g.* Fig 5.4) and by Horsburgh *et al.* (1998) show that in summer strong baroclinic jets are present in the region. Hence knowledge of the dispersal of the baroclinic currents is likely to be important for summertime oil and chemical spills.